NANYANG TECHNOLOGICAL UNIVERSITY

MODULAR PEPTIDE BINDING INTERACTIONS OF SUCKER-RING TEETH PROTEINS

HIEW SHU HUI

SCHOOL OF MATERIALS SCIENCE AND ENGINEERING

2016

MODULAR PEPTIDE BINDING INTERACTIONS OF SUCKER-RING TEETH PROTEINS

HIEW SHU HUI

SCHOOL OF MATERIALS SCIENCE AND ENGINEERING

A thesis submitted to the Nanyang Technological University in partial fulfilment of the requirement for the degree of Doctor of Philosophy

2016

Statement of Originality

I hereby certify that the work embodied in this thesis is the result of original research and has not been submitted for a higher degree to any other University or Institution.

11th August 2016
. . . . . .
Date


. . . . . .
Hiew Shu Hui

Abstract

Biomimetics is highly integrated into our lives, inspiring us with ideas to advance technology and to design novel materials. The sucker ring teeth (SRT) of the Humboldt squid (*Dosidicus gigas*) is one such intriguing example, being a natural biotool that is both hard and strong, yet non-mineralized and fully proteinaceous (comprising of proteins named suckerins). With the aim of identifying the main building block of the SRT that endows the material with its mechanical strength, a bottom-up approach was undertaken to gain insight into the material's design strategy and to obtain valuable molecular information.

The first study attempts to dissect the suckerin-19 protein and examine the interactions between the highly repetitive modular suckerin peptide sequences found within, at the molecular level. Using a partial combinatorial chemistry approach, a library of identified modular peptides was screened for interactions with a peptide macro-array binding assay. Peptides that exhibit the highest "hits" indicate strong interactions, providing an insight to the propensity of high affinities between peptide sequences within the bio-system. Further examination of suckerin peptides using CD spectroscopy and FTIR spectroscopy found that they have high propensities to adopt β-sheet secondary structures. His-rich suckerin peptides tend to adopt PPII and β–sheet secondary structures and remain stable and soluble at high concentrations, while Ala-rich suckerin peptides self-assemble into anisotropic microfibers, with characteristics resembling those of amyloid β-rich structures. *MD* simulations of Ala-rich fibers show the structures are highly stable while H/D exchange NMR experiments demonstrated their high stability even at elevated temperatures. These studies reveal that the assembly of SRT is most likely driven by β-sheet seeding, similar to that of amyloid growth.

The second study proceeds to explore the fabrication of new suckerin-peptide based material. Self-assembled Ala-rich microfibers were identified to have similar Young's modulus to that of the native SRT by nanoindentation, indicating that the β–sheet–forming sequence indeed contributes to the mechanical property of SRT. To

increase the size of these fibers, a longer suckerin peptide sequence comprising of Ala-rich and His-rich segments was synthesized. With a solvent-driven method, an accelerated assembly of these peptides yielded larger and longer fibers with extended and organized hierarchical structures that were rich in β–structures, as shown by WAXS and FTIR spectroscopy. By combining the two sequences that have β–sheet–forming propensities, the solubility of the β-sheet seeding Ala-rich suckerin peptide was drastically increased and longer fibers could be assembled at high peptide concentrations. These fibers maintained their mechanical robustness and possess a wide range of working conditions as they were highly tolerant of harsh environmental conditions; they resist degradation by strong denaturing chemical conditions and physical agitation, and have high melting point and thermal degradation temperature, as shown by DSC and TGA techniques respectively.

The thesis highlights the importance of both amino acid sequence and molecular interactions in constructing protein/peptide-based structural materials. By first performing fundamental research, we can equip ourselves with the knowledge and understanding of the roles of different building blocks. This then allows us to select peptide sequences according to their intrinsic properties for constructing materials with their intended application-based properties. The studies presented here serve as a platform that equip us with a plethora of possibilities towards engineering new biomimetic materials; to intricately design and recreate proteinaceous and peptidic materials with tailored mechanical properties.

Acknowledgements

There have been many people who have walked alongside me during the last four years. They have provided me with guidance, opportunities and encouragement, and some have weathered the storms with me. Each and every one of them has made a change in my life in one way or another, and I would like to take this opportunity to express my heartfelt appreciation.

First and foremost, I would like to extend my sincere gratitude to my supervisor, Professor Ali Miserez from School of Materials Science & Engineering (MSE), Nanyang Technological University (NTU), for giving me the opportunity to embark on my Ph.D. journey and for providing me with the greatest support and advice. Your guidance, teaching and dedication for research have always inspired and kept me motivated throughout these years. Not forgetting that you have always been supportive of my interest in Marine Science, offering me many opportunities to explore and learn in this field over the years, and you were always generous in your encouragements. I am proud to be your student, and grateful to be a part of the dynamic Biological & Biomimetic Material Laboratory (BBML) family!

Secondly, I would like to thank Professor Brendan Orner from King's College, London, for being a wonderful teacher and mentor whom I can always turn to and rely on whenever I meet with any scientific doubts. You have played an important role in my Ph.D. journey, and your passion for research have instilled in me the confidence to pursue this degree. I still remember when you told me right at the very start, that in pursuing this path, our passion for Science is what keeps us going - like it was just yesterday.

Thirdly, I would like to extend my sincere gratitude to Professor Li Tianhu from School of Chemistry & Biological Chemistry (CBC), NTU, for encouraging me to pursue this degree and for extending generosity and help to me throughout these years. I will always be grateful for your guidance and teachings, and am indebted to your kindness.

I wish to also thank Professor Bo Liedberg and Professor Su Haibin from MSE, NTU, for being on my Thesis Advisory Committee, providing me with invaluable guidance and mentorship during the preparation of my thesis.

I would like to thank Professor Raffaele Mezzenga from ETH, Zurich, Professor Konstantin Pervushin from School of Biological Sciences (SBS), NTU and Professor Su Haibin for the collaboration opportunities and for their profound guidance.

To Dr. Toni Sanchez-Ferrer, Dr. Margaret Phillips and Dr. Zhou Feng, thank you for your great help in the collaboration projects.

I would also like to thank Dr. Paul Guerette for his spontaneous and undoubtedly wonderful ideas that he always has, and for the invaluable guidance and mentorship throughout these years.

I would also like to extend my sincere gratitude to Dr. Ondrej Zvarec, who has been an irreplaceable mentor. To me, you have been the best mentor any student could have asked for. Thank you for your patience and guidance all these time, and for always encouraging me and looking out for me during tough times. Thank you for being just a message away whenever I have any questions, you have not only been an awesome mentor, but also a great friend.

To Dr. Shahrouz Amini, Dr. Maryam Tadayon, Dr. Chua Wei Sheng, Dr. Luigi Petrone, Dr. Bram Cantaert, Dr. Ding Dawei, Ingmar Polte, Ricardo Ramos, Nicolas Leclaire, Akshita Kumar, Loke Jun Jie, Tan Bee Yi and Ho Chin Guan, I am grateful for all your help in various areas and your sincere friendship, and also, my warmest thanks to all other wonderful lab members and colleagues from Centre for Biomimetic Sensor Science (CBSS) who have helped in one way or another.

I also wish to express heartfelt thanks to my close friends, Serena, Novi, Siew Hui, Kar Leng, Deniece, and Joel for their sincere friendship and support; to Khulan for her company during late lab nights and for being an awesome friend; to Stephen for his

insightful guidance and great help in completing this thesis and in other life aspects; to Abbas for being a friend whom I can always turn to in lab.

I am grateful for all the help extended to me from administrative staff and lab technicians from both MSE and CBC. Special thanks to Ai Hua, Jasmine, Zhang Hao, Kek Foo, Tee Guan, Mian Rong, Jefri, Novi and Shu Jun for their help during my lab work in CBC.

I would also like to thank NTU and MSE for my scholarship and the opportunity to pursue my Ph.D. degree.

Finally, I would like to express my utmost gratitude to my family for their unconditional love and support. To my dearest mom and dad, Yit Ngoh and Kok Wan, who have been my pillar of support, without whom this thesis would not have been possible: thank you for believing in me and for giving me the freedom to further my studies, despite knowing that many others at my age have joined the working force and that this is a road less traveled. Thank you for all your understanding, sacrifices and encouragements throughout these years.

To my dearest grandparents, my grandmother 陈凤英, and late grandfather 丘均喜 (1918 – 2016), who have been the proudest of my academic achievements since I was young and who have always been supportive of me in many aspects of my life: words cannot express how much I appreciate having both of you in my life, and thank you most sincerely, for your unconditional love and encouragements.

To my dear husband, Kok Yong, who stood by me through both the good and tough times: thank you for being most understanding and for your unconditional support.

This page is intentionally left blank.

Table of Contents

Table Captions

Figure Captions

Figure 1.1 Biogeographical distribution of *Dosidicus gigas* in the eastern Pacific. Records of the geographical range of the squids from at different periods are highlighted. Adapted from Staaf *et al*.

Figure 1.2 Drawing of Jumbo squid (*Dosidicus gigas*) and its appendages by French naturalist, Alcide D'Orbigny. SRTs are depicted as ring-like structures with triangular dentitions surrounding the rim of the ring, shown on both sides of the drawing. (Voyage dans l'Amerique Meridionale: Tome Neuvieme. 1847.)

Figure 2.1 Jumbo squid and their sucker ring teeth. (A) A pair of Jumbo squids and **(B)** a tentacle showing sucker cups with embedded teeth, both photographed by National Geographic Photographer, Brian J. Skerry. A zoom-in view of a single sucker cup with SRT is shown in inset figure. **(C)** A single SRT extracted from the sucker cup.

Figure 2.2 Mechanical properties and structure of Humboldt squid sucker ring teeth. Scanning electron microscope (SEM) image showing **(A)** the nano-tubular structure of a SRT fracture section and **(B)** the porous tubular cross-section of the teeth with inset presenting a scanning probe microscope image of the SRT's porous cross-section using a nanoindentor in the scanning mode. **(C)** Materials selection chart (Ashby plot of biological materials with SRT core and periphery indicated, and **(D)** Ashby plot of engineering materials such as polymers, metals and ceramic materials, with dried native squid sucker ring teeth (values ranging from core to periphery) indicated. **(E)** Tensile test curves performed on melt-cast processed SRT ribbons at different humidities, revealing ductile-to-brittle transition from wet to dry samples.

Figure 2.3 Cephalopod species, their sucker ring teeth and suckerins. (A) Scalar comparison of three cephalopod species, Jumbo squid (*D. gigas*)- top, Bigfin reef squid (*S. lessoniana*)- middle and Golden cuttlefish (*S. esulenta*)- bottom, and their respective SRT **(B)**. **(C)** Modular architecture of a representative Jumbo squid suckerin (suckerin-12) showing regular Pro placement, flanking [M1] modules. **(D)**

Distribution of the number of amino acid residues between consecutive Pro for all Jumbo squid suckerins. **(E)** Phylogenetic tree depicting relationships of all known suckerin proteins, with the classification of six clades.

Figure 2.4 Molecular design and nano-scale structure of SRT. (A) Raman spectra obtained in cross-polarized modes indicate that β-sheets within the SRT are randomly oriented. Radial integration pattern of intensities of **(B)** SAXS and **(C)** WAXS experiments performed on native SRT. **(D)** Schematic illustration of thermally induced transformations at the molecular (bottom) and nano-scale (top), as observed from WAXS and SAXS respectively. **(E)** Schematic illustration of molecular and nano-scale structure of native, reconstituted and stretched SRT.

Figure 2.5 Thermal processing processes and extrusion of filaments from native SRT. (A) Native SRT were grounded into powder form, then mixed with plasticizing agents (50% SRT, 25% water and 25% glycerol by weight) and heated to 150 °C. **(B)** A 1.5 mm diameter feed filament was vacuum formed from the molten SRT mixture, which could then be **(D)** thermally extruded into a 300 μm diameter filament through a fused filament fabrication print head attached to a robotic arm **(C)**.

Figure 2.6 Crosslinked suckerin-19 hydrogels. (A) Photographs of crosslinked suckerin-19 gels under normal light (top) and UV light (bottom), which illustrates the fluorescence arising from the formation of di-Tyr crosslinks. Spatial presentation of β-sheet strands, with **(B)** "β-sheet locking" present under moderate di-Tyr crosslinking density condition and **(C)** high di-Tyr crosslinking density, which results in the constrained flexibility of amorphous domains, eventually frustrating β-sheet formation. **(D)** Tissue elasticity of a range of biological tissues in comparison with the achieved elastic moduli of processed suckerin-19.

Figure 2.7 Growth of Au nanoparticles promoted by suckerins. (A) SEM and **(B)** TEM images of triangular or truncated triangular-shaped Au nanoparticles formed by the addition of suckerin-19 protein solution to a solution of $HAuCl_4$. **(C)** SEM images of fabricated suckerin-12 nanotubes covered with Au nanoparticles, with EDX (inset) validating the presence of gold on the nanotubes' surface. **(D)** Illustration of the

nanotubular structure fabrication procedure, followed by coating with Au nanoparticles. **(E)** UV-vis spectra of suckerin-12 film with the growth of Au nanoparticles and an image of the protein film on a glass slide (inset). **(F)** TEM image of suckerin-12 film covered with Au nanoparticles and the corresponding SAED pattern (inset).

Figure 2.8 Spider silk structural and mechanical properties. (A) A hierarchical illustration of spider silk fiber, adapted from Keten *et al*. **(B)** Stress-strain tensile curves of spider *Araneus diadematus* dragline and viscid silk, adapted from Gosline *et al*. **(C)** Schematic structure of MA silk, showing the arrangement of crystalline β-sheets amongst the amorphous phase, adapted from Romer and Scheibel.

Figure 2.9 Structural breakdown of amyloid fibers. (A) A hierarchical illustration of amyloid plaques, adapted from Knowles *et al*. **(B)** 3D illustration of cross-β structure of amyloid fibril formed by peptide GNNQQNY sequence, adapted from Nelson *et al*. **(C)** X-ray diffraction pattern of amyloid fibrils with fiber axis indicated, adapted from Rambaran and Serpell.

Figure 3.1 A Fmoc SPPS procedure. Solid phase resin with a selected functional group "X" is activated by the first amino acid attachment, (i). Fmoc protecting group is removed via a (ii) deprotection step before the amine is exposed to allow for subsequent amino acid coupling, (iii). The deprotection and coupling steps are repeated until the peptide sequence has been fully constructed then a final deprotection and (iv) cleavage will release the peptide from the resin.

Figure 3.2 TNBS (2,4,6-trinitrobenzene sulfonic acid) test on resin beads. TNBS test is used to detect primary amino groups. TNBS was used to monitor the coupling reactions; the presence of free $–NH_2$, gives a positive result where the beads turn orange (left image), indicating complete deptrotection. In the absence of free $–NH_2$ groups, a negative result can be observed where the beads remain colorless (right image), indicating successful and complete coupling reaction.

Figure 3.3 Diketopiperazine formation via β-elimination. Nucleophilic attack

from the second residue's amine group occurs at the carbonyl group of the first residue, resulting in the formation of a cyclic diketopiperazine byproduct and the removal of both residues from solid support.

Figure 3.4 Illustration of peptide immobilization onto cellulose membrane via SPOT synthesis. Peptides are first coupled onto cellulose membrane from their C-terminus by addition of coupling cocktail containing peptide and coupling agents. Capping of N-terminus is done by acetylation with acetic anhydride.

Figure 3.5 Example of bromophenol blue staining. Bromophenol blue-stained spots of immobilized peptides with free amine at N-terminus (at 2, 4 and 6 positions), indicating the successful immobilization of peptides onto cellulose via SPOT synthesis.

Figure 3.6 Molecular structure of Texas Red SE fluorescent dye. Succinimidyl ester (SE) functional group was selected for the conjugation to primary free amine group of peptides.

Figure 3.7 Colthup chart of functional groups in the mid-infrared region. Different functional groups absorb at different regions with varying intensities owing to their different vibration modes.

Figure 3.8 Assignment of secondary structures from de-convoluted amide I band. FTIR peaks de-convoluted from amide I band are assigned secondary structures, whereby in different solvent systems (H_2O or D_2O) the peak positions differ.

Figure 3.9 A schematic of indentation residual plastic impression and its loading-unloading curve. (A) A Loading-unloading curve that displays both elastic and plastic response is used to extract the stiffness (S) and contact depth (h_c) for the subsequent calculation of $\bar{E}$ and H. **(B)** Residual impression illustrated after loading tip is lifted, which can be used to find the contact area, A, between the sample and tip.

Figure 3.10 Examples of fully elastic and elastic-plastic loading-unloading curves. In a fully elastic response curve, the loading and unloading curves nearly overlap and sample returns to the original state with no residual depth of impression. A

sample that exhibits elastic-plastic response curve is left with a residual depth of impression as the unloading curve follows a different path.

Figure 3.11 Illustration of fibers embedded in epoxy and direction of indentation. The tangential cross section of the fibers were indented from the yy plane, while the transversal cross section of the fibers indented from the xx plane.

Figure 3.12 A schematic of chemical shift positions of protons attached to different functional groups. Protons attached to more electronegative groups are shifted downfield (higher ppm values) due to the increased nuclear shielding effect, and vice versa for protons attached to less electronegative groups.

Figure 3.13 Example of a polymer DSC thermogram. Exothermic and endothermic phase transitions can be observed by the positive or negative heat flow in the thermogram.

Figure 3.14 Illustration of differences that might be observed in fiber diffraction patterns of antiparallel β–structures. (A) Illustration of β-strands oriented parallel to the fiber axis (silk-like; also note that the hydrogen bonds are oriented perpendicular to the fiber axis) and its diffraction pattern **(B)**, and β-strands chains oriented perpendicular to the fiber axis (cross-β amyloid-like; hydrogen bonds oriented parallel to the fiber axis) **(C)** and its diffraction pattern **(D)**.

Figure 4.1 Full-length amino acid sequence of suckerin-19. Alignment of the residues are emphasized by highlighting the main modular peptides (bold and underlined: signal peptide; highlighted in red: Ala-rich and His-rich modules; highlighted in blue: Gly-rich modules).

Figure 4.2 Illustration of peptide macro-array binding assay. Peptide macro-array binding experiment: ligand peptides were immobilized onto a cellulose membrane and acetylated to cap the free amine. The fluorescent-tagged peptide analytes were then incubated, followed by stringent washing.

Figure 4.3 Results of peptide macro-array binding assay. The fluorescence intensity values, which indicate the extent of binding interactions between the analytes and ligands, were obtained from a quadruplicate screening of each interaction, and plotted versus the immobilized ligand peptides.

Figure 4.4 Heatmap of suckerin peptide macro-array binding assay. Relative interaction strength was obtained from the fluorescence intensity of each spot (blue shading: low level of interactions; red shading: high level of interactions). Average intensity values were obtained from quadruplicate screening of each interaction. The boxed diagonals indicate the intensity values derived from homo-interactions of a single peptide.

Figure 4.5 FESEM images of peptide microfibers. Fibers formed by peptide **A1** at **(A)** pH 4, **(B)** pH 7 and **(C)** pH 8.6 were all observed to have similar morphologies, with fiber thickness of 30–50 nm and appear to bundle together to form thicker fibers. Fibers formed by peptide **A2** at **(D)** pH 4, **(E)** pH 7 and **(F)** pH 8.6 were similar but appear to be randomly oriented with less directionality as compared to **A1** microfibers.

Figure 4.6 Self-assembly of peptides monitored by DLS. Peptides were incubated at pH 4 (red), 7 (green) and 8.6 (blue) at 50 μM peptide concentration. The peptides were also incubated in hydrogen-bond disrupting urea (black), serving as monomeric state controls (equilibrium state with the minimum self-assembly). **(A)** Peptide **H1**; **(B) H2**; **(C) A1** and **(D) A2**.

Figure 4.7 CD spectra of peptides monitored over a 50 day time period. His-rich peptides were incubated in buffers at pH 4, 7 and 8.6 over a period of 50 days and spectra were collected at different times. Left column, peptide **H1** and right column, peptide **H2**. Insets at pH 7 are a zoom-in view of the low ellipticity intensity spectra after 14 days.

Figure 4.8 Circular dichroism spectra of peptides monitored over 50 day time period. All four peptides were incubated in buffers at pH 4, 7 and 8.6 over a period of 50 days and spectra were collected at different times. Column 1, Peptide **H1**; column 2, **H2**; column 3, **A1**; column 4, **A2**. Insets at pH 7 are zoom-in of the low ellipticity

intensity spectra after 28 days (Ala-rich peptides) and 14 days (His-rich peptides).

Figure 4.9 ATR-FTIR spectra of suckerin peptides in solution and in dehydrated state. De-convoluted amide I region of FTIR spectra for each peptide after their incubation of 50 days at three different pHs, in solution and in dehydrated state.

Figure 4.10 ATR-FTIR spectra of suckerin Ala-rich peptide microfibers. Spectra were obtained for peptide microfibers formed at pH 4, 7 and 8.6. Insets show the zoomed-in regions of the Amide I band that was used for de-convolution of the original spectra, with sub-band location determined by secondary derivative of the spectra. Peptide **A1** at pH 4 **(A)**; pH 7 **(B)**; and pH 8.6 **(C)**. Peptide **A2** at pH 4 **(D)**; pH 7 **(E)**, and pH 8.6 **(F)**.

Figure 4.11 Congo red birefringent assay of suckerin A1 peptide microfibers. Fibers formed at **(A)** pH 4, **(B)** 7 and **(C)** 8.6. Panels show the brightfield optical microscope images of Congo red-stained fibers (top) and polarized light images of the fibers.

Figure 4.12 Congo red birefringent assay of suckerin A2 peptide microfibers. Fibers formed at **(A)** pH 4, **(B)** 7 and **(C)** 8.6. Panels show the brightfield optical microscope images of Congo red-stained fibers (top) and polarized light images of the fibers.

Figure 4.13 GGVVIA control peptide. **(A)** 3D Structure of Alzheimer's Aβ fibrils from PDB, ID: 2BEG. Five strands of Aβ (1–42) fibrils forming a β-sheet secondary structure. **(B)** Aβ (37-42) forming parallel β-sheet with a high shape complementarity parameter of S_c = 0.92. **(C)** Congo red birefringent assay of GGVVIA microfibers. Fibers were formed at pH 7 and showed positive result for the presence of amyloids. Left: brightfield optical microscope image, right: polarized light image.

Figure 4.14 Peptide A1 and its NMR proton assignment. A1 peptide molecule is illustrated in its skeletal chemical structure and 3D ball and stick model **(A)**. **(B)** A full

2D ^{1}H ^{1}H TOCSY spectrum of peptide **A1** measured at 600 MHz, 25 °C in DMSO-d_6 (left panel), and amide region of the TOCSY spectrum of **A1** showing Hα resonances of assigned residues (right panel). **(C)** ^{1}H ^{1}H- ROESY spectrum of peptide **A1** measured at 700 MHz , 25 °C in DMSO-d_6. **(D)** 1D ^{1}H NMR reference spectrum of peptide **A1** in DMSO-d_6 recorded at 700 MHz and 25 °C. The backbone amide region is magnified in inset, with assigned residues labeled.

Figure 4.15 A2 peptide and its NMR proton assignment. A2 peptide molecule is illustrated in its skeletal chemical structure and 3D ball and stick model **(A)**. **(B)** A full 2D ^{1}H ^{1}H TOCSY spectrum of peptide **A2** measured at 600 MHz, 25 °C in DMSO-d_6 (left panel), and amide region of the TOCSY spectrum of **A2** showing Hα resonances of assigned residues (right panel). **(C)** ^{1}H ^{1}H- NOESY spectrum of peptide **A2** measured at 700 MHz , 25 °C in DMSO-d_6. **(D)** 1D ^{1}H NMR reference spectrum of peptide **A2** in DMSO-d_6 recorded at 700 MHz and 25 °C. The backbone amide region is magnified in the inset, with assigned residues labeled.

Figure 4.16 1D ^{1}H NMR spectra of A1 fibers in time-series H/D exchange experiments. Spectra are shifted for illustration purposes, with the goal to highlight the decrease in signal intensities over H/D exchange time periods.

Figure 4.17 1D ^{1}H NMR H/D exchange studies on peptides A1 and A2. (A) 1D ^{1}H NMR spectra of peptide **A1** fibers showing the decrease in signal intensities as temperature increases; **(B)** Peptide **A1** residue specific hydrogen-exchange profiles as a function of temperature; **(C)** 1D ^{1}H NMR spectra of peptide **A2** fibers; **(D)** peptide **A2** residue specific hydrogen-exchange profile as a function of temperature.

Figure 4.18 ATR-FTIR spectra of peptide A1 and A2 after H/D exchange. After H/D exchange of 3 days at different temperatures, FTIR spectra were recorded for the peptide fibers and **(A)** de-convoluted amide I spectra of **A1** fibers (top) and **A2** fibers (bottom) were obtained. **(B)** Bar graphs summarizing the percentage composition of the secondary structures present in the peptide fibers after H/D exchange.

Figure 4.19 *MD* simulations of peptide fibers. Peptides were arranged in an

antiparallel fashion to impose a fibril setting that simulates the self-assembled β-sheet network of SRT peptides. **(A)** Hydrogen bond count and **(B)** β-sheet count from each peptide's *MD* simulation recorded at 0 and 200 ns of simulation. **(C)** The snapshot of simulated structure of peptide **H1** at 200 ns at pH 4 (left) and pH 7 (right), which did not show a stable β-sheet network of fibrils. **(D)** The snapshot of simulated structure of peptide **H2** at 200 ns, illustrating partial stacking of peptides that was maintained at both pH 4 (left) and pH 7 (right). Final simulated structure of **(E)** peptide **A1** and **(F)** peptide **A2**, showing highly stable fibrillar stacking structures (no differences between pH 4 and pH 7) with an increase in hydrogen bond and β-sheet counts for peptide **A2** over time.

Figure 5.1 Indentation results of A1 peptide dried microfibers. An average modulus of 6.90 ± 1.21 GPa was obtained from 59 indentations on the peptide microfibers.

Figure 5.2 Nanoindentation experiment and caveats taken. (A) An SPM image of a peptide fiber on silicon wafer substrate, taken prior to nanoindentation experiments, with indentation points indicated. **(B)** 3D view of same fiber, indicating the height of the fiber. **(C)** Comparison of loading-unloading curves obtained for substrate (glass), salt and fiber sample. **(D)** Example of indentations on peptide fibers that are affected by substrate, which can be identified from the shape of their loading-unloading curves.

Figure 5.3 Purification and verification of SPPS-synthesized AA12 peptide. (A) HPLC chromatogram of purified **AA12** peptide and **(B)** LC/MS mass spectrum of purified **AA12** peptide.

Figure 5.4 Self-assembly of peptide AA12 monitored by DLS. AA12 peptide was incubated in 3 different buffered solutions of pH 4, 7 and 8.2 at 50 μM peptide concentration and size measurements were recorded over 24 h at intervals of 10 min. The peptides were also incubated in hydrogen-bond disrupting urea (black), serving as monomeric state controls (equilibrium state with the minimum self-assembly).

Figure 5.5 CD spectra of AA12 peptide monitored over a 35 day time period. Recorded spectra of **AA12** peptide incubated in pH 4, pH 7 and pH 8.2 buffered solutions.

Figure 5.6 Analysis of CD spectra with BeStSel program. (A) BeStSel fitting of recorded spectra from Figure 5.5 obtained with RMSD values shown. **(B)** Estimated secondary structure content (%) from each fitted spectra, where 'Anti 1' refers to left-twisted antiparallel β-sheet, 'Anti 2' refers to relaxed antiparallel β-sheet, 'Anti 3' refers to right-twisted antiparallel β-sheet, 'Turn' refers to β-turn, and 'Others' refers to other structures that are non-helical, sheet or turn structures, and undefined by BeStSel program.

Figure 5.7 Illustration of competitive hydrogen-bonding for water molecules. Left panel: water and peptide molecules in solution, right panel: with the addition of acetonitrile molecules.

Figure 5.8 FESEM images of self-assembled fibers from peptide AA12. (A) Peptide fiber at 2,700 times magnification, showing a fiber's side view with a diameter > 20 μm, formed by many smaller fibrils with an average of ~1 μm diameter. Peptide fiber was imaged at **(B)** 6,500 times and **(C)** 16,000 times magnification, revealing filamentous strands of approximately 50 nm diameter. **(D)** Cross-sections of three broken fibers.

Figure 5.9 Proposed hierarchical structure of self-assembled AA12 peptide fibers. Constructed fiber and its composition of smaller fibrils and filamentous strands with measurements obtained from fiber in Figure 5.8 A to C.

Figure 5.10 Secondary structure characterization of the self-assembled peptide fibers. Optical microscopy images of **(A)** fibers observed under polarized light at 0 ° (top left) and 45 ° (top right) and after Congo red staining under normal light (bottom left) and polarized light microscopy (bottom right). **(B)** Deconvoluted FTIR spectra of fibers at the amide I region.

Figure 5.11 DSC and TGA characterizations. (A) DSC thermogram of **AA12** peptide fibers is shown, illustrating an endothermic peak at 239.7 °C (T_m), with onset at 234.3 °C and an energy requirement of 138 J/g. Insets show the zoom-in region of endothermic peak and fibers before and after DSC experiment, in Tzero pans. **(B)** TGA curve of **AA12** peptide powder is shown with the secondary derivative of the curve, highlighting the temperatures of degradation.

Figure 5.12 WAXS data of AA12 peptide fibers. (A) A representative 2D WAXS pattern and **(B)** the radial azimuthal integration pattern of the intensity as a function of the scattering vector *q*. Fiber axis was oriented vertically.

Figure 5.13 Mechanical characterization of peptide fibers via nanoindentation. (A) Schematic illustration of peptide fiber and direction of indentation to probe the mechanical properties from the xx and yy planes. **(B)** SPM images of (i) fiber's cross section (in the xx direction) and (ii) fiber's side section (in the yy direction). **(C)** Indentation results of the fibers in the xx and yy directions under hydrated and dry conditions.

Figure 5.14 Cross-section images of AA12 peptide fibers. Cross-section images of **AA12** fibers from xx direction under **(A)** optical microscope and **(B)** SEM, with berkovich tip indentation imprints enlarged. Cross-section images of **AA12** fibers from yy direction under **(C)** optical microscope and **(D)** SEM, with berkovich tip indentation imprints enlarged.

Figure 5.15 *MD* simulations of peptide AA12. Snapshots of simulation at **(A)** pH 4 and **(B)** pH 7. **(C)** Summary of simulation results, with hydrogen bond, β-sheet and β-bridge counts recorded before and after simulation.

Figure 5.16 Amyloid aggregation phases. Growth of amyloid fibrils classified into three phases, lag phase, growth phase and saturation phase.

Figure 5.17 Summary of size comparison between A1 and AA12 β-sheet forming SRT peptide. (A) Ball and stick models of peptide (i) **A1** (refer to Chapter 4) and (ii)

AA12. **(B)** FESEM images of self-assembled (i) **A1** fibers and (ii) side view of **AA12** peptide fiber, which is composed of many smaller fibrils. **(C)** Optical microscope images of (i) **A1** and (ii) **AA12** peptide fibers (viewed under polarized light for clearer illustration).

Figure 6.1 Example of sensograms and binding kinetics curves. (A) A sensogram obtained from SPR experiment between examples analyte 'A' and ligand 'B', with association, dissociation and regeneration segments indicated. **(B)** A processed binding kinetics curve obtained from sensogram, where K_{on} (association constant) and K_{off} (dissociation constant) can be derived from the respective curves.

Figure 6.2 Suckerin peptide hydrogel formed by self-assembly in water. (A) Photo of a hydrogel formed by suckerin peptide. **(B)** SEM image of hydrogel's porous network, with inset illustrating the fibrillar structures forming the gel. **(C)** Rheological measurements of peptide hydrogel showing G' and G" at a constant strain of 0.05% over a range of frequency. Inset shows amplitude sweep where linear viscoelastic region was obtained and strain % was selected for frequency sweep.

Figure 6.3 FESEM images of porous chitosan hydrogels. Chitosan hydrogels shown with and without addition of suckerin peptides. Pore size of hydrogels decreases with the addition of longer suckerin peptide.

Abbreviations

1D	1-Dimensional
2D	2-Dimemsional
3D	3-Dimensional
ACN	Acetonitrile
Ala/A	Alanine
APP	Amyloid Precursor Protein
Asp	Aspartic Acid
ATR	Attenuated Total Reflection
Au	Gold
B.mori	*Bombyx mori*
Boc	Tert-butyloxycarbonyl
BSA	bovine albumin serum
CD	Circular Dichroism
CTC	Chlorotrityl Chloride
Cys/C	Cysteine
D. gigas	*Dosidicus gigas*
DCM	Dichloromethane
DIC	N,N'-Diisopropylcarbodiimide
DIPEA/DIEA	N,N-diisopropylethylamine
DLS	Dynamic Light Scattering
DMAP	4-dimethylaminopyridine
DMF	Dimethyl Formamide
DMSO	Dimethyl Sulfoxide
DNA	Deoxyribonucleic Acid
DSC	Differential Scanning Calorimetry
DSF	Differential Scanning Fluorimetry
E.coli	*Escherichia coli*
EDS/EDX	Energy-dispersive X-ray spectroscopy
equiv.	Equivalent
ESI	Electrospray Ionization
EtOH	Ethanol

FESEM	Field Emission Scanning Electron Microscope
Fmoc	Fluorenylmethyloxycarbonyl
Fmoc-AA-OH	Fmoc Protected Amino Acid
FPLC	Fast Protein Liquid Chromatography
FTIR	Fourier Transform Infrared
Glu	Glutamic Acid
Gly/G	Glycine
H/D	Hydrogen-Deuterium Exchange
HATU	2-(1H-7-Azabenzotriazol-1-yl)--1,1,3,3-tetramethyluronium hexafluorophosphate Methanaminium
HAuCl4	Gold(III) chloride trihydrate
HDF	Human Dermal Fibroblast Cells
His/H	Histidine
hMSCs	mesenchymal stem cells
HOBt	Hydroxybenzotriazole
HPLC	High Performance Liquid Chromatography
IEP	Isoelectric Point
IEX	Ion-Exchange
Ile/I	Isoleucine
IMAC	Immobilized Metal Affinity Chromatography
IR	Infrared
L. vulgaris	*Loligo vulgaris*
LC/MS	Liquid Chromatography Mass Spectrometry
LEI	Lower secondary electron detector
Leu/L	Leucine
LVE	Linear Viscoelastic Region
MA	Major Ampullate
MD	Molecular Dynamics
MeOH	Methanol
MI	Minor Ampullate
MRW	Mean Residual Weight
MS	Mass Spectrometry
MTP	Microtiter Plate
MW	Molecular Weight

NaCl	Sodium Chloride
$NaHCO_3$	Sodium Bicarbonate
NMR	Nuclear Magnetic Resonance
NOESY	Nuclear Overhauser Effect SpectroscopY
PA	Polyamides
PAGE	Polyacrylamide Gel Electrophorosis
PBS	Phosphate-Buffered Saline
PCR	Polymerase Chain Reaction
PDI	Poly dispersity index
PE	Polyethelene
PMMA	Polymethyl Methacrylate
PMT	Photo multiplier tube
PNT	Peptide Nanotubes
PPII	Poly(Pro)II
Pro/P	Proline
Pt	Platinum
QCM	Quartz Crystal Microbalance
RACE	Rapid Amplification of cDNA Ends
RMSD	Route Mean Square Deviation
RNA	Ribonucleic Acid
ROESY	Rotating frame Overhauser Effect SpectroscopY
RP	Reversed-Phase
S. esulenta	*Sepia esulenta*
S. lessoniana	*Sepioteuthis lessoniana*
S/N	Signal to Noise
SAED	Selected Area Electron Diffraction
SAXS	Small Angle X-ray Scattering
SDS	Sodium Dodecyl Sulfate
SE	Succinimidyl Ester
SEC	Size-Exclusion Chromatography
SEI	Secondary Electron Upper Detector
SEM	Scanning Electron Microscope
Ser/S	Serine
SPM	Scanning Probe Microscopy

SPPS	Solid Phase Peptide Synthesis
SPR	Surface Plasmon Resonance
SRT	Squid Sucker Ring Teeth
TBTU	O-(Benzotriazol-1-yl)-N,N,N',N'-tetramethyluronium tetrafluoroborate
TEM	Transmission Electron Microscopy
TEV	Tabacco Etch Virus
TFA	Trifluoroacetic Acid
TGA	Thermogravimetric Analysis
Thr/T	Threonine
TIPS	Triisopropylsilane
TNBS	2,4,6-trinitrobenzenesulfonic acid
TOCSY	Total Correlation SpectroscopY
Tyr/Y	Tyrosine
UV	Ultra-violet
Val/V	Valine
WAXS	Wide Angle X-ray Scattering
ZnSe	Zinc Selenide

Chapter 1

Introduction

Nature has evolved biological materials over billions of years to facilitate their adaptation to the changing environments and to optimize their performances as they adopt specific functions. The science of biomimicry aims to enhance our environment and solve problems via adapting the unique design principles behind biological materials. One such biological system that has attracted significant interest in the past few years is the Sucker Ring Teeth (SRT) from cephalopods, notably of Humboldt (Jumbo) squids (Dosidicus gigas, D. gigas). This chapter briefly introduces the predatory squids and their unique SRT biotool, while the hypotheses and objectives surrounding this thesis are also presented.

1.1 Biological and biomimetic materials

Evolution has been ongoing for billions of years. Living organisms have developed highly-tuned designs and engineering features tailored for specific environments. Hence Nature provides inspirations for engineering designs suited to the benefit of mankind. Biomimicry, or biomimetics,[1] focuses on the study of these specific structural and functional features, with the goal of mimicking these principles to develop materials that duplicate Nature's structural or chemical principles.

Biological materials constitute the internal or external skeleton of plants and animals around us, and are usually complex composites assembled from weak building blocks.[2] The basic building blocks of 'soft' biological materials are usually made up of amino acids that form polypeptides and proteins, and of polysaccharides, or a combination of both. For hard biological materials, minerals are usually present as strengthening phases.[2] Via their specific structural design and hierarchical assembly, they bring about different defining characteristics and load-bearing functionality to the material.

Some structural biological materials can achieve outstanding mechanical properties and a lot of studies have been undertaken in the past decades to understand the multi-scale and chemical design strategies behind these properties. Examples of hard biological materials include, for instance, bone,[2-5] mantis shrimp dactyl appendage,[6-8] squid beak[9, 10] and chiton radula.[2, 11, 12] Some examples of soft structural materials include collagen,[13, 14] elastin,[15, 16] mussel byssus threads[17-19] and silk.[20, 21] By understanding the structure-function relationships of biological materials across multiple length scales, their design principles can be elucidated and adapted to engineer new biomimetic (or "bioinspired) materials.

Two general examples of well-established model biological structures and their engineering applications include: the adaptation of the tiny wax-coated rod-like structural features observed on lotus leaves, whose mimicry has led to the development of self-cleaning paint,[22, 23] and the adaptation of large tubercules of the humpback whales' flippers for turbine blades[24] that have been mimicked to achieve improved efficiency and reduce drag forces. With the enormous abundance of intriguing biological structures present in Nature, there are countless designs, which inspire and can be adapted to benefit mankind.[25]

1.2 Jumbo squids and their Sucker Ring Teeth (SRT)

One such biological system that has drawn increased interest in the biomimetic materials community is a member of the family of Ommastrephidae squids, namely the *Dosidicus Gigas.* These squids are perhaps better known by their common names, *i.e.* the Humboldt squids, as they live primarily in the Humboldt Current, off the coast of South America. They are also known as Jumbo squids, or red devils (*diablo rojo*) due to their metachrosis, flashing red and white when they communicate with one another.[26] In recent years, Jumbo squids have been invading the east Pacific waters up North (Figure 1.1), towards the west coasts of North America, including Canada and even Alaska.[27, 28] Speculations of the factors behind the expansion include climatic change that warms the oceans' temperatures, driving the squids to move towards and spawn in cooler waters.[27] Another possibility points toward climate-related changes in fish distribution and the drastic depletion of top predatory fishes such as billfish and tuna, which leads to the imbalance in the food chain and results in promoted growth and expansion of the Jumbo squid's territories.[28] In 2008, another study has attributed the ocean acidification effect on the squids' metabolic rates that drives these squids to shallower depths,[29] thus explaining the increased sightings and capture of these squids nearer to shore.

Some prominent characteristics of the Jumbo squids include their impressive sizes and speed. These squids are able to grow up to 2 m in length and weigh up to 50 kg in mass,[29] while they can swim up to speeds of 24 kph. They behave as aggressive predators with nocturnal feeding habits, rising up from their endemic depths of 700 m to the shallower surfaces in shoals of up to 1,200 individuals to feed on fishes, crustaceans and other cephalopods.

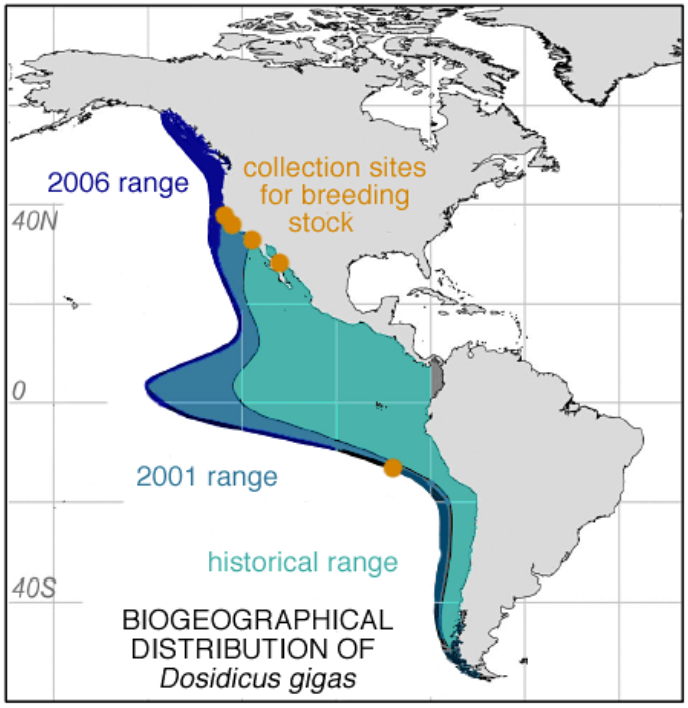

Figure 1.1 Biogeographical distribution of *Dosidicus gigas* in the eastern Pacific. Records of the geographical range of the squids from at different periods are highlighted. Adapted from Staaf *et al.*[27]

With their sharp beaks and toothed suckers the *Dosidicus Gigas* is a fearsome predator in the ocean. The hard beak[10, 30-32] of the squid is attached to a soft gelatinous buccal mass, providing inspiration for the design of limb prosthesis owing to the gradient hardness that enables ease and comfortable wearing. The hard non-mineralized teeth[33, 34] of the squid, which is embedded in the squids' sucker cuptions, could inspire the design of biocompatible surgical threads, tissue scaffolds or drug delivery capsules, to name a few possibilities. This project is inspired by the proteins isolated from squid's SRT, which will be elaborated in Chapter 2.

The first accounts of SRT from Jumbo squids date back to the expedition in the 1850's[35] by French naturalist Alcide D'Orbigny, who made beautiful drawings of SRT and other squid appendages, shown in Figure 1.2.

Figure 1.2 Drawing of Jumbo squid (*Dosidicus gigas*) and its appendages by French naturalist, Alcide D'Orbigny. SRTs are depicted as ring-like structures with triangular dentitions surrounding the rim of the ring, shown on both sides of the drawing. (Voyage dans l'Amérique Meridionale: Tome Neuvième. 1847.)

As a flexible weapon, the squid's arms come into contact with the prey and with a swift contract of the sucker cups' muscles, the cups latch onto the prey while the sharp SRT embedded within the sucker cups pierces the prey to anchor their grip.[36] With the combination of hundreds of angled hooked teeth, preys' struggling attempts to escape are often futile. The main biomechanical requirement of SRT is to firmly hold onto prey, which requires withstanding large dynamic compressive and shearing forces.

Given how recently suckerins, which are proteins that compose the SRT, were discovered in comparison to other well-known structural proteins that are being developed in the biomaterials field, such as silks,[37] resilin,[38] elastin,[15] or mussel threads,[39] only a few studies and applications of suckerin-based materials have been reported, and discussed in Chapter 2. With time, suckerins may or may not gather a wider interest from the biomaterials community. For now, with our existing knowledge about the unique physico-chemical characteristics of suckerins, there is definitely ample room for further developments of this protein material to be explored.

1.3 Hypothesis

Studies on the SRT to date have focused on the mechanical and structural properties of both the native teeth and the full suckerin proteins. In-depth biophysical characterizations have also been adequately performed to understand the sequence, structure and property relationship, whereby the general suckerin secondary structures have been established to comprise of randomly oriented β-sheet crystallites among amorphous phases. The main hypothesis of this thesis is that the highly modular design of peptide sequences that construct the suckerins greatly contribute to the robust mechanical properties of SRT. With the understanding of the individual role of each repetitive peptide building block that form the full-length proteins, suckerin-inspired materials can be fabricated from the rightfully selected peptide building blocks, which then preserves the chemical, physical, thermal, and robust mechanical properties of the native SRT material.

1.4 Objectives and Scope

This dissertation aims to: *(i)* provide a comprehensive understanding of the suckerin peptide building blocks, *(ii)* to identify the peptide sequences that are associated with enhancing the mechanical properties of the teeth, and *(iii)* explain their self-assembly mechanisms. Subsequently, the exploration of suckerin-inspired material fabrication is carried out by selecting specific peptide sequences from the suckerins, with the understanding of each peptide sequence's roles in the protein.

In order to achieve in-depth examination and detailed investigations of the peptides, a wide variety of characterization techniques have been employed: peptide macro-array binding assay, dynamic light scattering (DLS), Congo red birefringence assay, circular dichroism (CD) spectroscopy, Fourier transform infrared (FTIR) spectroscopy, field emission scanning electron microscopy (FESEM), nanoindentation, Nuclear magnetic resonance (NMR) spectroscopy, differential scanning calorimetry (DSC), thermogravimetric analysis (TGA), rheology, small angle X-ray scattering (SAXS), wide angle X-ray scattering (WAXS), optical microscope, UV-Vis spectroscopy and molecular dynamics (*MD*) simulation. Synthesis and purification of materials include application of techniques such as solid-phase peptide synthesis (SPPS), SPOT synthesis, the synthesis of fluorescently tagged peptides, high performance liquid chromatography (HPLC) and liquid chromatography mass spectrometry (LC/MS).

To address the hypotheses, the objectives covered by this thesis are as follow:

[1] To perform a comprehensive study of possible suckerin peptides binary interactions via a peptide macro-array binding assay;

[2] To understand these interactions at the molecular scale, and to provide explanation for the binding behaviors of the peptides via in-depth characterization of the peptides;

[3] To identify the peptide building blocks and their sequences that contribute to the SRT's robust mechanical properties;

[4] To fabricate suckerin-inspired peptide materials that mimic the mechanical properties of the native SRT via self-assembly process;

[5] To characterize the chemical, biophysical, thermal, and mechanical properties of the fabricated materials.

1.5 Dissertation Organization

Chapter 1 gives an introduction to biomimicry, followed by the introduction to the Jumbo squid and their SRT. Chapter 2 highlights the literature background of the existing research on the SRT and their detailed properties, structure and applications derived. Proteins that are similar to the SRT in terms of sequence and structural features –silk and amyloids– are presented, followed by the introduction to peptide materials developments and applications. Chapter 3 provides the rationale and the methodologies of the experimental procedures that have been employed for the synthesis of the materials and for characterization studies. Chapter 4 presents the results from the fundamental studies of the suckerin peptide interactions, while Chapter 5 explores the fabrication of suckerin peptide materials, with the selection of peptide sequence based on the understanding of the peptides in Chapter 4. Finally, Chapter 6 provides a general conclusion on the work presented in this thesis. The outlook and future studies on the suckerin peptides are discussed briefly.

References

[1] J. F. V. Vincent, *P I Mech Eng H*, **2009**, 223, 919-939.

[2] M. A. Meyers, P. Y. Chen, A. Y. M. Lin and Y. Seki, *Prog Mater Sci*, **2008**, 53, 1-206.

[3] S. Weiner, W. Traub and H. D. Wagner, *J Struct Biol*, **1999**, 126, 241-255.

[4] S. Weiner and H. D. Wagner, *Annu Rev Mater Sci*, **1998**, 28, 271-298.

[5] J. Y. Rho, L. Kuhn-Spearing and P. Zioupos, *Med Eng Phys*, **1998**, 20, 92-102.

[6] S. Amini, M. Tadayon, S. Idapalapati and A. Miserez, *Nat Mater*, **2015**, 14, 943-950.

[7] S. Amini, A. Masic, L. Bertinetti, J. S. Teguh, J. S. Herrin, X. Zhu, H. Su and A. Miserez, *Nat Commun*, **2014**, 5, 3187.

[8] J. C. Weaver, G. W. Milliron, A. Miserez, K. Evans-Lutterodt, S. Herrera, I. Gallana, W. J. Mershon, B. Swanson, P. Zavattieri, E. DiMasi and D. Kisailus, *Science*, **2012**, 336, 1275-1280.

[9] Y. Tan, S. Hoon, P. A. Guerette, W. Wei, A. Ghadban, C. Hao, A. Miserez and J. H. Waite, *Nat Chem Biol*, **2015**, 11, 488-495.

[10] A. Miserez, D. Rubin and J. H. Waite, *J Biol Chem*, **2010**, 285, 38115-38124.

[11] L. M. Gordon and D. Joester, *Nature*, **2011**, 469, 194-197.

[12] J. C. Weaver, Q. Q. Wang, A. Miserez, A. Tantuccio, R. Stromberg, K. N. Bozhilov, P. Maxwell, R. Nay, S. T. Heier, E. DiMasi and D. Kisailus, *Mater Today*, **2010**, 13, 42-52.

[13] M. D. Shoulders and R. T. Raines, *Annu Rev Biochem*, **2009**, 78, 929-958.

[14] P. Fratzl, K. Misof, I. Zizak, G. Rapp, H. Amenitsch and S. Bernstorff, *J Struct Biol*, **1998**, 122, 119-122.

[15] L. Debelle and A. M. Tamburro, *Int J Biochem Cell B*, 1999, 31, 261-272.

[16] V. J. F. V., in *Elastomeric Proteins*, ed. P. R. Shewry, Cambridge University Press, Cambridge, **2003**, pp. 352-365.

[17] E. Carrington and J. M. Gosline, *Am Malacol Bull*, **2004**, 18, 135-142.

[18] E. C. Bell and J. M. Gosline, *J Exp Biol*, **1996**, 199, 1005-1017.

[19] J. H. Waite, in *Structure, Cellular Synthesis and Assembly of Biopolymers*, ed. S. T. Case, Springer Berlin Heidelberg, Berlin, Heidelberg, **1992**, pp. 27-54.

[20] R. V. Lewis, *Chem Rev*, **2006**, 106, 3762-3774.

[21] J. M. Gosline, P. A. Guerette, C. S. Ortlepp and K. N. Savage, *J Exp Biol*, **1999**, 202, 3295-3303.

[22] P. Ragesh, V. A. Ganesh, S. V. Naira and A. S. Nair, *J Mater Chem A*, **2014**, 2, 14773-14797.

[23] V. A. Ganesh, H. K. Raut, A. S. Nair and S. Ramakrishna, *J Mater Chem*, **2011**, 21, 16304-16322.

[24] F. E. Fish, P. W. Weber, M. M. Murray and L. E. Howle, *Integr Comp Biol*, **2011**, 51, 203-213.

[25] B. Bhushan, *Philos T R Soc A*, **2009**, 367, 1445-1486.

[26] H. Rosen, W. Gilly, L. Bell, K. Abernathy and G. Marshall, *J Exp Biol*, **2015**, 218, 265-275.

[27] D. J. Staaf, L. D. Zeidberg and W. F. Gilly, *Mar Ecol Prog Ser*, **2011**, 441, 165-175.

[28] L. D. Zeidberg and B. H. Robison, *P Natl Acad Sci USA*, **2007**, 104, 12946-12948.

[29] R. Rosa and B. A. Seibel, *P Natl Acad Sci USA*, **2008**, 105, 20776-20780.

[30] A. Miserez, T. Schneberk, C. J. Sun, F. W. Zok and J. H. Waite, *Science*, **2008**, 319, 1816-1819.

[31] A. Miserez, Y. L. Li, J. H. Waite and F. Zok, *Acta Biomater*, **2007**, 3, 139-149.

[32] C. C. Broomell, R. K. Khan, D. N. Moses, A. Miserez, M. G. Pontin, G. D. Stucky, F. W. Zok and J. H. Waite, *J R Soc Interface*, **2007**, 4, 19-31.

[33] A. Miserez, J. C. Weaver, P. B. Pedersen, T. Schneeberk, R. T. Hanlon, D. Kisailus and H. Birkedal, *Adv Mater*, **2009**, 21, 401-406.

[34] A. Miserez, J. C. Weaver, D. Kisailus and H. Birkedal, *Mater Res Soc Symp P*, **2009**, 1187, 41-46.

[35] d'Orbigny, A.D. *et al. Voyage dans l'Amérique méridionale: Tome Neuvième* (Pitois-Levrault, Paris, **1847**).

[36] W. Nachtigall, *Biological mechanisms of attachment: the comparative morphology and bioengineering of organs for linkage, suction, and adhesion*, Springer-Verlag, **1974**.

[37] M. B. Hinman and R. V. Lewis, *J Biol Chem*, 1992, 267, 19320-19324.

[38] D. H. Ardell and S. O. Andersen, *Insect Biochem Molec*, **2001**, 31, 965-970.

[39] K. J. Coyne, X. X. Qin and J. H. Waite, *Science*, **1997**, 277, 1830-1832.

Chapter 2

Literature Review

Through millions of years of existence, Decapodiforme Cephalods has gradually evolved and became equipped with numerous efficiently-designed biotools for their hunting and survival needs. One structural biotool of the Jumbo Squid that has raised recent interest in the biomimicry research community is their SRT, owing to their unique composition and mechanical properties. In this chapter, a comprehensive review of the SRT will be presented, detailing their mechanical properties, protein composition and sequence design, the hierarchical molecular and nanoscale structural design of the teeth, their thermoplastic properties and some applications that have been explored in recent studies. Structural proteins sharing molecular and structural homology, namely silk and amyloids, will be discussed, with a focus on their structure-property relationships. A short introduction to research and recent development of peptide-based materials and their applications will also be touched upon. Finally the scope of the thesis will be defined in this chapter.

* Portions of this chapter were extracted from: Hiew, S. H. and Miserez, A. "Squid Sucker Ring Teeth: Multi-Scale Structure-Property Relationships, Sequencing, and Protein Engineering of a Thermoplastic Biopolymer." ACS Biomaterials Science & Engineering 2016, DOI: 10.1021/acsbiomaterials.6b00284.

2.1 Review of Jumbo Squid SRT

Jumbo squids (Figure 2.1 A) are formidable predators of the East Pacific Ocean, endowed with intelligence, sheer size and agility. They hunt prey with their appendages, which are lined with hundreds of sharp SRTs. The SRTs are embedded within the sucker cuptions found on all 8 arms and 2 feeding tentacles of the squid (Figure 2.1 B), and can be easily identified by their triangular dentitions. When extracted from the sucker cuptions, these teeth have a round basal ring where the dentitions protrude from (Figure 2.1 C). Nature has adapted SRTs with properties to withstand compressive and shearing stresses from their struggling prey and the remarkable properties of SRTs will be thoroughly covered in the following sections.

Figure 2.1 Jumbo squid and their sucker ring teeth. (A) A pair of Jumbo squids and **(B)** a tentacle showing sucker cups with embedded teeth, both photographed by National Geographic Photographer, Brian J. Skerry. A zoom-in view of a single sucker cup with SRT is shown in inset figure. **(C)** A single SRT extracted from the sucker cup.

2.1.1 SRT materials: mechanical properties and thermal processing

Mechanical characterization by nanoindentation have revealed that *D. gigas* SRT exhibit a relatively high elastic modulus considering the absence of common strengthening phases, such as minerals,[1, 2] metal ions,[3, 4] or even chitin.[5, 6] In dry conditions, the elastic modulus ranges from 7.5 GPa to 4.5 GPa from the tooth periphery to the core, respectively.[7] This modulus gradient is related to the presence of a nano-tubular gradient (Figure 2.2 A), with the tubular fraction concomitantly increasing from the periphery to the core (Figure 2.2 B). Under hydrated conditions, these moduli values drop to 2.75 GPa and 1.75 GPa, which is still considered quite

high for a fully biopolymeric material in the hydrated state. These values, in combination with SRT hardness, are shown in Figure 2.2 C on a materials selection chart of biological materials.[8] Compared to common engineering polymers,[9] SRT under dry conditions appear stiffer than many synthetic polymers (such as polyamides (PA), polymethyl methacrylate (PMMA) and high-molecular weight polyethylene (PE)) as shown in Figure 2.2 D and based on this combination of properties, the wear resistance of SRT has also been predicted to be quite high.

Another distinctive feature of SRT is their thermoplastic properties, which is very unusual for biological materials. This property was first suggested by realizing that SRT became pliable when heated in water, a characteristics that was reversible.[7] It was further confirmed by heating crushed SRT in a small volume of water until the structure displayed a solid-liquid phase transition into a viscous melt that could be processed into complex shapes.[9] Native SRT could be used directly for thermal processing into different 3D geometries, and this melting and shaping process could be repeated on the same sample without affecting the elastic modulus of the final material. Detailed understanding of SRT thermo-mechanical properties have been gained by correlating differential scanning calorimetry (DSC) with nanoindentation experiments, which demonstrated that the elastic modulus of SRT is highly dependent on the temperature as well as on the hydration state of the structure. Under dry conditions, the modulus remains high at 6 GPa and even increases up to nearly 12 GPa above 100 °C because of water evaporation, while the modulus drops 50% to 3 GPa under hydrated conditions, and further decreases in the sub-GPa range as temperature increases.[10] Further investigations of the elastic-plastic response of reconstituted SRT as a function of water content[11] have revealed a ductile-to-brittle transition as water is gradually removed from the network (Figure 2.2 E), which provides key insights into the role played by water as a plasticizer during thermo-processing. This distinctive combination of mechanical properties and thermoplastic behavior arises from the composition and molecular structure of SRT, which is discussed below in further details.

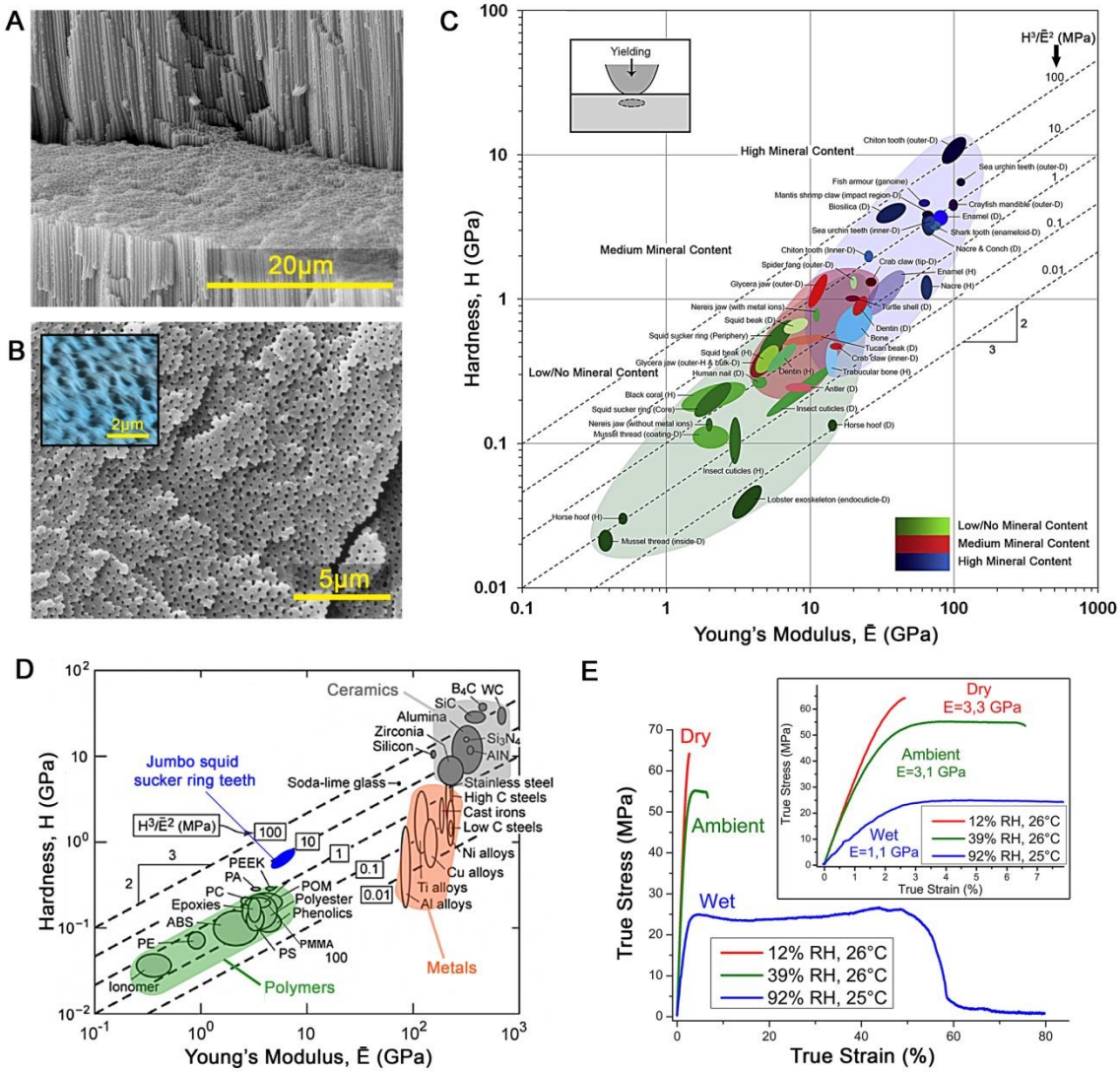

Figure 2.2 Mechanical properties and structure of Humboldt squid sucker ring teeth. Scanning electron microscope (SEM) image showing **(A)** the nano-tubular structure of a SRT fracture section and **(B)** the porous tubular cross-section of the teeth with inset presenting a scanning probe microscope image of the SRT's porous cross-section using a nanoindentor in the scanning mode. **(C)** Materials selection chart (Ashby plot of biological materials with SRT core and periphery indicated, and **(D)** Ashby plot of engineering materials such as polymers, metals and ceramic materials, with dried native squid sucker ring teeth (values ranging from core to periphery) indicated. **(E)** Tensile test curves performed on melt-cast processed SRT ribbons at different humidities, revealing ductile-to-brittle transition from wet to dry samples. Panel C reproduced from Ref. 8. Panel D reproduced from Ref. 9. Panel E reproduced from Ref. 11.

2.1.2 SRT proteins

SRT is composed only of proteins, while chitin and minerals are notably absent from the teeth's composition.[7] Traces of sulfur and fluorine have been detected via EDS in the native material, though their role is unclear at this stage. Overall, the SRT proteins are biased towards 9 naturally-occurring amino acids, the most abundant being Gly (37 mole%) followed by Tyr (14 mole%) and His (13 mole%), both of which can be exploited to either expand the properties of artificial SRT proteins or to modulate their solubility as a function of pH. Finally hydrophobic Leu, Ala and Val, as well as polar residues such as Thr and Ser, and Pro are also present in significant amounts.

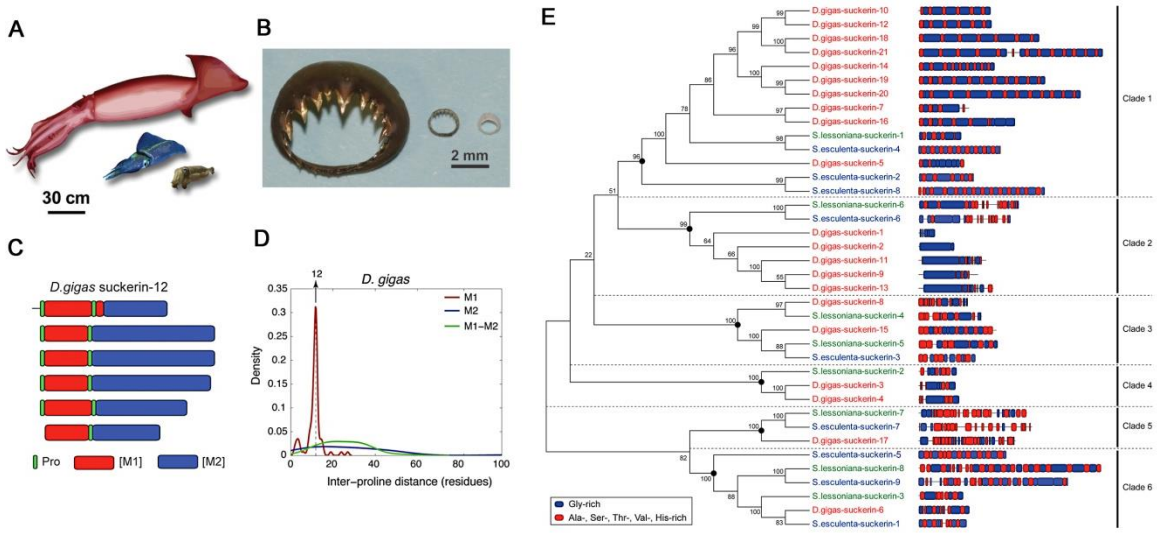

Figure 2.3 Cephalopod species, their sucker ring teeth and suckerins. (A) Scalar comparison of three cephalopod species, Jumbo squid (*D. gigas*)- top, Bigfin reef squid (*S. lessoniana*)- middle and Golden cuttlefish (*S. esulenta*)- bottom, and their respective SRT **(B)**. **(C)** Modular architecture of a representative Jumbo squid suckerin (suckerin-12) showing regular Pro placement, flanking [M1] modules. **(D)** Distribution of the number of amino acid residues between consecutive Pro for all Jumbo squid suckerins. **(E)** Phylogenetic tree depicting relationships of all known suckerin proteins, with the classification of six clades. All panels reproduced from Ref. 17.

2.1.2.1 Suckerin sequencing

SRT proteins ("suckerins") have been sequenced using Next Generation RNA sequencing (RNA-seq) analysis[12-14] in conjunction with proteomic techniques, including liquid chromatography tandem mass spectroscopy (LC-MS/MS) and traditional N-terminal sequencing.[9] In short, the translated assembled transcriptome from the sucker cuptions was used as an internal database that can be uploaded within the high-throughput mass spectrometry software PEAKS.[15] In parallel, extracted suckerins from SRT were purified, digested, and subjected to LC-MS/MS, allowing to generate *de novo* internal sequences using PEAKS. By screening the *de novo* peptides against the transcriptome libraries, suckerin peptides can be identified with a high coverage against the translated sequences. RACE-PCR[16] was eventually employed to confirm the full-length sequences. Other traditional proteomic techniques were also employed. For instance, SDS-PAGE protein bands of SRT extracts were subjected to Edman sequencing, and the obtained N-termini were probed against transcriptome libraries, resulting in very quick suckerin identification from the transcripts. If the amino acid composition of the individual suckerins is known (either in the purified form or from individual SDS-PAGE bands), its amino acid composition can also be probed against the libraries and that also resulted in quick sequence identification. Using this approach a total of 21 suckerins were sequenced from the Jumbo squid[17] with molecular weights ranging from ~5 to 57 kDa. In a comparative study, suckerins from distantly related decapodiform cephalopods were also sequenced using the same techniques. 8 suckerin sequences were obtained from the Bigfin reef squid (*Sepioteuthis lessoniana, S. lessoniana*), while 9 were obtained from the Golden cuttlefish (*Sepia esculenta, S. esculenta*) (Figure 2.3 A and E). Jumbo squid SRT was found to contain a larger repertoire of proteins than the two other cephalopods, and almost all suckerins were revealed to exhibit similarity in amino acid composition. Replicating this approach, others have sequenced suckerins from the common squid (*Loligo vulgaris*), although not all full-length sequences were obtained.[18] A quick perusal at the reported sequences for *L. vulgaris* also confirms the block co-polymer-like structure identified in the highlighted comprehensive study of other species, described in the next section.

2.1.2.2 Molecular design of suckerins

A key feature emerging from this comprehensive sequencing study is that suckerins have a highly modular design that holds resemblance to silk proteins. Indeed, ampullate spider silk proteins are generally constructed from highly modular Gly repeats with alternating poly-Ala motifs.[19-21] Most suckerins are also composed of silk-like GGY repeats with alternating Ala-rich modules. More specifically, Jumbo squid suckerins are composed of consecutive repetitive modules [M1] and [M2], which can be classified as such: [M1] modules are rich in Ala, Val, His, Thr and Ser residues, ranging from 3–15 residues in length, with the archetypal presence of Pro residues flanking these modules. The second iconic modules are [M2] modules, which are rich in Gly, Tyr and Leu, and can extend to above 50 residues in length.[17] With a few exceptions, these two types of modules are ubiquitous in suckerins, and each module confers to the suckerin distinct characteristics. A significant amount of the repeats constituting the suckerins are hydrophobic in nature (enriched in Ala, Val, Pro, Gly and Leu residues). The other abundant residues are Thr, Ser, as well as the aromatic Tyr (14 mole%) and the slightly basic His (13 mole%), which are useful for chemical functionalization and processability, respectively. Owing to the versatility of the imidazole moiety, His residues play an important role in structural proteins by forming metal-coordination interactions.[3, 4, 22] or covalent bonds with other residues[6, 23] to stablilize the network. However these interactions have not been detected in SRT.

The [M1] modules enriched in hydrophobic Ala and Val residues resemble the β–sheet forming Ala-rich repeats of silk proteins[19] and are reminiscent of the peptide sequence **GGVVIA**, which contributes to cross-β structures in beta amyloids.[24, 25] On the other hand, [M2] modules rich in Gly as well as Tyr and Leu residues, is reminiscent of the amorphous-forming sequences in dragline silk proteins.[26] Pro residues have been observed to consistently flank the [M1] modules, acting as a divider between the [M1] and [M2] modules. The repeating unit of Pro-flanking [M1] modules followed by [M2] modules is reiterated through the full length of suckerins (Figure 2.3 C and D), and observed across most of the highly conserved suckerins from different cephalopod species. For example in the case of *D. gigas* suckerin-19, Pro-[M1]-Pro-[M2] repeats 11 times in the full sequence. Similar to silk proteins, the Ala-rich [M1] modules have been shown to form β-sheets, while the Gly-rich [M2]

modules are thought to be mostly amorphous, such that the overall structure is similar to semi-crystalline synthetic polymers. Pro residues, which are known to be β-sheet disruptors,[27, 28] are strategically placed to restrict the dimensions of the β-sheets formed by [M1], resulting in β-sheets[17] that are typically 10-11 amino acid long or 3-3.5 nm long. These nanoconfined β-sheet domains are embedded within the longer [M2] amorphous domains that provide flexibility and elasticity. Hence with this semi-crystalline molecular design arising from the repeat peptide building blocks, a suitable combination of rigidity and elasticity is obtained within the SRT supramolecular network.

The majority of biophysical data on suckerins to date have been obtained from recombinant *D. gigas* suckerin-19. There are three main reasons for this choice. First suckerin-19 is the most abundant protein in the *D. gigas* SRT. Second, its molecular weight (MW) of 39 kDa is mid-way between the smallest (~ 10 kDa) and the largest (~57 kDa) suckerins. And third it exhibits the classical Pro-[M1]-Pro-[M2] modular architecture, such that it represents an illustrative example of the suckerin protein family. However it should be emphasized that there are subtle variations within the suckerin gene family in terms of the length of modules [M] or the isoelectric points due to the occurrence of a few basic residues on some suckerins. The roles of such variations have not been explored in detail yet.

2.1.2.3 Homology and conservation of suckerins

In a comparative study across three species of cephalopods shown in Figure 2.3 A (*D. gigas*, *S. lessoniana* and *S. esculenta*),[17] suckerins were identified to be encoded by members of a multigene family. Typical signal peptide lengths of suckerins are *ca*. 17 – 23 residues while amino acid composition appears very similar (Section 2.2.3.2), with sequence similarity between the suckerins exhibiting ~20 – 90% identity. Large scale modular architecture of Pro-[M1]-Pro-[M2] units (Figure 2.3 C and D) were also observed between some suckerins, with variation in modular design for others. [M2] Gly-rich modules containing small peptide building blocks of GGY and GGLY are observed to vary in frequency of occurrences and lengths for different suckerins, which could result in differences in mechanical behaviour and assembly of the SRT.

Similar to studies carried out on different species of spiders,[29, 30] the suckerins' modular design from all three species could be used to construct phylogenetic trees, which demonstrated that suckerin genes can be classified into 6 different clades (Figure 2.3 E), and that the origin of suckerins traces back to the Devonian period. Genetic divergence of the suckerin proteins of these three species includes gene duplication and segmental expansion or deletions. This can be observed clearly in *D. gigas* via analysis of the strikingly similar exon-intron patterns between suckerins of different lengths and modular architectures, suggesting that suckerin genes were derived from a common ancestral gene. Future transcriptomic and genetic analyses of suckerins from a wider range of cephalopods should provide interesting insights into molecular evolutionary processes behind SRT functional mechanics. For instance, it is intriguing that Humboldt squids have evolved a larger repertoire of suckerins (21 of them) than the bigfin reef squid (8 suckerin) and the golden cuttlefish (9 suckerins). Such variations could be related to their aggressive predatory strategies, by allowing Humboldt squids to construct stiffer and stronger SRT for prey catching using a higher number of suckerins, but this hypothesis remains to be verified.

2.1.3 Interplays between molecular design and nano-scale structure

2.1.3.1 Molecular scale: WAXS, FTIR and Raman spectroscopy

Following the initial investigations of SRT from Humboldt squid,[7] subsequent studies have revealed deeper insights into their biophysical and hierarchical structural characteristics. As a biomaterial constructed exclusively from proteins and apparently assembled together via weak hydrogen bonding, the intriguing question is: what makes the structure robust against high compressive and shearing forces? The answer lies in the molecular structure and supramolecular packing of suckerins, which is directly related to their modular organization discussed above. Raman spectroscopy on embedded and microtomed cross-sections of native SRT revealed the extensive presence of β-sheets throughout the teeth, which is notable by the location of the Amide I band centered at a Raman shift value of 1666 cm^{-1}.[9] Silks are well-established to be reinforced by β-sheet crystals.[31-34] But in contrast to silk, where the β-sheets are

highly aligned along the fiber axis,[35-37] the β-sheets in the teeth are randomly oriented, as revealed by polarized Raman spectroscopy (Figure 2.4 A). This prevalence of β-sheets was confirmed by ATR-FTIR studies and even more clearly by Wide-Angle X-ray Scattering (WAXS) investigations, which further corroborated the isotropic orientation of β-sheets. WAXS revealed a circular scattering pattern of equal intensities at all azimuths (Figure 2.4 C), indicating random orientation of crystalline domains within the native SRT.[10, 17] Integration of all azimuthal[37, 38] angles gave reflection positions similar to that of silk, with the most intense peaks coming from the combination of [120] and [200] reflections, [002] reflection and [100] reflection.

Comprehensive molecular modeling studies by Buehler and co-workers[31, 33] have revealed that β-sheets of restricted nano-scale dimensions play a fundamental role in enhancing the materials' mechanical robustness, including strength and fracture toughness at the molecular level. In silk, the highest energy barrier that could be achieved in a uniformly loaded H-bond assembly, such as that between two β-strands, is restricted by an intrinsic upper limit of 3–4 H-bonds, whereby the highest shear resistance was computed for a length scale of 3.1 residues.[31] These 3–4 H-bonds under homogenous shear loading can break concurrently, with a uniform deformation of multiple bonds contributing to the energy barrier. Exceeding the critical geometric strand length, shear strength drops rapidly and the system is prone to localization of deformation and rupture of H-bond clusters. Thus, computational modeling suggests that there exists a critical size providing optimized mechanical performance, with estimated dimensions of 1–2 nm (along peptide backbone) by 2–4 nm (in the H-bond direction).[39] Analysis of the WAXS patterns in suckerins using the Debye-Scherrer equation estimated that β-sheets exhibit dimensions of 2.4–2.6 nm in the H-bond direction and 3–3.5 nm along the peptide backbone.[17] An amorphous halo was also detected, implying the presence of a semi-crystalline structure at the molecular scale. β-sheets in SRT are thus predicted to be ~8-10 amino acids long and 5 strands wide, existing as uniform and size-restricted nanocrystals, which are randomly oriented within an amorphous matrix. The β-sheets size correlates well with the mean number (10-11) of residues flanked by β-sheet breaker Pro in the [M1] modules, which leads to the suggestion that β-strands are mostly made from the [M1] modules (disregarding

residues directly adjacent to Pro due to their likelihood to be involved in disordered or β-turn structures), whereas the longer [M2] modules constitute the amorphous phase.

The isotropic orientation is fully consistent with the biological function of SRT: as opposed to spider dragline silks[26] whereby the aligned β-sheet crystals must sustain uniaxial tension, SRT are subjected to a combination of compressive and shearing stresses *in vivo*. Thus an isotropic orientation of load-bearing molecular blocks ensures that the structure can sustain stresses in multiple directions, with β-sheets mostly providing rigidity and the amorphous domains ensuring an adequate degree of flexibility.

2.1.3.2 Nano-scale: SAXS

In contrast to the molecular level, small-angle x-ray scattering (SAXS) studies on native SRT have revealed an anisotropic organization at the nanoscale (Figure 2.4 B). 2D SAXS patterns, which were obtained for entire teeth with about 60 µm spatial resolution, exhibited an ellipsoidal shape with enhanced scattering intensity along the equatorial direction, denoting a preferred orientation of fibrillar elements that generally follows the contour of the teeth.[10] Radial integration of the 2D SAXS patterns led to the distinction of several orders of Bragg reflections that were generally consistent with a hexagonal packing of elongated nanofibrils (Figure 2.4 D). An average inter-fibrillar distance of *ca.* 12.5 nm was calculated in this hexagonal packing. The multi-scale structural model of SRT, emerging from the combined molecular and nano-scale studies, is that of nanofibrils formed by the suckerin proteins. These fibrils are made up of randomly oriented β-sheet crystal about 3 to 5 nm embedded within an amorphous protein matrix, and these nanofibril units are packed into a hexagonal lattice in the native state (Figure 2.4 D). The isotropic molecular orientation design results in structural stability in multiple loading directions, including high bending rigidity, which is required for the biological function of SRT.

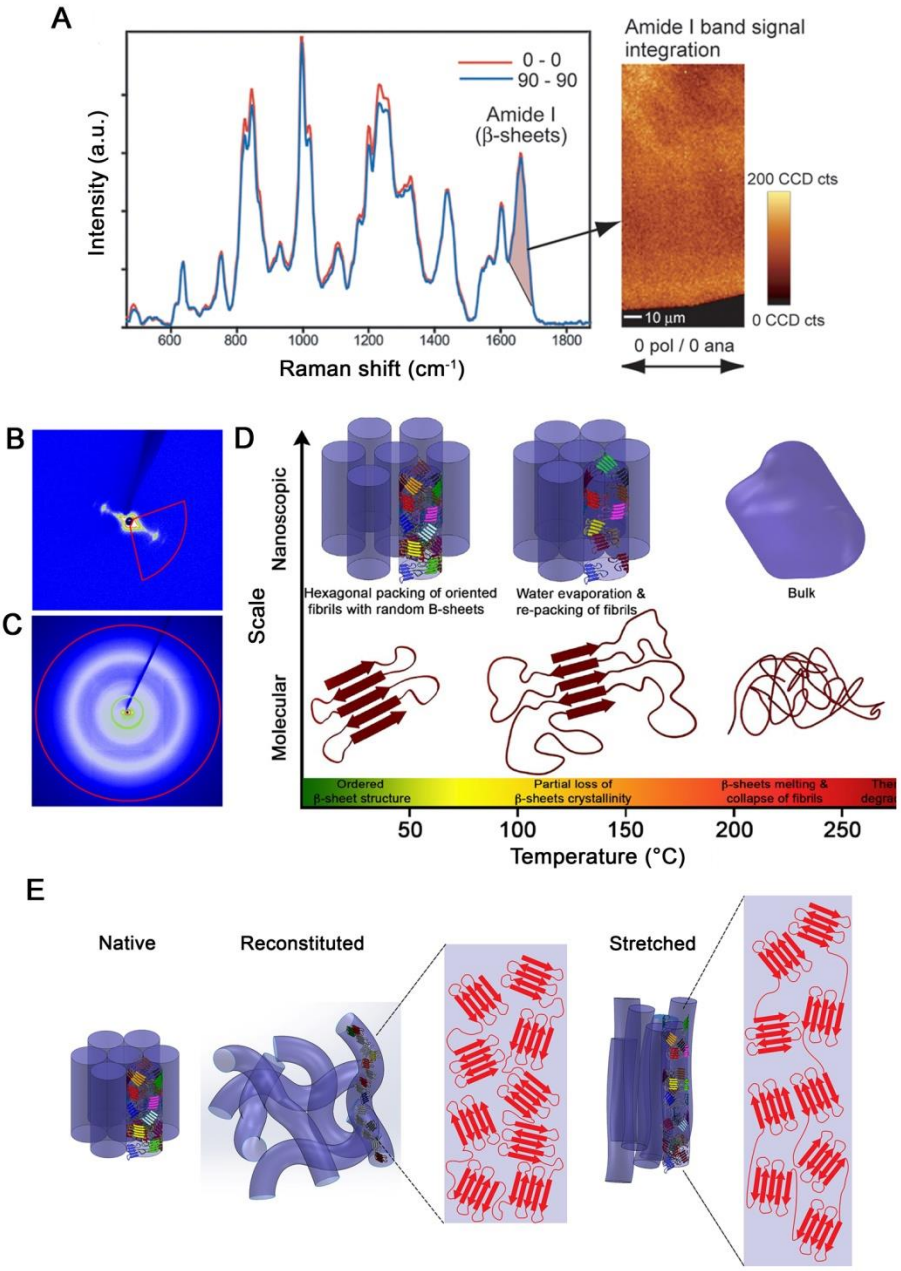

Figure 2.4 **Molecular design and nano-scale structure of SRT. (A)** Raman spectra obtained in cross-polarized modes indicate that β-sheets within the SRT are randomly oriented. Radial integration pattern of intensities of **(B)** SAXS and **(C)** WAXS experiments performed on native SRT. **(D)** Schematic illustration of thermally induced transformations at the molecular (bottom) and nano-scale (top), as observed from WAXS and SAXS respectively. **(E)** Schematic illustration of molecular and nano-scale structure of native, reconstituted and stretched SRT. Panel A reproduced from Ref. 9. Panels B, C and D reproduced from Ref. 10. Panel E reproduced from Ref. 11.

2.1.3.3 Thermo-mechanical properties and processing

Thermal gravimetric analysis (TGA) indicates that SRT contains about 13 wt.% water, and the teeth are stable up to 250 °C. At the molecular scale, thermal transitions were probed by WAXS, as illustrated in Figure 2.4 D. Slight disordering along the β–strand direction was noticed due to water content removal around 80 °C, while melting of the nanoconfined β-sheets was observed from the broadening of the main β-sheet reflection at 230 °C.[10] This reflection further decreased and disappeared as temperature was raised up to 250–300 °C, indicating polymer network degradation above 250 °C.

At the nanoscale, SAXS profiles indicated loss and re-packing of the ordered hexagonal packing at 80 °C, which has been attributed to water removal from the network. As the temperature increased, new reflections appeared, suggesting the rearrangement and compaction of the nanofibrillar lattice. Finally the reflections disappeared completely above 230 °C indicating structural collapse. After thermal processing, it is interesting to note that the isotropic WAXS signal remained almost unchanged, whereas the higher order reflections of the SAXS pattern disappeared. These features provide structural explanations for the thermo-plastic behaviour of SRT: since thermal treatment leads to loss of nano-scale packing while the molecular scale remains intact, the emerging model is that the amorphous regions locally melt during thermal processing while the β-sheets domains remain rigid, leading to collapse of the nanofibrillar network (Figure 2.4 D). Upon cooling, the nanofibrils are not reformed but the material largely maintains its mechanical properties[11] because the load-bearing β-sheets are not affected by heat-treatment. This model also implies that it should be possible to process elongated fibers, by taking advantage of the viscous nature of the (collapsed) amorphous domains which could be elongated during extrusion (Figure 2.4 E). This was indeed confirmed in proof-of-concept experiments where 1.5 mm and 300 μm diameter SRT filaments were formed through vacuum casting (Figure 2.5).[10] Optimization of processing conditions can be obtained using a plasticizing agent that facilitates chain movement of amorphous domains at the molecular and the nano scales.

2.1.4 Emerging applications of SRT and recombinant suckerins

Concurrently to the establishment of multi-scale structural/property relationships of SRT, materials made of suckerins have been initiated using both native and recombinant suckerins. These proof-of-concept developments have so far mostly been conducted towards biomedical applications.

2.1.4.1 Recombinant production and purification

With suckerins sequences elucidated, the natural next steps have been to express the proteins, investigate their physico-chemical properties, and exploit these characteristics to develop novel suckerin-based materials. Most of the work so far has been conducted using *D. gigas* suckerin-19, because as mentioned above it is representative of the block co-polymer structure of the suckerin protein family.

Given the molecular similarity to silks, much of the work using recombinant suckerins has been inspired by previous research on recombinant silk fibroins. An increasing number of biomedical and engineering applications have been described for artificial silk and other structural recombinant proteins, and their eventual commercial success will likely depend on improving protein production yields and costs. This optimization remains somehow empirical because it is challenging to predict which cell lines and conditions will lead to high yields. In the case of silk, for instance, the highly repetitive GC-rich gene sequences can be a detrimental problem during the production of these silk proteins, hence limiting the efficiency of production in *E. coli*.[40-42] Another issue arises from the large molecular sizes of the silk proteins, for example the *B. mori* silk heavy-chain fibroin protein is approximately 350 kDa while the light-chain is *ca.* 26 kDa, and these proteins have the tendency to form insoluble aggregates due to their premature assembly into β-sheet structures.[43, 44] Nevertheless some of these challenges have been addressed in recent years and several groups are now producing silk fibroins in reasonably high yields,[42,45] including high MW silk. For instance, Xiao *et al.*[46] have employed metabolically-engineered expression host in order to obtain silk fibroins with MW as high as 285 kDa, which resulted in elevated mechanical properties compared to lower MW fibroins. In other studies, fibers from recombinant spider silk achieving the same mechanical toughness as the native silk

have been obtained,[47] whereas a wide range of functional materials (films, hydrogels, sponges, adhesives) with tailorable properties have been reported from silk fibroins obtained from the milk of transgenic goats.[48]

In the case of suckerins, the MWs of suckerins from Humboldt squid, bigfin reef squid, and cuttlefish range from 4 kDa to less than 60 kDa, almost all of which exhibit the bi-modular, block co-polymer-like structure.[17] This provides a large palette of suckerins to choose for recombinant expression and only a handful have so far been explored. Given the large number of suckerins identified and their significant differences at the primary structure level, it is anticipated that the range of physico-chemical characteristics and applications could be expanded further. In recent studies, both poly-His tagged suckerin-19 and full-length suckerin-19 were expressed in *E*. coli BL21 (DE3) cells and Rosetta cells.[49] Successfully expressed His-tagged suckerin-19 was purified via immobilized metal affinity chromatography (IMAC) followed by TEV protease cleavage at the designed cleavage site, and then a final ion exchange fast protein liquid chromatography (FPLC). However, this method proved too time-consuming and alternative approaches have been developed. Instead of the tedious chromatography processes, one can take advantage of the slightly basic iso-electric point (IEP) to conduct IEP precipitation by simple dialysis against a buffer close to the protein's IEP. Full-length suckerin-19 could be obtained with high purity when salted-out with a pH 8.4 buffer containing denaturing agents, providing an alternative method that required fewer steps and reagents. Another technical improvement to enhance protein yield is to use microfluidization for cell lysis, which has so far led to expression yield of purified proteins in the range of ~50 mg/L in flask culture. While such yield is sufficient at the laboratory scale, it is clear that further improvements will be necessary in the future. However, to date only expression in *E. coli* has been attempted and no specific efforts to optimize the process have been undertaken, leaving ample room for optimization (fermentation conditions, metabolic engineering, etc). Likewise bioprocessing methods using insect or yeast cells have yet to be explored and are anticipated to further enhance production yields.

2.1.4.2 Thermoplastic forming

Owing to their thermoplastic characteristics, native SRT can be thermally processed and shaped into 3D geometrical structures. Under hydrated conditions, the glass transition temperature (T_g) is in the range 30-40 °C as observed by DSC measurements,[10, 50] but is much higher in dry conditions. Theoretically, it is possible for T_g to be above the degradation temperature, meaning that thermo-processing is physically impossible in the absence of water or of another plasticizing agent. Water thus plays a key plasticizing role during thermo-processing by lowering the operation temperature at which SRT can be thermo-formed. Using these conditions, SRT have been casted into films, bulk samples[11] or nano-pillars[9]. Plasticizing agents with a high boiling temperature, such as glycerol can also be added to the system to improve the mouldability of the melt and this approach was for instance applied to extrude SRT melt into feed filaments with geometrical characteristics suitable for 3D printing applications (Figure 2.5).[10] A key aspect of this process is to maintain the processing temperature below the melting temperature of the β-sheets typically in the range 100–150 °C. Critically, molded and re-constituted SRT could be recycled and re-processed many times without affecting the mechanical properties of the material.[10, 11] Exploiting the thermoplastic characteristics, SRT have also been processed into pressure-sensitive adhesives[50], by processing the materials above T_g, which may find applications as bio-adhesives.

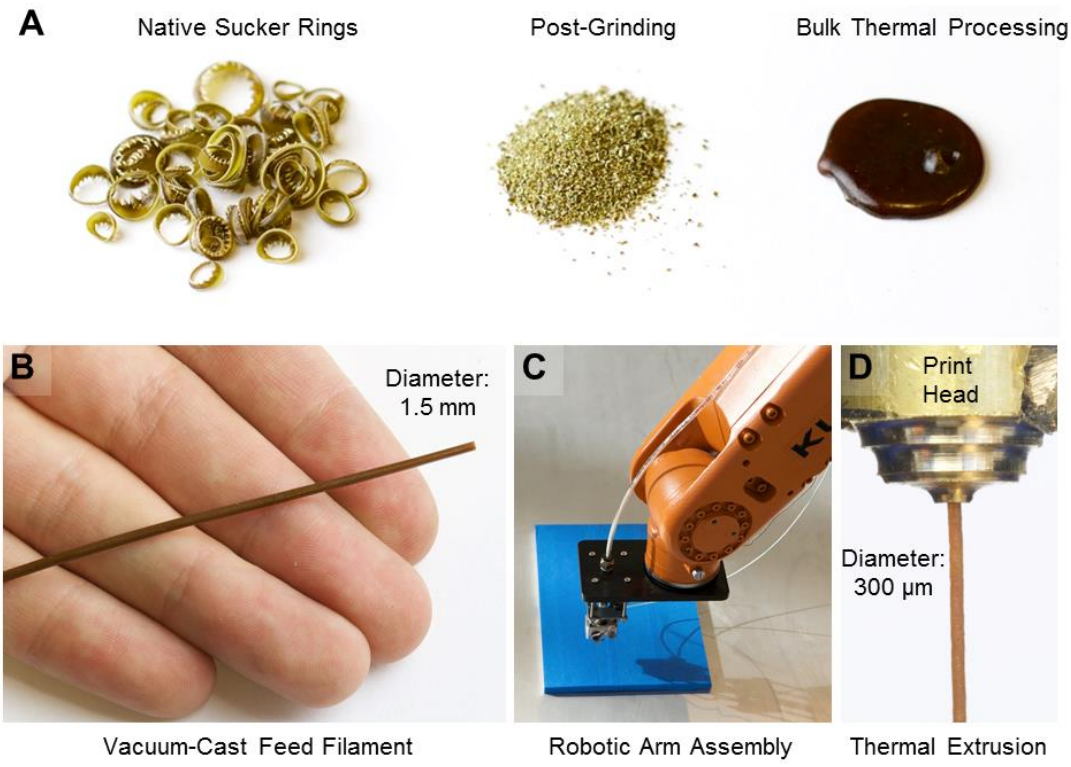

Figure 2.5 Thermal processing processes and extrusion of filaments from native SRT. (A) Native SRT were grounded into powder form, then mixed with plasticizing agents (50% SRT, 25% water and 25% glycerol by weight) and heated to 150 °C. **(B)** A 1.5 mm diameter feed filament was vacuum formed from the molten SRT mixture, which could then be **(D)** thermally extruded into a 300 µm diameter filament through a fused filament fabrication print head attached to a robotic arm **(C)**. Figure reproduced from Ref. 10.

2.1.4.3 From soft gels to stiff films using Di-Tyr cross-linking

The solubility of suckerin-19 is below 10 mg/mL in water, but it can be increased to as high as 70.9 mg/mL in 5% acetic acid solution,[49] with the solution forming a colloidal suspension of nano-scale particle size that remains stable at 4 °C over a two week period. DLS analysis has indicated nearly constant size distributions over this time period, and high zeta potentials of the colloidal solutions were measured (in general > 30 mV), indicating high colloidal stability. Furthermore, suitable adjustments of the buffer conditions allow for preparation of suckerin-19 nanoparticles with well-controlled sizes. This stability of suckerin-19 colloidal suspensions combined with their high solubility under certain conditions makes them favorable for further processing into various functional and structural materials. Exploiting the

abundant Tyr residues located in the amorphous [M2] modules, di-Tyr cross-linking can be achieved using a photo-cross-linking method,[51] and the cross-linking density can be varied to tune the final mechanical response. Using this approach, di-Tyr cross-linked gels (Figure 2.6 A) and films exhibiting a wide range of elastic properties (Figure 2.6 D) could be prepared, from soft gels with storage modulus in the sub-KPa range to stiff films with elastic modulus above 1 GPa under hydrated conditions.[52] The implication is that the suckerin-19 could in principle match the elasticity of a wide range of tissues, which could be exploited in biomedical applications and tissue engineering. For such applications, the assessment of biocompatibilities is of course essential. Suckerin-19 films have been evaluated for biocompatibility and such assays have so far indicated negligible *in vitro* cyto-toxicity against various cell lines, including human dermal fibroblast cells (HDF) and mesenchymal stem cells (hMSCs), even leading to faster cell proliferation than on commercial tissue culture plates. However biocompatibility studies have so far remained limited and comprehensive *in vivo* studies are needed in order to obtain a more thorough assessment of the suitability of suckerins for biomedical applications.

From a polymer physics perspective, it is of interest to note that suckerin-based materials exhibit several features that can be attributed to their modular architecture. For instance, the rheological behaviour of suckerin-19 gels is consistent with a semi-flexible polymer network in which β-sheets form the rigid elements and the amorphous domains the entropic springs. For suckerin-19 films, the relationship between the modulus and the cross-link density is peculiar, since higher cross-linking density led to films with a lower modulus (Figure 2.6 B and C).[52] This "non-classical" dependence of the modulus on the cross-link density was reconciled by observing that higher cross-linking density resulted in a lower β-sheet content (Figure 2.6 C), and thus to smaller moduli since β-sheets are the dominant load-bearing building blocks in suckerins. This phenomenon is explained by the fact that Tyr residues, which are the cross-linking sites, are strictly located in the amorphous domains. Thus when the cross-linking density increases, the backbone flexibility of the amorphous domains becomes restricted, thus limiting the formation of adjacent [M1] modules into β-sheets (Figure 2.6 C). In other words, β-sheet formation is frustrated, resulting in films with a lower modulus at higher cross-linking density.

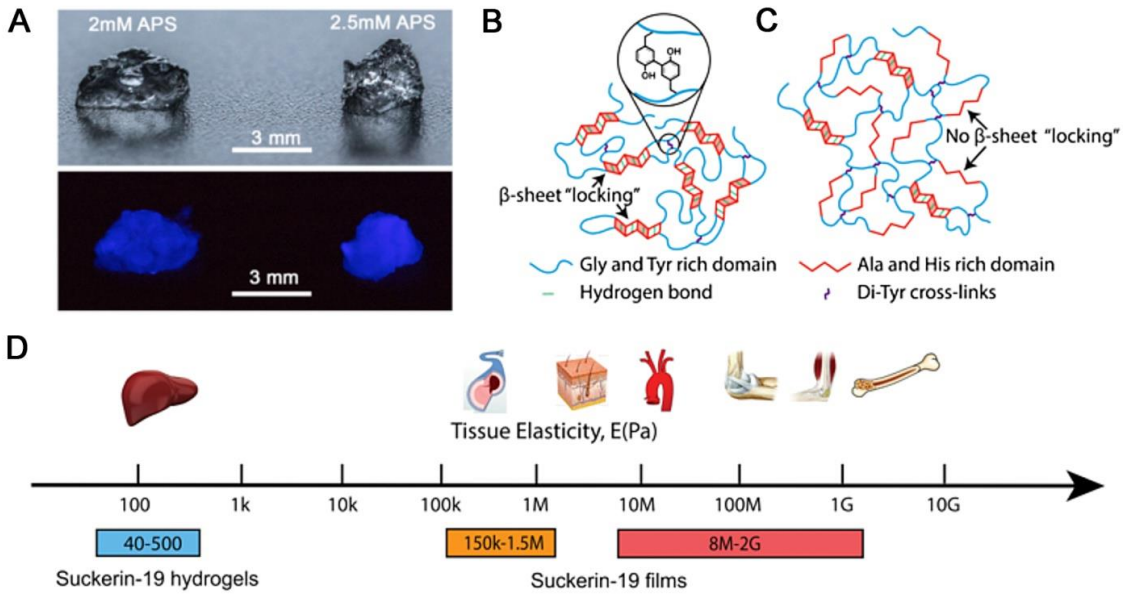

Figure 2.6 Crosslinked suckerin-19 hydrogels. (A) Photographs of crosslinked suckerin-19 gels under normal light (top) and UV light (bottom), which illustrates the fluorescence arising from the formation of di-Tyr crosslinks. Spatial presentation of *β*-sheet strands, with **(B)** "*β*-sheet locking" present under moderate di-Tyr crosslinking density condition and **(C)** high di-Tyr crosslinking density, which results in the constrained flexibility of amorphous domains, eventually frustrating *β*-sheet formation. **(D)** Tissue elasticity of a range of biological tissues in comparison with the achieved elastic moduli of processed suckerin-19. Panels reproduced from Ref. 52.

2.1.4.4 Suckerins as substrates to grow of gold nanoparticles

Owing to their intrinsic high content of Tyr residues (up to 15 mol.%), suckerins (suckerin-12 and suckerin-19) can be used as macromolecular templates to trigger the growth of metallic nanoparticles exhibiting the classical plasmonic effect,[53] with the Tyr side-chain playing the role of reducing agent when the pH of the solution is raised above its pKa. Growing Au nanoparticles with controlled sizes using proteins has been previously demonstrated, for instance with BSA[54] as well as silk.[55] In the latter case, Tyr residues were identified as the moieties promoting the reduction of $HAuCl_4$ salts into Au nanoparticle suspensions, which remained highly stable owing to silk fibroins surrounding the nanoparticles and preventing aggregation by steric repulsion. The same mechanism allowed Au nanoparticles to form from suckerin solution.[56] In addition, changing the suckerin concentration allowed preparation of Au nanoplatelets of triangular or hexagonal shape (Figure 2.7 A and B), which is

especially useful for surface-enhanced Raman spectroscopy analysis.[57] Formation of Au nanoplatelets from biomacromolecules is usually promoted by acidic residues that preferentially adsorb on {111} facets of Au crystals,[54, 58] therefore suppressing growth in the <111> direction and promoting planar geometry. Since there are no acidic residues in suckerin-12 and -19 (employed in the study), the planar geometry is triggered by a different mechanism. One possibility is that Tyr residues are weakly protonated at pH above their pKa used to trigger the reduction of Au salts, such that the charged Tyrosyl may adsorb onto {111} facets in the same fashion as Asp or Glu residues at lower pH. The other plausible explanation is linked to the high β-sheet content of suckerins, especially at high concentration of suckerins,[49] where β-sheets may also exhibit enhanced adsorption onto {111} facets, a mechanism supported by molecular dynamic simulations which showed that β-sheets exhibit a strong affinity for {111} planes.[59]

The ability to grow Au nano-objects from suckerins opens several opportunities in nanotechnology. For instance, it allows for immobilization of Au nanoparticles onto solid substrates without aggregation, which often causes the immobilized nanoparticles to lose their size-dependent optical and electronic properties.[60] Another noteworthy feature demonstrated in Reference 56[56] is the capacity to cast high concentration of suckerin solutions into micro- or nano-templates followed by solvent evaporation, leading to the formation of nano-structured suckerins templates (Figure 2.7 C and D). In the subsequent step, a thin Au film can be grown over the suckerin template by simple dipping into an Au salt solution, with the suckerin template playing the role of a redox active solid substrate (Figure 2.7 E and F). Suckerins can therefore serve as a potential alternative to evaporation and sputtering techniques for the selective spatial deposition of Au films onto solid surfaces. A further expansion of this application would be to use suckerins as sacrificial templates that could be readily solubilized following Au nanoparticle film growth, leaving only the metal film behind. This may be employed in micro- or nano-fabrication or to prepare gold aerogels, similar to the way it has been achieved using amyloid templates.[61]

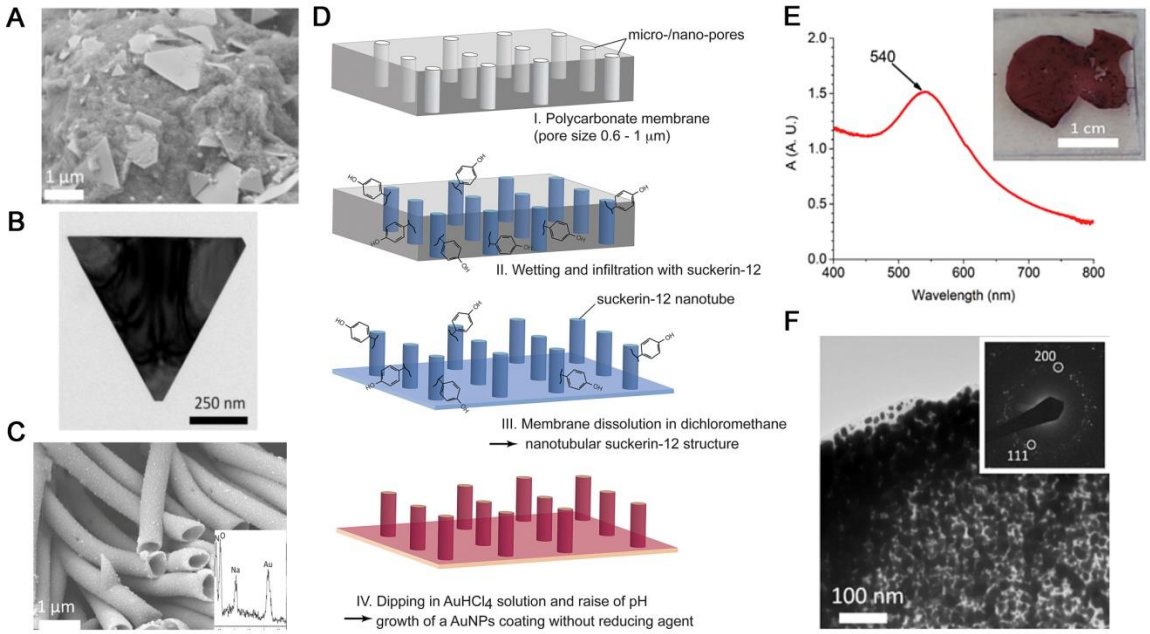

Figure 2.7 Growth of Au nanoparticles promoted by suckerins. (A) SEM and **(B)** TEM images of triangular or truncated triangular-shaped Au nanoparticles formed by the addition of suckerin-19 protein solution to a solution of $HAuCl_4$. **(C)** SEM images of fabricated suckerin-12 nanotubes covered with Au nanoparticles, with EDX (inset) validating the presence of gold on the nanotubes' surface. **(D)** Illustration of the nanotubular structure fabrication procedure, followed by coating with Au nanoparticles. **(E)** UV-vis spectra of suckerin-12 film with the growth of Au nanoparticles and an image of the protein film on a glass slide (inset). **(F)** TEM image of suckerin-12 film covered with Au nanoparticles and the corresponding SAED pattern (inset). Panels reproduced from Ref. 56.

2.2 Similar structural proteins

2.2.1 Silk

Silk proteins are biopolymers with remarkable load-bearing properties. Both silk moth *Bombyx mori* (*B. mori*) silk[62, 63] and spider silks[19, 26] have been widely studied silk materials, whereby each silk type has specific functions and applications for each species. For instance, *B. mori* silk moths spin their silk fibroins to form a cocoon structure[64] for their metamorphosis stage, and spiders use two different silk types, dragline silk for pitching and holding up their web frame, and viscid silk as their orb web for prey capture (illustrated in Figure 2.8 B).[26]

Silk fibroins are generally made from Gly and Ala-rich sequences, with the crystalline domain of *B. mori* silk fibroin constructed by GAGAGS hexapeptide repeats.[26, 63, 65] Spider major ampullate (MA) fibroins are constructed by multiple consecutive Ala and Gly repeats, while minor ampullate (MI) fibroins are constructed by alternating Gly and Ala repeats and pure Ala segments.[26, 63] These Ala-rich repeats form crystalline nano β-sheet structures amongst Gly-rich segments, which constitute the amorphous phase in the silk fibers (Figure 2.8 C).[26, 62, 66] While the β-sheet crystals reinforce the polymer network within the silk fibers, the amorphous Gly network provides the material with elasticity due to their flexible and unordered structures.[26] X-ray scattering analysis of spider silk reveals that the β-sheet crystals are strongly aligned with the fiber axis, with some weakly oriented and unaggregated β-sheets.[26, 62, 67]

The robust tensile properties of silk originate from their sequence, structure and function relationship, and the reason for their mechanical strength lies in the crystalline and amorphous phases, which play different roles during the extension of the fibers. The mechanical behavior of silk is non-linear: at low tensile strains, the material gives an elastic response due to the homogeneous and reversible extension of the amorphous matrix. The amorphous matrix deforms and untangles with the breaking of intermolecular hydrogen bonds, until a yielding point is reached where all amorphous chains have been extended. At higher strain, the β-sheet crystals become

involved in the process and start to break via a slip-stick mechanism. This strain-hardening process is irreversible and eventually the fiber breaks.[33, 39, 62]

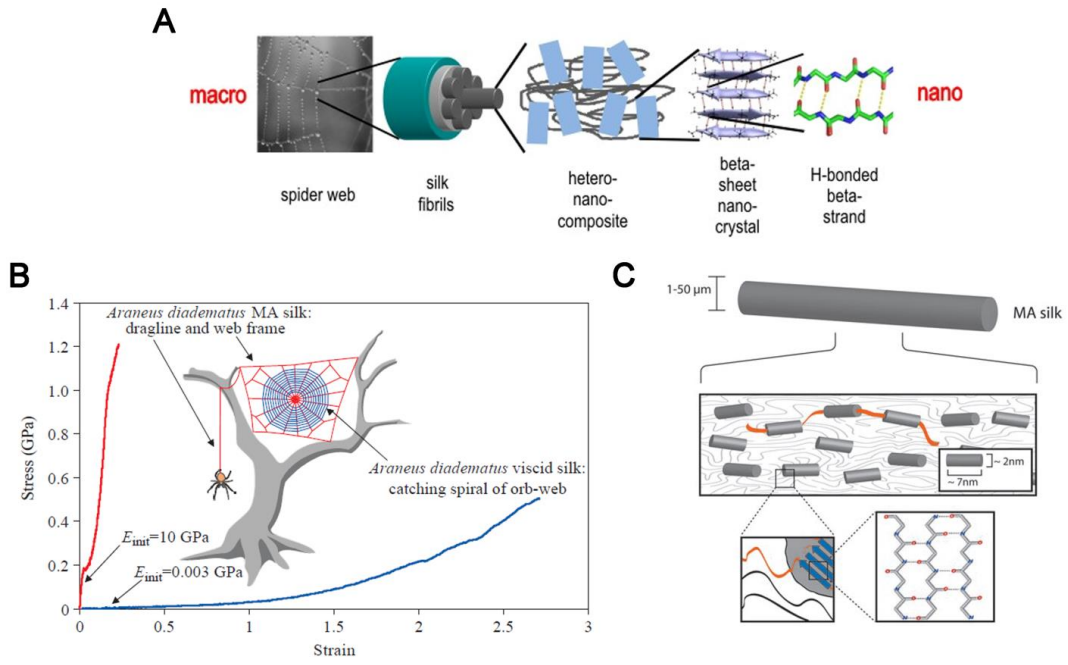

Figure 2.8 Spider silk structural and mechanical properties. (A) A hierarchical illustration of spider silk fiber, adapted from Keten *et al*.[39] **(B)** Stress-strain tensile curves of spider *Araneus diadematus* dragline and viscid silk, adapted from Gosline *et al*.[26] **(C)** Schematic structure of MA silk, showing the arrangement of crystalline β-sheets amongst the amorphous phase, adapted from Romer and Scheibel.[66]

Spider *Araneus diadametus* MA silks exhibit 27% elasticity, while viscid silk have elasticity of up to 270%. *B. mori* silk exhibits 18% elasticity.[26, 66] On a weight-to-weight basis comparison, spider silks are able to absorb more energy during a tensile stress event than Kevlar (2.7% elasticity), and all three silk types have tensile properties superior to steel, which has 0.8% elasticity.

Silks have been studied for the past 50 years, and their superior tensile properties have been exploited for many applications.[62, 63] Other advantages of silk include their biocompatibility, biodegradable properties, lightness and malleability.[68] *B. mori* silk has been long used in the textile industry,[62] while synthetic spider silk is beginning to spur interest in the textile sector.[62] Other applications include the use of spider silk in biomedicine, as drug delivery systems,[63] scaffolds for tissue

regeneration[62] and wound repair.[68] Further interesting applications also include the use of silk as an actuator for the possible development of artificial muscles,[62] and the development of optically transparent fibroin materials for bioactive devices.[62]

2.2.2 Amyloids

Amyloids are insoluble and fibrous aggregated proteins that form from the abnormal folding of otherwise normal functional proteins.[69, 70] The extracellular deposition and accumulation of amyloids in different parts of the human body are known as amyloidosis,[71] and are associated with diseases, with examples such as Parkinson's and Alzheimer's disease. [70, 72] A widely studied amyloid is the beta-amyloid (Aβ), known for its role in Alzheimer's disease, where these Aβ form plaques that deposit in the brain tissues.[69, 73] Numerous Aβ species can be derived from the enzymatic cleavage of the amyloid precursor protein (APP), whereby the metabolism process generates Aβ (1–40) as the most abundant species at ~80–90%, and the principal toxic species deposited in the brain Aβ (1–42) at ~5–10%.[73] These two species differ in the number of residues, with the sequence of Aβ (1–42) being:

"DAEFRHDSGYEVHHQKLVFFAEDVGSNKGAIIGLMVGGVVIA"

and Aβ (1–40) with two residues less from the C-terminus of the same sequence.[74, 75]

Amyloids are in general rich in β-sheet structures,[69, 76] and their growth into mature fibrils involve three phases, namely a seeding phase followed by growth phase and finally saturation.[77, 78] A breakdown of the fibrils' hierarchical structure includes the formation of β-strands constructed from the protein or peptide sequence, which then stack to form protofilaments that precede the formation of mature fibrils (Figure 2.9 A).[79] Amyloid fibrils can also be induced to form from the misfolding of commonly found proteins,[80] such as lysozyme,[81] insulin[82] and bovine albumin serum.[83] These amyloid fibrils possess a common cross-β core fibril structure,[84] as shown in Figure 2.9 B. X-ray diffraction patterns (Figure 2.9 C) obtained from amyloid fibrils typically reveal the dimensions of the cross-β structure, with two major reflections observed at orthogonal axes that indicate a hydrogen-bonding distance of ~

4.7 Å between β-strands and side chain packing distance between β-sheets of ~ 10 Å.[76, 85, 86]

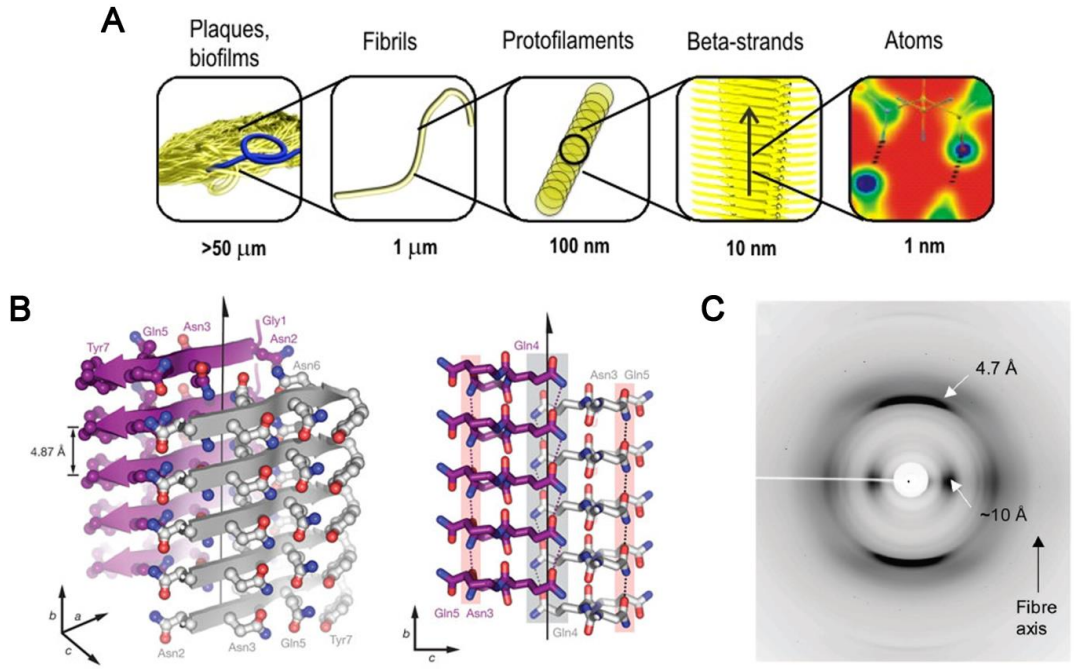

Figure 2.9 Structural breakdown of amyloid fibers. (A) A hierarchical illustration of amyloid plaques, adapted from Knowles *et al*.[79] **(B)** 3D illustration of cross-β structure of amyloid fibril formed by peptide GNNQQNY sequence, adapted from Nelson *et al*.[84] **(C)** X-ray diffraction pattern of amyloid fibrils with fiber axis indicated, adapted from Rambaran and Serpell.[85]

Computational model studies of amyloids have shown that they can achieve a Young's modulus from 4–40 GPa depending on the type of fibrils formed (construct symmetry) and their sizes.[87] Experimental data of amyloid fibrils with twofold and threefold symmetries have measured Young's modulus values of 20–30 GPa, falling within the simulated range, and these values are comparatively on par with those obtained from spider silk (10–30 GPa).[79, 87] The mechanical robustness of amyloid fibrils are attributed to their β-sheet-rich structures, whereby their dimensions and amino acid side chains can further modulate their mechanical properties.

Amyloid fibrils have been employed and utilized for various applications due to their robust properties. For instance, recent applications of functional amyloids include hybrid membranes for water filtration purposes, wherein protein amyloid

fibrils in combination with activated porous carbon can effectively remove pollutants such as heavy metal ions and radioactive waste from water at relatively low costs.[88] Other interesting applications are multi-functional hybrid nanocomposites of amyloid fibrils and gold platelets crystals. These hybrid structures have water-sensing properties and possess surface plasmon resonance features, potentially making them useful as pH sensors.[89]

2.3 Peptide materials and applications

Peptides have been increasingly utilized for the fabrication of materials or have been incorporated into existing materials to form hybrid materials. There are many advantages of using these organic building blocks: they are biocompatible and biodegradable, synthesis can be scaled up with ease and sequence design can be tailored easily to incorporate chemical modification of side chains, hence, tailorable structural properties of resultant materials.[90]

A plethora of peptide materials and applications have been developed in recent years. For example, structural peptide nanotubes (PNT) have been created with amphiphilic self-assembling cyclic and linear peptides.[91] These PNTs have wide applications, and one such application in the biomedical industry is to function as controlled drug release and delivery vehicles.[92] PNTs have also been played the roles of biosensors, by functionalizing them with complementary enzymes to their targeted substrates.[93-95] PNTs have also been successfully employed as scaffolds to support neural growth in damaged optic nerves.[96] In the electronics industry, some PNTs have also been self-assembled for microelectronics devices.[97]

With the various secondary structures that peptides can self-assemble into, peptides have been utilized as secondary structural molecular switches, such as β-sheet and α-helical switches.[98] Amphiphillic peptides have also been explored to function as self-assembled constructs in regenerative medicine therapy.[98-100]

Rationally designed amyloid peptide fibrils have been used as templates for metal binding and for the fabrication of silver, gold and platinum nanoparticle nanowires.[101] The biotemplating of inorganic materials such as silica could also be achieved via the use of the designed peptide fibrils.[102]

Peptides have also employed to fabricate hydrogels as scaffolds for 3D culture of human dermal fibroblasts cells, with promising potential as model scaffolds for the 3D culture of other anchorage-dependent cells and for tissue engineering.[103, 104] Certain peptides hydrogels can also be used as slow drug release delivery vehicles.[105]

2.4 Scope of Thesis

Amongst the various hard structures of the Jumbo squid that are crucial to their survival, namely the cartilaginous cranium, pen, beak and SRT, the SRT is the only structure that is constituted wholly by proteins. Despite their composition and lack of cross-link bonds, the mechanical strength of the teeth are superior to many synthetic polymers. These prominent features are brought about by suckerin proteins and their hierarchical structure, while research surrounding the SRT and fabrication of SRT materials are mainly focused on the full proteins and the native SRT only. Detailed studies and analysis of the suckerin's modular building blocks and their interactions have so far yet to be undertaken. The scope of this thesis is to conduct in-depth examination of the suckerin peptide building blocks and to identify the basis of their mechanical strength brought about by otherwise weak fundamental interactions at the molecular scale. Thereby, the understanding of the roles each building block plays would provide further information on the self-assembly mechanism of the SRT, and new suckerin peptide materials could be fabricated with tailored properties.

References

[1] A. J. Ruys, *Biomimetic Biomaterials: Structure and Applications*, Elsevier Science, **2013**.

[2] M. A. Meyers and P. Y. Chen, *Biological Materials Science: Biological Materials, Bioinspired Materials, and Biomaterials*, Cambridge University Press, **2014**.

[3] C. C. Broomell, F. W. Zok and J. H. Waite, *Acta Biomater*, **2008**, 4, 2045-2051.

[4] E. Degtyar, M. J. Harrington, Y. Politi and P. Fratzl, *Angew Chem Int Edit*, **2014**, 53, 12026-12044.

[5] A. C. Neville, *Biology of Fibrous Composites: Development Beyond the Cell Membrane*, Cambridge University Press, **1993**.

[6] A. Miserez, T. Schneberk, C. J. Sun, F. W. Zok and J. H. Waite, *Science*, **2008**, 319, 1816-1819.

[7] A. Miserez, J. C. Weaver, P. B. Pedersen, T. Schneeberk, R. T. Hanlon, D. Kisailus and H. Birkedal, *Adv Mater*, **2009**, 21, 401-406.

[8] S. Amini and A. Miserez, *Acta Biomater*, **2013**, 9, 7895-7907.

[9] P. A. Guerette, S. Hoon, Y. Seow, M. Raida, A. Masic, F. T. Wong, V. H. Ho, K. W. Kong, M. C. Demirel, A. Pena-Francesch, S. Amini, G. Z. Tay, D. Ding and A. Miserez, *Nat Biotechnol*, **2013**, 31, 908-915.

[10] V. Latza, P. A. Guerette, D. Ding, S. Amini, A. Kumar, I. Schmidt, S. Keating, N. Oxman, J. C. Weaver, P. Fratzl, A. Miserez and A. Masic, *Nat Commun*, **2015**, 6, 8313.

[11] C. Rieu, L. Bertinetti, R. Schuetz, C. Salinas, J. C. Weaver, P. Fratzl, A. Miserez and A. Masic, *Biomimetics and Bioinspiration*, **2016** (accepted).

[12] Z. Wang, M. Gerstein and M. Snyder, *Nat Rev Genet*, **2009**, 10, 57-63.

[13] M. L. Metzker, *Nat Rev Genet*, **2010**, 11, 31-46.

[14] F. Ozsolak and P. M. Milos, *Nat Rev Genet*, **2011**, 12, 87-98.

[15] B. Ma, K. Z. Zhang, C. Hendrie, C. Z. Liang, M. Li, A. Doherty-Kirby and G. Lajoie, *Rapid Commun Mass Sp*, **2003**, 17, 2337-2342.

[16] E. Scotto-Lavino, G. W. Du and M. A. Frohman, *Nat Protoc*, **2006**, 1, 2742-2745.

[17] P. A. Guerette, S. Hoon, D. W. Ding, S. Amini, A. Masic, V. Ravi, B. Venkatesh, J. C. Weaver and A. Miserez, *Acs Nano*, **2014**, 8, 7170-7179.

[18] A. Pena-Francesch, S. Florez, H. Jung, A. Sebastian, I. Albert, W. Curtis and M. C. Demirel, *Adv Funct Mater*, **2014**, 24, 7401-7409.

[19] R. V. Lewis, *Chem Rev*, **2006**, 106, 3762-3774.

[20] J. Gatesy, C. Hayashi, D. Motriuk, J. Woods and R. Lewis, *Science*, **2001**, 291, 2603-2605.

[21] P. A. Guerette, D. G. Ginzinger, B. H. F. Weber and J. M. Gosline, *Science*, **1996**, 272, 112-115.

[22] H. C. Lichtenegger, T. Schoberl, J. T. Ruokolainen, J. O. Cross, S. M. Heald, H. Birkedal, J. H. Waite and G. D. Stucky, *P Natl Acad Sci USA*, **2003**, 100, 9144-9149.

[23] Y. Tan, S. Hoon, P. A. Guerette, W. Wei, A. Ghadban, C. Hao, A. Miserez and J. H. Waite, *Nat Chem Biol*, **2015**, 11, 488-495.

[24] L. K. Chang, J. H. Zhao, H. L. Liu, K. T. Liu, J. T. Chen, W. B. Tsai and Y. Ho, *J Biomol Struct Dyn*, **2009**, 26, 731-740.

[25] M. R. Sawaya, S. Sambashivan, R. Nelson, M. I. Ivanova, S. A. Sievers, M. I. Apostol, M. J. Thompson, M. Balbirnie, J. J. W. Wiltzius, H. T. McFarlane, A. O. Madsen, C. Riekel and D. Eisenberg, *Nature*, **2007**, 447, 453-457.

[26] J. M. Gosline, P. A. Guerette, C. S. Ortlepp and K. N. Savage, *J Exp Biol*, **1999**, 202, 3295-3303.

[27] E. Monsellier and F. Chiti, *Embo Rep*, **2007**, 8, 737-742.

[28] S. Rauscher, S. Baud, M. Miao, F. W. Keeley and R. Pomes, *Structure*, **2006**, 14, 1667-1676.

[29] T. A. Blackledge, N. Scharff, J. A. Coddington, T. Szuts, J. W. Wenzel, C. Y. Hayashi and I. Agnarsson, *P Natl Acad Sci USA*, **2009**, 106, 5229-5234.

[30] R. C. Chaw, Y. H. Zhao, J. Wei, N. A. Ayoub, R. Allen, K. Atrushi and C. Y. Hayashi, *Bmc Evol Biol*, **2014**, 14.

[31] S. Keten and M. J. Buehler, *Nano Lett*, **2008**, 8, 743-748.

[32] A. T. Nguyen, Q. L. Huang, Z. Yang, N. B. Lin, G. Q. Xu and X. Y. Liu, *Small*, **2015**, 11, 1039-1054.

[33] A. Nova, S. Keten, N. M. Pugno, A. Redaelli and M. J. Buehler, *Nano Lett*, **2010**, 10, 2626-2634.

[34] G. Q. Xu, L. Gong, Z. Yang and X. Y. Liu, *Soft Matter*, **2014**, 10, 2116-2123.

[35] A. H. Simmons, C. A. Michal and L. W. Jelinski, *Science*, **1996**, 271, 84-87.

[36] M. E. Rousseau, T. Lefevre, L. Beaulieu, T. Asakura and M. Pezolet, *Biomacromolecules*, **2004**, 5, 2247-2257.

[37] A. Martel, M. Burghammer, R. J. Davies and C. Riekel, *Biomacromolecules*, **2007**, 8, 3548-3556.

[38] S. Ulrich, A. Glisovic, T. Salditt and A. Zippelius, *Eur Phys J E*, **2008**, 27, 229-242.

[39] S. Keten, Z. P. Xu, B. Ihle and M. J. Buehler, *Nat Mater*, **2010**, 9, 359-367.

[40] S. Arcidiacono, C. Mello, D. Kaplan, S. Cheley and H. Bayley, *Appl Microbiol Biot*, **1998**, 49, 31-38.

[41] R. V. Lewis, M. Hinman, S. Kothakota and M. J. Fournier, *Protein Expres Purif*, **1996**, 7, 400-406.

[42] T. Scheibel, *Microb Cell Fact*, **2004**, 3.

[43] E. Bini, D. P. Knight and D. L. Kaplan, *J Mol Biol*, **2004**, 335, 27-40.

[44] G. Y. Li, P. Zhou, Z. Z. Shao, X. Xie, X. Chen, H. H. Wang, L. J. Chunyu and T. Y. Yu, *Eur J Biochem*, **2001**, 268, 6600-6606.

[45] A. Heidebrecht and T. Scheibel, *Adv Appl Microbiol*, **2013**, 82, 115-153.

[46] X. X. Xia, Z. G. Qian, C. S. Ki, Y. H. Park, D. L. Kaplan and S. Y. Lee, *P Natl Acad Sci USA*, **2010**, 107, 14059-14063.

[47] A. Heidebrecht, L. Eisoldt, J. Diehl, A. Schmidt, M. Geffers, G. Lang and T. Scheibel, *Adv Mater*, **2015**, 27, 2189-2194.

[48] J. A. Jones, T. I. Harris, C. L. Tucker, K. R. Berg, S. Y. Christy, B. A. Day, D. A. Gaztambide, N. J. C. Needham, A. L. Ruben, P. F. Oliveira, R. E. Decker and R. V. Lewis, *Biomacromolecules*, **2015**, 16, 1418-1425.

[49] D. W. Ding, P. A. Guerette, S. Hoon, K. W. Kone, T. Cornvik, M. Nilsson, A. Kumar, J. Lescar and A. Miserez, *Biomacromolecules*, **2014**, 15, 3278-3289.

[50] A. Pena-Francesch, B. Akgun, A. Miserez, W. P. Zhu, H. J. Gao and M. C. Demirel, *Adv Funct Mater*, **2014**, 24, 6227-6233.

[51] J. W. Bjork, S. L. Johnson and R. T. Tranquillo, *Biomaterials*, **2011**, 32, 2479-2488.

[52] D. W. Ding, P. A. Guerette, J. Fu, L. H. Zhang, S. A. Irvine and A. Miserez, *Adv Mater*, **2015**, 27, 3953-3961.

[53] N. Li, P. X. Zhao and D. Astruc, *Angew Chem Int Edit*, **2014**, 53, 1756-1789.

[54] J. P. Xie, J. Y. Lee and D. I. C. Wang, *J Phys Chem C*, **2007**, 111, 10226-10232.

[55] Y. Zhou, W. X. Chen, H. Itoh, K. Naka, Q. Q. Ni, H. Yamane and Y. Chujo, *Chem Commun*, **2001**, 2518-2519.

[56] B. Cantaert, D. W. Ding, C. Rieu, L. Petrone, S. Hoon, K. H. Kock and A. Miserez, *Macromol Rapid Comm*, **2015**, 36, 1877-1883.

[57] S. Schlucker, *Angew Chem Int Edit*, **2014**, 53, 4756-4795.

[58] Y. Liu and R. Guo, *Mater Chem Phys*, **2011**, 126, 619-627.

[59] M. Hoefling, S. Monti, S. Corni and K. E. Gottschalk, *Plos One*, **2011**, 6.

[60] Z. M. Qi, I. Honma, M. Ichihara and H. S. Zhou, *Adv Funct Mater*, **2006**, 16, 377-386.

[61] G. Nystrom, M. P. Fernandez-Ronco, S. Bolisetty, M. Mazzotti and R. Mezzenga, *Adv Mater*, **2016**, 28, 472-478.

[62] T. Lefevre and M. Auger, *Int Mater Rev*, **2016**, 61, 127-153.

[63] C. Vepari and D. L. Kaplan, *Prog Polym Sci*, **2007**, 32, 991-1007.

[64] F. J. Chen, D. Porter and F. Vollrath, *Acta Biomater*, **2012**, 8, 2620-2627.

[65] C. Z. Zhou, F. Confalonieri, M. Jacquet, R. Perasso, Z. G. Li and J. Janin, *Proteins*, **2001**, 44, 119-122.

[66] L. Romer and T. Scheibel, *Prion*, **2008**, 2, 154-161.

[67] L. F. Drummy, B. L. Farmer and R. R. Naik, *Soft Matter*, **2007**, 3, 877-882.

[68] G. H. Altman, F. Diaz, C. Jakuba, T. Calabro, R. L. Horan, J. S. Chen, H. Lu, J. Richmond and D. L. Kaplan, *Biomaterials*, **2003**, 24, 401-416.

[69] F. Chiti and C. M. Dobson, *Annu Rev Biochem*, **2006**, 75, 333-366.

[70] E. H. Koo, P. T. Lansbury and J. W. Kelly, *P Natl Acad Sci USA*, **1999**, 96, 9989-9990.

[71] M. Sunde, L. C. Serpell, M. Bartlam, P. E. Fraser, M. B. Pepys and C. C. F. Blake, *J Mol Biol*, **1997**, 273, 729-739.

[72] C. A. Ross and M. A. Poirier, *Nat Med*, **2004**, 10, S10-S17.

[73] M. P. Murphy and H. LeVine, *J Alzheimers Dis*, **2010**, 19, 311-323.

[74] M. Schmidt, C. Sachse, W. Richter, C. Xu, M. Fandrich and N. Grigorieff, *P Natl Acad Sci USA*, **2009**, 106, 19813-19818.

[75] M. Ahmed, J. Davis, D. Aucoin, T. Sato, S. Ahuja, S. Aimoto, J. I. Elliott, W. E. Van Nostrand and S. O. Smith, *Nat Struct Mol Biol*, **2010**, 17, 561-567.

[76] O. S. Makin and L. C. Serpell, *Febs J*, **2005**, 272, 5950-5961.

[77] C. C. Lee, A. Nayak, A. Sethuraman, G. Belfort and G. J. Mcrae, *Biophys J*, **2007**, 92, 3448-3458.

[78] P. Arosio, T. P. J. Knowles and S. Linse, *Phys Chem Chem Phys*, **2015**, 17, 7606-7618.

[79] T. P. J. Knowles and M. J. Buehler, *Nat Nanotechnol*, **2011**, 6, 469-479.

[80] A. L. Fink, *Fold Des*, **1998**, 3, R9-R23.

[81] D. R. Booth, M. Sunde, V. Bellotti, C. V. Robinson, W. L. Hutchinson, P. E. Fraser, P. N. Hawkins, C. M. Dobson, S. E. Radford, C. C. F. Blake and M. B. Pepys, *Nature*, **1997**, 385, 787-793.

[82] J. L. Jimenez, E. J. Nettleton, M. Bouchard, C. V. Robinson, C. M. Dobson and H. R. Saibil, *P Natl Acad Sci USA*, **2002**, 99, 9196-9201.

[83] M. Bhattacharya, N. Jain and S. Mukhopadhyay, *J Phys Chem B*, **2011**, 115, 4195-4205.

[84] R. Nelson, M. R. Sawaya, M. Balbirnie, A. O. Madsen, C. Riekel, R. Grothe and D. Eisenberg, *Nature*, **2005**, 435, 773-778.

[85] R. N. Rambaran and L. C. Serpell, *Prion*, **2008**, 2, 112-117.

[86] L. C. Serpell, *Bba-Mol Basis Dis*, **2000**, 1502, 16-30.

[87] Z. P. Xu, R. Paparcone and M. J. Buehler, *Biophys J*, **2010**, 98, 2053-2062.

[88] S. Bolisetty and R. Mezzenga, *Nat Nanotechnol*, **2016**, 11, 365-371.

[89] C. X. Li, S. Bolisetty and R. Mezzenga, *Adv Mater*, **2013**, 25, 3694-3700.

[90] J. H. Collier and T. Segura, *Biomaterials*, **2011**, 32, 4198-4204.

[91] A. B. Seabra and N. Duran, *Peptides*, **2013**, 39, 47-54.

[92] Y. Zhou, *Recent Pat Nanotech*, **2007**, 1, 21-28.

[93] R. de la Rica and H. Matsui, *Chem Soc Rev*, **2010**, 39, 3499-3509.

[94] S. Scanlon and A. Aggeli, *Nano Today*, **2008**, 3, 22-30.

[95] N. Nuraje, I. A. Banerjee, R. I. MacCuspie, L. T. Yu and H. Matsui, *J Am Chem Soc*, **2004**, 126, 8088-8089.

[96] R. G. Ellis-Behnke, Y. X. Liang, S. W. You, D. K. C. Tay, S. G. Zhang, K. F. So and G. E. Schneider, *P Natl Acad Sci USA*, **2006**, 103, 5054-5059.

[97] X. Y. Gao and H. Matsui, *Adv Mater*, **2005**, 17, 2037-2050.

[98] C. Aleman, A. Bianco and M. Venanzi, *Peptide Materials: From Nanostructures to Applications*, Wiley, **2013**.

[99] H. Hosseinkhani, P. D. Hong and D. S. Yu, *Chem Rev*, **2013**, 113, 4837-4861.

[100] H. G. Cui, M. J. Webber and S. I. Stupp, *Biopolymers*, **2010**, 94, 1-18.

[101] E. Kasotakis, E. Mossou, L. Adler-Abramovich, E. P. Mitchell, V. T. Forsyth, E. Gazit and A. Mitraki, *Biopolymers*, **2009**, 92, 164-172.

[102] E. Kasotakis and A. Mitraki, *Biopolymers*, **2012**, 98, 501-509.

[103] M. Zhou, A. M. Smith, A. K. Das, N. W. Hodson, R. F. Collins, R. V. Ulijn and J. E. Gough, *Biomaterials*, **2009**, 30, 2523-2530.

[104] A. Dasgupta, J. H. Mondal and D. Das, *Rsc Adv*, **2013**, 3, 9117-9149.

[105] Y. Nagai, L. D. Unsworth, S. Koutsopoulos and S. G. Zhang, *J Control Release*, **2006**, 115, 18-25.

Chapter 3

Experimental Methodology

A wide range of experimental approaches have been employed to investigate the interactions between suckerin peptides and to characterize the secondary structures formed by these peptides. Biophysical, thermal and mechanical characterization techniques have also been employed to study the properties of materials formed from suckerin peptides. In this chapter, all sample preparation methods and experimental techniques including their general theoretical principles are introduced.

3.1 Rationale for selection of Methods/Materials

A range of synthesis, sample preparation and characterization methods have been used in the project. In this chapter, these methods will be described in detail and presented as four main sections: (i) synthesis; (ii) purification and analysis; (iii) peptide macro-array binding assay; and (iv) characterization. Sample preparation and analysis of data will be described in (iv) characterization, according to different characterization technique employed.

3.2 Synthesis

3.2.1 Solid Phase Peptide Synthesis (SPPS)

Solid Phase Peptide Synthesis (SPPS) is a well-established and common peptide synthesis method that has been employed for short peptides, pioneered by Bruce Merrifield in 1963.[1] Many developments and automation technology have since sprouted, modifying and improving on the method to increase the efficiency and peptide length; such as microwave synthesis,[2] modified supports and linkers[3-5] and automated peptide synthesizers.[5] SPPS consists of repetitive coupling and deprotection steps, whereby N-terminus protected amino acids are added to the peptide one residue at a time, and synthesis starts from the C-terminus. Tert-butyloxycarbonyl (Boc) and 9-Fluorenylmethyloxycarbonyl (Fmoc) protection groups are common in SPPS. The latter method has been favored, mainly due to fewer toxic reagents required for post-synthesis cleavage of peptide from the solid supports, and to the ease in synthesis and purification steps. A general Fmoc SPPS synthesis procedure is displayed in Figure 3.1. It includes (i) activation, (ii) deprotection, (iii) coupling, and (iv) cleavage procedures which will be elaborated in detail. Two resins, Wang resin and Chlorotrityl chloride resins have been used for the Fmoc SPPS in this work.

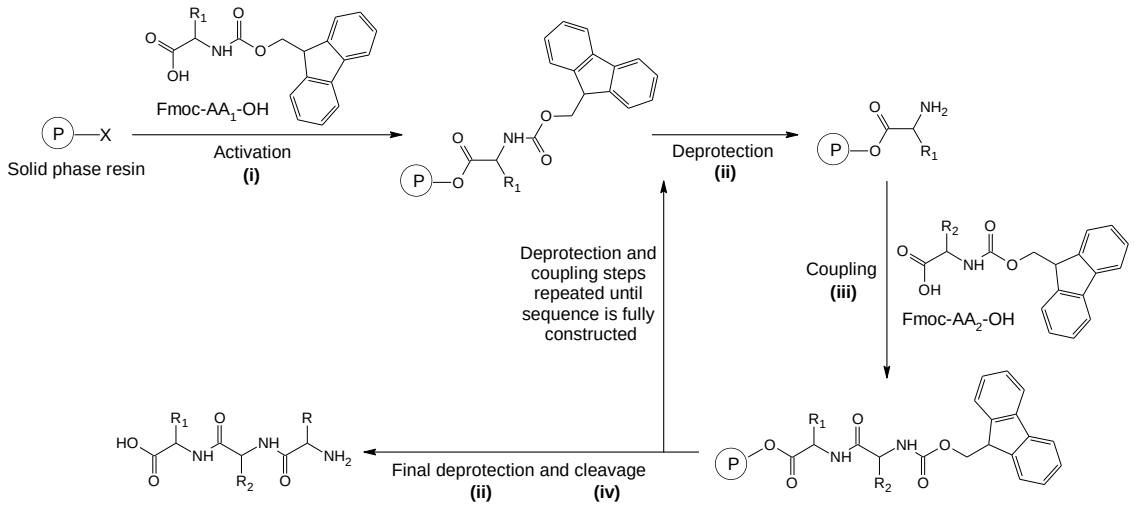

Figure 3.1 A Fmoc SPPS procedure. Solid phase resin with a selected functional group "X" is activated by the first amino acid attachment, (i). Fmoc protecting group is removed via a (ii) deprotection step before the amine is exposed to allow for subsequent amino acid coupling, (iii). The deprotection and coupling steps are repeated until the peptide sequence has been fully constructed then a final deprotection and (iv) cleavage will release the peptide from the resin.

Wang resin SPPS method

Wang resin (0.52 mmol/g) was swelled for 1 hour in anhydrous dimethylformamide (DMF), which was prepared by adding 3.0 Å molecular sieves 24 hours prior to swelling. (i) Fmoc–protected amino acid (Fmoc-AA-OH) coupling/activation cocktail was prepared by first stirring 10 equivalents (equiv.) of Fmoc-AA-OH and 5 equiv. of N,N'-Diisopropylcarbodiimide (DIC) in anhydrous dichloromethane (DCM) at 0 °C for 1 hour. DCM was then removed to redissolve the residue in anhydrous DMF and 1 equiv. of 4-dimethylaminopyridine (DMAP). Activation was initiated by addition of coupling cocktail to pre-swelled Wang resin. The reaction mixture was stirred for 16 hours in a reaction vessel. Following the activation step, the resins were washed thoroughly with 3x DMF, 3x methanol (MeOH) and 3x DCM. Unreacted hydroxyl groups on the resins were capped by adding 5 equiv. of acetic anhydride and 10 equiv. of pyridine in minimal DCM and stirred for 30 minutes. The resins were then washed thoroughly with 3x DMF, 3x MeOH and 3x DCM, and treated with (ii) deprotection solution of 25% piperidine in DMF twice for

30 minutes each time. The resins were washed thoroughly (3x DMF, 3x MeOH, 3x DCM) again and a 2,4,6-trinitrobenzenesulfonic acid (TNBS) test was done on a few resin beads to monitor the activation step of coupling the amino acid to the resins and the deprotection step (addition of 2 µL of picrylsulfonic acid and 10% v/v N,N-diisopropylethylamine (DIPEA) in DMF). For subsequent couplings, (iii) 2 equiv. Fmoc-AA-OH, 1.9 equiv. HATU and 5 equiv. DIPEA were added to the resins. Each coupling step was repeated twice (double coupling), for 1 hour and 16 hours, to ensure that maximum coupling was achieved. Deprotection and coupling steps with thorough washings in between were repeated until the peptide sequences were attained, and TNBS test (Figure 3.2) was conducted after each amino acid coupling and deprotection step to monitor coupling reactions and complete deprotection, respectively.

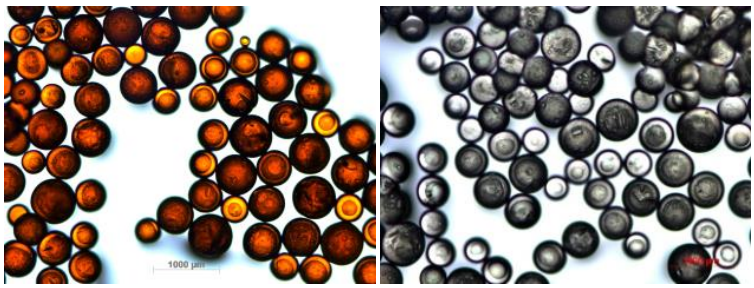

Figure 3.2 TNBS (2,4,6-trinitrobenzene sulfonic acid) test on resin beads. TNBS test is used to detect primary amino groups. TNBS was used to monitor the coupling reactions; the presence of free $–NH_2$, gives a positive result where the beads turn orange (left image), indicating complete deprotection. In the absence of free $–NH_2$ groups, a negative result can be observed where the beads remain colorless (right image), indicating successful and complete coupling reaction.

In the final step, the amino acid side chain protecting groups were removed and peptides cleaved off resins by (iv) incubation in 95% trifluoroacetic acid (TFA), 2.5% triisopropylsilane (TIPS) and 2.5% water for 2 hours. The resins were removed by filtration and TFA evaporated slowly by nitrogen gas. The cleaved peptides were then precipitated by washing the remaining solution with diethyl ether (5x) and then dried under vacuum. Peptides were then stored at -20 °C.

Chlorotrityl chloride resin SPPS method

Chlorotrityl chloride (CTC) resins are employed when a peptide sequence consists of a C-terminus or penultimate Gly or Pro residue.[3, 6] These residues are capable of forming a cyclic diketopiperizine side-product (Figure 3.3) via β-elimination, where the residue adjacent to C-terminus does a nucleophilic attack at the C-terminus's carbonyl. In such cases, the bulky chlorotrityl linker group of the CTC resins helps prevent diketopiperazine formation in sequences with the abovementioned residues.

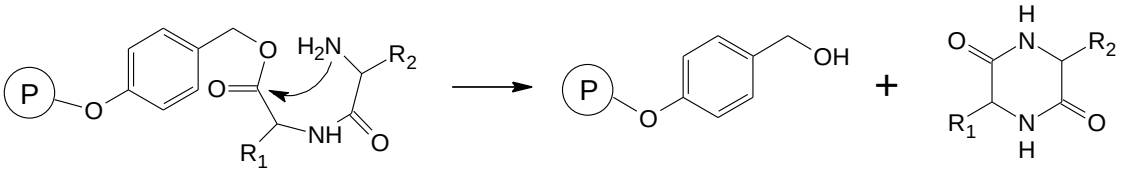

Figure 3.3 Diketopiperazine formation via β-elimination. Nucleophilic attack from the second residue's amine group occurs at the carbonyl group of the first residue, resulting in the formation of a cyclic diketopiperazine byproduct and the removal of both residues from solid support.

CTC resins (1.22 mmol/g) were swelled in anhydrous DCM for 1 hour and a (i) activation/coupling cocktail of 1.5 equiv. Fmoc-AA-OH and 2 equiv. DIPEA was added to the resins and stirred for 16 hours in a reaction vessel. Following the activation step, the resins were washed thoroughly with 3x DMF and 3x DCM, and any remaining unreacted chloride groups on the resins were capped by adding DCM, MeOH and DIPEA (85:10:5) and stirred for 1 hour. The resins were then washed thoroughly with 3x DMF and 3x DCM. Deprotection steps, subsequent coupling procedures and TNBS tests are the same as that of Wang resin, and these steps were repeated with thorough washings in between until the desired peptides were attained. The cleavage of peptide from resin and removal of amino acid side chain protecting groups was the same as that of Wang resin.

In SPPS, production of peptides can easily reach up to grams scale, depending on the loading of the solid resin selected, the sequence of the peptides (hydrophobic peptides tend to aggregate during synthesis, lowering the overall yield) and the number

of residues in a sequence. Truncation of peptides can be a problem when the number of residues increases, as the yield of the peptide decreases exponentially with the increasing length of the peptide. Therefore although SPPS is an excellent method to achieve large scale synthesis of peptides, it has its limits for consideration, especially for sequences longer than 25 amino acid residues.

3.2.2 SPOT synthesis

Peptide synthesis on cellulose, namely SPOT synthesis, is a method that is time and cost efficient,[7, 8] allowing one to generate large peptide libraries in a controlled and parallel fashion. Via SPOT synthesis, quantities of reagents used are reduced, and hundreds of spots of peptides can be completed in a day, saving both time and money.

In SPOT synthesis, there are various surfaces and surface-modified functional groups that can be selected, depending on the intended application after peptide synthesis. Once the activation step is complete (the first amino acid synthesized onto the surface support), the procedure of peptide synthesis is very similar to SPPS, using the standard Fmoc SPPS reagents and methods.

SPOT synthesis is generally targeted for small scale synthesis and large peptide libraries. The most common application of SPOT synthesis is the array screening for interaction activity of peptides and proteins.[9] Interaction screening requires only a minute amount of immobilized ligands and optimally the maximum ligand targets to be screened against.

When peptides are synthesized from scratch via SPOT synthesis, no purification steps are required. However, as the peptide length increases, the same issues of truncation and peptide material impurities exist. Therefore as an alternative to synthesize peptides from scratch on a selected SPOT synthesis surface, fully constructed peptide sequences can be purified and analyzed for their purity prior to immobilizing them[10] onto the surface via SPOT synthesis methods. This ensures the correct peptide sequences of high purity to be immobilized in each spot prior to array screenings.

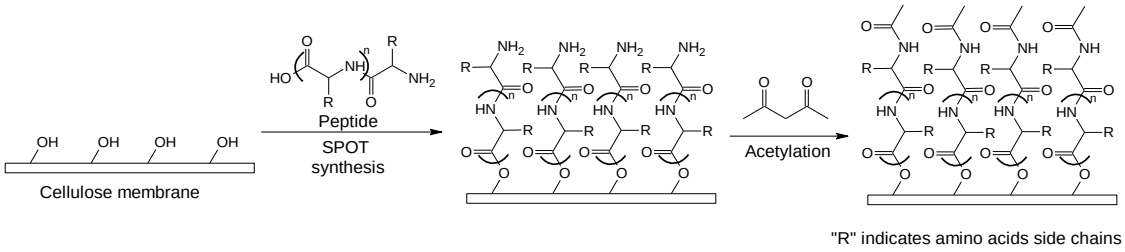

Figure 3.4 Illustration of peptide immobilization onto cellulose membrane via SPOT synthesis. Peptides are first coupled onto cellulose membrane from their C-terminus by addition of coupling cocktail containing peptide and coupling agents. Capping of N-terminus is done by acetylation with acetic anhydride.

Peptides purchased from GL Biochem were verified with a high purity of > 98% via reverse-phase HPLC and LC-MS prior to SPOT synthesis (Figure 3.4). Protocol for SPOT synthesis was partially modified from Hilpert *et al.*[7] Coupling cocktail was prepared as peptide/HOBt/TBTU/DIEA (1 : 4.9 : 4.9 : 5, equiv.) in DMF and spotted at 1μL per spot on Whatman Chr1 cellulose. Spots were left to dry before respotting again for a total of 3 cycles to maximize coupling. Thorough washing was done in DMF with agitation on a lab shaker, followed by staining with bromophenol blue in methanol (20-50 mg in 1 liter) to check for spots. Bromophenol blue stains free amines, and blue spots on the cellulose support indicates successful coupling of peptide onto the surface (Figure 3.5). Methanol was used to destain bromophenol blue, and subsequent acetylation of the N-terminus α-amino group was done by immersing the cellulose sheet in a capping solution of acetic anhydride/DIEA/DMF (1 : 1 : 8, v/v). Bromophenol blue staining was used to check for the completion of acetylation, and previously stained blue spots that remain colorless after acetylation would indicate successful acetylation. The cellulose sheet was then left to dry under ambient conditions after a final destaining step with methanol.

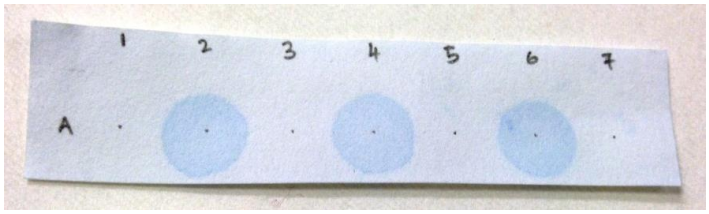

Figure 3.5 Example of bromophenol blue staining. Bromophenol blue-stained spots of immobilized peptides with free amine at N-terminus (at 2, 4 and 6 positions), indicating the successful immobilization of peptides onto cellulose via SPOT synthesis.

3.2.3 Fluorescent tagging of peptides

Fluorescent dyes are commonly used as indicators in proteomics for detection purposes via fluorescent imaging or fluorescent spectra. A carefully selected fluorescent dye was used to label peptides that are used as analytes for the designed binding assay in this work, to function as a tool for detecting interaction activities. Preliminary binding assay trials were conducted to ascertain whether the dye could affect the peptides' interaction activity. Primary binding assay trials were first conducted on a selected positive control peptide Aβ(37–42), Ac-GGVVIA-$CONH_2$,[11, 12] which is a β-sheet forming sequence from the beta-amyloid protein, followed by secondary preliminary binding assay trials between a few peptides from this work. After ensuring that the interaction activities were unaffected, Texas Red dye was selected with a succinimidyl ester functional group to label the free amine group of the peptides (Figure 3.6).

Termini-modified peptides (N-terminus acetylated and C-terminus amidated) were labeled at their amidated C-terminus with Texas Red fluorescent dye (purchased from Invitrogen, Texas Red SE Mixed Isomers), with a modified labeling protocol (original protocol from Invitrogen). 0.2 mg of Texas Red SE dye was dissolved in 10 µL DMSO and mixed with a solution of 2 mg peptide dissolved in 200 µL of 75 mM $NaHCO_3$ at pH 8.3. The labeling mixture was incubated overnight while vortexing to maximize fluorescent dye attachment. This mixture was purified with dye removal column (Pierce^{TM}) to remove any excess unreacted dye. All labeling procedures were conducted in the dark as the dye is light sensitive, and labeled peptides were stored in the dark at -20 °C.

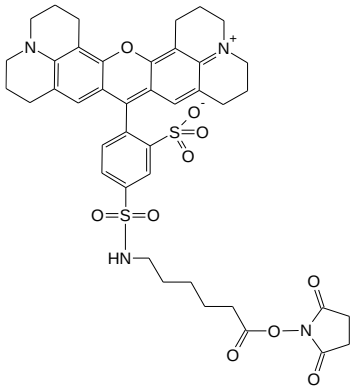

Figure 3.6 Molecular structure of Texas Red SE fluorescent dye. Succinimidyl ester (SE) functional group was selected for the conjugation to primary free amine group of peptides.

Immediately prior to using the labeled peptides, UV-Vis excitation and emission spectra was obtained to determine the concentration of fluorescently-labeled peptide by comparing with a Texas Red dye concentration standard prepared (Section 3.5.13).

3.3 Purification and analysis

3.3.1 High Performance Liquid Chromatography (HPLC)

High Performance Liquid Chromatography (HPLC) is an analytical method to separate and purify compounds. Columns containing functionalized resins are used to separate compounds ranging from small molecules to proteins and polymers. Columns can be customized by packing with different resins (of different functionalization, particle sizes, pore sizes and material) and column length and diameter. Commonly used columns for protein chromatography are size-exclusion chromatography (SEC) columns, reversed-phase (RP) chromatography columns and ion-exchange (IEX) chromatography columns, with variations on the functionalization of their resins.

SEC or gel filtration columns separate compounds via their molecular sizes, eluting larger compounds first while smallest compounds are retained longer in the

pores of the resins and get eluted last; RP columns separate compounds via their polarity, whereby the carbon-chain functionalized (C4, C8, or C18) resins act as hydrophobic stationary phases, and polar compounds are eluted first; IEX columns separate compounds via their charges, whereby compounds of the same charge as the stationary phase are eluted first, and with the change in pH of the mobile phase or with an introduction of a stronger counter ion, the compounds bounded to the stationary phase gets eluted.

HPLC was used for both trace analysis and purification of peptides in this work. An Agilent Infinity 1260 HPLC system and Agilent Zorbax 300SB-C18 (300 Å pore size, 5 µm resin diameter) RP columns were used for all trace analysis and purification of peptides.

Trace analysis – Trace amount of purchased peptides were dissolved in 5% Acetonitrile (ACN)/95% water and eluted through a RP-C18 analytical column at 1 mL/min flow rate. A gradient elution of 2% ACN/min was set to increase from 5% ACN to 40% ACN. UV wavelengths of 210 nm (absorbance of C-H bonds), 220 nm (absorbance of peptide bond), 254 nm (absorbance of aromatic amino acids) and 280 nm (absorbance of His, Tyr and Trp amino acids) were recorded. The obtained chromatograms were analyzed for percentage purity via Agilent 1260 Infinity software, by integrating the area under the eluted peaks.

Purification – The synthesized peptides were dissolved in 7% ACN and 93% water at concentrations of 5–10 mg/mL and filtered with 0.2 µm filter prior to injection. A RP-C18 preparative column was used for purification, with sample injection of 1mL per run and 3 mL/min flow rate. A gradient of 2% ACN/min was set to increase the ACN concentration of the mobile phase from 7.5% to 30%. Collection of elute was set to 0.3 min per vial, and similar fractions were combined and lyophilized. Subsequent purification process was repeated, with minor adjustments to the gradient elution for optimized separation, until > 95% pure peptides were obtained. Trace analysis was done to determine the percentage purity of the peptides prior to use.

3.3.2 Liquid Chromatography Mass Spectrometry (LC/MS)

Liquid Chromatography Mass Spectrometry (LC/MS) is an analytical technique used for the detection and identification of the molecular masses of compounds present in a sample. After a liquid chromatography separation, the fractions are ionized via electrospray ionization (ESI) creating charged ions, which then get separated by the analyzer's electromagnetic fields according to their mass-to-charge ratio. These ions are then detected by the detector quantitatively and processed into a mass spectrum. Via LC/MS, unknown compounds or trace impurities in samples can be identified by their masses, and the purity of a compound can be determined quantitatively.

LC/MS was used to detect the molecular weight of the peptides and impurities present in the samples. Measurements were conducted in ESI+ mode with a Thermo Scientific LCQ Fleet Ion Trap LC/MS. Sample preparation was done by dissolving a trace amount of peptide powder in 200 µL of 5% ACN/ 95% water and filtered with 0.2 µm filter. Subsequently, 20 µL of sample was injected into the system and an elution chromatogram was collected for 2 minutes. Mass spectra were obtained with an average of at least 15 scans of the elution peaks, then used for further analysis. De-convolution and assignment of mass peaks were done manually by subtracting positive adduct ions from the masses obtained to get the true mass of the compounds and to identify impurities.

3.4 Peptide macro-array binding assay

A peptide microarray is a collection of peptides immobilized in an organized grid fashion on a solid surface, such as a glass slide or chip. They are usually fabricated by automated printing technologies, printing up to thousands of peptide spots per cm^2.[7, 8] Peptide microarrays allow for the high throughput screening of thousands of peptide candidates in a short amount of time with the requirement of only a small quantity of sample, thus making this technique favorable and widely used in the biomedical and research industries.

In conjunction with combinatorial chemistry concepts, a peptide macro-array binding assay was designed to screen interactions between peptides in this work.

Immobilization of peptide spots was done manually (Section 3.2.2) and these peptides synthesized onto the cellulose surface and act as ligands. Fluorescently labeled analyte peptides (Section 3.2.3) were incubated with the immobilized ligand peptides under different pH conditions and concentrations to assess their affinity under the different environments for a stipulated time period. Positive interactions, also known as "hits" are indicated by the fluorescent intensities detected with a fluorescent imager.

Preparation and experiment

Prior to conducting the binding assay, different blocking buffers were tested to assess their suitability for the peptide binding assay system. Selecting a good blocking buffer that inhibits non-specific interactions without compromising the specific interactions of the binding assay is crucial. Skim milk at 0.1% and 2% (w/v), and BSA at 0.1% and 2% (w/v) were used as blocking agents in 0.2% (v/v) Tween 20 pH-buffered solution. Preliminary binding assays were first conducted with the positive control peptide Ac-GGVVIA-CONH. Peptides from this work were then assayed using the same method. From the preliminary assays conducted, 0.1% BSA (w/v) in 0.2 % (v/v) Tween 20 pH-buffered solution was selected as the ideal blocking buffer.

Spots were punched out from the cellulose sheets from Section 3.2.2 and inserted into a 96-well microtiter plate (MTP).[7] Contents of each well were soaked with methanol for 1 hour then washed 3x with the following respective pH buffers: 0.1 M sodium acetate at pH 4; 0.1 M phosphate buffered saline at pH 7; 0.1 M tris-buffered saline at pH 8.6. The spots were then incubated in their blocking buffers (0.2% (v/v) Tween 20 and 0.1% (w/v) BSA in their respective pH buffers) for 2 hours on a rocker.

Immediately prior to using the fluorescently-labeled peptides from Section 3.2.3, they were diluted with the respective blocking buffers to make up analyte peptide solutions of concentrations 0.1 µM, 0.5 µM and 1 µM. Blocking buffer was then removed and 40 µL of analyte peptide solution was added and incubated for 3 hours on a rocker. Stringent washing of the spots were done at the end of incubation (3x blocking buffer, 3x Tween 20 pH-buffered solution and 3x pH buffer). All steps were conducted at ambient temperature and in the dark, and each condition was done in quadruplicates to obtain average values.

Measurements and analysis

A Typhoon fluorescent imager was used to image the MTPs immediately after the final washing. High sensitivity setting with 595 PMT, using red laser and a 610 nm band-pass filter was selected for all fluorescent imaging. GelAnalyzer software was used to analyze images obtained and to calculate the average intensities of each spot subsequently. Intensities were normalized with a standard MTP plate containing cellulose spots with immobilized peptides in the same arrangement as all binding assay MTPs used. Background subtraction was done by subtracting fluorescent intensities obtained from the fluorescent images taken of the respective ligand-immobilized cellulose in MTPs after blocking and stringent washing procedures (right before analyte incubation procedure).

3.5 Characterization

3.5.1 Dynamic light scattering (DLS)

DLS measurements are obtained by detecting the fluctuations in the light scattering intensity of a solution containing scattering objects. Particles and molecules that are dispersed in solution and undergo Brownian motion (governed by Stokes-Einstein equation) scatter light, and correlation functions and hydrodynamic diameters of the particles can be obtained from the measurements. The Poly Dispersity Index (PDI) of a sample can be obtained as well, and this value tells us whether the sample is monodispersed (PDI < 0.1) or multimodal (PDI > 0.1). The distribution profile can be presented using different parameters, such as intensity, volume, and number. The Z-average (cumulants mean) is also a parameter that can be obtained from intensity-based calculations. As Z-average values are insensitive to noise, it is a preferred parameter when reporting the sizes of particles measured by DLS, especially in monodispersed samples. Known as “harmonic intensity averaged particle diameter”, the Z-average (D_z) is calculated by the DLS software using Eq. 3.1, where S_i is the scattered intensity of particle *i* and D_i is its diameter:

$$D_z = \frac{\sum S_i}{\sum(\frac{S_i}{D_i})} \quad \text{(Eq. 3.1)}$$

As the purpose of DLS technique in this work was to monitor the trend of the self-assembly process, the PDI of the samples tended to increase as the sample became highly poly-dispersed, and expected sedimentation of larger particles over time would resulting in a non-ideal fit of the correlation function. For this objective, Z-average values were used as references to best represent the system's trend (note is taken that the hydrodynamic size of the self-assembling particles do not represent the true sizes).

Sample preparation

Malvern Zetasizer Nano ZS was used for all DLS measurements in this work. Peptides were dissolved at a concentration of 50 μM in buffers of pH 4 (0.1 M sodium acetate), 7 (0.1 M phosphate buffered saline), 8.2 (0.1 M tris-buffered saline) and 8.6 (0.1 M tris-buffered saline), and in urea. All buffers were double-filtered prior to use.

Measurements and analysis

Z-average size measurements were collected at 90 ° detector angle, at 25 °C and intervals of 10 minutes. Each measurement was averaged over 15 readings per measurement, over a period of 24 hours. Results were plotted with OriginPro 9.1 and presented in 30 min segments with error bars.

3.5.2 Congo red birefringence assay

Congo red birefringence assay detects the presence of amyloid structures by using a staining reagent, Congo red dye, which specifically binds to the cross-β structure of amyloids.[13] Speculated Congo red binding mechanisms are: intercalation interaction between peptide chains [14] and via binding to the same type of positively-charged residue along the β–sheet (in the H-bond direction) spaced 5 strands apart,[15] although a definite mechanism has yet to be confirmed. In the presence of amyloid structures, the Congo red dye stains the sample, which appears red under bright field optical microscopy, and yellow/apple-green birefringence under polarized light.[14, 16]

Sample preparation

Ac-GGVVIA-$CONH_2$ was used as a positive control, as this fibril-forming peptide forms amyloid cross-β-structures. All fibers self-assembled in their respective buffer solutions were pipetted onto a glass microscope slide, with excess solution blotted away with lint-free filter paper. Fibers were then rinsed with MilliQ water to remove any residual salt and allowed to air dry.

Experiment and analysis

Congo red staining was done on fiber samples in this work to identify if any amyloid β-structure was present in the fibers. A solution of 80% (v/v) ethanol (EtOH) and 20% (v/v) MilliQ water was added with a saturating amount of sodium chloride (NaCl) and vortexed until no more salt could be dissolved. Excess NaCl was filtered off and a saturating amount of Congo red was added and vortexed until no more dye could be dissolved. This staining solution was then filtered with 0.2 µm filter and used immediately.

Staining solution was pipetted onto the dried fibers, ensuring that all fibers were covered with the staining solution. Excess staining solution was then blotted away with lint-free filter paper after 20 s. Fibers were allowed to dry at ambient temperature before viewing them under the microscope.

3.5.3 Circular Dichroism (CD) spectroscopy

Circular Dichroism (CD) spectroscopy is a technique for studying the differential absorption of left- or right-handed circularly polarized light by optically active chiral compounds. Active chiral compounds that exhibit absorption between 160 nm to 850 nm wavelength range can be studied using a CD spectrometer, and commonly studied molecules include organic molecules, DNA, and proteins.

In an AVIV 420 CD spectrometer, a Xenon light source emits a monochromatic light which is converted to circularly polarized light by a 50 Hz photoelastic modulator. By de-convoluting the CD spectra obtained, which is usually measured in delta absorbance or ellipticity (θ) and expressed in units of millidegrees (mdeg), structures of the chiral molecules can be elucidated.

Delta absorbance (ΔA) measured, is the difference in absorption between the left- and right-handed circularly polarized light when the polarized light passes through an active chiral compound. It can be defined as:

$$\Delta A = A_L - A_R \quad \text{(Eq. 3.2)}$$

Correlating to Beer-Lambert law, it can also be expressed as:

$$\Delta A = (\epsilon_L - \epsilon_R)Cl \quad \text{(Eq. 3.3)}$$

where ϵ is the molar extinction coefficients for the polarized light (L – left-handed and R – right-handed), C is the molar concentration and l is the path length (in cm). The molar circular dichroism is expressed as Δϵ,

$$\Delta\epsilon = \epsilon_L - \epsilon_R \quad \text{(Eq. 3.4)}$$

and is usually converted to molar ellipticity $[\theta]$ by:

$$[\theta] = 3298.2 \times \Delta\epsilon \quad \text{(Eq. 3.5)}$$

where $[\theta]$ is reported in units of degrees cm^2 $dmol^{-1}$, taking into account and normalizing the circular dichroism with the molarity of the compound measured.

For proteins or peptides, an important factor is the mean residue ellipticity $[\theta]_{MR}$, which averages the molar ellipticity for individual amino acid residues present, thereby allowing fair and normalized comparisons between proteins and peptides of different molecular sizes. This can be determined by the following equation, substituting in the mean residual weight (MRW), which can be calculated by dividing the molecular weight of the protein or peptide by the number of amino acid residues present.

$$[\theta]_{MR} = (\theta) \times \left(\frac{0.1 \times MRW}{Cl}\right) \quad \text{(Eq. 3.6)}$$

Sample preparation

Peptides were prepared at concentrations of 2 mg/mL or 5 mg/mL in their respective buffer solutions (pH 4 (0.1 M sodium acetate), 7 (0.1 M phosphate buffered saline), 8.2 (0.1 M tris-buffered saline) and 8.6 (0.1 M tris-buffered saline)).

Measurements and data analysis

In this work, the peptides' secondary structural changes over a time period were examined with CD spectroscopy. With the α-carbon of amino acids (except for Gly) serving as a chiral center for application of this technique, the amide bonds absorbs at the far UV region (180–250 nm), providing information on the secondary structure of the peptides.[17]

A quartz cuvette with optical path length of 0.2 mm was used. Data acquisition was performed by the AVIV 420 CD spectrometer in wavelength steps of 0.5 nm in the range 190–260 nm, and with an averaging time of 0.1 s over 3 scans. The obtained spectra were averaged over the 3 scans and background (CD spectra of respective buffer) was subtracted. $[\theta]_{MR}$ or $[\theta]$ in short, was used to plot spectra for further analysis. Spectra were smoothed with "adjacent-averaging" function for 10 points on OriginPro 9.1 to reduce the noise in the spectra.

Subsequent analysis of the peptides was done via peptide secondary structure CD spectra fitting programs, PEPFIT,[18] and BeStSel,[19] which analyzes CD spectra and calculates the relative contents of different types of β-sheet structures. As short peptides are versatile and can adopt unique structures that may be uncommon in proteins, secondary structure analysis programs such as K2D[17] and Contin[17] are not suitable for analyzing short peptides as they compare CD spectra from libraries of known proteins. PEPFIT program runs a macro that enables the de-convolution of CD spectra according to nine secondary structures that can be adopted by peptides: α-helix, β-sheet, coil, reverse turn types I, II and III, γ-turn, general β-turn and gfas (spectrum resembling that typical of unordered conformation with extrema red-shifted by 10 nm). BeStSel program analyzes both protein and peptide CD spectra and determines their secondary structure content. A notable feature of the program is the ability to distinguish between parallel β-sheets and antiparallel β-sheets of different twists.

3.5.4 Fourier Transform Infrared (FTIR) Spectroscopy

Fourier Transform Infrared (FTIR) spectroscopy is a technique employed for obtaining the infrared spectrum of compounds. Molecules absorb at specific frequencies that are characteristic to their structure, owing to unique natural vibrational modes or oscillations of different intra-molecular bonds. They are known as resonant frequencies, whereby the frequency of the absorbed radiation harmonizes with the transition energy of the oscillating bond. FTIR utilizes these resonant frequencies to record the spectrum of absorbance or transmittance. These spectra can help identify compounds present in the samples, based on the assignment of the recorded peak frequencies that correlate to specific bonds. However, not all molecules are "IR active". There are several vibrational modes for covalent bonds in molecules: stretching (symmetric and asymmetric) and bending (rocking, scissoring, wagging and twisting). A molecule that experiences dipole moment during its vibration would be "IR active" and observable by IR spectroscopy, while molecules that do not produce a dipole do not appear in the IR spectrum (eg. symmetric diatomic gases). Characteristic IR bands of different functional groups can be found in the comprehensive Colthup chart[20] in the mid-infrared region (Figure 3.7), where the various vibrational modes of each functional group can contribute to absorption peaks at different wavenumbers (or frequencies).

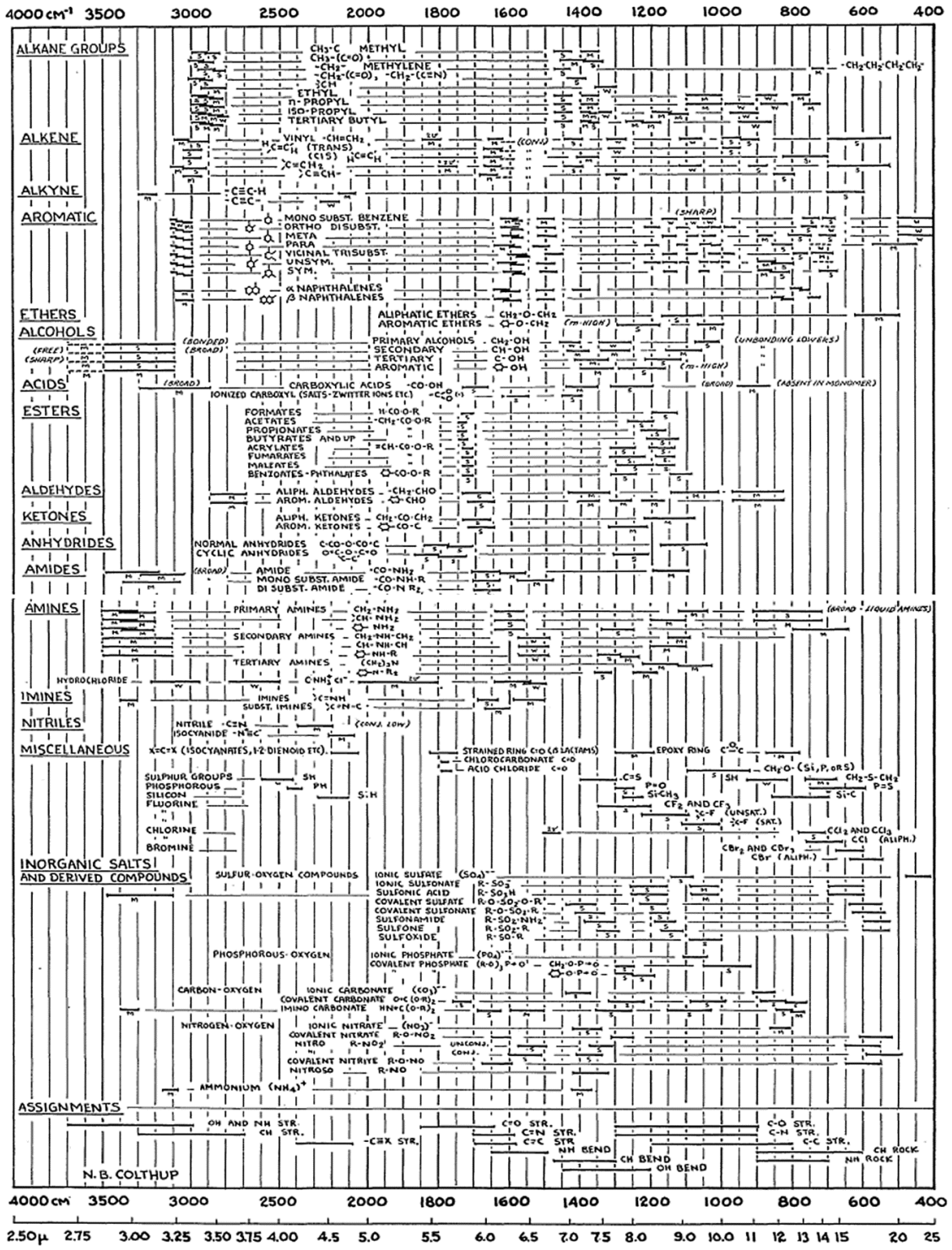

Figure 3.7 Colthup chart of functional groups in the mid-infrared region. Different **f**unctional groups absorb at different regions with varying intensities owing to their different vibration modes.[20]

In this work, FTIR technique was used as a tool to examine the peptides' secondary structures. Amide bonds can be identified by IR bands known as amide I, II

and III bands, which are observed at 1600–1690 cm^{-1}, 1480–1575 cm^{-1} and 1229–1301 cm^{-1}, respectively.[21] Amide I bands arise from the contribution of 80% C=O bond stretching, amide II bands is contributed by 60% N-H bending and 40% C-N stretching, while amide III bands is contributed by 40% C-N stretching and 30% N-H bending.[22] By further de-convoluting the Amide I band, the type of secondary structures (such as helix, sheets, random coil, etc.) that absorb in the range of the band could be identified, and their relative content could be determined by calculating the area under the de-convoluted peaks.

Sample preparation

Liquid samples - Peptides were prepared at 2 mg/mL (0.2%) at ambient temperature. Samples were homogenized with a vortex mixer prior to being pipetted onto the ZnSe crystal. Spectra were recorded immediately, and as the samples dried with steady flow of nitrogen gas.

Fiber samples – Fibers were placed onto the crystal and secured by pressing them down onto the surface of the crystal using a sample clamp. Since in the Attenuated Total Reflection (ATR) mode, the IR beam can only detect samples that are close to the crystal surface (< 1 μm), the fibers need to be secured as close to the surface as possible.

Measurements and data analysis

All samples were measured with Bruker Vertex 70 FTIR spectrometer via ATR mode on a ZnSe crystal with 3 internal reflections. Spectra were recorded in the range of 800–4000 cm^{-1} with 4 cm^{-1} resolution and averaged over 280 scans.

OPUS 6.5 program was used for processing the spectra and water compensation was manually applied by subtracting a water vapor spectra recorded prior to the experiments. The inverted secondary derivative of the original spectra were obtained and maxima peaks from the secondary derivative graph indicate the de-convoluted IR peak values contributing to the original spectra. De-convoluted IR bands in the amide I region of 1600–1700 cm^{-1} was optimized by manual peak-fitting with Gaussian band profiles. After peak-fitting, the resulting peaks were then assigned to secondary structures according to Barth *et al*.[23] and Kong *et al*.[21] Spectra were recorded in buffers that were prepared from H_2O and D_2O, and the de-convoluted

peaks were assigned according to their solvent type.[21] It is important to differentiate the buffers for the right assignment of secondary structures as the peak position shifts under deuterated conditions. (Figure 3.8)

$H_2O^{\dagger}$		$D_2O^{\ddagger}$	
Mean frequencies	Assignment	Mean frequencies	Assignment
1624±1.0	β-sheet	1624±4.0	β-sheet
1627±2.0	β-sheet		
1633±2.0	β-sheet	1631±3.0	β-sheet
1638±2.0	β-sheet	1637±3.0	β-sheet
1642±1.0	β-sheet	1641±2.0	3_{10} Helix
1648±2.0	Random	1645±4.0	Random
1656±2.0	α Helix	1653±4.0	α-Helix
1663±3.0	3_{10} Helix	1663±4.0	β-Turn
1667±1.0	β-Turn	1671±3.0	β-Turn
1675±1.0	β-Turn	1675±5.0	β-sheet
1680±2.0	β-Turn	1683±2.0	β-Turn
1685±2.0	β-Turn	1689±2.0	β-Turn
1691±2.0	β-sheet	1694±2.0	β-Turn
1696±2.0	β-sheet		

Figure 3.8 Assignment of secondary structures from de-convoluted amide I band. FTIR peaks de-convoluted from amide I band are assigned secondary structures according to their solvent system (H_2O or D_2O).[21]

3.5.5 Field Emission Scanning Electron Microscopy (FESEM)

Scanning Electron Microscope (SEM) image samples via a focused beam of high-energy electrons emitted by an electron gun (Thermionic emitter with Tungsten or Lanthanun Hexaboride filament source). Focusing of the electron beams is done with two condenser lens and an objective lens prior to the beam hitting the sample. As the electrons penetrate the sample, secondary electrons, backscattered electrons (primary electrons) and characteristic X-rays are produced depending on the beam's accelerating voltage and the sample's density. The emitted electrons from the sample collected by their respective secondary electron detector or backscattered electron detector are then processed into micrographs.

Field Emission SEM (FESEM) uses a cold cathode field emitter instead, and images with the same principles as an SEM. FESEM cold field emitter avoid the problem of heating up the filament, which creates thermal drift during operation. It is able to project a smaller electron spot size than SEM, and obtain higher-quality images at lower voltages. Overall with FESEM, images obtained are clearer at higher magnifications and less electrostatically distorted.

Sample preparation

Fibers in liquid – Fibers self-assembled in buffer solutions were pipetted onto a double-sided carbon tape pasted on a sample puck. After the fibers sediment and adhere to the carbon tape surface, remaining buffer was removed by pipetting and MilliQ water was used to rinse the fibers to remove residual salt. The fibers were then left to air dry under ambient condition. As fibers were non-conducting, fine-coating of the fibers with platinum (Pt) was done at < 5 Pa at 20 mA for 60 seconds prior to imaging.

Fibers in epoxy – Fibers were mounted in epoxy and left to solidify overnight. The embedded samples were polished as described in Section 3.5.6 to both obtain transversal as well as tangential cross sections of the fibers. Polished cross sections were fine-coated with Pt with the same settings as above.

Hydrogel samples – Hydrogels (see Section 3.5.10) were placed into liquid nitrogen for snap freezing. The frozen hydrogels were immediately placed onto a lyophilizer and freeze-dried overnight. The hydrogels maintain their integrity and size with this method, avoiding collapse of their porous structure. The lyophilized gels were then taken out and broken into smaller pieces with tweezers and placed onto carbon tape with their fractured cross-sections facing upwards. Fine-coating with Pt done with the same settings as above, prior to imaging.

Imaging

FESEM was used to investigate the samples' surface and cross section morphologies. Pt coated fibers were imaged with an FESEM JEOL JSM7600F. Samples were imaged at 5.0 kV accelerating voltage, 195 µA emission current and 7 µA probe current. The lower secondary electron detector (LEI) mode was used for most images, with a stage working distance of 15 mm and focal working distance

between 10–15 mm depending on sample height offset. In the case of images obtained using the secondary electron upper detector (SEI) mode, the stage working distance was set at 8mm and the focal working distance adjusted accordingly.

3.5.6 Nanoindentation

The Oliver-Pharr theory was used to extract the elastic modulus ($\bar{E}$) and hardness (H) of the samples probed via nanoindentation under both hydrated and dry conditions. These parameters were calculated from the loading-unloading curves obtained from indentation experiments with a Berkovich (cube corner) tip and a 2D standard transducer.

Oliver-Pharr theory

In indentation experiments, the elastic response, maximum applied load and the calculated tip area function were used to measure $\bar{E}$ and H of the samples. In the loading-unloading curve obtained from indentation on a sample that exhibits both elastic and plastic behavior, the initial unloading segment provides us with information on the elasticity of the material, as the material recovers elastically during the initial unloading phase. According to the Oliver-Pharr theory, this initial unloading curve section is used to calculate the stiffness and contact depth of the sample, and the tip area function is used to fit the unloading curve (Figure 3.9).[24, 25]

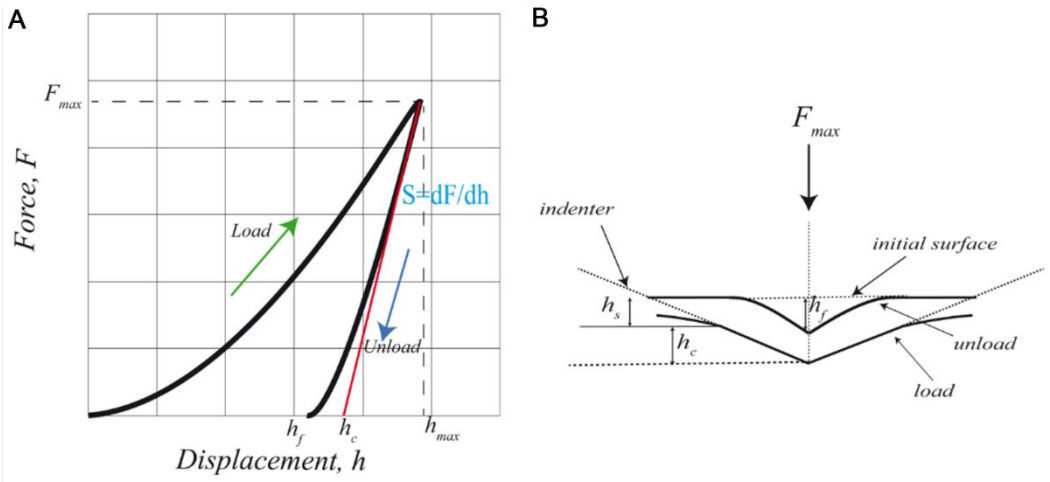

Figure 3.9 A schematic of indentation residual plastic impression and its loading-unloading curve. (A) A Loading-unloading curve that displays both elastic and plastic response is used to extract the stiffness (*S*) and contact depth (h_c) for the subsequent calculation of $\bar{E}$ and *H*. **(B)** Residual impression illustrated after loading tip is lifted, which can be used to find the contact area, A, between the sample and tip.

$\bar{E}$ and *H* are obtained according to:

$$\bar{E} = \frac{dF}{dh}\frac{1\sqrt{\pi}}{2\sqrt{A}} \qquad \text{(Eq. 3.7)}$$

and

$$H = \frac{F}{A} \qquad \text{(Eq. 3.8)}$$

where $\frac{dF}{dh}$ is the initial slope of the unloading curve, A is the contact area between the tip and the sample, and F is the maximum applied force of loading.

To be sure that we are considering the elastic response of the sample, the unloading segment of the loading-unloading curve was used to extract $\bar{E}$ according to the Oliver-Pharr method, while H was obtained only from curves that exhibit elastic-plastic response (Figure 3.10).

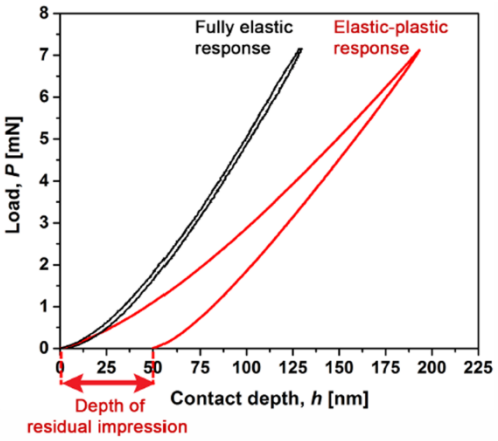

Figure 3.10 Examples of fully elastic and elastic-plastic loading-unloading curves. In a fully elastic response curve, the loading and unloading curves nearly overlap and sample returns to the original state with no residual depth of impression. A sample that exhibits elastic-plastic response curve is left with a residual depth of impression as the unloading curve follows a different path.

Sample preparation

Fibers in liquid – Self-assembled peptide fibers in buffer solutions were pipetted onto gold-coated silicon wafer surface and excess solution was blotted away with lint-free filter paper. The fibers were then rinsed with MilliQ water to remove any residual salt and allowed to air dry.

Fibers embedded in epoxy – Fibers were embedded in epoxy in a puck holder and left to solidify overnight. The epoxy puck was polished on a polisher with P800 (25.8 µm), P1200 (15.3 µm) and P4000 (2.5 µm) silicon carbide abrasive paper, respectively to obtain the transversal/tangential cross section of the embedded fibers (Figure 3.11). Polished surfaces were observed under an optical microscope to monitor the process. Final polishing was done with colloidal silica (40 nm) on a polishing cloth to obtain a smooth surface. Samples were then sonicated for at least 5 minutes to remove any residual polishing particles.

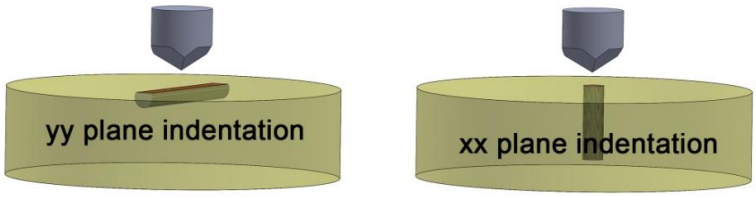

Figure 3.11 Illustration of fibers embedded in epoxy and direction of indentation. The tangential cross section of the fibers were indented from the yy plane, while the transversal cross section of the fibers indented from the xx plane.

Nanoindentation experiments

Nanoindentation experiments were done on the self-assembled peptide fibers to obtain their $\bar{E}$ and H values. Scanning probe microscopy images were first obtained prior to each set of nanoindentation experiments.

Scanning Probe Microscopy (SPM)

All SPM images and indentations were performed using Hysitron TI 950 Triboindenter, and a Berkovich (cube-corner) indentation tip was used for all indentations. The tip was calibrated with a fused quartz standard sample of $\bar{E}$ = 69.9 GPa ± 10%. Prior to indentation, samples were placed onto the indentation stage and focused through a 20x magnification lens. Thereafter, areas containing the fibers of interest were selected for SPM imaging to get a 3D topological depth-profile of the area prior to probing with a cube corner indentation tip. SPM imaging was conducted at scan rates of 0.5 Hz to 1.0 Hz for areas between 20 μm^2 to 40 μm^2.

Dry sample indentation

Samples were air-dried overnight (for at least 12 hours) under ambient conditions prior to indentation measurements. SPM imaging was first obtained and only fibers with detected thickness of above 200 nm were selected for probing, so as to prevent substrate effects due to the stiffer substrate. Indentations were performed with loading forces between 5 to 50 µN, depending on the sample. Load-hold-unload indentation function setup was used for all indents, with each segment interval being 5 s (load), 2 s (hold) and 5 s (unload).

Successful indentations with displacements falling within one-third of the fiber thickness were selected for further analysis so as to eliminate any possible substrate effect that may skew the indentation response.[26]

Hydrated sample indentation

SPM image of the area of interest was first obtained in dry conditions. With the cube corner indentation tip still in contact with the sample surface, an adequate amount of water was added carefully onto the sample to submerge the area of interest containing the fibers and the tip. The fibers were left to hydrate for at least an hour under ambient condition prior to indentation measurements. The cube corner indentation tip was left in contact with the sample to allow for equilibration under hydrated conditions. Indentations were then performed with smaller loading forces between 3 to 20 μN, as the fibers soften after hydration. Similarly, load-hold-unload indentation setup was used and likewise successful indentations with displacements falling within one-third of fiber thickness were selected for further analysis.

3.5.7 Nuclear Magnetic Resonance (NMR) spectroscopy

Nuclear Magnetic Resonance (NMR) spectroscopy is a technique which utilizes the NMR phenomenon of atomic nuclei to study the electromagnetic radiation's effect on the atom. In the NMR phenomenon exhibited by only certain atomic nuclei, the charged nuclei in a magnetic field absorbs electromagnetic radiation or photons to excite to a higher energy spin state. The energy of the electromagnetic radiation absorbed corresponds to the difference in energy between the higher energy and the lower energy spin state (resonance frequency) of the nuclei in that particular magnetic field. Upon relaxation to the lower energy state, this energy is re-emitted by the nuclei. Depending on the type of atomic nuclei surrounding the nuclei of interest and their distances apart, the surrounding nuclei can impose a nuclear shielding effect, thus creating a chemical shift of the nuclei of interest. Examples of chemical shift of proton in a common proton NMR spectroscopy are shown in Figure 3.12, whereby the resonance signals of the protons are expected to appear in different resonance signal range, depending on the type of surrounding atoms. Apart from their characteristic chemical shift positions, protons on adjacent atoms induce signal splitting. These

observations and unique characteristics enable de-convolution of the spectra and the identification of molecular structures present in a sample.

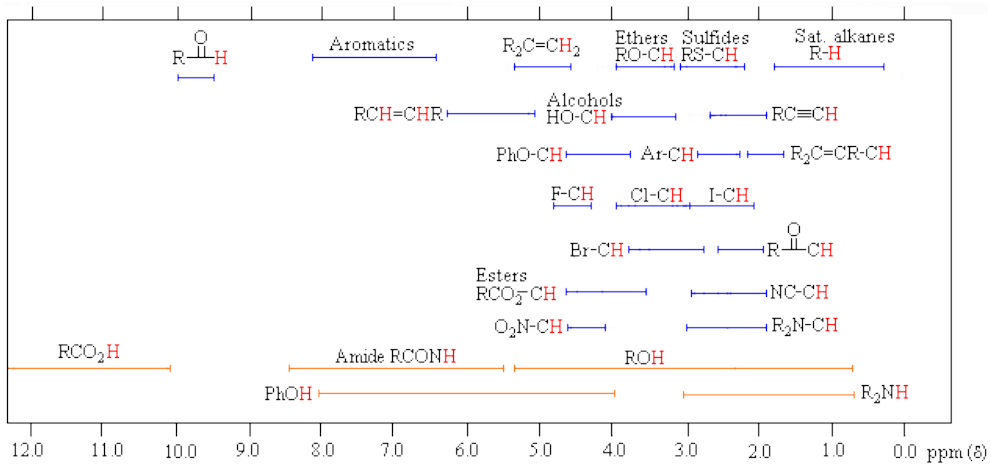

Figure 3.12 A schematic of chemical shift positions of protons attached to different functional groups. Protons attached to more electronegative groups are shifted downfield (higher ppm values) due to the increased nuclear shielding effect, and vice versa for protons attached to less electronegative groups.

In this work, NMR spectroscopy was first used to obtain the molecular structure of the peptides for the assignment of the protons on the peptides' amide backbone. This was done by obtaining homonuclear 2D NMR spectra. In contrast to traditional 1D NMR, 2D NMR help to better resolve signals that would normally overlap in 1D NMR for complex molecules. In homonuclear 2D proton NMR, this is done by adding another dimension, which yields two proton frequency axes and cross peaks. Cross peaks originate from nuclei that interact with one another, therefore through-bond or through-space (depending on the type of 2D NMR technique used) proximity information of these nuclei can be deduced from the cross peaks observed.

The 2D NMR spectra obtained for the peptides were: Total Correlation SpectroscopY (TOCSY), which correlates all protons of a spin system, as well as Nuclear Overhauser Effect SpectroscopY (NOESY) and Rotating frame Overhauser Effect SpectroscopY (ROESY), which correlate protons that are spatially positioned within 5 Å from each other. TOCSY correlates all protons (up to 5-6 bonds apart) within a spin system as long as they are mutually coupled, therefore the resonances of distant protons could be identified using a TOCSY spectrum, which allows for the

subsequent assignment of all protons within the peptide. NOESY and ROESY spectra identify protons that are close in spatial proximity, hence providing structural information. These information can further corroborate the signals of the peptide's amide backbone protons in their respective TOCSY spectra, to deduce the full connectivity and structure of the peptides. Ultimately, 1D ^{1}H NMR spectra were obtained for Hydrogen-Deuterium exchange (H/D) experiments designed to study the stability of peptide fibers and their protection factors, which will be further elaborated in Chapter 4.

Sample preparation

Peptides were incubated in pH 8.6 buffer for 5 days at a concentration of 2 mg/mL to allow the peptides to self-assemble into fibers, and subsequently the solution was snap-freezed with liquid nitrogen and lyophilized. The lyophilized samples containing the assembled fibers were then exposed to deuterium oxide for a range of 3 days at 25 °C, 45 °C, 65 °C and 85 °C for H/D exchange, followed by snap freezing to stop the exchange and lyophilization. The final lyophilized sample was then dissolved in 500 µL deuterated dimethyl sulfoxide (DMSO-d_6) and 1D ^{1}H NMR spectra were recorded. As a control for each peptide, self-assembled fibers prepared in the same manner were subjected to 1D ^{1}H NMR in 500 µL DMSO-d_6 after the first lyophilization process.

Measurements and analysis

NMR measurements were performed with Dr. Margaret Phillips, in collaboration with Professor Konstantin Pervushin (NTU, SBS). All NMR spectra were measured at 25 ^{o}C using 600 MHz (with room temperature probe) or 700 MHz (with cryoprobe) Bruker Avance II spectrometers. The ^{1}H Chemical shifts were referenced directly to the ^{1}H signal observed at 2.50 ppm in DMSO-d_6.

Backbone and side chain assignments of all peptides were done using 2D homonuclear NMR experiments such as TOCSY, NOESY and ROESY. For 2D TOCSY (containing DIPSI 2 spin-lock sequence) a mixing time of 80 ms was chosen, while for 2D ROESY and NOESY, a mixing time of 200 ms was used. In all experiments, 256 (t1) and 2048 (t2) points were collected with 16 scans and zero filing

was done using 2K X 2K data points along F2, F1 dimensions prior to Fourier transformation.

All 1D ^{1}H experiments were recorded with 16K data points and 32 scans with 2 s interscan delay and zero filled to 32K data points.

NMR data were processed using TopSpin 2.1 (www.bruker-biospin.com) and 2D spectra analyzed using CARA (www.nmr.ch).[27] Methyl peaks intensities were used for normalization between spectra. Signal to noise (S/N) ratios were calculated from intensities after normalization and divided by the S/N ratios of the control spectra. Each S/N ratio obtained was averaged over 3 spectra with standard deviations calculated.

3.5.8 Differential Scanning Calorimetry (DSC)

Differential Scanning Calorimetry (DSC) is a thermoanalytical technique that monitors heat changes associated with a sample's phase transitions. It measures the difference in heat flow between a reference cell and a sample cell as the temperature changes, and this difference is recorded as a function of temperature:

$$\Delta\frac{dH}{dt} = \frac{dH}{dt}sample - \frac{dH}{dt}reference \qquad \text{(Eq. 3.9)}$$

where H is enthalphy, t is time, and $\frac{dH}{dt}$ refers to heat flow, measured in mcal sec^{-1}.

A DSC thermogram displays the positive or negative heat flow (exothermic and endothermic, respectively) of the sample as temperature changes. These peaks can be identified and assigned to different phase transitions depending on whether the transition is exothermic or endothermic, and according to their sequence of occurrence. For example, phase transitions of a polymer such as glass transition (endothermic), crystallization (exothermic), melting (endothermic), cross-linking (exothermic) and decomposition (exothermic) can be identified from its thermogram (Figure 3.13).

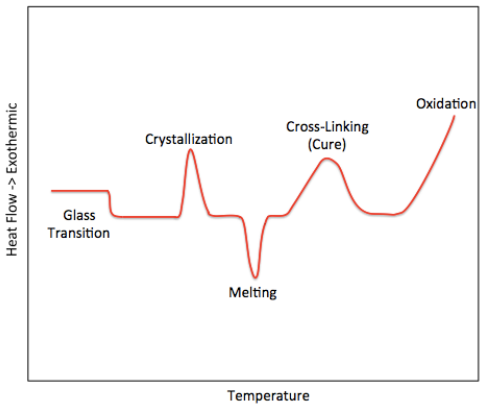

Figure 3.13 Example of a polymer DSC thermogram. Exothermic and endothermic phase transitions can be observed by the positive or negative heat flow in the thermogram.

Sample preparation

Peptide fiber (0.02 mg) and powder (> 0.1 mg) samples were placed into Tzero pans, covered with lids and crimped, while empty Tzero pans crimped with lids are used as references.

Measurements and analysis

DSC was used to acquire the melting point and identify phase transition/s of peptide fibers and powder. All DSC measurements were performed with TA Instruments Discovery DSC. Dry fibers of known mass were placed into pre-weighed Tzero pan and lid, and DSC measurements were recorded from 40 °C to 400 °C, under nitrogen atmosphere with 50 mL/min flow rate. Temperature was increased at a rate of 5 °C/min, while the heat change between a reference Tzero pan and lid of known weight and the sample-containing pan and lid were recorded. The obtained calorimetry curves were normalized with the sample weights, and analysis was done on TA Universal Analysis software.

3.5.9 Thermogravimetric Analysis (TGA)

Thermogravimetric Analysis (TGA) is thermoanalytical technique that monitors the amount of weight change of a material associated with the material's phase transitions. Material weight change as a function of temperature or time can be obtained via TGA, and this technique is commonly used to determine characteristic phase transitions of materials such as vaporization, sublimation and decomposition.

Sample preparation

Peptide powder (2.2 mg) was weighed prior to placing into a DSC standard aluminum pan and lid set. A hole was made in the lid with a needle to allow for any natural expansion or evaporation of material that may occur during the experiment process. The lid was inverted and fitted to the pan to cover the powder sample so as to prevent the powder from being blown away during the experiment.

Measurement and analysis

TGA was used to find out the decomposition temperature of peptide powder. All measurements were done on TA Instruments TGA Q500 equipment, under nitrogen atmosphere, with a nitrogen gas flow rate of 60 mL/min. TGA measurements were recorded from room temperature to 400 °C, with a temperature increase rate of 5 °C/min. Subsequent analysis was done on TA Universal Analysis software.

3.5.10 Rheology

Rheology is the study of flow and deformation of viscoelastic materials under external applied forces, and rheology measurements are conducted using a rheometer. External forces that can affect a material's rheological properties include stress, strain, temperature and as well as stress- or strain rates, while internal sample variations such as sample solute concentration and stability etc., also play key roles in determining the rheological properties of the material.

Storage (G') and loss (G") modulus are parameters that describe the stress response for viscoelastic materials under oscillatory shear, with examples such as connective tissues in our body and hydrogels.[28] G' describes the elastic response or

solid-like property, while G" describes the viscous behavior or liquid-like property of the material measured.[29, 30] Usually in gel samples, G' > G" at low oscillation frequencies, and with the increase in frequency until a critical yielding point, the force exerted would result in the collapse of the gel's internal network and liquid-like behavior (G" > G').[29, 31] G' can also be equated to the Young's modulus (elastic modulus) of the material, and these parameters are important for the characterization of a gel material, and to assess their mechanical suitability in tissue engineering applications.[29]

Sample preparation

Peptide hydrogels were prepared by dissolving peptides powder in ultrapure water at a concentration of 20 mM. The mixture was stirred for at least 5 minutes to ensure homogeneity and complete solvation of peptides. A 1 mL syringe with a cut syringe opening (for the purpose of maintaining a constant internal syringe diameter) was then used to draw the mixture and stored overnight for the gelation process.

Measurements

Rheology measurements was done on peptide hydrogel samples in order to acquire their G' and G". All measurements were done using Anton Paar Physica MCR 501 rheometer and PP10 accessory at ambient temperature. Gel samples were pushed carefully out of the syringe and sliced across the opening to obtain flat circular disk-shaped gels of about 1mm thickness. A fresh piece of gel was placed at the center of the stage for each measurement and excess liquid was removed with filter paper. Oscillation mode was used for all measurements. An amplitude sweep was first done at a constant frequency of 1 Hz over 0.001% to 100% strain. A modulus against strain plot was obtained, and the linear viscoelastic region (LVE) of the gel was identified over the range of strain whereby the G' remained constant.[29] After identifying the LVE, a frequency sweep was done with constant strain (average strain value selected from LVE) over a range of frequency from 0.01 Hz to 100 Hz.

3.5.11 Wide Angle X-ray scattering (WAXS)

X-ray scattering techniques have been used to obtain molecular-scale structural information of materials,[32, 33] such as the crystalline structures of polymers and proteins. Owing to their small wavelengths that fall within the molecular and subatomic size scales, X-rays provide the resolution to probing structural properties at these scales (Figure 3.14). X-ray scattering utilizes the concept of Bragg's law,[34] whereby X-rays incident upon a crystalline sample are scattered by the atoms within, and their resultant constructive interference abide by the equation:

$$n\lambda = 2d\ sin\theta \qquad \text{(Eq. 3.10)}$$

where n is the order, λ is the X-ray wavelength, d is the spacing between the scattering planes in the crystal, and θ is scattering angle between the incident ray and the scattered beams.

In this work, Wide Angle X-ray Scattering (WAXS) was used to probe the molecular structure of the self-assembled peptide fibers. The structural information of the peptide fiber sample was obtained by focusing an incident collimated X-ray beam with fixed wavelength on the sample, which was scattered according to the Bragg's law. By analyzing the scattered pattern and intensity as a function of the scattering vector, $q = (4\pi \sin\theta)/\lambda$, the *d*-spacing values and dimensions of the structural components can be extracted (Eq. 3.10). Figure 3.14 illustrates WAXS diffraction patterns of the two classical types of antiparallel β–structures.[35] In the silk-like β-structure (Figure 3.14 A), the β-strands and hydrogen bonds are oriented parallel and perpendicular to the fiber axis, respectively. In the cross-β structure (Figure 3.14 C), the situation is inverted with the β-strand oriented perpendicular, and the hydrogen bonds parallel, to the fiber axis. In the silk-like pattern, the main reflections in the 2D patterns are located along the equator and correspond to *d*-spacings of inter-β strands (*ca*. 0.48 nm) and inter-β-sheets (*ca*. 1.1 nm), respectively (Figure 3.14 B). In the cross-β structure, on the other hand, owing to the orientation of β-strands perpendicular to the fiber axis, the inter-β-strand reflection is located along the meridian in the 2D diffraction pattern (Figure 3.14 D).

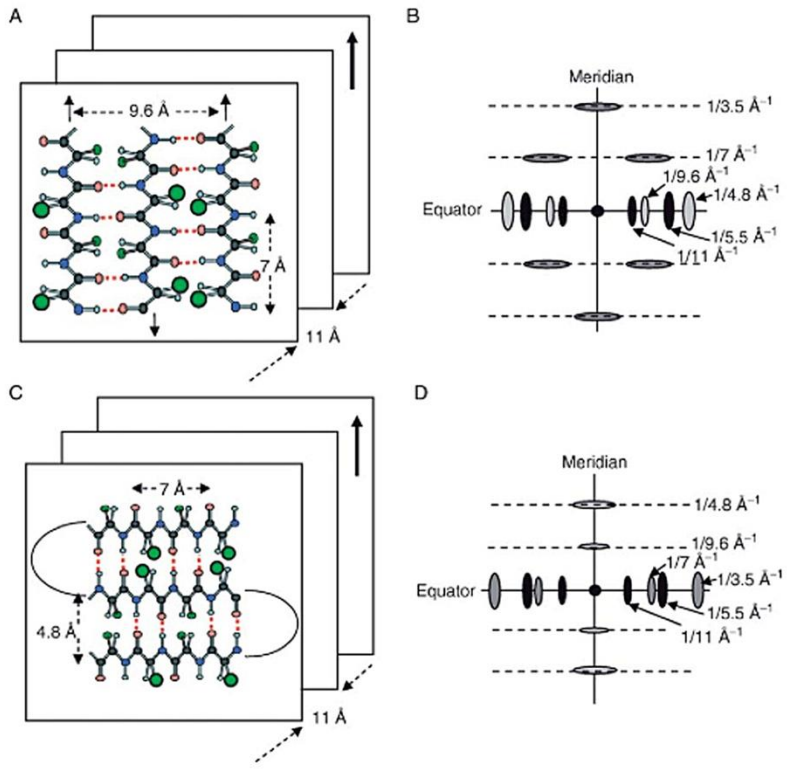

Figure 3.14 Illustration of differences that might be observed in fiber diffraction patterns of antiparallel β–structures. (A) Illustration of β-strands oriented parallel to the fiber axis (silk-like; also note that the hydrogen bonds are oriented perpendicular to the fiber axis) and its diffraction pattern **(B)**, and β-strands chains oriented perpendicular to the fiber axis (cross-β amyloid-like; hydrogen bonds oriented parallel to the fiber axis) **(C)** and its diffraction pattern **(D)**.[35]

Sample preparation

Synthesized peptides (sequence AATAVSHTTHHA) were purified and lyophilized (Sections 3.2.1 and 3.3.1) into powdered samples. Fibers were prepared by adding 5% Acetonitrile/ 95% ultrapure water mixture to the lyophilized peptides to form self-assembled fibers at above 20 mg/mL peptide concentration. These fibers were then dried and bundled tightly together for X-ray measurements.

Measurement and analysis

All measurements were done by Dr. Antoni Sanchez-Ferrer, in collaboration with Professor Raffaele Mezzenga (ETH, Zurich). WAXS experiments were performed using a Rigaku MicroMax-002+ microfused beam (40 W, 45 kV, 0.88 mA).

Cu Kα radiation (λCu Kα = 0.15418 nm) was collimated by three pinhole collimators (0.4, 0.3 and 0.8 mm).The scattered WAXS intensity was collected in transmission mode by a Fujifilm BAS-MS 2025 imaging plate system (15.2 × 15.2 cm^2, 50 μm resolution).

3.5.12 Optical microscopy imaging

Fibers in buffer solutions were placed on a glass microscope slide and excess solution was blotted away with lint-free filter paper. The fibers were then rinsed with MilliQ water to remove any residual salt and allowed to air dry. All optical microscopy images were obtained via Carl Zeiss Axio Imager. Bright field images were obtained in reflective mode, whereas birefringence was detected using polarized light filters.

3.5.13 UV-Vis spectroscopy

Perkin Elmer Lambda 35 UV-Vis Spectrophotometer was used to obtain excitation and emission spectra of Texas Red dye-labeled samples. A concentration standard curve was prepared by obtaining the excitation/emission spectra maxima of Texas Red dye for concentrations at 2 mM, 1 mM, 0.5 mM, 0.1 mM, 50 μM, 10 μM, 5 μM and 1 μM. UV-Vis spectra of each concentration was obtained from 200–800 nm and maxima (~589 nm) was obtained by averaging over 3 spectra. Standard curve of absorbance against concentration was plotted.

Subsequent UV-Vis measurements of Texas Red labeled peptide samples were recorded from 200–800 nm and maxima absorption was compared with standard curve above to obtain the concentration of dye.

3.5.14 Molecular dynamics (*MD*) simulations

Molecular dynamics (*MD*) simulation is one of the principal tools used in theoretical studies involving dynamics and kinetics of biomolecules, such as proteins.[36-38] It records the time-dependent behavior of molecular systems where

energy fluctuations and conformational changes of biomolecules can be observed. The basis of *MD* simulation stems from Newton's law of motion, whereby by numerically solving Newton's second law of motion *i.e.*, **F = ma** where **F** is the force exerted on particle of mass **m** and **a** is acceleration,[36, 39] the structural fluctuations within the system with respect to time can be observed.

To overcome the energy barriers in the potential energy surface at room temperature, atoms jump from one conformation to other by using their kinetic energy. *MD* simulations assign the velocities of each atom of the system corresponding to the temperature, and the assigned initial positions and velocities of all the particles of the system would be used for *MD* calculations. Force field parameters and potential functions are used to calculate the force on each particle when the particle is allowed to move. The whole motion of particle from one position to another position with respect to time is recorded in the form of a trajectory, which is generated by the simultaneous integration of Newton's equations of motion.[39] In addition, to more accurately mimic the experimental conditions, physical parameters such as pressure and temperature can be defined for these simulations.

MD simulations were performed in complementary to experimental data to gain insight into the atomic scale processes occurring between the peptides. Peptides were arranged into antiparallel fibrillar packing and simulated under conditions similar to experimental conditions to study their fibrillar structure stability over a period of time.

Measurements

All simulations were performed by Dr. Zhou Feng, in collaboration with Professor Su Haibin (NTU, MSE). The simulations were performed by using the GROMACS4.5.3 package.[40] The overall temperature of the water and peptides was kept constant, coupling independently each group of molecules at 300 K with a V-rescale thermostat.[41] The pressure was coupled to a Parrinello-Rahman[42, 43] barostat at 1 atm separately in every dimension. The temperature and pressure time constants of the coupling were 0.1 and 2 ps, respectively. The integration of the equations of motion was performed by using a leap frog algorithm with a time step of 2 fs. Periodic boundary conditions were implemented in all systems. A cutoff of 1 nm was implemented for the Lennard–Jones and the direct space part of the Ewald sum for

Coulombic interactions. The Fourierspacepart of the Ewald splitting was computed by using the particle-mesh-Ewald method,[44] with a grid length of 0.16 nm on the side and a cubic spline interpolation. TIP3P water model[45] was used, and the peptide parameters were from CHARM force field.[46, 47]

References

[1] R. B. Merrifield, *J Am Chem Soc*, **1963**, 85, 2149-2154.

[2] J. K. Murray and S. H. Gellman, *Nat Protoc*, **2007**, 2, 624-631.

[3] M. Amblard, J. A. Fehrentz, J. Martinez and G. Subra, *Mol Biotechnol*, **2006**, 33, 239-254.

[4] I. Coin, M. Beyermann and M. Bienert, *Nat Protoc*, **2007**, 2, 3247-3256.

[5] J. K. Jensen, P. Tofteng Shelton and L. S. Pedersen, *Peptide Synthesis and Applications*, Humana Press, Totowa, NJ, **2013**.

[6] J. S. Davies and G. C. Barrett, *Amino Acids, Peptides and Proteins*, Royal Society of Chemistry, Cambridge, **2003**.

[7] K. Hilpert, D. F. H. Winkler and R. E. W. Hancock, *Nat Protoc*, **2007**, 2, 1333-1349.

[8] R. Frank, *J Immunol Methods*, **2002**, 267, 13-26.

[9] D. F. H. Winkler and W. D. Campbell, in *Peptide-Based Drug Design*, ed. L. Otvos, Humana Press, Totowa, NJ, **2008**, pp. 47-70.

[10] A. Friedler and C. Katz, in *Encyclopedia of Biophysics*, ed. G. C. K. Roberts, Springer Berlin Heidelberg, Berlin, Heidelberg, **2013**, pp. 1955-1959.

[11] M. R. Sawaya, S. Sambashivan, R. Nelson, M. I. Ivanova, S. A. Sievers, M. I. Apostol, M. J. Thompson, M. Balbirnie, J. J. W. Wiltzius, H. T. McFarlane, A. O. Madsen, C. Riekel and D. Eisenberg, *Nature*, **2007**, 447, 453-457.

[12] L. K. Chang, J. H. Zhao, H. L. Liu, K. T. Liu, J. T. Chen, W. B. Tsai and Y. Ho, *J Biomol Struct Dyn*, **2009**, 26, 731-740.

[13] B. Bouma, L. M. J. Kroon-Batenburg, Y. P. Wu, B. Brunjes, G. Posthuma, O. Kranenburg, P. G. de Groot, E. E. Voest and M. F. B. G. Gebbink, *J Biol Chem*, **2003**, 278, 41810-41819.

[14] R. Khurana, V. N. Uversky, L. Nielsen and A. L. Fink, *J Biol Chem*, **2001**, 276, 22715-22721.

[15] W. E. Klunk, J. W. Pettegrew and D. J. Abraham, *J Histochem Cytochem*, **1989**, 37, 1273-1281.

[16] A. J. Howie, D. B. Brewer, D. Howell and A. P. Jones, *Lab Invest*, **2008**, 88, 232-242.

[17] N. J. Greenfield, *Nat Protoc*, **2006**, 1, 2876-2890.

[18] J. Reed and T. A. Reed, *Anal Biochem*, **1997**, 254, 36-40.

[19] A. Micsonai, F. Wien, L. Kernya, Y. H. Lee, Y. Goto, M. Refregiers and J. Kardos, *P Natl Acad Sci USA*, **2015**, 112, E3095-E3103.

[20] N. B. Colthup, *J Opt Soc Am*, **1950**, 40, 397-400.

[21] J. Kong and S. Yu, *Acta Bioch Bioph Sin*, **2007**, 39, 549-559.

[22] J. T. Pelton and L. R. McLean, *Anal Biochem*, **2000**, 277, 167-176.

[23] A. Barth and C. Zscherp, *Q Rev Biophys*, **2002**, 35, 369-430.

[24] W. C. Oliver and G. M. Pharr, *J Mater Res*, **2004**, 19, 3-20.

[25] W. C. Oliver and G. M. Pharr, *J Mater Res*, **1992**, 7, 1564-1583.

[26] R. Saha and W. D. Nix, *Acta Mater*, **2002**, 50, 23-38.

[27] CARA: computer aided resonance assignment. http://cara.nmr.ch/ (**2004**) by R. Keller.

[28] M. Ahearne, Y. Yang, A. J. El Haj, K. Y. Then and K. K. Liu, *J R Soc Interface*, **2005**, 2, 455-463.

[29] J. M. Zuidema, C. J. Rivet, R. J. Gilbert and F. A. Morrison, *J Biomed Mater Res B*, **2014**, 102, 1063-1073.

[30] T. G. Mezger, *The Rheology Handbook: For Users of Rotational and Oscillatory Rheometers*, Vincentz Network, **2006**.

[31] S. Sathaye, A. Mbi, C. Sonmez, Y. C. Chen, D. L. Blair, J. P. Schneider and D. J. Pochan, *Wires Nanomed Nanobi*, **2015**, 7, 34-68.

[32] B. L. Henke, E. M. Gullikson and J. C. Davis, *Atom Data Nucl Data*, **1993**, 54, 181-342.

[33] J. Als-Nielsen and D. McMorrow, *Elements of Modern X-ray Physics*, Wiley, **2011**.

[34] W. H. Bragg and W. L. Bragg, *P R Soc Lond a-Conta*, **1913**, 88, 428-438.

[35] A. V. Kajava, J. M. Squire and D. A. Parry, *Adv Protein Chem*, **2006**, 73, 1-15.

[36] S. A. Adcock and J. A. McCammon, *Chem Rev*, **2006**, 106, 1589-1615.

[37] M. Karplus, B. R. Gelin and J. A. Mccammon, *Biophys J*, **1980**, 32, 603-618.

[38] E. R. Lindahl, in *Molecular Modeling of Proteins*, ed. A. Kukol, Humana Press, Totowa, NJ, **2008**, pp. 3-23.

[39] W. F. Vangunsteren and A. E. Mark, *Eur J Biochem*, **1992**, 204, 947-961.

[40] D. Van der Spoel, E. Lindahl, B. Hess, G. Groenhof, A. E. Mark and H. J. C. Berendsen, *J Comput Chem*, **2005**, 26, 1701-1718.

[41] G. Bussi, D. Donadio and M. Parrinello, *J Chem Phys*, **2007**, 126, 014101.

[42] S. Nose and M. L. Klein, *Mol Phys*, **1983**, 50, 1055-1076.

[43] M. Parrinello and A. Rahman, *J Appl Phys*, **1981**, 52, 7182-7190.

[44] T. Darden, D. York and L. Pedersen, *J Chem Phys*, **1993**, 98, 10089-10092.

[45] W. L. Jorgensen, J. Chandrasekhar, J. D. Madura, R. W. Impey and M. L. Klein, *J Chem Phys*, **1983**, 79, 926-935.

[46] A. D. MacKerell, D. Bashford, M. Bellott, R. L. Dunbrack, J. D. Evanseck, M. J. Field, S. Fischer, J. Gao, H. Guo, S. Ha, D. Joseph-McCarthy, L. Kuchnir, K. Kuczera, F. T. K. Lau, C. Mattos, S. Michnick, T. Ngo, D. T. Nguyen, B. Prodhom, W. E. Reiher, B. Roux, M. Schlenkrich, J. C. Smith, R. Stote, J. Straub, M. Watanabe, J. Wiorkiewicz-Kuczera, D. Yin and M. Karplus, *J Phys Chem B*, **1998**, 102, 3586-3616.

[47] A. D. Mackerell, M. Feig and C. L. Brooks, *J Comput Chem*, **2004**, 25, 1400-1415.

Chapter 4

Fundamental interactions between SRT peptides

The hard sucker ring teeth (SRT) from decapodiforme cephalopods, located inside the sucker cups lining the arms and tentacles of the animal, have recently emerged as a unique model structure for biomimetic structural biopolymers. SRT are entirely made of modular, block co-polymer-like proteins that self-assemble into a large supramolecular network. In order to unveil the molecular principles behind SRT's self-assembly and robustness, in this chapter a combinatorial screening assay has been designed to map the molecular-scale interactions between the most abundant modular peptidic blocks of suckerin proteins. In-depth biophysical characterizations have been conducted by various techniques in this chapter. The chapter sheds light on how Nature has evolved modular sequence design for the self-assembly of mechanically robust structures, and expands our biomolecular toolkit to prepare load-bearing biomaterials from short peptidic building blocks.

* Portions of this chapter were extracted from: Hiew, S. H., *et al.*, "Modular peptides of thermoplastic squid sucker ring teeth form amyloid-like cross–β supramolecular networks." Acta Biomaterialia 2016, 46, 41-54.

4.1 Introduction

Humboldt (*Dosidicus gigas*) squids have evolved robust sucker ring teeth (SRT) embedded within the suction cups coating the inner surfaces of their arms and tentacles. Each appendage contains hundreds of SRT,[1] making them formidable biotools that are instrumental to the survival of this ancient predatory creature. As discussed in Chapter 2, SRT represent an intriguing biological biomaterial exclusively made of protein building blocks called "suckerins" and exhibit structural properties[2] that match those of robust synthetic polymers, owing to the supramolecular assembly of suckerins.

A combinatorial peptide macro-array interaction assay was first designed to map out the interactions between the modular peptides that form the suckerins, and DLS experiments were used to monitor the self-assembly trend. Peptides that showed high relative interactions during the assay were selected for further secondary structure studies by CD and FTIR. Ala-rich peptides were observed to spontaneously self-assemble into micro-fibers and displayed amyloidogenic characteristics, which was proposed to play a central role in SRT self-assembly. The stability of these amyloid-like sequences were then assessed by H/D exchange NMR experiments, which demonstrated a high protection factor of the residues involved in the hydrogen bonded network. Finally, *MD* simulations confirmed the propensity of Ala-rich peptides to form β-sheets, which were highly stable. In contrast, His-rich peptides have low propensity towards β-sheets formation. *MD* simulations also provided insights into the role of Pro on the stability of the modular β–sheets forming peptides.

The hypothesis of this chapter is that these repetitive and modular units greatly contribute to the robust mechanical properties of SRT. In order to unveil the physico-chemical factors that are responsible for the material's robustness, this chapter focuses on further understanding the physico-chemical behavior of the modular units in different environmental conditions.

4.2 Experimental Methods

In order to address the questions in this chapter and to test the hypothesis, a range of experiments were designed and techniques were employed to characterize the modular suckerin peptides.

4.2.1 SPOT synthesis

Peptides without modifications were purchased from GL Biochem and verified for their purity (> 98%) with HPLC (Section 3.3.1) and LC/MS (Section 3.3.2) prior to use for SPOT synthesis. Whatman Chr1 cellulose sheet with light pencil markings were used for the spotting of peptides at equi-distances. Synthesis was done according to Section 3.2.2. Peptides were acetylated at their N-terminus after the immobilization onto cellulose to eliminate any termini charge-charge interaction effects.

4.2.2 Preparation of dye-labeled peptides

Peptides with termini modifications – acetylated N-terminus and amidated C-terminus were purchased from GL Biochem and verified for their purity (> 98%) with HPLC (Section 3.3.1) and LC/MS (Section 3.3.2) prior to use. Texas Red dye with succinimidyl ester functional group was used for the labeling of these peptides at their amidated C-terminus. Labeling was done according to Section 3.2.3.

4.2.3 UV-Vis spectroscopy

UV-Vis spectroscopy was used to determine the concentration of Texas Red dye-labeled peptides. A concentration standard curve of Texas Red fluorescent dye was prepared and absorption spectra of dye-labeled peptides were used to determine the peptides' concentration according to Section 3.5.13.

4.2.4 Peptide macro-array binding assay

In conjunction with combinatorial chemistry concepts, a peptide macro-array binding assay was designed for the purpose of screening binding interactions between modular suckerin peptides in this chapter. The control peptide Ac-GGVVIA-$CONH_2$ was selected to perform preliminary binding assay experiments and to screen blocking buffers prior to carrying out binding assays for the suckerin peptides. The peptide macro-array binding assay was prepared and conducted according to Section 3.4.

4.2.5 DLS

DLS measurements were conducted on peptides with termini modifications – acetylated N-terminus and amidated C-terminus (purchased from GL Biochem). Peptides were dissolved in their respective buffered solutions at a concentration of 50 μM. DLS measurements were done according to Section 3.5.1, and the Z-average sizes were used to identify the self-assembly trend of the peptides over a 24-hour period.

4.2.6 CD spectroscopy

CD spectroscopy was used to study the secondary structures of the suckerin peptides in their buffered solutions, over a time period of 50 days. Termini-modified peptides were dissolved in their respective buffered solutions at a concentration of 2 mg/mL and CD spectroscopy measurements were done according to Section 3.5.3.

4.2.7 FTIR spectroscopy

FTIR spectroscopy was used in complementary to CD spectroscopy to study the secondary structures formed by the suckerin peptides in buffered solutions (from Section 4.2.6) and the secondary structures of dried microfibers formed by these peptides. FTIR spectroscopy measurements were done according to Section 3.5.4.

4.2.8 FESEM imaging

FESEM imaging was used to investigate the microfibers' morphologies. Samples were prepared and imaged according to Section 3.5.5.

4.2.9 Congo red birefringence assay

Congo red birefringence assay was done on microfiber samples to detect for the presence of amyloid structures. Staining of the microfibers were done according to Section 3.5.2 and observed with an optical microscope under normal light and polarized light, according to Section 3.5.12.

4.2.10 NMR spectroscopy

NMR spectroscopy was first used to obtain the molecular structure of suckerin peptides for the purpose of assigning the amide backbone protons in their 1D spectra. 2D NMR TOCSY and ROESY spectra were first obtained and subsequent processing of spectra and assignment of protons was done using the CARA software. H/D exchange experiments were then conducted and 1D proton NMR spectra of the samples were obtained and normalized using the methyl peak intensity prior to comparison and analysis. NMR sample preparation and measurements were done according to Section 3.5.7.

4.2.11 *MD* simulations

MD simulations were used to study the stability of peptides initially arranged in antiparallel fibrillar packing. Over a simulation period of 200 ns, the number of different types of secondary structures and hydrogen bonds formed were obtained. *MD* simulations were done according to Section 3.5.14.

4.3 Results and Discussion

The primary sequence of the most abundant suckerin protein, suckerin-19 (molecular weight 39 kDa, Figure 4.1) was dissected to identify the key modular units and explore their fundamental interactions at the molecular scale. Importantly, the modular peptides found in suckerin-19 are the same as those found in the other members of the suckerin gene family,[3] allowing for narrowing down the initial selection to suckerin-19 from the wide pool of the suckerin protein family.

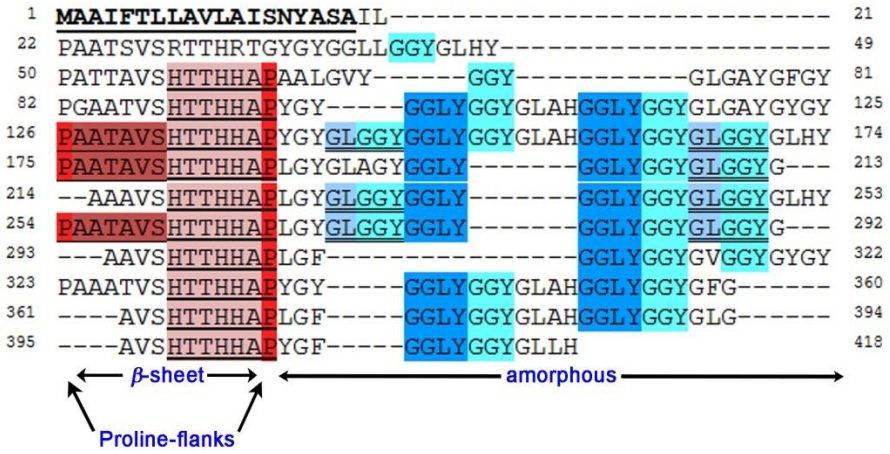

Figure 4.1 Full-length amino acid sequence of suckerin-19. Alignment of the residues are emphasized by highlighting the main modular peptides (bold and underlined: signal peptide; highlighted in red: Ala-rich and His-rich modules; highlighted in blue: Gly-rich modules).

4.3.1 Selection of modular peptides

In order to identify the building blocks that drives the self-assembly of SRT structure and contribute significantly to the robust property of the material, the fundamental interactions of these building blocks at the molecular level need to be evaluated. Suckerin-19 was selected for the subsequent studies because ***(i)*** it is the most abundant protein of the suckerin gene family, and ***(ii)*** the modular peptides identified in suckerin-19 are representative of the ensemble of modular peptides present in the entire suckerin protein family that form the SRT supramolecular network.[3] The selection of peptides was further refined based on recent Wide-Angle X-ray Scattering (WAXS) synchrotron experiments of native SRT, which revealed the

existence of a network of nanoconfined β-sheet structures with dimensions of 2.4–2.6 nm by 3–3.5 nm (estimated 5 strands of ~8–10 residues)[3, 4] arranged isotropically within an amorphous matrix. Based on the β-sheet propensities of amino acids and the well-known formation of β-sheets in silk arising from poly-Ala sequences,[5] the combination of Ala- and His-rich domains were hypothesized to be the likely source of β strands in the nanoconfined β-sheet network. Gly-rich modules, on the other hand, were proposed to form mostly amorphous domains. From these considerations, seven highly abundant and repetitive small peptides (< 8 residues) were identified from suckerin-19 (Table 4.1), which are classified into three sub-classes of peptides. Type 1 His and Thr-rich modules (**H1**: HTTHHA and **H2**: HTTHHAP); type 2 Ala–rich modules (**A1**: AATAVS and **A2**: PAATAVS), and type 3 modules enriched with Gly, Leu, and Tyr residues (**G1**: GGY, **G2**: GGLY; **G3**: GLGGY). A and H modules in native suckerins are usually flanked by proline (Pro) residues in the form Pro-AH-Pro. Given the established role of Pro as β-sheet disruptors,[6, 7] Pro was postulated to restrict the self-assembly of the Ala- and His-rich domains into β-sheets of specific dimensions. Thus **H2** peptide was identical to **H1** with the exception of a Pro residue at the N-terminus. Likewise, **A2** is identical to **A1** with a Pro residue at the C-terminus. It is interesting to note that these His-rich, Ala-rich and Gly-rich peptides possess sequences similar to various natural protein-based hard biological materials (Table 4.1).

Table 4.1 Modular peptides from Suckerin-19 protein selected for this study, together with protein-based peptides exhibiting sequence homology with the suckerin peptides.

	Sequence	Code	Similarity and resemblance
1	Ac-**GGY**-$CONH_2$	G1	Silk, Ml. wing cuticle, Pinctada shell matrix, Chicken claw keratin
2	Ac-**GGLY**-$CONH_2$	G2	
3	Ac-**GLGGY**-$CONH_2$	G3	
4	Ac-**HTTHHA**-$CONH_2$	H1	***Dosidicus gigas*** beak, Nereis worm jaw
5	Ac-**HTTHHAP**-$CONH_2$	H2	
6	Ac-**AATAVS**-$CONH_2$	A1	Silk, Ml. wing cuticle, Pinctada shell matrix, Chicken claw keratin
7	Ac-**PAATAVS**-$CONH_2$	A2	

4.3.2 Peptide macro-array binding assay reveal molecular interactions

A combinatorial peptide macro-array interaction assay[8-12] with the selected suckerin peptide library was designed in order to obtain a preliminary screening and to identify binding interactions of binary peptide combinations (Illustration of binding assay shown in Figure 4.2). All binary combinations of peptides were screened at three different pHs and three analyte concentrations to generate 441 different conditions. For all experiments, selected suckerin peptides were acetylated at the N-terminus and amidated at the C-terminus to eliminate termini charge-charge interactions. pHs were selected (4.0, 7.0 and 8.6) in order to specifically investigate the possible influence of the imidazole ring protonation of His side chains, as well as to mimic the pH environment of the growth and development of the SRT. Indeed, the pH is likely to increase incrementally from the specialized epithelial cells[13-17] which produce the SRT proteins (~ pH 4) to the confined extracellular interface at the base of the SRT, and finally to their final supramolecular self-assembly at the ocean's aquatic pH of about 8.3. The overall goal of the assay was to gain insights into which peptides are the most active in interacting with their counterparts at each pH condition.

The interaction assay, carried out at a concentration of 1 µM analyte incubation, is displayed in the form of a heat map in Figure 4.4, with detailed bar charts shown in Figure 4.3. The map allowed to identify interaction "hotspots" and provided a comparative way to assess the relative strength of peptide-peptide interactions.

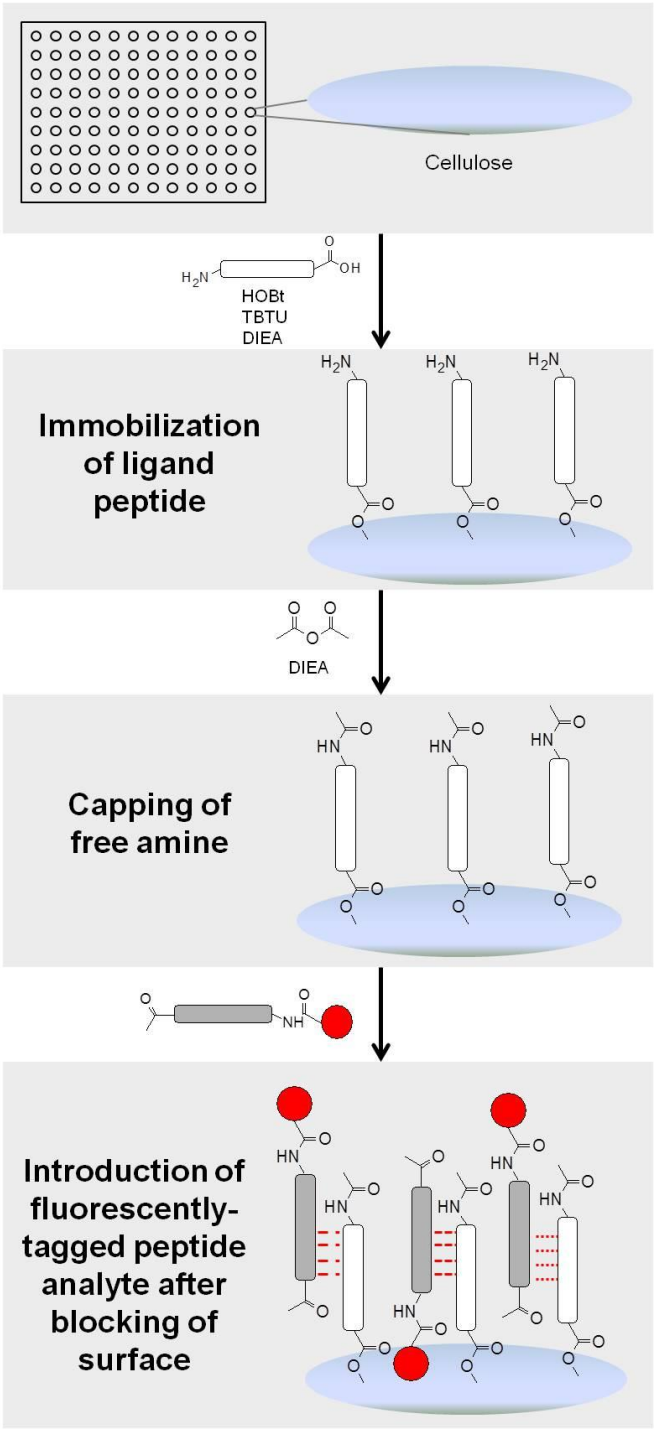

Figure 4.2 Illustration of peptide macro-array binding assay. Peptide macro-array binding experiment: ligand peptides were immobilized onto a cellulose membrane and acetylated to cap the free amine. The fluorescent-tagged peptide analytes were then incubated, followed by stringent washing. See Experimental Methodology section for details.

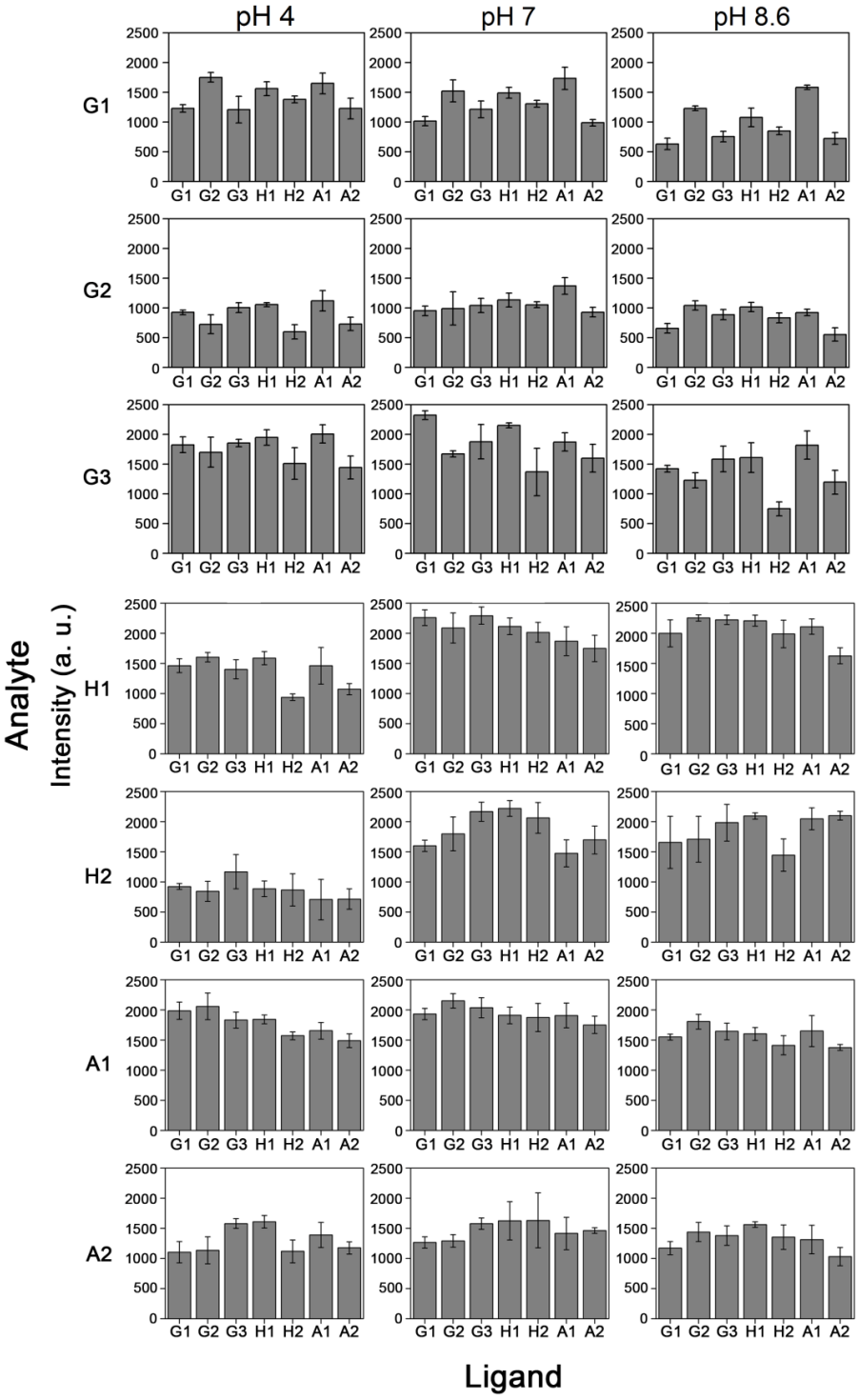

Figure 4.3 Results of peptide macro-array binding assay. The fluorescence intensity values, which indicate the extent of binding interactions between the analytes and ligands, were obtained from a quadruplicate screening of each interaction, and plotted versus the immobilized ligand peptides.

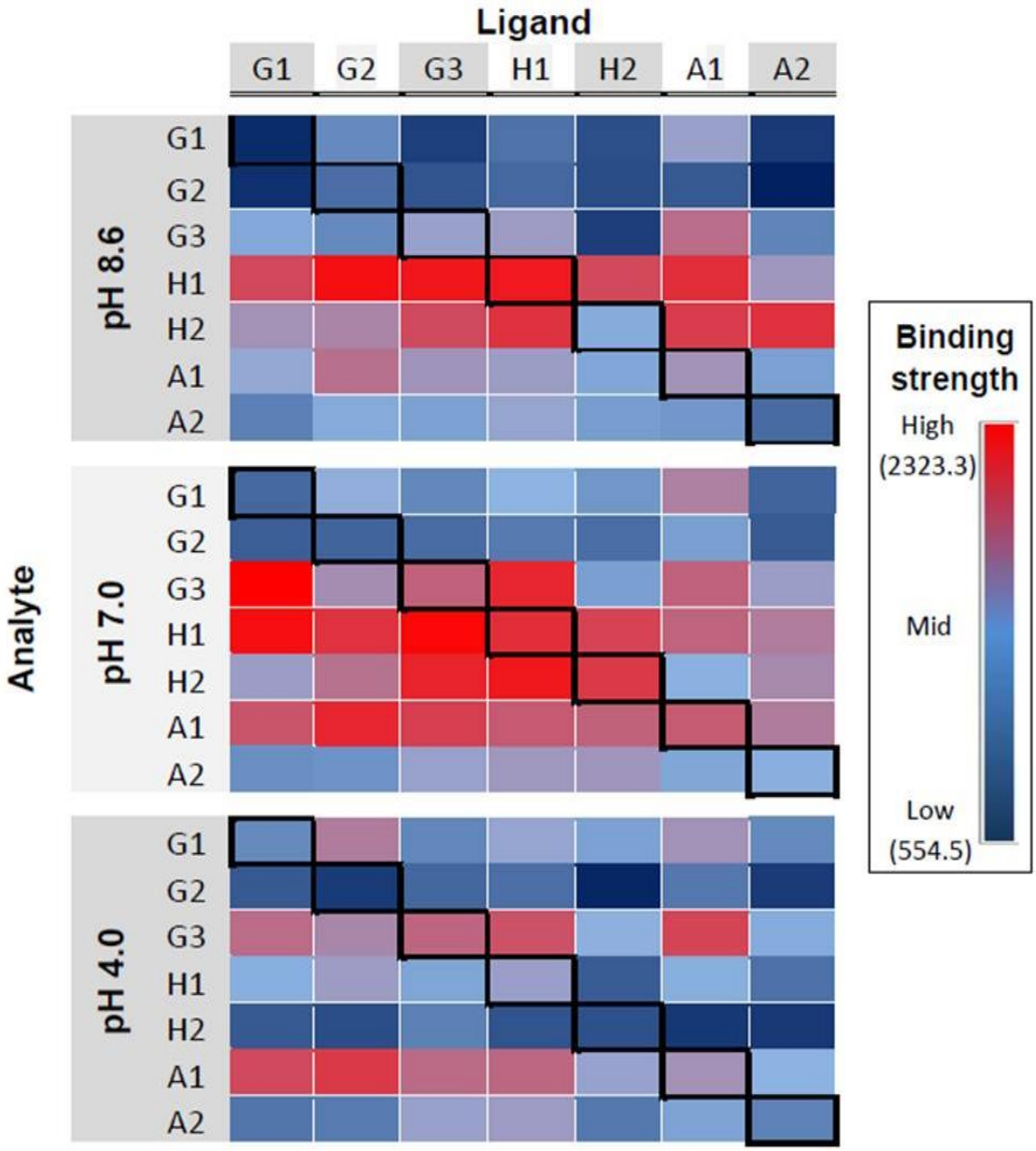

Figure 4.4 Heatmap of suckerin peptide macro-array binding assay. Relative interaction strength was obtained from the fluorescence intensity of each spot (blue shading: low level of interactions; red shading: high level of interactions). Average intensity values were obtained from quadruplicate screening of each interactions. The boxed diagonals indicate the intensity values derived from homo-interactions of a single peptide.

Four main trends were observed. First, for most peptides selected, homo- and hetero-interactions increased in the sequence pH 7.0 > pH 8.6 > pH 4.0, and this trend was particularly obvious for His-rich peptides. At pH 4.0, where the imidazole ring of

His residues is protonated, relatively weak interactions were observed, a trend noticed for both cases where the peptide was the ligand (immobilized on the membrane) or the analyte (free flowing solution over the immobilized ligand), as well as for both homo- and hetero-interactions. Moderate interactions were observed at pH 8.6 (deprotonated His residues), whereas the highest interaction activity was obtained at pH 7.0, corresponding to partial protonation of His residues. The protonation state of His thus appears to be an important factor in mediating peptide-peptide interactions.

Second, Ala-rich and His-rich peptides generally exhibited the highest interaction activities, consistent with β-sheet formation. Gly-rich peptides, on the other hand, generally exhibited low activity at the varying pH levels, especially for the homo-interactions. This suggests that Gly-rich sequences are not actively involved in strong binding interactions within the protein, although it should be mentioned that moderate hetero-interactions of Gly-rich peptides with **H1** as the analyte were noticed at pH 7.0 and 8.6. The weak-to-moderate interactions of Gly-rich peptides is consistent with the suggestion that Gly-rich sequences mostly constitute the amorphous regions of the semi-crystalline SRT network, similar to sequence/structure relationships observed in silk.[5, 18]

Third, the ligand-analyte roles are not identical, with an asymmetric pattern observed across the diagonals of the heat map. Short peptides (< 8 residues long) selected for this study tend to be conformationally restricted when immobilized on one end, while the analyte peptides are not limited by such conformational restrictions. This conformation-restriction effect may be more pronounced for shorter peptides; therefore an asymmetric pattern across the diagonals is not unexpected.

As the purpose of this screening assay was to identify interaction hotspots when the peptides play both roles as ligand and analyte, the assay provides a broader perspective of the interaction possibilities and the asymmetric pattern does not affect our objectives. Peptides with hotspots in the interaction map were further examined.

4.3.3 Self-assembly of SRT peptides

Based on the combinatorial assay results, peptides exhibiting the highest homo-interaction activities, **A1** and **H1**, were selected for further analysis. Peptides **A2**

and **H2** were also investigated to examine the effect of flanking Pro residues as explained above. During peptide incubation at 2 mg/mL, prominent differences were observed between Ala-rich and His-rich peptides. Ala-rich peptides spontaneously formed aggregates and subsequent observations via FESEM imaging indicated that these aggregates consisted of microfibers made up of smaller fibrils (Figure 4.5). The fibrils appeared to be of uniform dimensions of *ca*. 30–50 nm thick with some evidence of bundling to form microfibers larger than 1 μm in thickness. The fibers were stable when exposed to sonication and to a strong denaturing solution of 8 M urea.

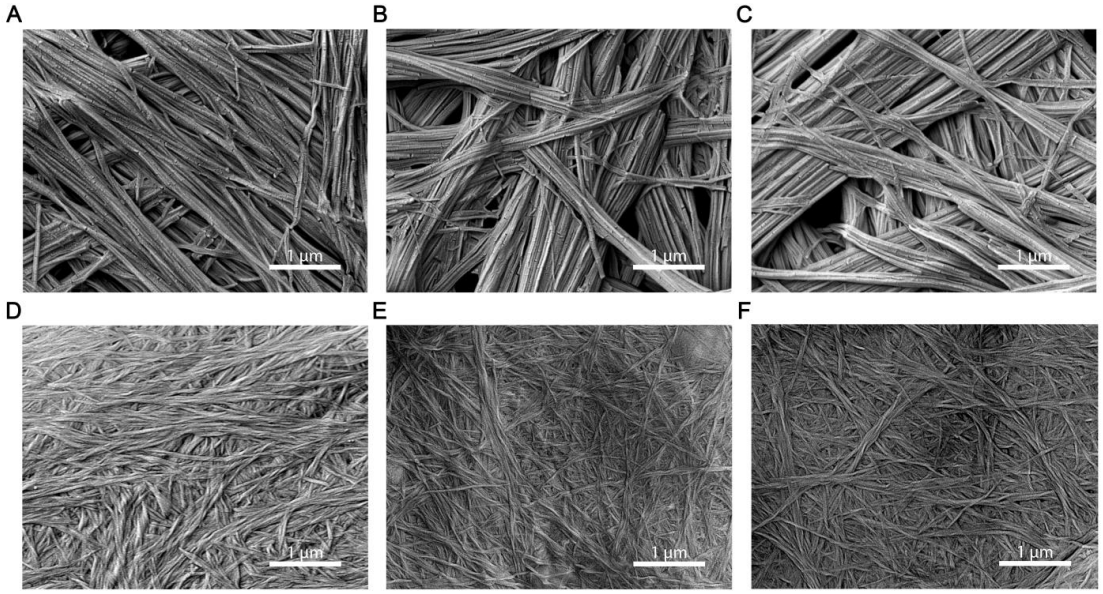

Figure 4.5 FESEM images of peptide microfibers. Fibers formed by peptide **A1** at **(A)** pH 4, **(B)** pH 7 and **(C)** pH 8.6 were all observed to have similar morphologies, with fiber thickness of 30–50 nm and appear to bundle together to form thicker fibers. Fibers formed by peptide **A2** at **(D)** pH 4, **(E)** pH 7 and **(F)** pH 8.6 were similar but appear to be randomly oriented with less directionality as compared to **A1** microfibers.

In stark contrast, His-rich peptides **H1** and **H2** did not form any noticeable microfibers under any of the conditions tested. To further assess the assembly of these microfibers, the kinetics of formation was investigated using DLS measurements at 50 μM peptide concentrations and under identical pH conditions used in the macro-array and peptide incubation assays (Figure 4.6). For all DLS measurements, it is important to mention that the polydispersity (PDI) index was expected to be large due

to the broad distribution of the peptide oligomeric populations present during self-assembly. Therefore, the absolute size values were used as estimations with the main objective of monitoring the general trends of peptide growth over time. At pH 7, the Z-average size, or cumulants mean size of **A1** and **A2** peptides increased as soon as the peptide incubation began (Figure 4.6 C and D). At pHs 4 and 8.6, on the other hand, only minimal changes in peptide sizes were noticed by DLS, which is consistent with the weaker interaction activity measured in the macro-array assay. For peptide **A2** (pH 7) the Z-average size of the peptides reached a maximum value of *ca*. 15 µm, followed by an apparent decrease in size (Figure 4.6 D). This peak value coincided with the formation of microfibers which sedimented as they formed and did not contribute to light scattering. The apparent size decrease was attributed to the remaining soluble peptides that did not contribute to the assembly of larger, sedimented microfibers during measurement. The presence of Pro at the N-terminus (peptide **A2**) led to some noticeable growth at pH 8.6, with Z-average size values in the range 1 to 2.5 µm, whereas no growth was observed for peptide **A1** (Figure 4.6 C).

His-rich peptides displayed a similar trend, namely the peptide size of **H1** only increased at pH 7 (though the sizes were significantly smaller than those observed for **A1** and **A2** peptides), whereas no growth was measured at either pH 4 or 8.6 (Figure 4.6 A). The effect of Pro at the C-terminus (peptide **H2**) parallels the findings of Ala-rich peptides (Figure 4.6 B), namely peptide growth was noticed at pH 8.6, which is clearly distinct from the behaviour of peptide **H1** where no size increase was detected. In summary, DLS measurements indicated that: *(i)* peptide fibrillization/aggregation into larger sizes is highly dependent on pH and is maximum at pH 7; and *(ii)* termini Pro residues affect growth only at pH 8.6.

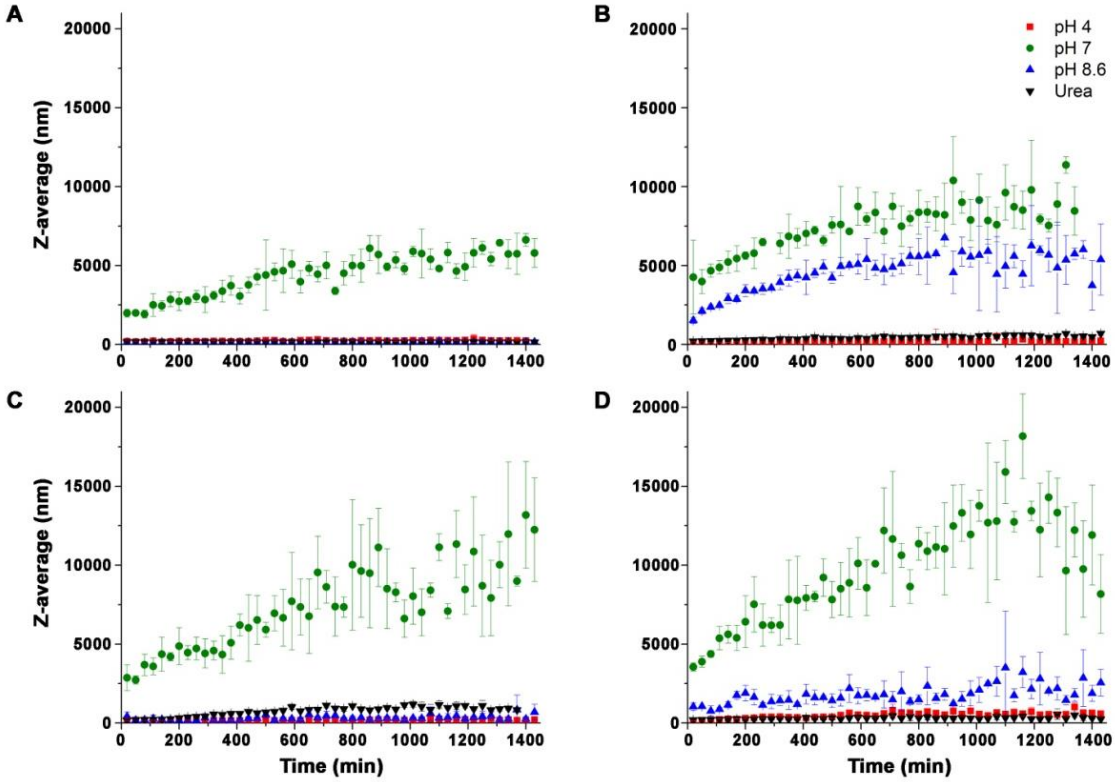

Figure 4.6 Self-assembly of peptides monitored by DLS. Peptides were incubated at pH 4 (red), 7 (green) and 8.6 (blue) at 50 μM peptide concentration. The peptides were also incubated in hydrogen-bond disrupting urea (black), serving as monomeric state controls (equilibrium state with the minimum self-assembly). **(A)** Peptide **H1**; **(B) H2**; **(C) A1** and **(D) A2**.

4.3.4 Secondary structure characterization of SRT peptides

In order to investigate whether suckerin peptides exhibit significant secondary structural changes[19] in solution over time, CD spectroscopy studies were conducted at 2 mg/mL peptide concentration under the same pH conditions and over a time period of up to 50 days. Similar to microfiber formation by Ala-rich peptides and DLS measurements for both Ala-rich and His-rich peptides, the pH strongly affected conformational transitions over time and such transitions were particularly obvious at pH 7. For His-rich peptides at pH 4, the spectra did not significantly change over time and consists of an intense minima at 195-200 nm and of weak positive broad shoulder near 220 nm (see for instance the left column in Figure 4.7 for **H1** peptide). Systematic investigations by CD of β-sheet-rich proteins[20] have demonstrated that this spectral

signature can be assigned to so-called β_{II}-type proteins, which are β-sheet-rich protein that also contain short stretches of poly(Pro)II-like conformations (PPII).[21] According to Sreerama and Woody,[20] β-sheet proteins can be classified as β_I or β_{II}, respectively, with the main difference arising from their PPII to β-sheet ratio. This ratio is less than 0.4 in β_I proteins and larger than 0.4 in β_{II} proteins. In turn, the CD signature of β_I proteins exhibit the typical positive and negative bands near 195 and 210-220 nm, whereas that of β_{II} proteins have a intense negative band at 195-200 nm and a weaker positive band at *ca*. 220 nm.[22] These features are consistent with **H1** peptides at pH 4. Over time, the CD spectra did not change significantly, although the molar ellipticity increased at 7 days and then remained unchanged until 50 days. Very similar CD spectra were observed at pH 8.6 for **H1** peptide (Figure 4.7 left column, row 3), where the spectra can essentially be separated into two sub-groups, namely 0 and 7 days and at 14 and 50 days. While the minima and maxima are located around the same wavelength, the molar ellipticity decreased for 14 days and above.

For **H1** peptide at pH 7, much more dramatic changes in CD spectra were observed (Figure 4.7 left column, row 2). The initial spectrum at day 0 was again characteristic of β_{II} proteins. However, the molar ellipticity sharply decayed over time. After 7 days, the minimum at 195 nm was about 3-fold its initial values. At days 14 and 50, the molar ellipticities were just a fraction of their initial values, and a zoom-in view in the low intensity region (Figure 4.7 left column, row 2 inset) revealed spectra characteristic of the standard β_I type proteins, with the typical positive band at 195 nm and the broad negative band centered at 220 nm. Given the propensity of His-rich peptides to assemble into larger structures over time as observed from DLS measurements (Figure 4.6 A and B), the large decay in ellipticity values was postulated to be due to the sedimentation of oligomeric peptide populations that decreases the peptide concentration in solution. Furthermore, the residual peptides tend towards β_I-type protein conformation. The role of Pro appeared to be marginal, with similar overall spectral features for **H2** (Figure 4.7 right column) compared to **H1** peptide. The one noticeable difference was that in comparison to **H1** peptide, the CD spectra of **H2** peptide at pH 4 and 8.6 did not change over time, with the intensity at day 50 remaining essentially the same as at day 0. At pH 7, a comparable large decrease in intensity was noticed over time and the residual peptides in solution also exhibited β_I-type structure (Figure 4.7 right column, row 2 inset).

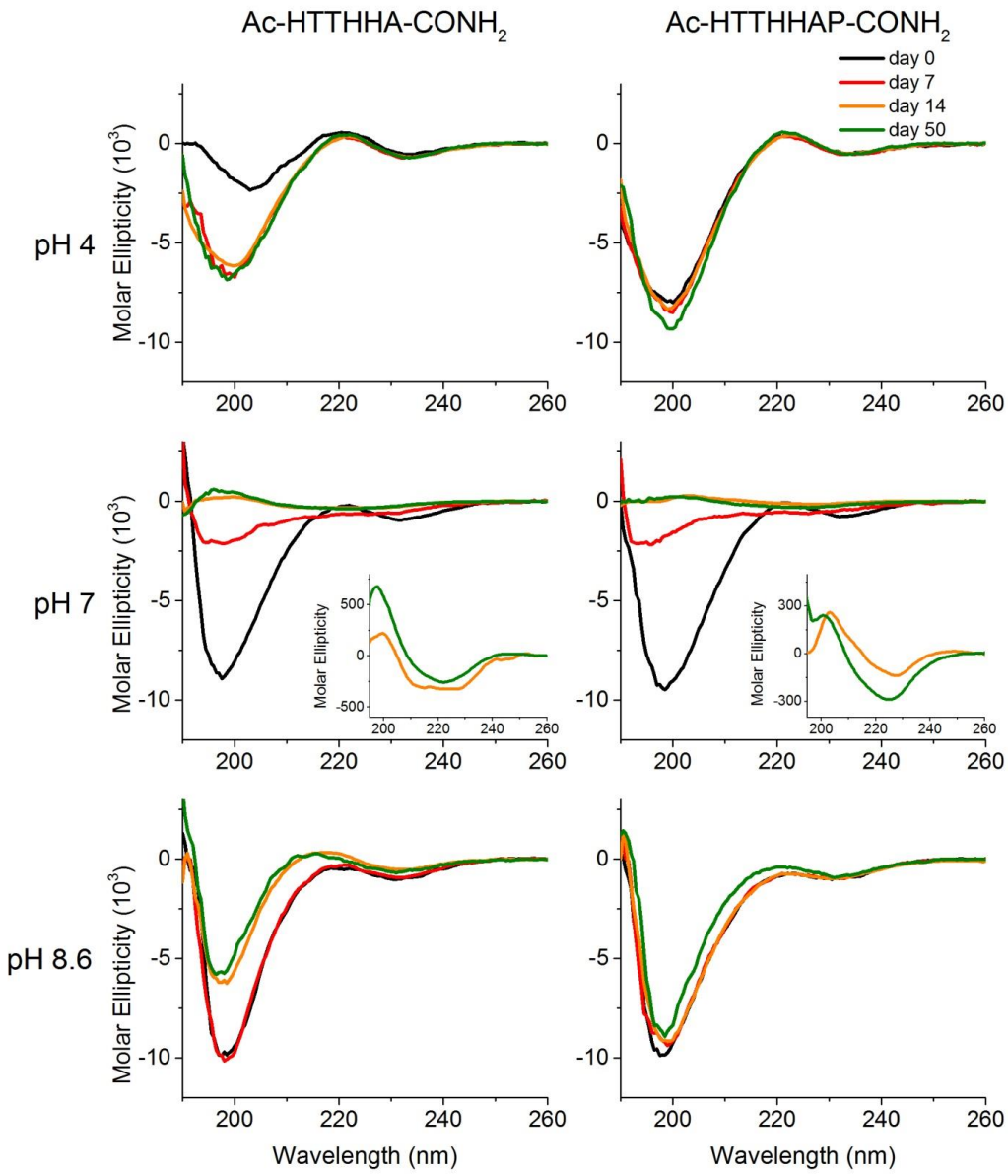

Figure 4.7 CD spectra of peptides monitored over a 50 day time period. His-rich peptides were incubated in buffers at pH 4, 7 and 8.6 over a period of 50 days and spectra were collected at different times. Left column, peptide **H1** and right column, peptide **H2**. Insets at pH 7 are a zoom-in view of the low ellipticity intensity spectra after 14 days.

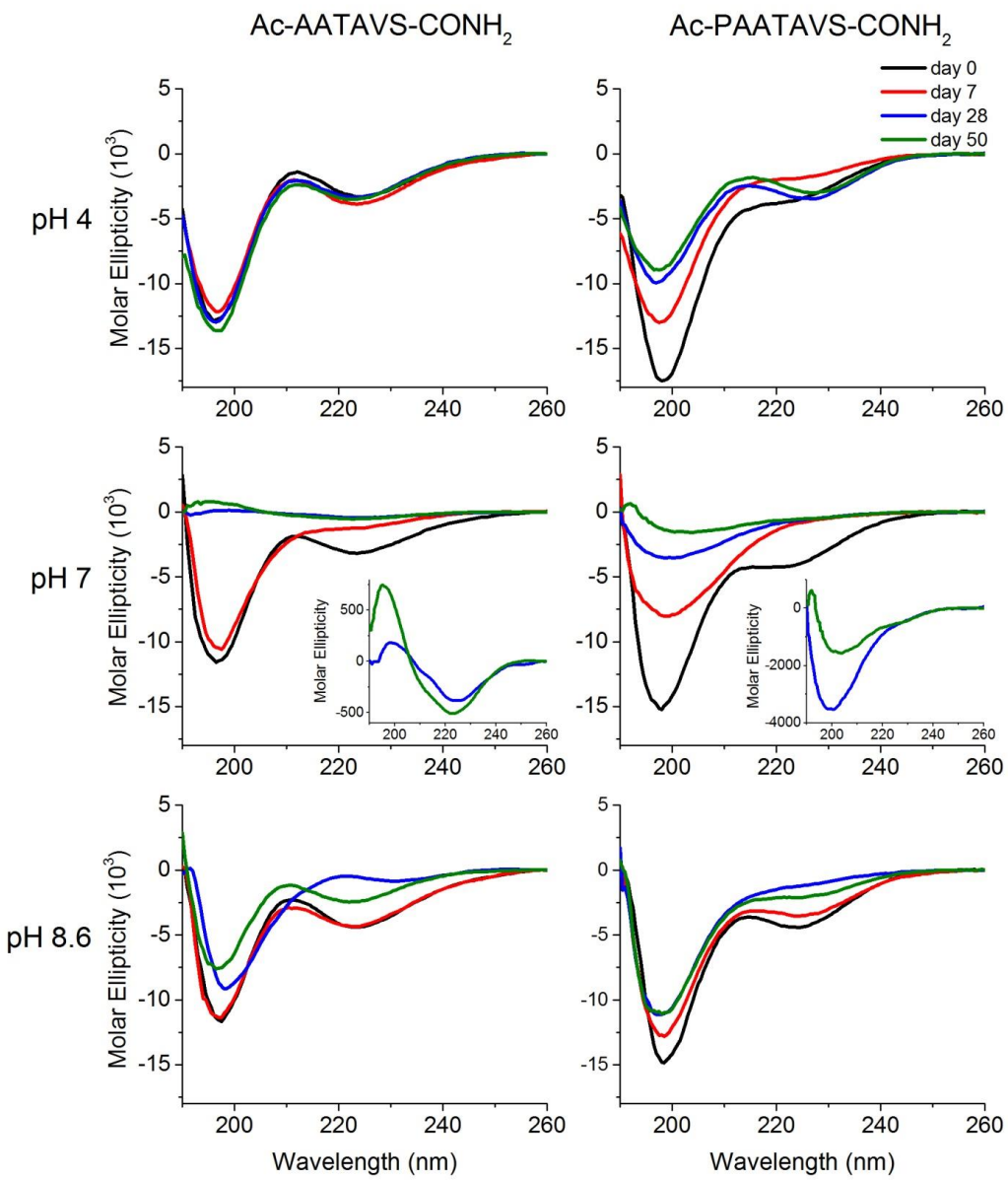

Figure 4.8 Circular dichroism spectra of peptides monitored over 50 day time period. All four peptides were incubated in buffers at pH 4, 7 and 8.6 over a period of 50 days and spectra were collected at different times. Column 1, Peptide **H1**; column 2, **H2**; column 3, **A1**; column 4, **A2**. Insets at pH 7 are zoom-in of the low ellipticity intensity spectra after 28 days (Ala-rich peptides) and 14 days (His-rich peptides).

Ala-rich peptides exhibited slightly different CD spectra features (Figure 4.8 for **A1** and **A2** peptides), but the same general trends were observed with respect to the effect of time and pH. For peptide **A1** (Figure 4.8 for **A1** peptide) at pH 4, the most prominent characteristics were an intense minima at 195–200 nm and a secondary

negative shoulder at ~ 220 nm. These features are also characteristic of β_{II}-type polypeptide,[20] and have also been reported for short peptides shown to adopt the PPII conformation.[23-25] The location of these characteristic bands features and the ellipticities values did not evolve significantly over time. At pH 8.6, the CD spectrum of **A1** was initially similar. However over time the molar ellipticity decreased, and at 50 days the main minima slightly shifted towards lower wavelengths. At pH 7, and similarly to His-rich peptides, spectral changes were much more distinct, with the ellipticity values strongly decreasing by orders of magnitude (Figure 4.8 row 2). Based on DLS and microscopy observations, Ala-rich peptides rapidly self-assemble into fibrillar structures. Thus the dramatic decrease in intensity is likely related to depletion of peptides from the solution. Closer inspection of the low-intensity region (Figure 4.8 row 2 insets) indicates that the residual peptides in solution were in the β_{I}-protein conformation, which could reflect an increased proportion of peptides forming β-sheets. Given the very small intensity values, the spectral changes at day 28 and above were taken with a level of circumspection. Finally, the presence of Pro at the N-terminus (**A2** peptide) did not dramatically affect the CD spectra (Figure 4.8 for **A2** peptide). The main differences with **A2** were a regular decrease in ellipticity values at pH 4 (while it remained constant with **A1**) and a lack of shift for the 195 nm minima. At pH 7, the large ellipticity decrease observed over time for **A1** was again clearly apparent for **A2**.

In order to complement the conformational information obtained by CD, the peptides were also investigated using ATR-FTIR spectroscopy. Two main characteristics of the peptides were of specific interest: first, to confirm the main structural features of the peptides in solution as measured by CD, and secondly to characterize the self-assembled microfibers, *i.e.* in the solid state, which is not accessible with the CD spectroscopy method used. FTIR spectroscopy was done on the same samples used for CD spectroscopy, after the incubation in their respective buffered solutions for 50 days.

For the characterization of peptides in solution, attention was focused specifically to the peptides at pH 4 since both DLS and CD experiments indicated that the peptides exhibited minimal conformation changes and self-assembly at this condition, which thus represented the most stable state in solution. For self-assembled

microfibers formed by Ala-rich peptides, the combination of DLS and CD all point towards rapid fibrillization of peptides in solution at neutral pH, which was especially prominent where visible fibers could be seen with the naked eye at all three pHs. Hence in this case ATR-FTIR measurements were conducted on self-assembled **A1** and **A2** microfibers that were manually separated from solution (described in Section 4.3.5).

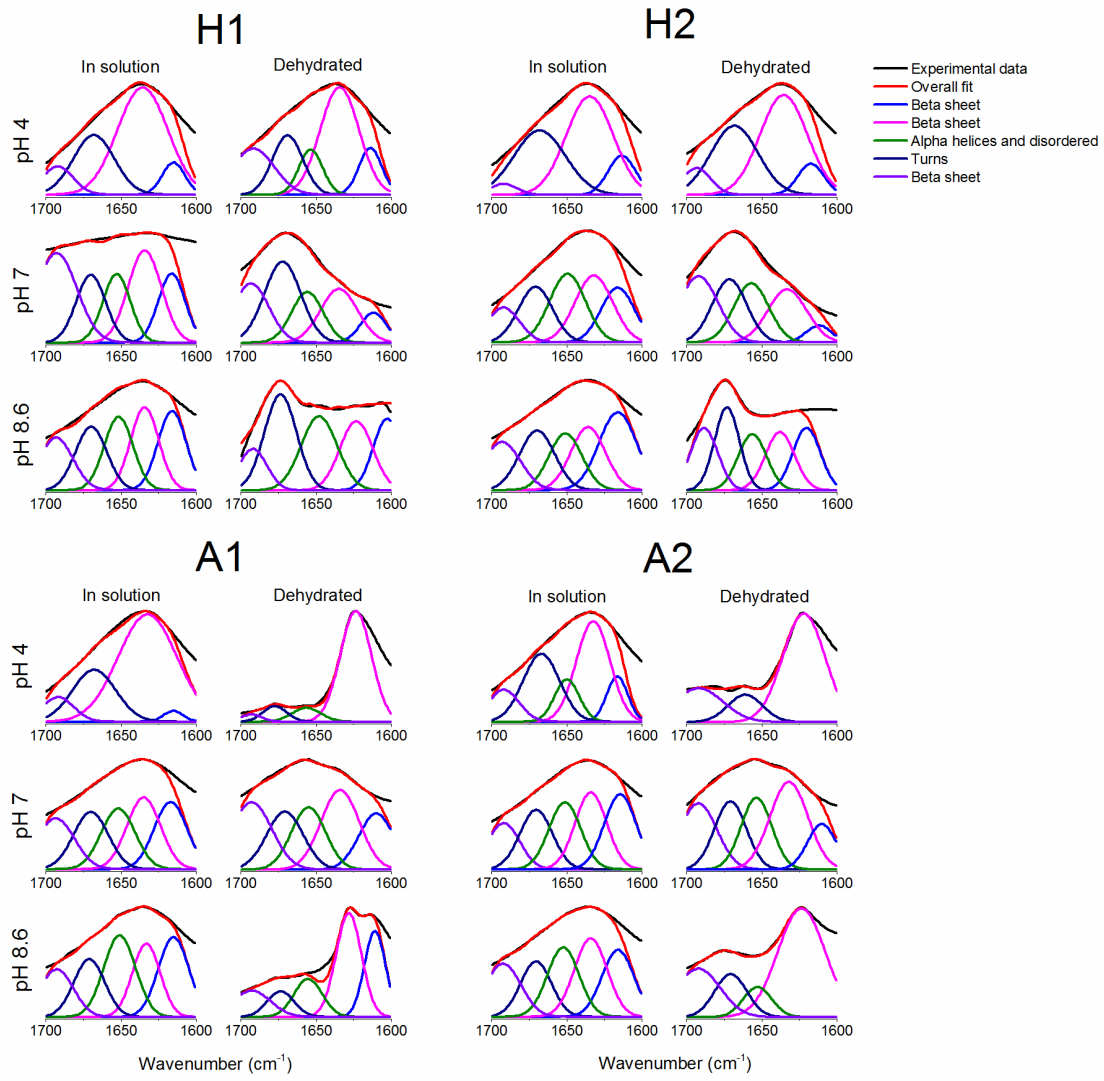

Figure 4.9 ATR-FTIR spectra of suckerin peptides in solution and in dehydrated state. De-convoluted amide I region of FTIR spectra for each peptide after their incubation of 50 days at three different pHs, in solution and in dehydrated state.

Table 4.2 Tabulated percentage composition of β-sheet content estimated by de-convoluting FTIR spectra obtained at three different pHs.

	H1	H2	A1	A2	
pH 4	74.0	64.4	76.3	60.1	In solution
	71.4	65.8	82.0	86.7	Dehydrated
pH 7	68.7	55.5	61.6	60.7	In solution
	51.7	54.4	64.4	61.7	Dehydrated
pH 8.6	60.5	63.3	58.0	62.6	In solution
	48.6	58.3	75.4	76.2	Dehydrated

The de-convoluted amide I region of FTIR spectra of peptide solutions incubated at pH 4 and after 50 days are shown in Figure 4.9. By de-convoluting the Amide I band, peak positions[26] for the different secondary structures were assigned from the second derivative of the spectra. For all peptides, the Amide I band was centered at 1620–1622 cm^{-1} indicating β-sheet enrichment. Peak integration of the de-convoluted Amide I band was used to estimate the secondary structure contributions. All four peptides exhibited high β-sheet content in excess of 60 %. Since water is well-known to affect the Amide I band and can thus lead to artifacts over the relative secondary structure contents, all samples were also measured in the dehydrated state, which was conducted by steadily blowing nitrogen gas over the adsorbed peptide solution. No significant differences were observed for the His-rich peptides **H1** and **H2** (Figure 4.9). For Ala-rich peptides, on the other hand, there was a noticeable increase in β-sheet content with up to above 80% β–sheet for the dehydrated peptide solution (Table 4.2), which may not only reflect that Ala-rich peptides have a very high β-sheet content, but also a β-sheet enrichment upon desolvation, a common mechanism in Amyloid fibers.[27] While quantification of protein secondary structure by ATR-FTIR must be judged with caution, including for amyloid-like peptides[28], the semi-quantitative analysis nonetheless lies in agreement with the CD data, and allows for the conclusion that all peptides exhibit a high propensity for β-sheet formation.

4.3.5 Secondary structure characterization of microfibers

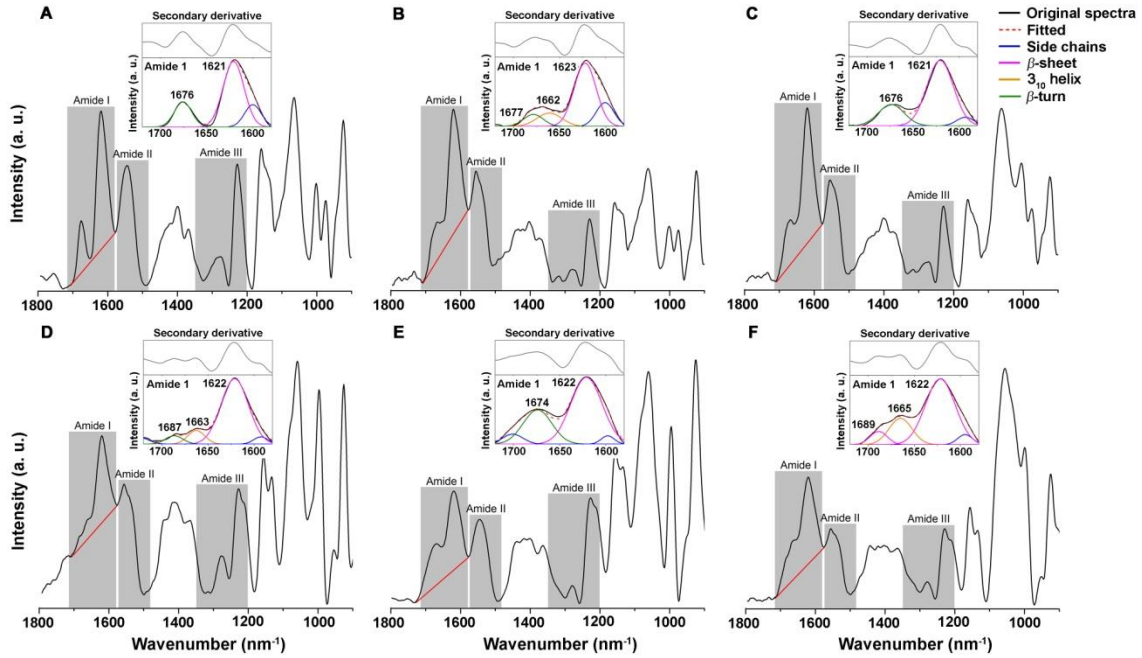

Figure 4.10 ATR-FTIR spectra of suckerin Ala-rich peptide microfibers. Spectra were obtained for peptide microfibers formed at pH 4, 7 and 8.6. Insets show the zoomed-in regions of the Amide I band that was used for de-convolution of the original spectra, with sub-band location determined by secondary derivative of the spectra. Peptide **A1** at pH 4 **(A)**; pH 7 **(B)**; and pH 8.6 **(C)**. Peptide **A2** at pH 4 **(D)**; pH 7 **(E)**, and pH 8.6 **(F)**.

ATR-FTIR analysis of Ala-rich peptides that aggregated into microfibers is displayed in Figure 4.10. The most prominent contribution of the Amide I band was unambiguously located at 1621 cm^{-1} and semi-quantitative analysis of all peptides confirmed a β-sheet content of *ca*. 70 % for both **A1** and **A2** peptides. As a final confirmation that the aggregated microfibers were enriched with β-sheets, they were also stained with Congo red and analyzed under polarized microscopy (Figures 4.11 and 4.12).[29, 30]

4.3.6 Amyloidogenic properties of self-assembled microfibers

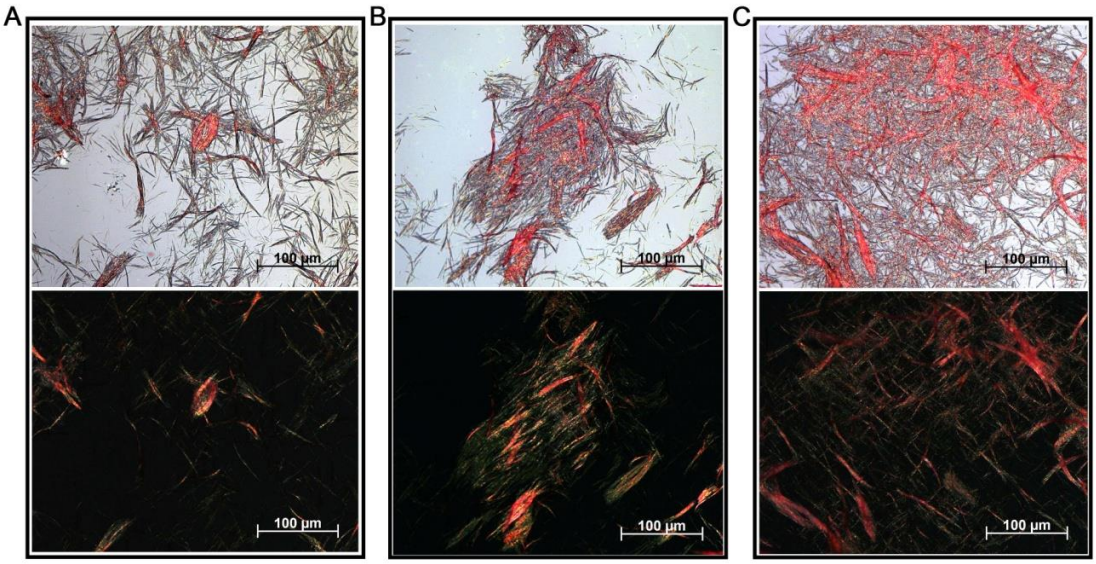

Figure 4.11 Congo red birefringent assay of suckerin A1 peptide microfibers. Fibers formed at **(A)** pH 4, **(B)** 7 and **(C)** 8.6. Panels show the brightfield optical microscope images of Congo red-stained fibers (top) and polarized light images of the fibers.

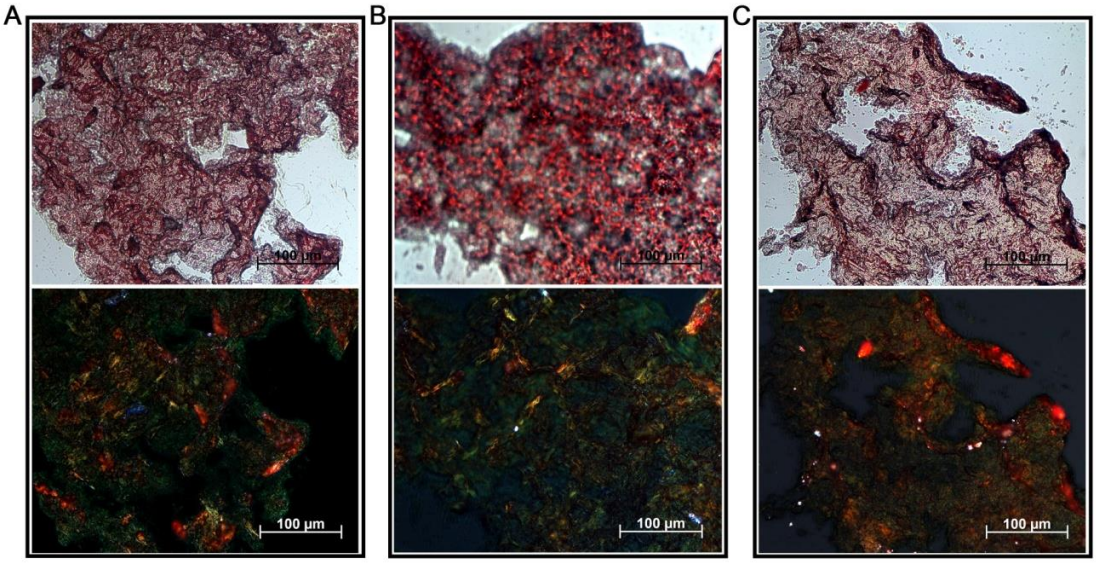

Figure 4.12 Congo red birefringent assay of suckerin A2 peptide microfibers. Fibers formed at **(A)** pH 4, **(B)** 7 and **(C)** 8.6. Panels show the brightfield optical microscope images of Congo red-stained fibers (top) and polarized light images of the fibers.

After staining the microfibers formed by peptides **A1** and **A2** with Congo red dye, the microfibers displayed the characteristic yellow-green birefringence of Congo

red positive structures (Figures 4.11 and 4.12) characteristic of cross-β structures[31] under polarized light microscopy. Positive controls of the amyloid peptide GGVVIA[32, 33] confirmed the same birefringence characteristics (Figure 4.13). Taken together, ATR-FTIR and Congo red staining assay allow us to conclude that Ala-rich peptides assemble into cross-β structures, the characteristic feature of amyloidogenic peptides.

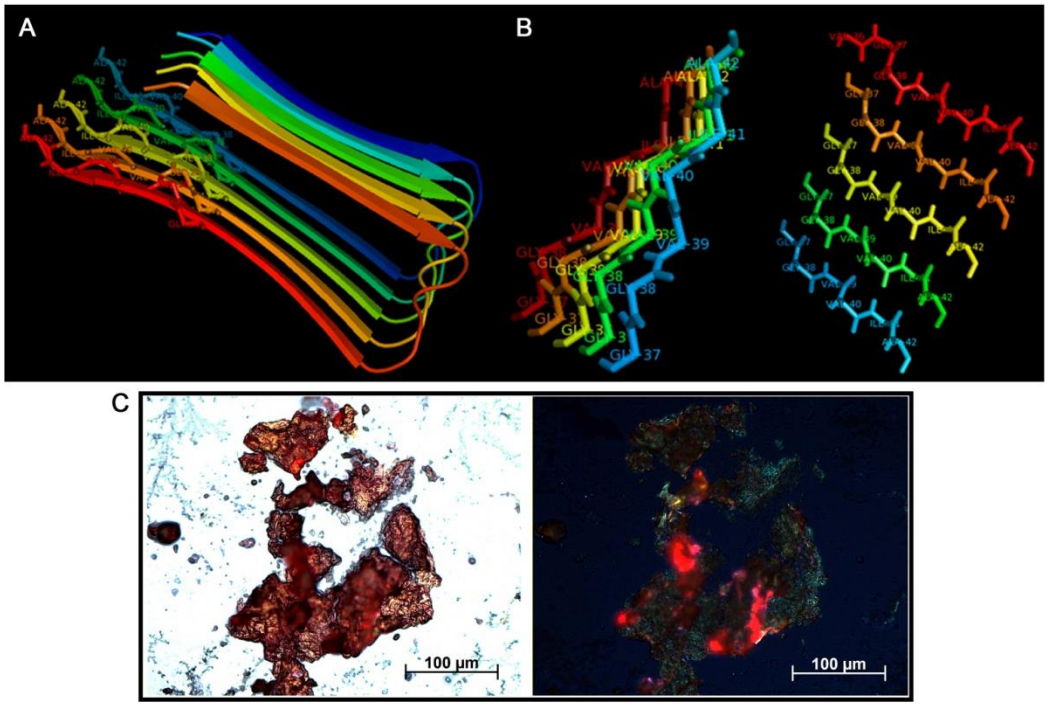

Figure 4.13 GGVVIA control peptide. (A) 3D Structure of Alzheimer's Aβ fibrils from PDB, ID: 2BEG. Five strands of Aβ (1-42) fibrils forming a β-sheet secondary structure. **(B)** Aβ (37–42) forming parallel β-sheet with a high shape complementarity parameter of S_c = 0.92. **(C)** Congo red birefringent assay of GGVVIA microfibers. Fibers were formed at pH 7 and showed positive result for the presence of amyloids. Left: brightfield optical microscope image, right: polarized light image.

4.3.7 1D ^{1}H NMR H/D exchange NMR

The rapid self-assembly of Ala-rich peptides into fibrillar structures, together with CD and FTIR measurements as well as Congo red staining, all point toward a β-sheet-rich fibrillization process which is reminiscent of amyloid formation.[34] In order to gain a deeper understanding of the stability of residues involved in stabilizing these β-sheet rich fibers, the microfibers were subjected to hydrogen-deuterium (H/D) exchange and NMR spectroscopy, according to a method previously developed to identify residues constituting the amyloid core.[35] In brief, the method identifies the core residues involved in hydrogen bonding by monitoring which backbone amides of the β-sheet stabilized fibers are the most susceptible to H-bonding disruption. Accordingly, when the fibers are exposed to deuterium, the labile backbone amide protons exchange with deuterium at a rate controlled by the extent of solvent exposure. DMSO-d_6 was used to dissolve the peptides after D_2O exposure as it slowed down the H/D exchange as opposed to aqueous buffers[36] and breaks down the fibers into their monomer units.[37] Full details on the exchange experimental procedure are provided in Chapter 3.

Chemical shift assignments for the two peptides **A1** and **A2** in DMSO-d_6 were first obtained using 2D TOCSY, ROESY and NOESY spectra,[38] as illustrated in Figures 4.14 and 4.15. Each spin system within the residue as well as the sequential assignment of **A1** could be readily identified. However, there were two sets of peaks for the last two residues (Val6 and Ser7) observed for **A2** that were undistinguishable due to severe overlap. These pairs of peaks in the **A2** peptide are suggested to arise due to cis-trans isomerization of Pro1, resulting in the presence of multiple conformations in solution that manifests as multiple peaks in the 1D 1H NMR spectra (Figure 4.15 D). Peptide fibers dissolved in DMSO-d_6 were used for the reference spectrum and the degree of exchange for each residue was calculated as the peak intensity ratio (signal-to-noise ratio, S/N) of the residues for the exposed and the reference samples, respectively.

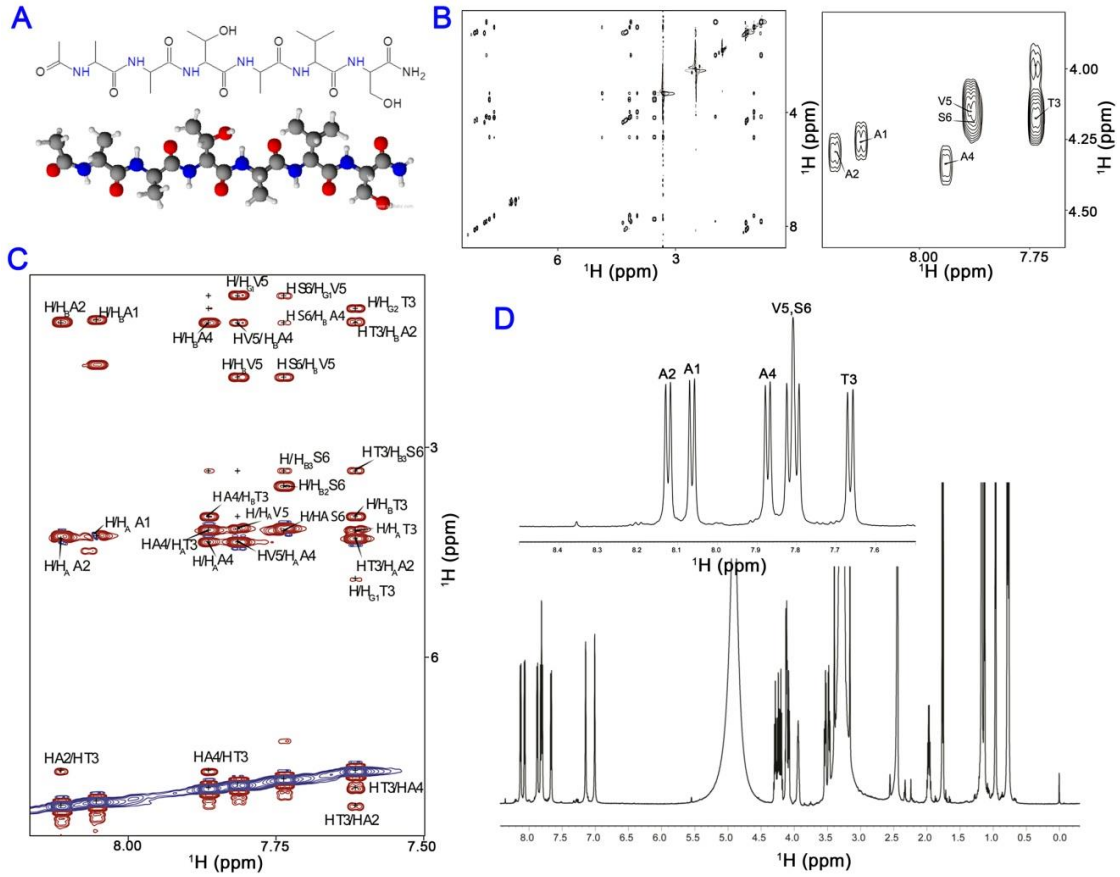

Figure 4.14 Peptide A1 and its NMR proton assignment. A1 peptide molecule is illustrated in its skeletal chemical structure and 3D ball and stick model **(A)**. **(B)** A full 2D ^{1}H ^{1}H TOCSY spectrum of peptide **A1** measured at 600 MHz, 25 °C in DMSO-d_6 (left panel), and amide region of the TOCSY spectrum of **A1** showing Hα resonances of assigned residues (right panel). **(C)** ^{1}H ^{1}H- ROESY spectrum of peptide **A1** measured at 700 MHz , 25 °C in DMSO-d_6. **(D)** 1D ^{1}H NMR reference spectrum of peptide **A1** in DMSO-d_6 recorded at 700 MHz and 25 °C. The backbone amide region is magnified in inset, with assigned residues labeled.

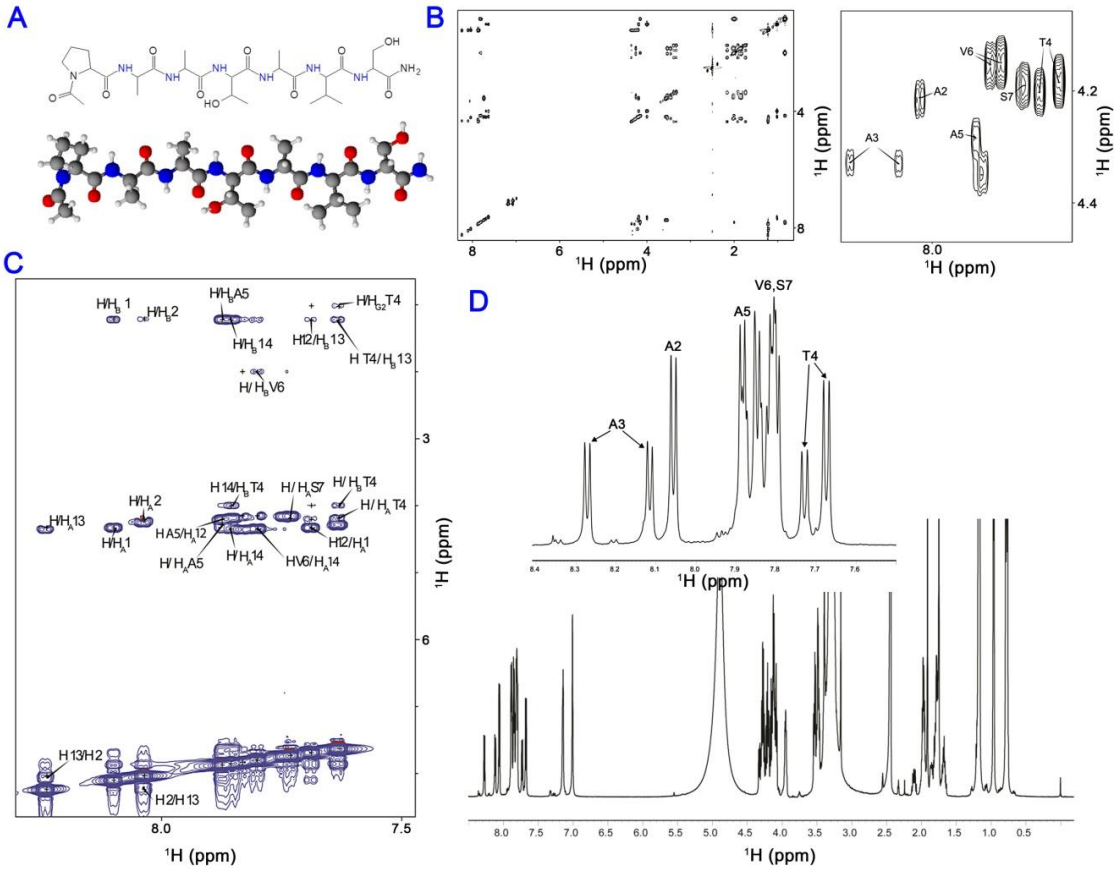

Figure 4.15 A2 peptide and its NMR proton assignment. **A2** peptide molecule is illustrated in its skeletal chemical structure and 3D ball and stick model **(A)**. **(B)** A full 2D ^{1}H ^{1}H TOCSY spectrum of peptide **A2** measured at 600 MHz, 25 °C in DMSO-d_6 (left panel), and amide region of the TOCSY spectrum of **A2** showing Hα resonances of assigned residues (right panel). **(C)** ^{1}H ^{1}H- NOESY spectrum of peptide **A2** measured at 700 MHz , 25 °C in DMSO-d_6. **(D)** 1D ^{1}H NMR reference spectrum of peptide **A2** in DMSO-d_6 recorded at 700 MHz and 25 °C. The backbone amide region is magnified in the inset, with assigned residues labeled.

H/D exchange experiments were conducted to identify the amide backbone protons that are involved in the H-bonding within the self-assembled microfibers. Self-assembled **A1** and **A2** peptide fibers were exposed to D_2O for time periods ranging from 30 minutes to 10 days at ambient temperature. Figure 4.16 shows the 1D ^{1}H spectra region of all backbone amide proton peaks (downfield 7.0–8.5 ppm), for **A1** peptide self-assembled in pH 8.6 buffer: control spectra, 5 hours of H/D exchange and 10 days of H/D exchange. These spectra were normalized with the methyl peak and

slightly shifted for illustration purposes, to focus on the change in signal intensities as the H/D exchange period increases. As the labile amide backbone protons exchange over time, decrease in proton signal intensities of the peptide was observed. However only a slight decrease was observed after 10 days of H/D exchange, indicating a strong filament protection factor and that all amides protons are involved in H-bonding interactions or buried tightly within the self-assembled fibers.

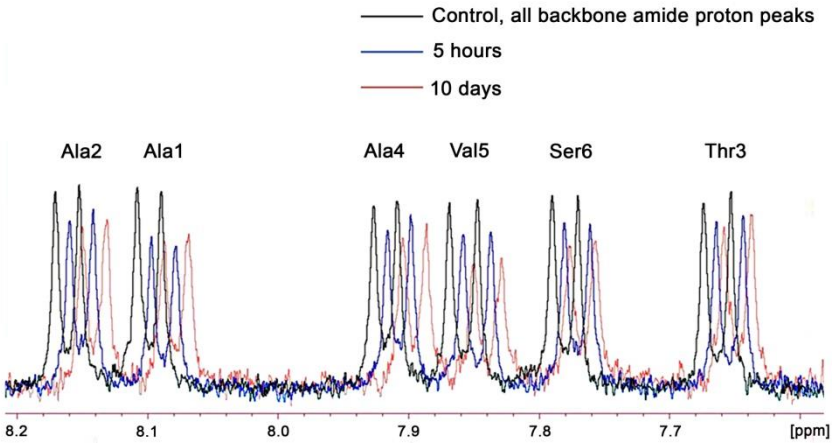

Figure 4.16 1D ^{1}H NMR spectra of A1 fibers in time-series H/D exchange experiments. Spectra are shifted for illustration purposes, with the goal to highlight the decrease in signal intensities over H/D exchange time periods.

Next, a characteristic series of 1D ^{1}H spectra for peptide **A1** and **A2** at various H/D exchange incubation temperatures is shown in Figure 4.16 A and C. The corresponding S/N ratio calculated from the 1D series are plotted as a function of temperature in Figure 4.16 B and D for both **A1** and **A2** peptides. All residues of **A1** (Figure 4.17 B) displayed high signal intensity even after three days of exposure to D_2O at temperatures of up to 85 °C, indicating that the residues are uniformly and highly protected from the solvent and that they are involved in a tight network of H-bonded β-strands throughout the fibers. The exchange rates and protection factors of the fibers are comparable to those of robust Aβ (1–42) and Aβ (25–35) amyloid fibrils.[35, 39]

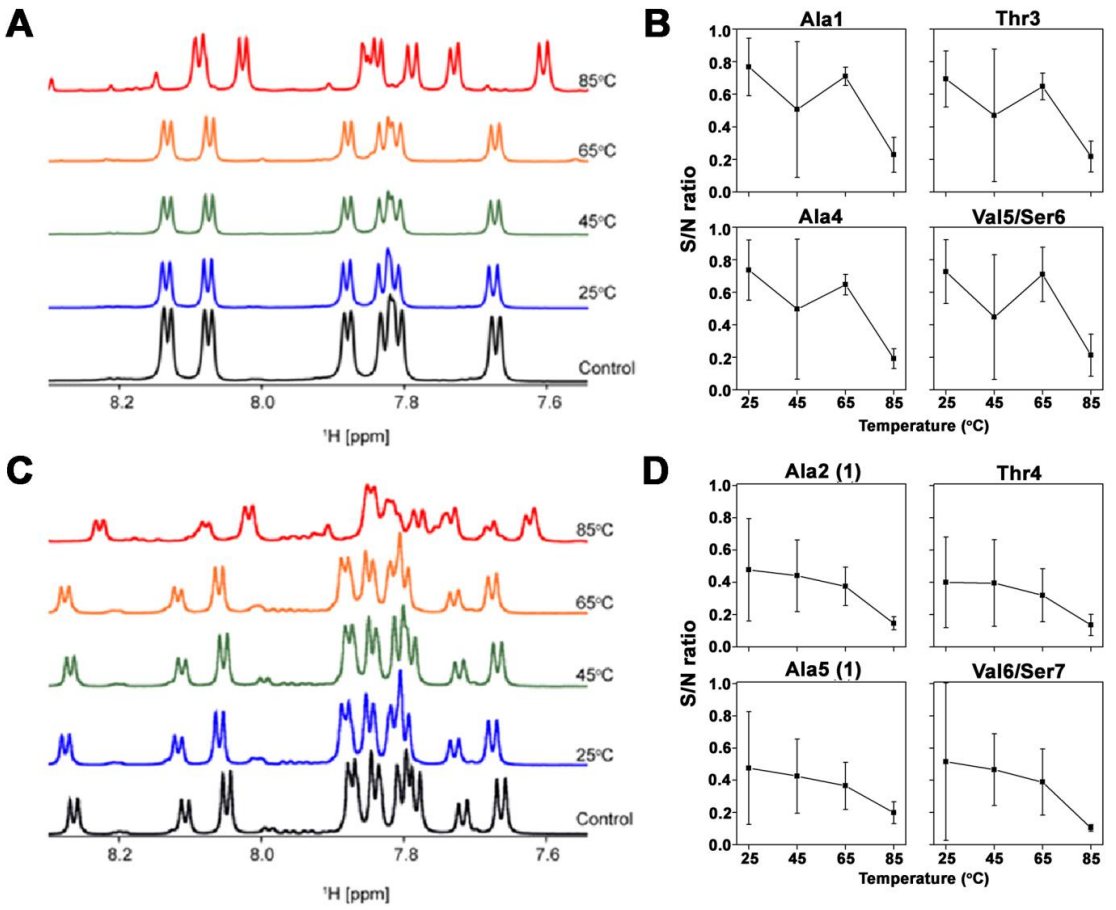

Figure 4.17 1D ^{1}H NMR H/D exchange studies on peptides A1 and A2. (A) 1D ^{1}H NMR spectra of peptide **A1** fibers showing the decrease in signal intensities as temperature increases; **(B)** Peptide **A1** residue specific hydrogen-exchange profiles as a function of temperature; **(C)** 1D ^{1}H NMR spectra of peptide **A2** fibers; **(D)** peptide **A2** residue specific hydrogen-exchange profile as a function of temperature.

While the H/D exchange for all residues generally increased with temperature, an abnormal behavior was noted at 45 ºC, where all residues not only exhibited a higher exchange than at 65 ºC but also a large fluctuation in peak intensity, which is evidenced by the large error bars. It is important to note that such high standard deviations appear to be especially prominent at 45 ºC and not at other temperatures, indicating that it represents an intrinsic feature of the peptide, and not due to experimental uncertainties. A suggestion for this behavior is that **A1** peptide exhibits a phase-transition near this temperature, thereby inducing conformational changes that result in large variability in H/D exchange. Temperature-induced phase transition of

peptides is not an uncommon phenomenon[40] and has been documented in amyloid β-peptides as well.[41] These observations will be investigated in greater detail in further studies. In addition, the S/N intensity ratios of residues in **A2** peptide were observed to be lower than their counterparts from **A1** peptide up to 65 ºC (Figure 4.17 D), indicating that the N-terminal Pro present in **A2** leads to a slightly higher solvent accessibility and that the packing of the β-sheet network is perhaps more relaxed in this case.

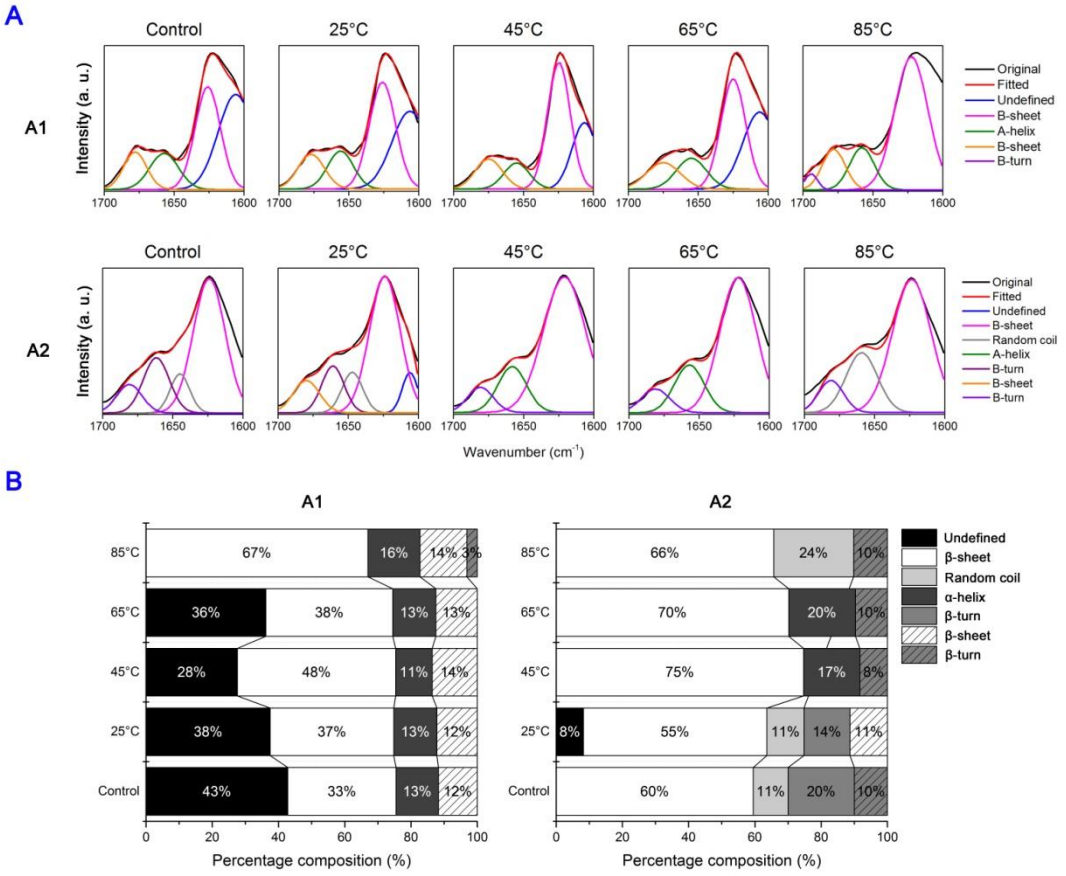

Figure 4.18 ATR-FTIR spectra of peptide A1 and A2 after H/D exchange. After H/D exchange of 3 days at different temperatures, FTIR spectra were recorded for the peptide fibers and **(A)** de-convoluted amide I spectra of **A1** fibers (top) and **A2** fibers (bottom) were obtained. **(B)** Bar graphs summarizing the percentage composition of the secondary structures present in the peptide fibers after H/D exchange.

After H/D exchange, the remaining fibers were subjected to FTIR spectroscopy. From the de-convolution and fitting of the amide I bands (Figure 4.18 A), β-sheet

content of the fibers remains high, summarized by bar graphs (Figure 4.18 B) for both peptides. β-sheet content for peptide **A1** increased gradually along with exposure to higher temperatures, and was highest after exposure to 85 ºC. β-sheet content was observed to increase up to 45 ºC and dropped after 65 ºC exposure, then increased sharply again after exposure to 85 ºC. Peptide **A2** was observed with highest β-sheet content after exposure to 45 ºC, whereby the β-sheet content increased then dropped when exposure temperature pasts 45 ºC. Future studies would include the exploration of the secondary structure and phase transitions observed in these peptides.

4.3.8 Proposed structures of self-assembled microfibers

Based on the experimental evidences that SRT peptides self-assemble into β-sheet rich fibrillar structures with a high structural stability, and with previous understanding that native SRT are semi-crystalline biopolymers in which nanoconfined β-sheets[3] represents the crystalline phase, a plausible structure for the SRT peptides investigated in this study can be proposed. Accordingly, the peptides are stacked into antiparallel β-strands, with the strands oriented perpendicular to the fibrils axis and hydrogen bonds along the fibril axis, namely the classical cross-β structure observed in amyloid fibrils.[28, 34] In order to verify whether these suckerin peptides could form stable cross-β supramolecular lattices, *MD* simulations were performed on all four peptides using the GROMACS4.5.3 package.[42-47] Specifically, the peptides were arranged into oligomeric lattices made of three extended chains, thereby imposing an initial conformational bias towards antiparallel β-strands similar to the work reported by Rauscher *et al.* on elastin and amyloid fibers.[7] Simulations were conducted in explicit water and allowed to relax in an unconstrained fashion and the evolution of the lattice was monitored for up to 200 ns (Table 4.3). In addition to assessing the stability of the oligomeric cross-β networks, the aim of these simulations was to gain further insights into the role of pH and flanking Pro residues. The cross-β lattices were assessed under aqueous conditions at different pHs (pH 4.0 and 7.0).

Table 4.3 Tabulated H-bonds, β-sheet, and β-bridge counts obtained from molecular dynamic simulation studies.

Peptide	pH	H-bond count	β-sheet count	β-bridge count
H1	7	346 (0ns) **358 (200ns)**	0 (0ns) **0 (200ns)**	0 (0ns) **2 (200ns)**
	4	217 (0ns) 137 (200ns)	0 (0ns) 0 (200ns)	0 (0ns) 3 (200ns)
H2	7	367 (0ns) **372 (200ns)**	24 (0ns) **19 (200ns)**	7 (0ns) **8 (200ns)**
	4	205 (0ns) 155 (200ns)	4 (0ns) 12 (200ns)	4 (0ns) 7 (200ns)
A1	7	357 (0ns) 355 (200ns)	249 (0ns) 190 (200ns)	2 (0ns) 4 (200ns)
A2	7	336 (0ns) 511 (200ns)	129 (0ns) 211 (200ns)	2 (0ns) 0 (200ns)

Whereas **H1** peptide lattice evolved towards a disordered structure at both pH 4.0 and 7.0 (Figure 4.19 C), **H2** peptide exhibited a distinct behaviour, with low-range order partially maintained at pH 7 (Figure 4.19 D). To quantify the relative stability of β-sheets, the H-bond and β-sheet counts were compared at 0 and 200 ns. At both pHs, a higher number of H-bonds were recorded for the lattice made of peptide **H2** in comparison to the lattice made of **H1** after 200 ns simulation (Figure 4.19 A). More obvious distinctions between the peptides were obtained in terms of β-sheet content, with no β-sheet predicted for **H1** (β-sheet count = 0) and a significant amount of β-sheet for **H2** (β-sheet count = 19), which was notably higher at pH 7 (Figure 4.19 B). These results are consistent with the destabilization of the lattice at pH 4 due to the protonation of the imidazole ring, resulting in electrostatic repulsion of adjacent peptides. They also indicate that the C-terminus Pro in peptide **H2** stabilizes the β-sheet network, no matter the imidazole rings of His residues are in their protonated or deprotonated states.

Lattices constructed from Ala-rich peptides displayed a much higher propensity towards β-sheet formation, which were highly stable under both acidic and neutral conditions (Figure 4.19 E and F). The stability of the β-sheet network is particularly apparent from the β-sheet count, which is well in excess to that computed for His-rich peptides, with a β-sheet count close to 200 (Figure 4.19 B). At time 0, β-sheet content obtained for **A1** peptide was noted to be higher as compared to **A2** peptide. However, after 200 ns the β-sheet content in **A1** decreased, whereas that of

A2 increased, resulting in a higher β-sheet content for the Pro-containing **A2** peptide. The stability of Ala-rich peptides was not affected by pH, which is not surprising given the absence of titratable side-chains in these peptides.

To emphasize, the cross-β lattices that were constructed in these simulations only represent approximations of the actual β-structures of the SRT peptides, which will need to be refined once structural data become available (for instance by x-ray crystallography or solid-state NMR). Notwithstanding these limitations, some general conclusions from the *MD simulations* can be made, namely that Ala-rich peptides are able to form highly stable amyloid-like cross-β lattices under most conditions. His-rich peptides, on the other hand, display a much lower β-sheet forming potential, which is nevertheless favorable under conditions when the imidazole ring is deprotonated.

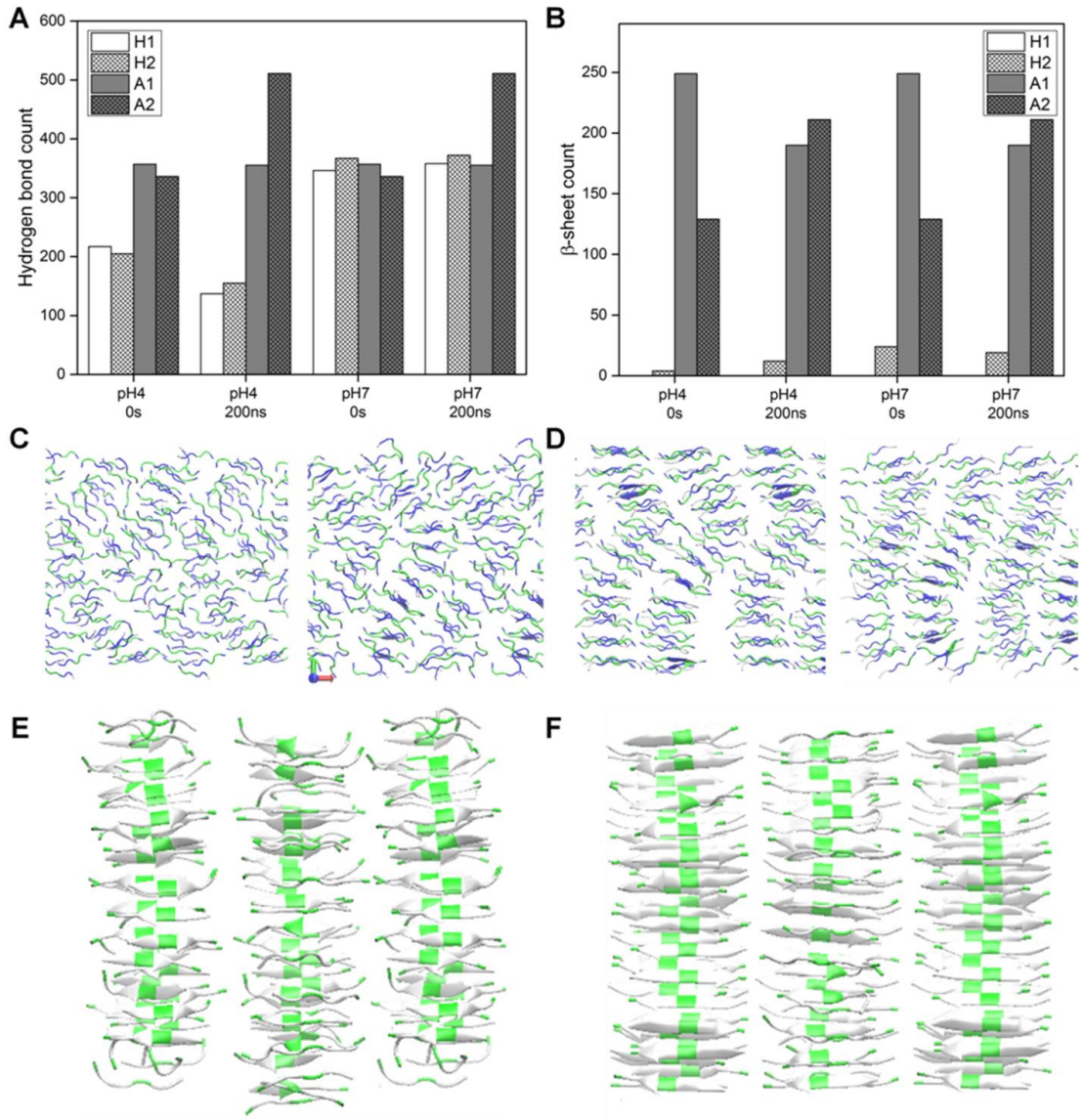

Figure 4.19 ***MD*** **simulations of peptide fibers.** Peptides were arranged in an antiparallel fashion to impose a fibril setting that simulates the self-assembled *β*-sheet network of SRT peptides. **(A)** Hydrogen bond count and **(B)** *β*-sheet count from each peptide's *MD* simulation recorded at 0 and 200 ns of simulation. **(C)** The snapshot of simulated structure of peptide **H1** at 200 ns at pH 4 (left) and pH 7 (right), which did not show a stable *β*-sheet network of fibrils. **(D)** The snapshot of simulated structure of peptide **H2** at 200 ns, illustrating partial stacking of peptides that was maintained at both pH 4 (left) and pH 7 (right). Final simulated structure of **(E)** peptide **A1** and **(F)** peptide **A2**, showing highly stable fibrillar stacking structures (no differences between pH 4 and pH 7) with an increase in hydrogen bond and *β*-sheet counts for peptide **A2** over time.

4.3.9 Discussion

SRTs are entirely constructed from a family of modular, block co-polymer-like proteins. Because of their extreme repetitive primary amino acid sequences, a reductionist approach focusing on the interactions between the most abundant peptide building blocks was undertaken in this study. Three major types of modules were initially selected, namely Gly-rich, Ala-rich, and His-rich modules. It is notable that these modules share sequence similarities with other peptides present in protein-based biological materials. Ala-rich motifs resemble β-sheet forming regions of spider dragline spidroins [48-51] and Gly-containing motifs are highly similar to the sequences constituting the amorphous regions of these silk proteins.[48] Both Ala and Gly-rich motifs also exhibit resemblance to peptide sequences from the wing cuticles of migratory locusts,[52] oyster shell matrix proteins (*Pinctada* genus)[53] and chicken claw keratins.[54] Finally, His-rich SRT motifs exhibit similarity to His-rich proteins[55] of the King ragworm jaw (*Nereis virens*), another hard tissues made of sclerotized proteins that are mechanically reinforced via His-Zn coordination bonds[56-58] and dense covalent cross-linking.[59, 60]

Generally speaking, from the peptide macro-array assay, Ala-rich and His-rich peptides were shown to exhibit the strongest homo-peptidic interactions and such interactions are pH-dependent, being weaker under acidic conditions and the strongest near neutral pH. Time-dependent DLS measurements demonstrate that His-rich and Ala-rich and peptides rapidly aggregate at neutral pH, a behavior that is particularly prominent for Ala-rich peptides (Figure 4.6 C and D). Further examination by optical and SEM microscopy further indicated that these Ala-rich aggregates were in fact composed 30–50 nm nanofibrils bundled together into larger µm diameter fibrils (Figure 4.5).

The characteristic propensity of Ala-rich peptides to spontaneously self-assemble into β-sheet-rich microfibrillar structures is strongly reminiscent of amyloidogenesis, which support previous hypothesis that these modular repeats constitute the main source of β-sheet structure in native SRT. Their size (6 to 7 residues long) falls within the peptide length of amyloidogenic core sequences, usually four to seven amino acids.[61] In amyloid, fibril assembly is mediated by the formation of inter-peptidic β-sheet interfaces.[62] Face-to-face interactions orthogonal to the β-

sheet plane occur by inter-digitation (hydrophobic interactions) or by knob-in-hole interactions involving tight packing of small residue side chains entrapped between bulkier ones.[63] Ala is one of the most abundant amino acids present in such interactions, and Ala/Val pairs have been found in many amyloid structures. With an AATAVS sequence (**A1** peptide), it is tempting to suggest that these interactions are dominant in Ala-rich SRT peptides as well. H/D exchange experiments and the quantification of solvent exchange by NMR (Figure 4.17) further confirm the high protection factor of all residues in this sequence (> 60% when exposed to D_2O at 65 ºC for 3 days), and point to a high stability of the cross-β structure adopted by Ala-rich modular peptides, which are thus suggested to form the seeds for β-sheet supramolecular polymer network self-assembly in native SRT. Towards understanding the kinetics of assembly in SRT, a fundamental question arising is how the suckerin proteins transition from the soluble state to the supramolecular solid-state material.

CD spectroscopy studies of the peptides at different pH provide useful clues to answer this question. The CD spectra indicate that the Ala-rich peptides are initially dominated by PPII conformation, with spectral features similar to those reported for other short peptides established to adopt PPII conformation.[24, 64] A consensus has emerged in the past decade that "disordered" proteins are in fact often dominated by residues that temporally adopt extended (or semi-extended) PII conformations,[22] notably for short peptides.[65, 66] For instance NMR studies demonstrated that a 7-residue poly-Ala in aqueous solution adopted a PPII conformation,[23] and similar results were obtained for the penta-peptide GGAGG.[25] Thus the PPII conformation has been suggested to be a precursor of folding for short peptides[65] as well as to represent an initial semi-extended conformation that facilitates β-sheet aggregation, which is consistent with the fact that PPII structure is closely located to the β-sheet region in the Ramachandran plot.[21, 67] Furthermore *MD* simulations have predicted that in the presence of water, PPII exhibits the lowest conformational free energy, whereas in the absence of water β-strand become the most stable backbone,[68] indicating that upon desolvation and/or aggregation, β-sheets can be readily nucleated from PPII conformation because their conformational energies are similar. Such a mechanism is supported here by the time-dependent CD measurements. As the pH increases and microfibers are formed from the solution, the concentration of peptide in solution decreases over time (Figures 4.7 and 4.8), with residual peptides in solution

transitioning toward β-sheets structure. Interestingly, this time-dependent evolution of CD spectra is strongly reminiscent of that reported for silk fibroins,[69] where an overall CD signature resembling those measured here for the Ala-rich peptides (Figure 4.8) has been reported, and where a strong decrease in ellipticity a few days after initial incubation has also been attributed to a decrease in protein concentration in solution. Furthermore, fibroin conformation has been shown to be strongly pH-dependent,[13] with β-sheet content increasing with pH. A reasonable potential pathway therefore emerges for suckerin peptide based fibril self-assembly, whereby small stretches of Ala-rich modules initially adopt a PPII conformation in solution, which act as a precursor for the formation of amyloid-like cross-β structures in the fibrillar state. This mechanism is also supported by the following *MD* simulations computations. When the peptide lattice initially was allowed to relax in an unconstrained fashion, β-sheets remained strongly favored, with amplification in β-sheet content after 200 ns. Semi-quantitative FTIR of solid-state microfibers as well as Congo red staining confirm that the solid-state fibers assembled from the Ala-rich peptide solution consist of amyloid-like cross-β structures.[28]

The role of His-rich modular peptides is likely complementary to that of the Ala-rich modules. Given that charges in the full-length suckerin proteins are almost exclusively located in these modules, they are likely to play an important role for protein storage in secretory vesicles before aggregation. While the tendency of His-rich peptides to form β-sheets is weaker than Ala-rich peptides, the data in this chapter indicate that the His-rich modules are nevertheless also able to form larger structures near neutral pH and above, as evidenced from DLS data (Figure 4.6). According to CD measurements, these peptides also tend towards β-sheet formation over time (Figure 4.7), and *MD* simulations also indicate that they have the capability to form cross-β structures, albeit to a lesser extent than Ala-rich modules (Figure 4.19 C-F). Therefore, a plausible mechanism is that His-rich modular peptides play a role in maintaining the solubility of suckerins if the pH of the micro-environment where they are stored is acidic. It is increasingly recognized that the pH of secretory glands of extra-cellular materials is acidic. For instance during mussel adhesive thread formation, the pH of the glands located in the mussel feet where threads are secreted is as low as ~2.[17] In spider silks, the pH in spinning duct where elongation flow occurs is also acidic,[13, 14]

and this tight control of pH eventually regulates the final aggregation and assembly of fibroins into silk fibers,[15, 16] with β-sheets forming from the concentrated dope under precise conditions of pH and salt concentration.[13] A similar mechanism is suggested here for SRT, whereby His-rich modules contribute to maintaining a high concentration of suckerins while preventing aggregation. Upon secretion and encountering the higher pH of seawater, the solubility of suckerin would likely decrease. Ala-rich modules that are in the semi-extended PPII conformation then have the potential to quickly form β-sheet nuclei (heterogeneous nucleation), thereby overcoming the activation energy barrier for subsequent aggregation and fibrillization (Figure 4.5). This phase transition into a solid polymeric network would eventually involve growth of the β-sheet nuclei extending to the His-rich domains, and the collective assembly of the block co-polymeric protein into a supramolecular polymer network reinforced by β-sheet domains as the final step of assembly.

Pro residues precisely flank Ala-rich and His-rich modules in all suckerins, and in this chapter, the initial postulation is that this placement controls the size of β-sheets. Pro has been established as a β-sheet disruptor and exhibits the lowest propensity to form β-sheets amongst all amino acids.[70, 71] According to the DLS experiments (Figure 4.6), peptides containing Pro (**H2** and **A2**) form larger structures at higher pH when compared to their counterparts without Pro, with both types of peptides found to be enriched in β-sheets by FTIR (Figure 4.10 D and E) and Congo red (Figures 4.11 and 4.12) assay. SEM observations of **A1** and **A2** microfibers reveal that the morphology of microfibers is notably different (Figure 4.5). While both peptides form nano-scale fibrils, those without Pro (**A1**) bundle into larger microfibers (Figure 4.5 A-C). H/D exchange NMR studies denote strong protection factors for residues in **A2** microfibers (Figure 4.17 B) comparable to amyloid peptides.[35, 39] However, residues in **A1** microfibers (Figure 4.17 D) exhibit even higher protection factors. These observations suggest that the presence of Pro allows the cross-β structure packing to relax by extending the hydrogen bond lengths,[72] possibly preventing premature aggregation and in turn ensuring further assembly of the supramolecular network, which could be consistent with the higher amount of β-sheet content predicted by *MD* simulations for the Pro-containing **A2** peptide at equilibrium. However this assumption remains to be confirmed through further structural analysis of the peptides. In addition, Pro residues

also causes a kink in the peptide backbone,[73] and this effect is likely amplified when Pro is placed in the middle of a longer peptide and not at its termini as explored here.

The microfibers formed by A1 and A2 peptides exhibit different nanoscale structures as compared to the native SRT, whereby β-sheets crystals are randomly oriented in an amorphous phase in the latter (Section 2.1.3). This could be explained by the lack of Gly-rich sequences, which mostly compose the amorphous regions, therefore the Ala-rich peptides in this chapter mainly form oriented β-sheets and assemble into fibers with amyloid-like cross-β structures. It is important to note that although the Ala-rich peptide fibers do not achieve the same structure as that of the native SRT, these studies provide us with important insight on how Ala-rich suckerin peptide sequences are capable to form highly stable β-sheets via hydrophobic interactions that could contribute to the robust property of the native SRT.

4.4 Conclusions

This chapter helps to refine our understanding for the role of modular suckerin peptides on the self-assembly of the SRT supramolecular biopolymer. A combinatorial chemistry approach identified Ala- and His-rich modular peptides as exhibiting strong inter-molecular interactions, which were then studied in detail both experimentally and by computational methods. The results in this chapter strongly suggest that Ala-rich modules of SRT act as nuclei for the initial formation of β-sheets, initially adopting PPII conformation that subsequently transform into amyloid-like cross-β structures, indicating that SRT modular peptides could be used as alternative model system to study amyloidogenesis. His-rich modules can also be involved in cross-β structures, though this ability is not as favorable. pH plays a key role, as both type of modular peptides appear to exhibit aggregation and fibrillization triggered by pH increase. Flanking Pro residues appear to play a subtle role in the stabilization of β-sheet networks. Because of their propensity to self-assemble into cross-β structures, SRT modular peptides also expand our toolkit of functional peptide-based materials for usage in various nanotechnology and health-care applications.[74]

There remain several interesting unanswered questions that will be tackled in future research. First, it has been established in the recent decade that amyloid fibrils

exhibit a richer range of structures than the two-dimensional β-sheet arrangement assumed here, such as the β-solenoids, the cross-β prism, or the β-hairpin.[34] It is possible that SRT peptides form similar complex β-sheets dominated structures and conducting solid-state NMR on these peptides in the near future can help to answer this question. Recent data on native SRT using SAXS has also revealed a nano-scale assembly of fibrils into a hexagonal lattice.[4] It will be of interest to reconcile this nano-scale arrangement with the peptide secondary structure. Second, Gly-rich modules were not studied in detail in this study since the focus was placed on the modular peptides exhibiting relatively stronger interactions in the combinatorial assay. In addition, according to the current model, Gly-rich domains are mostly amorphous[3] and play a central role in facilitating the thermo-plastic behaviour of native SRT. During thermal treatment, Gly-rich domains are suggested to exhibit viscous flow, allowing re-arrangement of the supramolecular network. Biophysical studies focusing on the Gly-rich peptides will allow a better understanding of this process. Finally, the processing pathway from a concentrated soluble form to the robust solid-state network, which could involve a pH-triggered aggregation mechanism from a concentrated colloidal phase (for instance a coacervate) or a liquid crystalline phase, is an attractive topic that also warrants further investigations.

References

[1] J. B. M. Roger T. Hanlon, *Cephalopod Behaviour*, Cambridge University Press, **1996**.

[2] P. A. Guerette, S. Hoon, Y. Seow, M. Raida, A. Masic, F. T. Wong, V. H. Ho, K. W. Kong, M. C. Demirel, A. Pena-Francesch, S. Amini, G. Z. Tay, D. Ding and A. Miserez, *Nat Biotechnol*, **2013**, 31, 908-915.

[3] P. A. Guerette, S. Hoon, D. W. Ding, S. Amini, A. Masic, V. Ravi, B. Venkatesh, J. C. Weaver and A. Miserez, *Acs Nano*, **2014**, 8, 7170-7179.

[4] V. Latza, P. A. Guerette, D. Ding, S. Amini, A. Kumar, I. Schmidt, S. Keating, N. Oxman, J. C. Weaver, P. Fratzl, A. Miserez and A. Masic, *Nat Commun*, **2015**, 6, 8313.

[5] A. T. Nguyen, Q. L. Huang, Z. Yang, N. B. Lin, G. Q. Xu and X. Y. Liu, *Small*, **2015**, 11, 1039-1054.

[6] E. Monsellier and F. Chiti, *Embo Rep*, **2007**, 8, 737-742.

[7] S. Rauscher, S. Baud, M. Miao, F. W. Keeley and R. Pomes, *Structure*, **2006**, 14, 1667-1676.

[8] H. Benyamini and A. Friedler, *Future Med Chem*, **2010**, 2, 989-1003.

[9] K. Hilpert, D. F. H. Winkler and R. E. W. Hancock, *Nat Protoc*, **2007**, 2, 1333-1349.

[10] C. Katz, L. Levy-Beladev, S. Rotem-Bamberger, T. Rito, S. G. D. Rudiger and A. Friedler, *Chem Soc Rev*, **2011**, 40, 2131-2145.

[11] K. S. Lam, M. Lebl and V. Krchnak, *Chem Rev*, **1997**, 97, 411-448.

[12] K. S. Lam, S. E. Salmon, E. M. Hersh, V. J. Hruby, W. M. Kazmierski and R. J. Knapp, *Nature*, **1991**, 354, 82-84.

[13] C. Dicko, F. Vollrath and J. M. Kenney, *Biomacromolecules*, **2004**, 5, 704-710.

[14] F. Vollrath and D. P. Knight, *Nature*, **2001**, 410, 541-548.

[15] G. Askarieh, M. Hedhammar, K. Nordling, A. Saenz, C. Casals, A. Rising, J. Johansson and S. D. Knight, *Nature*, **2010**, 465, 236-239.

[16] F. Hagn, C. Thamm, T. Scheibel and H. Kessler, *Angew Chem Int Edit*, **2011**, 50, 310-313.

[17] L. Petrone, A. Kumar, C. N. Sutanto, N. J. Patil, S. Kannan, A. Palaniappan, S. Amini, B. Zappone, C. Verma and A. Miserez, *Nat Commun*, **2015**, 6, 8737.

[18] A. H. Simmons, C. A. Michal and L. W. Jelinski, *Science*, **1996**, 271, 84-87.

[19] N. J. Greenfield, *Nat Protoc*, **2006**, 1, 2876-2890.

[20] N. Sreerama and R. W. Woody, *Protein Sci*, **2003**, 12, 384-388.

[21] A. A. Adzhubei, M. J. Sternberg and A. A. Makarov, *J Mol Biol*, **2013**, 425, 2100-2132.

[22] J. L. S. Lopes, A. J. Miles, L. Whitmore and B. A. Wallace, *Protein Sci*, **2014**, 23, 1765-1772.

[23] Z. S. Shi, C. A. Olson, G. D. Rose, R. L. Baldwin and N. R. Kallenbach, *P Natl Acad Sci USA*, **2002**, 99, 9190-9195.

[24] Z. S. Shi, K. Chen, Z. G. Liu, A. Ng, W. C. Bracken and N. R. Kallenbach, *P Natl Acad Sci USA*, **2005**, 102, 17964-17968.

[25] L. Ding, K. Chen, P. A. Santini, Z. S. Shi and N. R. Kallenbach, *J Am Chem Soc*, **2003**, 125, 8092-8093.

[26] A. Barth and C. Zscherp, *Q Rev Biophys*, **2002**, 35, 369-430.

[27] S. Mukherjee, P. Chowdhury and F. Gai, *J Phys Chem B*, **2009**, 113, 531-535.

[28] R. Nelson and D. Eisenberg, *Adv Protein Chem*, **2006**, 73, 235-282.

[29] C. L. Masters, K. Beyreuther and M. Trillet, *Amyloid Protein Precursor in Development, Aging and Alzheimer's Disease*, Springer-Verlag Berlin Heidelberg, **2013**.

[30] R. Khurana, V. N. Uversky, L. Nielsen and A. L. Fink, *J Biol Chem*, **2001**, 276, 22715-22721.

[31] R. Nelson, M. R. Sawaya, M. Balbirnie, A. O. Madsen, C. Riekel, R. Grothe and D. Eisenberg, *Nature*, **2005**, 435, 773-778.

[32] M. R. Sawaya, S. Sambashivan, R. Nelson, M. I. Ivanova, S. A. Sievers, M. I. Apostol, M. J. Thompson, M. Balbirnie, J. J. W. Wiltzius, H. T. McFarlane, A. O. Madsen, C. Riekel and D. Eisenberg, *Nature*, **2007**, 447, 453-457.

[33] L. K. Chang, J. H. Zhao, H. L. Liu, K. T. Liu, J. T. Chen, W. B. Tsai and Y. Ho, *J Biomol Struct Dyn*, **2009**, 26, 731-740.

[34] A. V. Kajava, J. M. Squire and D. A. Parry, *Adv Protein Chem*, **2006**, 73, 1-15.

[35] J. H. Ippel, A. Olofsson, J. Schleucher, E. Lundgren and S. S. Wijmenga, *P Natl Acad Sci USA*, **2002**, 99, 8648-8653.

[36] Y. Z. Zhang, Y. Paterson and H. Roder, *Protein Sci*, **1995**, 4, 804-814.

[37] N. Hirota-Nakaoka, K. Hasegawa, H. Naiki and Y. Goto, *J Biochem*, **2003**, 134, 159-164.

[38] K. Wüthrich, *NMR of Proteins and Nucleic Acids*, Wiley, New York, **1986**.

[39] A. Olofsson, A. E. Sauer-Eriksson and A. Ohman, *J Biol Chem*, **2006**, 281, 477-483.

[40] F. G. Quiroz and A. Chilkoti, *Nat Mater*, 2015, 14, 1164-1172.

[41] J. Danielsson, J. Jarvet, P. Damberg and A. Graslund, *Febs J*, **2005**, 272, 3938-3949.

[42] H. Bekker, H. J. C. Berendsen, E. J. Dijkstra, S. Achterop, R. Vondrumen, D. Vanderspoel, A. Sijbers, H. Keegstra, B. Reitsma and M. K. R. Renardus, *Journal*, **1993**, 252-256.

[43] H. J. C. Berendsen, D. Vanderspoel and R. Vandrunen, *Comput Phys Commun*, **1995**, 91, 43-56.

[44] E. Lindahl, B. Hess and D. van der Spoel, *J Mol Model*, **2001**, 7, 306-317.

[45] D. Van der Spoel, E. Lindahl, B. Hess, G. Groenhof, A. E. Mark and H. J. C. Berendsen, *J Comput Chem*, **2005**, 26, 1701-1718.

[46] B. Hess, C. Kutzner, D. van der Spoel and E. Lindahl, *J Chem Theory Comput*, **2008**, 4, 435-447.

[47] D. v. d. Spoel, E. Lindahl, B. Hess, A. R. v. Buuren, E. Apol, P. J. Meulenhoff, D. P. Tieleman, A. L. T. M. Sijbers, K. A. Feenstra, R. v. Drunen and H. J. C. Berendsen, Gromacs User Manual version 4.5, www.gromacs.org).

[48] J. M. Gosline, P. A. Guerette, C. S. Ortlepp and K. N. Savage, *J Exp Biol*, **1999**, 202, 3295-3303.

[49] R. V. Lewis, *Chem Rev*, **2006**, 106, 3762-3774.

[50] C. Y. Hayashi and R. V. Lewis, *Science*, **2000**, 287, 1477-1479.

[51] J. Gatesy, C. Hayashi, D. Motriuk, J. Woods and R. Lewis, *Science*, **2001**, 291, 2603-2605.

[52] T. N. Krogh, L. Skou, P. Roepstorff, S. O. Andersen and P. Hojrup, *Insect Biochem Molec*, **1995**, 25, 319-329.

[53] S. Sudo, T. Fujikawa, T. Nagakura, T. Ohkubo, K. Sakaguchi, M. Tanaka, K. Nakashima and T. Takahashi, *Nature*, **1997**, 387, 563-564.

[54] L. A. Whitbread, K. Gregg and G. E. Rogers, *Gene*, **1991**, 101, 223-229.

[55] C. C. Broomell, S. F. Chase, T. Laue and J. H. Waite, *Biomacromolecules*, **2008**, 9, 1669-1677.

[56] C. C. Broomell, M. A. Mattoni, F. W. Zok and J. H. Waite, *J Exp Biol*, **2006**, 209, 3219-3225.

[57] C. C. Broomell, F. W. Zok and J. H. Waite, *Acta Biomater*, **2008**, 4, 2045-2051.

[58] H. C. Lichtenegger, T. Schoberl, J. T. Ruokolainen, J. O. Cross, S. M. Heald, H. Birkedal, J. H. Waite and G. D. Stucky, *P Natl Acad Sci USA*, **2003**, 100, 9144-9149.

[59] H. Birkedal, R. K. Khan, N. Slack, C. Broomell, H. C. Lichtenegger, F. Zok, G. D. Stucky and J. H. Waite, *Chembiochem*, **2006**, 7, 1392-1399.

[60] R. K. Khan, P. K. Stoimenov, T. E. Mates, J. H. Waite and G. D. Stucky, *Langmuir*, **2006**, 22, 8465-8471.

[61] J. D. Pham, N. Chim, C. W. Goulding and J. S. Nowick, *J Am Chem Soc*, **2014**, 136, 4446-4446.

[62] J. D. Pham, R. K. Spencer, K. H. Chen and J. S. Nowick, *J Am Chem Soc*, **2014**, 136, 12682-12690.

[63] P. N. Cheng, J. D. Pham and J. S. Nowick, *J Am Chem Soc*, **2013**, 135, 5477-5492.

[64] Z. G. Liu, K. Chen, A. Ng, Z. S. Shi, R. W. Woody and N. R. Kallenbach, *J Am Chem Soc*, **2004**, 126, 15141-15150.

[65] T. P. Creamer and M. N. Campbell, *Determinants of the polyproline II helix from modeling studies*, **2002**.

[66] Z. S. Shi, K. Chen, Z. G. Liu and N. R. Kallenbach, *Chem Rev*, **2006**, 106, 1877-1897.

[67] B. Bochicchio and A. M. Tamburro, *Chirality*, **2002**, 14, 782-792.

[68] R. L. Baldwin, *Unfolded Proteins*, **2002**, 62, 361-367.

[69] C. Dicko, D. Knight, J. M. Kenney and F. Vollrath, *Biomacromolecules*, **2004**, 5, 758-767.

[70] D. L. Minor and P. S. Kim, *Nature*, **1994**, 367, 660-663.

[71] C. K. Smith, J. M. Withka and L. Regan, *Biochemistry-Us*, **1994**, 33, 5510-5517.

[72] S. Y. Sheu, D. Y. Yang, H. L. Selzle and E. W. Schlag, *P Natl Acad Sci USA*, **2003**, 100, 12683-12687.

[73] C. M. Deber and A. G. Therien, *Nat Struct Biol*, **2002**, 9, 318-319.

[74] C. Aleman, A. Bianco and M. Venanzi, *Peptide Materials: From Nanostructures to Applications*, Wiley, **2013**.

Chapter 5

Fabricating peptide material inspired by SRT peptides

This chapter aims to explore the fabrication of suckerin peptide materials, and mimic the mechanical properties of the native SRT material with the careful selection of the right building blocks. With the optimization of peptide sequence and self-assembly conditions, suckerin peptide fibers were obtained and characterized via various techniques. Nanoindentation was employed to probe the mechanical properties of the peptide fiber material, while in-depth biophysical characterizations were conducted by employing multiple techniques. The fibers' mechanical and biophysical properties were compared with those of the native SRT material to validate the preservation of these properties, and the mechanism of fiber formation has been discussed. The chapter brings us a step further to the biomimicry of SRT material, and sheds light on how the peptide building blocks' sequence and length play important roles in the material's hierarchical structure assembly, and ultimately their biophysical and mechanical properties.

5.1 Introduction

Based on the previous chapter, it was found that a suckerin peptide sequence of 6 residues (AATAVS, known as peptide **A1**) was capable of spontaneously forming cross-β amyloidogenic short fibers in solution. With the findings described in Chapter 4 and supporting recent studies on suckerin-19 protein (Chapter 2), this Ala-rich modular and repetitive short peptide was therefore hypothesized to be the nucleus (or seeding) building block of the β-sheet secondary structures driving the SRT's self-assembly process. With the intriguing self-assembly behavior of the peptide building blocks, the natural next step of progress from a materials science perspective was to fabricate suckerin-based materials that preserve the mechanical properties of the SRT.

The hypothesis in this chapter is that, with the appropriate building blocks selected and adding to the β-sheet seeding **A1** peptide sequence, it is possible to mimic the SRT's self-assembly system, whereby longer and larger fibers could be achieved, while maintaining its mechanical properties.

Although His-rich suckerin peptide sequences (**H1** and **H2**) were shown (Chapter 4) not to self-assemble into structures visible by the naked eye, they adopted poly-proline II secondary structures in solution. Over time, the secondary structures transitioned to β–sheets, with the transition being more pronounced at pH 7. *MD* simulation results also show that these His-rich peptide sequences are capable of forming semi-stable antiparallel β-sheet fibrils. However, hydrogen bonds that are required for forming β-sheet secondary structures appear to be transient and less stable than in Ala-rich peptides.

Hence as a continuation of Chapter 4, with the deduction that Ala-rich peptides seed the formation of β-sheets whereas His-rich peptides maintain the solubility of the suckerins prior to their self-assembly into solid-state material, this chapter explores the combination of these two β-sheet forming peptides into a 12-residue peptide, **AA12** (AATAVSHTTHHA), to fabricate peptide materials inspired by SRT.

5.2 Experimental Methods

In order to address the questions in this chapter and to test the hypotheses, a range of experiments were designed and techniques were employed to characterize the modular suckerin peptides.

5.2.1 Peptide synthesis via SPPS

Peptide was synthesized via manual SPPS method according to Section 3.2.1 on 2 g of CTC resins with 1.22 mmol/g loading. 1.8 g of crude peptide was obtained after cleavage from resin and removal of side chain protecting groups. Synthesized peptide was washed thoroughly then precipitated with diethyl ether an stored at -20 °C.

5.2.2 HPLC purification and LC/MS verification

Crude **AA12** peptide from Section 5.2.1 was purified with HPLC according to Section 3.3.1 for 2 to 3 cycles until > 95% pure. Trace analysis was done using HPLC to verify the percentage purity and LC/MS (Section 3.3.2) was performed to check the mass of the peptide.

5.2.3 CD spectroscopy

CD spectroscopy was used to study the secondary structures of the suckerin peptides in their buffered solutions (pH 4, 7 and 8.2), over a time period of 35 days. **AA12** peptides were dissolved in their respective buffered solutions at a concentration of 5 mg/mL and CD spectroscopy measurements were done according to Section 3.5.3.

5.2.4 DLS

DLS measurements were performed on **AA12** peptides dissolved in their respective buffered solutions (pH 4, 7 and 8.2) at a concentration of 50 μM. DLS

measurements were done according to Section 3.5.1, and the Z-average sizes were used to study the self-assembly trend of the peptides over a 24-hour period.

5.2.5 Self-assembly of peptide fibers

Self-assembly of **AA12** peptide into fiber material was attempted with buffered solutions (pH 4, 7 and 8.2) over the incubation of 35 days at 5 mg/mL, with no fibers forming. Subsequently organic solvents were added to drive self-assembly of **AA12** peptide fibers. Firstly, different percentages (vol. %) of polar protic solvent (methanol) in water was used to dissolve **AA12** peptides. However, no visible fibers were formed. Thereafter, different percentages (vol. %) of polar aprotic solvent(acetonitrile) in water was used to dissolve **AA12** peptides, driving self-assembly of the peptides into fibers, which increased with the increase in vol. % of acetonitrile composition. The lowest vol. % of acetonitrile used that reproducibly drives the self-assembly of peptides into fibers was at 5% vol. %, which was then used as the self-assembly condition in subsequent experiments.

5.2.6 FESEM imaging

FESEM imaging was used to investigate the fibers' morphologies. Samples were prepared and imaged according to Section 3.5.5. Fibers that were broken for the imaging of their cross-section were first immersed into liquid nitrogen for snap freezing and broken with tweezers.

5.2.7 Congo red birefringence assay

Congo red birefringence assay was done on the fiber samples to detect for the presence of amyloid structures. Staining of the fibers were done according to Section 3.5.2 and observed with an optical microscope under normal light and polarized light.

5.2.8 Optical microscopy imaging

All optical microscope images were taken according to Section 3.5.12.

5.2.9 FTIR spectroscopy

FTIR spectroscopy was performed on **AA12** peptide fibers to study the secondary structures of dried fibers formed by the peptide. FTIR spectroscopy measurements were done according to Section 3.5.4

5.2.10 DSC

DSC was performed on dried **AA12** peptide fibers to determine the melting temperature of the fibers, according to Section 3.5.8.

5.2.11 TGA

TGA was performed on lyophilized **AA12** peptide powder to investigate the thermal degradation properties of the peptide; sample preparation and experimental procedure was done according to Section 3.5.9.

5.2.12 Nanoindentation

A1 peptide fibers were pipetted onto gold-coated silicon wafer surface and **AA12** peptide fibers were embedded in epoxy and polished to obtain the different cross sections for indentation experiments. The mechanical characterization of fibers was done by nanoindentation, to obtain the elastic modulus and hardness of the fibers. Sample preparation and indentation experiments were done according to Section 3.5.6.

5.2.13 WAXS

Purified and lyophilized **AA12** peptide powder was used to assemble fibers in 5% acetonitrile and 95% water mixture. Fibers obtained were bundled tightly together without twisting, and then secured between two transparency films under a microscope. WAXS was used to examine the fibers' structure in the molecular length-scale. Experiments were performed by our external collaborators, mentioned in Section 3.5.11.

5.2.14 *MD* simulations

MD simulation was used to study the stability of peptides arranged in antiparallel fibrillar packing. Over a simulation period of 200 ns, the number of β-sheets and hydrogen bonds formed were obtained. *MD* simulations were done according to Section 3.5.14.

5.3 Results and Discussion

Based on studies performed in Chapter 4, Ala-rich peptides spontaneously self-assemble into microfibers that are highly stable and resistant to urea degradation. These fibers are rich in β-sheet secondary structures and are postulated to construct the nanoconfined β-sheets found in the suckerins,[1] which reinforces the SRT structure's robust mechanical properties. To find out if these self-assembled fibers possess mechanical properties similar to the native SRT, preliminary mechanical characterization of the short peptide microfibers were performed.

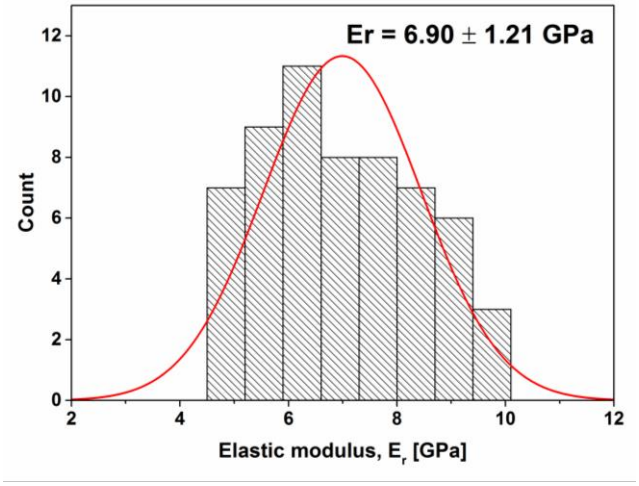

Figure 5.1 Indentation results of A1 peptide dried microfibers. An average modulus of 6.90 ± 1.21 GPa was obtained from 59 indentations on the peptide microfibers.

Mechanical properties of the self-assembled peptide **A1** microfibers were probed by nanoindentation in both hydrated and dried conditions. As the fibers were in the µm scale and not easy to manipulate, only few successful indents were obtained under hydrated conditions, with an average modulus of 1-2 GPa. Under dried conditions, an average elastic modulus of 6.90 ± 1.21 GPa was obtained, shown in Figure 5.1. These values are similar to the modulus obtained for the native SRT, whereby under dry conditions the elastic modulus ranges from 7.5 GPa to 4.5 GPa, and decreases between 2.75 GPa and 1.75 GPa under hydrated conditions (Section 2.1.1).[2, 3]

Procedures of indentation and caveats taken for all indentation experiments are presented in Figure 5.2. Prior to all indentation experiments, a scanning probe

microscope (SPM) image (Figure 5.2 A) of the area of interest was obtained, and the location for subsequent indents was selected at the highest points of the fiber sample to ensure maximum thickness for indents and thereby limiting substrate effects, as indicated in Figure 5.2 A. Indentation on the substrate were also performed to compare the modulus between sample and substrate, and any modulus found to be affected by the substrate was discarded. 3D images of the fiber (Figure 5.2 B) obtained via the SPM of the nanoindenter was used to assist in identifying the highest points along the fiber. Figure 5.2 C compares loading-unloading curves obtained from indentation of the substrate, salt and fiber sample. The curves can be distinguished by their characteristics, and only curves that exhibit the characteristics of sample indentation were used for further analysis. Figure 5.2 D illustrates representative examples of loading-unloading curves of indentations performed on peptide fibers that were affected by the substrate. These curves experience an inflexion point followed by an abrupt increase in gradient halfway during loading, and exhibit steep unloading gradients that resemble that of the substrate's unloading curve. Modulus values obtained for the substrate, salt or substrate-affected curves are much higher than that of the fibers' modulus, and these curves were discarded from the dataset.

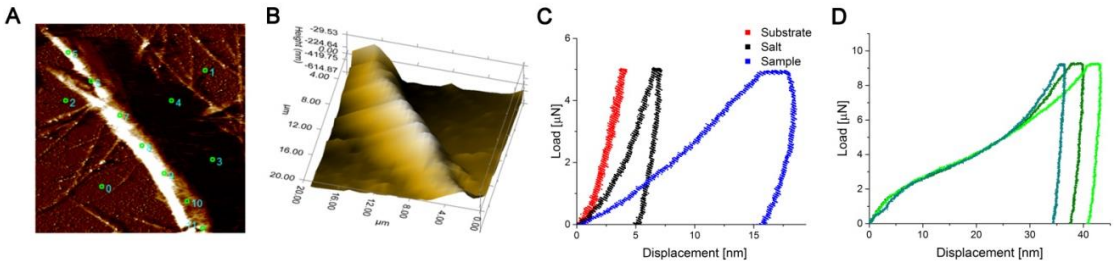

Figure 5.2 Nanoindentation experiment and caveats taken. (A) An SPM image of a peptide fiber on silicon wafer substrate, taken prior to nanoindentation experiments, with indentation points indicated. **(B)** 3D view of the same fiber, indicating the height of the fiber. **(C)** Comparison of loading-unloading curves obtained for the substrate (glass), salt and a fiber sample. **(D)** Examples of indents on peptide fibers that are affected by substrate, which can be identified from the shape of their loading-unloading curves.

5.3.1 Synthesis and purification of AA12 peptide

The peptide with amino acid sequence AATAVSHTTHHA (**AA12**) was successfully synthesized via SPPS method and purified with HPLC for at least 2 purification cycles to achieve > 95% purity. Trace analysis and LC/MS spectra of purified peptide used for subsequent experiments are shown in Figure 5.3 A and B, respectively.

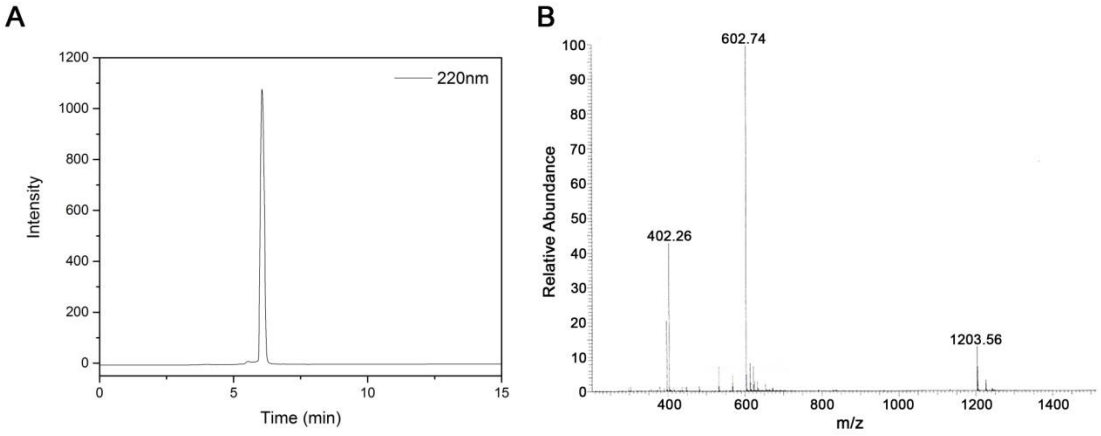

Figure 5.3 Purification and verification of SPPS-synthesized AA12 peptide. (A) HPLC chromatogram of purified **AA12** peptide and **(B)** LC/MS mass spectrum of purified **AA12** peptide.

5.3.2 Secondary structure characterization of AA12 peptide in solution

The **AA12** peptide was incubated in buffered solutions of pH 4 (0.1 M Sodium acetate), 7 (0.1 M phosphate buffered saline) and 8.2 (0.1 M Tris buffered saline) at a concentration of 50 μM, to investigate their self-assembly properties by DLS measurements over a time period of 24 hours (Figure 5.4). No clear trend of size increment was observed, with peptides incubated at pH 7 and 8.2 fluctuating at sizes close to the monomeric sizes recorded in denaturing urea. Peptides incubated at pH 4 showed only a slight increase in Z-average sizes after 800 min. Overall, Z-average sizes recorded over the time period of 24 hours were generally below 1μm.

Little change was observed from the size measurements and their high polydispersity index (PDI) values during measurements, which could point to the peptide's dynamic behavior in solution. It is plausible that at the given concentration

and conditions, the peptides exist in solution in various oligomeric size populations, and the sedimentation of larger oligomers could also be occurring over the 24 h period, thus accounting for the fluctuation in size and PDI values.

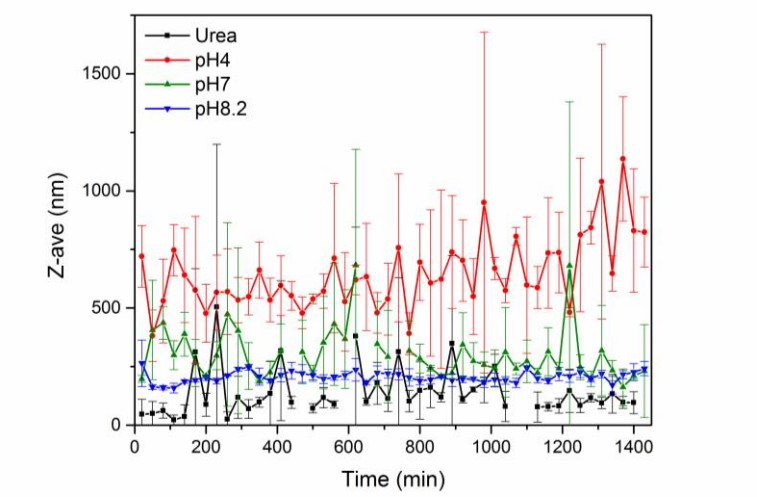

Figure 5.4 Self-assembly of peptide AA12 monitored by DLS. AA12 peptide was incubated in 3 different buffered solutions of pH 4, 7 and 8.2 at 50 μM peptide concentration and size measurements were recorded over 24 h at intervals of 10 min. The peptides were also incubated in hydrogen-bond disrupting urea (black), serving as monomeric state controls (equilibrium state with the minimum self-assembly).

In order to investigate whether **AA12** exhibits significant secondary structural changes in solution over longer time periods, CD spectroscopy experiments were conducted at 5 mg/mL peptide concentration under the same pH conditions as DLS, over a time period of up to 35 days as shown in Figure 5.5. At pH 4, no significant changes in the spectra were observed: the spectrum at day 0 shows a minima at 204 nm with a weak negative shoulder centered ~232 nm. Subsequent spectra show a consistent blue-shifted minima at 202 nm, with an unchanged negative shoulder at 232 nm. At pH 8.2, the initial spectrum recorded at day 0 displayed a minima at 202 nm and a weak negative shoulder centered ~230 nm. Over time the intensities of the minima and shoulder decreased to half their initial values, with both blue-shifted by 2 nm, to 200 nm and 228 nm respectively. In contrast, significant transitions were observed over time at pH 7. The initial spectrum recorded at day 0 displayed an intense minima at 201 nm and a weak negative shoulder at 228 nm. The intensity of the spectra decreased over time, with the minima at 201 nm gradually blue-shifted to

197 nm. A new maxima appeared at 213 nm, while the weak negative shoulder disappeared.

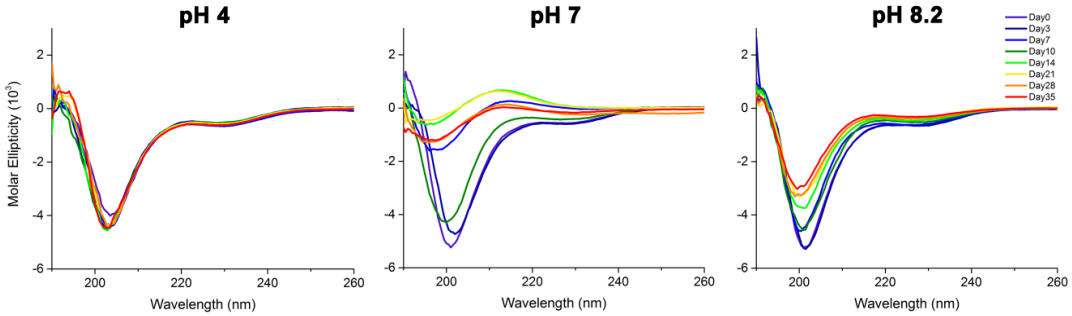

Figure 5.5 CD spectra of AA12 peptide monitored over a 35 day time period. Recorded spectra of **AA12** peptide incubated in pH 4, pH 7 and pH 8.2 buffered solutions.

The initial spectra obtained for the peptides at all 3 pH levels resembled those of random coil or β-sheet-rich structures[4]. The spectra of **AA12** peptide after 35 days at pH 7 can be assigned to β_{II}-type proteins. These structures display similar signature maxima and minima signals and are β-sheet-rich proteins that also contain short stretches of poly(Pro)II-like conformations (PPII). Sreerama and Woody have established in their systematic studies of β-sheet proteins that they can be classified as β_I or β_{II},[5] with the main difference arising from their PPII to β-sheet ratio (described in Chapter 4).

At pH 4, the peptide remains unchanged, exhibiting the same conformation over 35 days of incubation. This is possibly due to the presence of protonated His residues in the sequence that could create stable charge-charge inter-peptide repulsions. The charge-charge repulsion forces limit the conformations that the peptides can adopt, and after achieving equilibrium in solution, they are prevented from further conformational changes. This would enable the peptides to remain in their soluble state rather than aggregating. At pH 7 and 8.2, His residues become deprotonated and in the absence of the charge-charge repulsive forces, the peptides would be able to interact more, including via hydrophobic forces and hydrogen bonding. However, there was no observable aggregate over the 35 day incubation period.

Therefore, these data strongly suggest that His residues play a role of increasing the solubility of the peptides, which would otherwise aggregate spontaneously into β-rich structures under these similar conditions, as observed from the previous study on shorter peptides (Chapter 4). Under such fully aqueous conditions, self-assembly of the **AA12** peptide into larger structures may be retarded due to the high solubility of His-rich domains.

To further investigate the structural changes observed by CD spectroscopy, the BeStSel program[4] was used to comprehensively estimate the secondary structure content (Figure 5.6). As both Ala-rich and His-rich peptides exhibit high propensities to adopt β-sheet secondary structures and the spectra obtained of **AA12** peptides indeed resemble that of β-sheet structure, BeStSel program was selected. β-structures exhibit spectral diversity, whereby many algorithms and programs available for fitting of CD spectra do not account for spectra that derive from unusual β-structures. Samples such as protein aggregates and amyloid fibrils that possess unusual β-structures tend to obtain less reliable secondary structure predictions, and BeStSel has been developed to tackle the problem of secondary structure prediction for β-structure-rich proteins or peptides. Taking into account the spectral diversity of β-structures, BeStSel analyses both secondary structure content and identify the type of β-sheet present - parallel β-sheets and antiparallel β-sheets of different twists. Spectra intensities were converted to delta ellipticity prior to performing BeStSel fittings for the wavelength range of 190–250 nm. Secondary structures obtained from the fittings were derived from DSSP algorithm, and the RMSD values indicate the closeness of the fit. Lower RMSD values indicate better fittings, and these values of each fit are presented in each spectrum as shown in Figure 5.6 A. Low RMSD values below 0.1 were obtained for most spectra, providing good fittings, with the exception of pH 7, after day 7, due to low delta ellipticity intensities. The decrease in intensities is attributed to the decrease of peptide concentration in solution, which could have formed larger oligomeric protofibrils and then sedimented, thus lowering the CD signal of the remaining peptides.

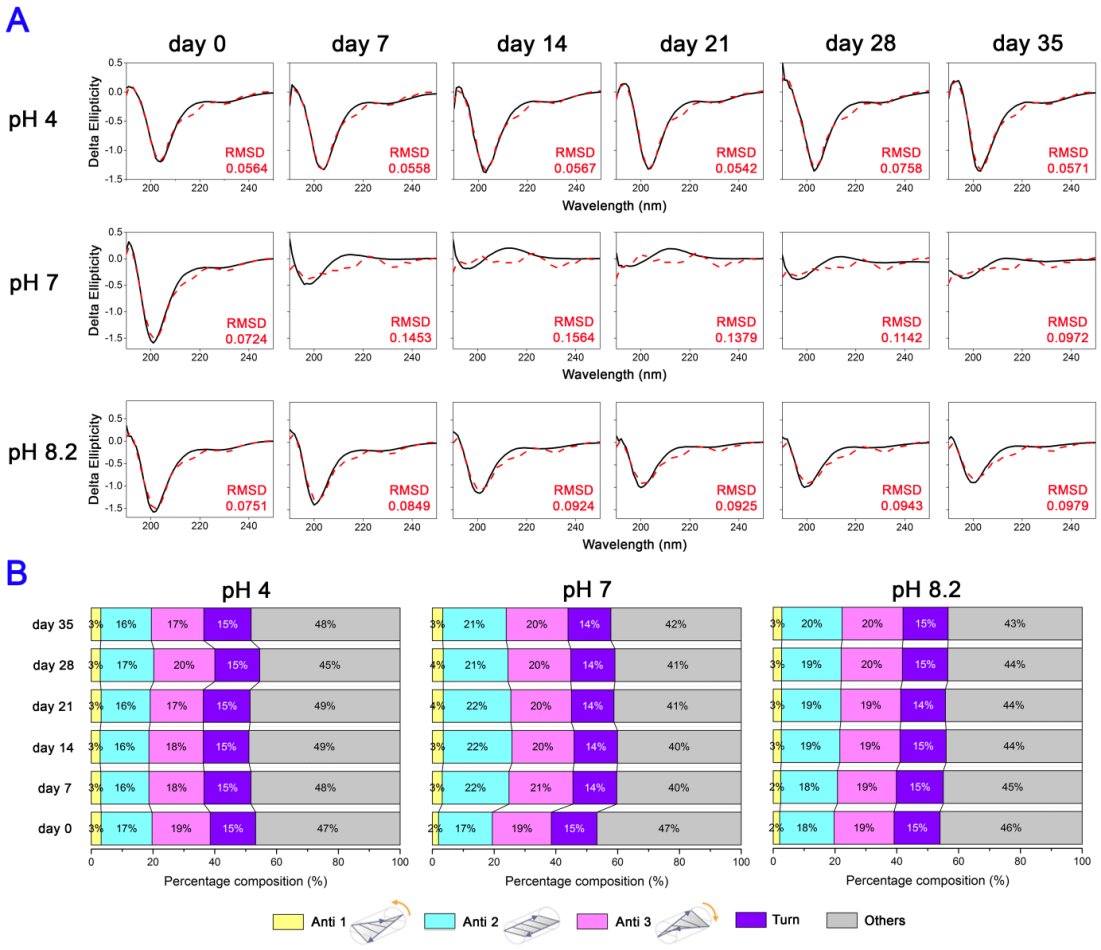

Figure 5.6 Analysis of CD spectra with BeStSel program. (A) BeStSel fitting of recorded spectra from Figure 5.5 obtained with RMSD values shown. **(B)** Estimated secondary structure content (%) from each fitted spectra, where 'Anti 1' refers to left-twisted antiparallel β-sheet, 'Anti 2' refers to relaxed antiparallel β-sheet, 'Anti 3' refers to right-twisted antiparallel β-sheet, 'Turn' refers to β-turn, and 'Others' refers to other structures that are non-helical, sheet or turn structures, and undefined by BeStSel program.

A summary of the estimated secondary structure content is shown in Figure 5.6 B. For spectra recorded at pH 4 and 8.2, antiparallel β-sheet, β-turn and 'Others' secondary structures were assigned for all the fitted spectra, which was generally consistent over 35 days. 'Others' secondary structures refer to structures that are neither helical, turns or sheet. These could include unordered and PPII structures. Across all pH levels, no helical or parallel β-sheet structures were identified from the fitting.

AA12 peptide at pH 4 consisted of 45–49% 'others' structure, 15% β-turn, and 37–40% antiparallel β-sheets. Antiparallel β-sheets were further classified into right-twisted, relaxed and left-twisted antiparallel β-sheets. The antiparallel β-sheet component was assigned to 17–20% right-twisted, 16–17% relaxed and 3% left-twisted.

At pH 8.2, **AA12** peptide consisted of 43–46% 'others' structure, 14–15% β-turn, and 39–43% antiparallel β-sheet. The antiparallel β-sheet consisted of 19–20% right-twisted, 18–20% relaxed and 2–3% left-twisted.

As for pH 7, fitting of spectra obtained at day 0 gave a 47% others' structure, 15% β-turn, and 38% antiparallel β-sheet. With further de-convolution of antiparallel β-sheet components, 19% right-twisted, 17% relaxed and 2% left twisted sheets were assigned. Spectra from day 7 onwards obtained fittings with higher RMSD readings > 0.1, and secondary structure components consisted of 40 – 42% 'others' structure, 14% β-turn and 43–46% antiparallel β-sheet. Antiparallel β-sheet was further assigned to 20–21% right-twisted, 21–22% relaxed and 3–4% left twisted.

From the fitting results, peptide **AA12** demonstrates a high propensity to form antiparallel β-sheet and β-turn structures, with no helical or parallel β-sheet propensity. In the antiparallel β-sheets, relaxed and right-twisted structures were preferred over left-twisted structures. **AA12** peptide at pH 7, after 7 days, appeared to consist of an increased amount of β-sheets, which could be indicative of a pH-dependency of β-sheet formation. However, as the RMSD increased after day 7 due to the lower signal intensity, this speculation remains to be confirmed. For the largest fraction of 'others' structures obtained for peptide **AA12** at all pHs, it is postulated to be the result of a high content of PPII secondary structure, and this postulation will be further discussed in Section 5.4.

5.3.3 Driving self-assembly of AA12 peptide

In order to optimize the self-assembly process of peptide **AA12** from solution to solid-state material, different solvent systems were investigated. With the idea of employing solvent properties to drive self-assembly, mixtures of different solvent combinations were tested, with the aim of altering solvent-peptide interactions. A solvent system consisting of a combination of polar protic (water) and aprotic solvent (acetonitrile) was found to produce reproducible results after exploring several solvent systems. Acetonitrile and water could accelerate the assembly of peptide fibers, and also increase the size and length of these self-assembled fibers,[6-8] in comparison to smaller **A1** peptide fibers obtained in Chapter 4.

Since acetonitrile is an aprotic solvent, it is unable to form hydrogen bonds with other acetonitrile molecules. In turn, it forms hydrogen-bonds with other available protic molecules that can act as hydrogen bond donors, the classical agent being water. Mixing acetonitrile to a water/peptide system alters the hydrogen-bonding targets, whereby the peptide and acetonitrile molecules compete to hydrogen-bond with water molecules. Water molecules with both protons hydrogen-bonded to acetonitrile molecules become unavailable for hydrogen-bonding with peptides, therefore creating binding competition as illustrated in Figure 5.7. Reducing the number of available water molecules in solution that can solvate and form hydrogen-bonds with peptides will result in the peptides having a higher probability of coming into closer proximity to form hydrogen bonds with one another. This in principle induces more efficient self-assembly of the peptide molecules, while still maintaining the same high concentration of peptide in solution.

AA12 peptide was readily soluble up to 800 mg/mL in fully aqueous conditions. By adding an azeotrope combination of acetonitrile (84% v/v) and water (16% v/v) dropwise to dissolve the peptides, peptide fibers were observed to self-assemble spontaneously. As the concentration of acetonitrile decreased in the mixture, fewer fibers were formed in solution. At a low acetonitrile concentration of 5% v/v in water, peptide fibers could be reproducibly self-assembled. Hence subsequent fibers used in the following studies were produced with the mild solvent system of 5% v/v acetonitrile and 95% v/v water with above 20 mg/mL peptide concentration.

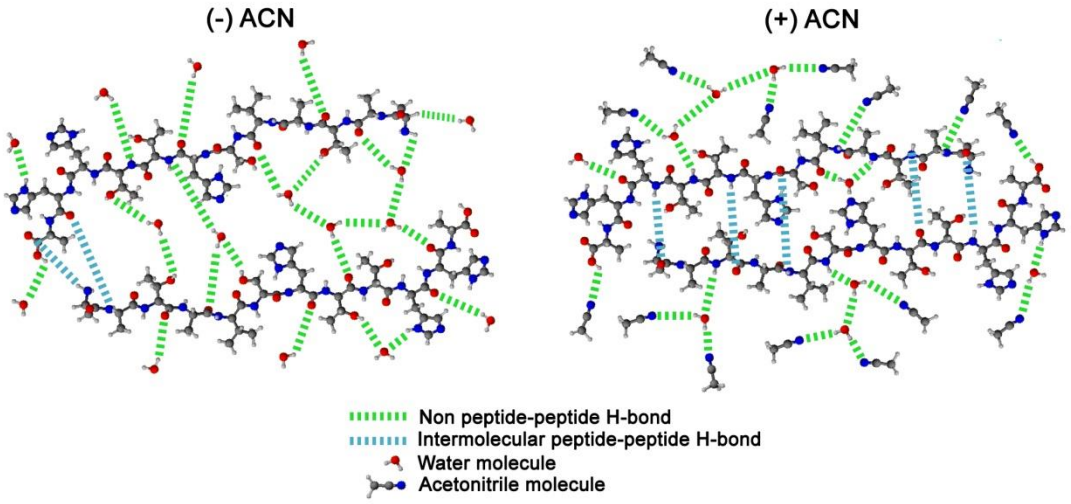

Figure 5.7 Illustration of competitive hydrogen-bonding for water molecules. Left panel: water and peptide molecules in solution, right panel: with the addition of acetonitrile molecules.

Long fibers of up to 1 cm could be formed from **AA12** peptides under the conditions explored. While applying the same conditions for the shorter **A1** peptides, the **A1** peptide fibers formed did not increase in length, remaining at similar lengths as previously formed in buffered aqueous solutions (Chapter 4). Hence, inducing self-assembly of longer fibers via the introduction of an aprotic solvent to alter the solvent system does not apply for all peptide sequences, suggesting that this method could be peptide length- and sequence-dependent.

5.3.4 Self-assembled fibers

Self-assembled **AA12** peptide fibers were imaged with FESEM to examine their morphologies. SEM images revealed that the fibers were hierarchically constructed by an organized assembly of hundreds of smaller fibrils. Fibers observed were > 20 μm in diameter (Figure 5.8 A), while fibrils with an average of ~1 μm diameter (Figure 5.8 B) aligned along the fiber's axis, closely bundled together to construct the main fibers. In Figure 5.8 C, smaller filamentous strands of approximately 50 nm in diameter were observed to construct the fibrils, and they run perpendicular to the fibril axes in a tightly packed fashion over the full length of the

fibrils. Measurements were obtained via ImageJ, and averaged over > 50 measurements for each reported measurement.

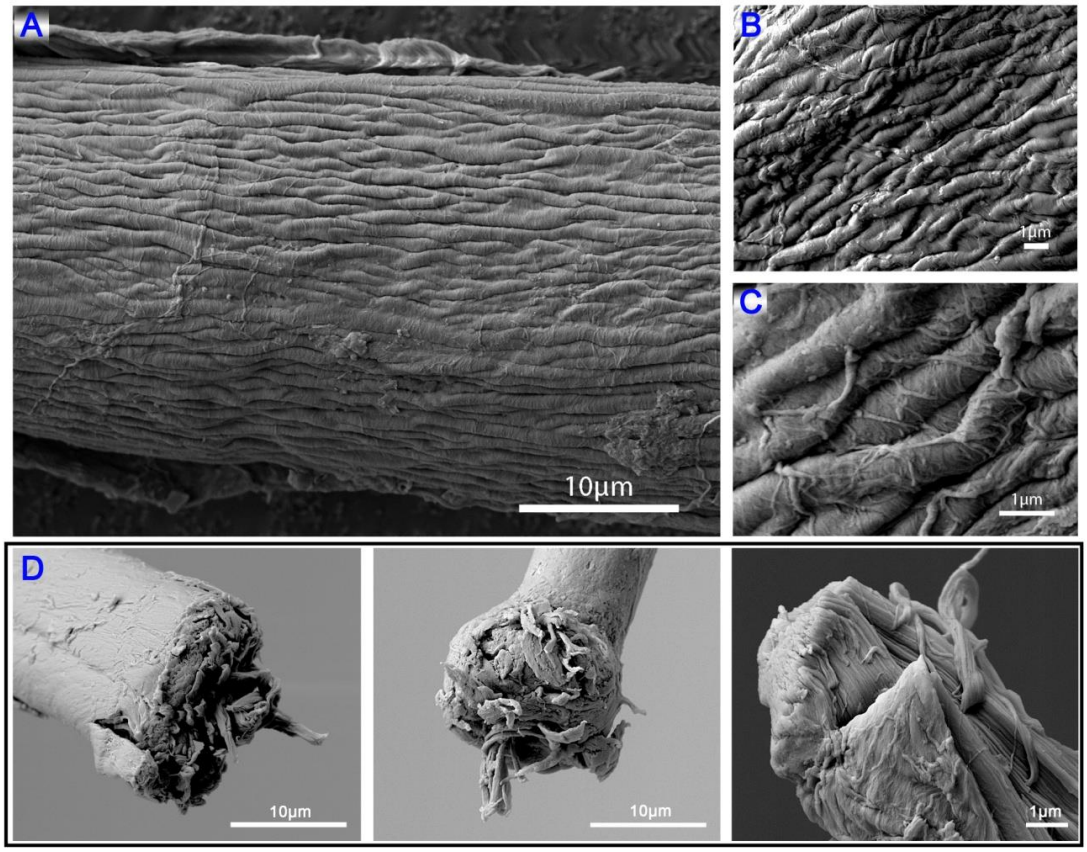

Figure 5.8 FESEM images of self-assembled fibers from peptide AA12. (A) Peptide fiber at 2,700 times magnification, showing a fiber's side view with a diameter > 20 µm, formed by many smaller fibrils with an average of ~1 µm diameter. Peptide fiber was imaged at **(B)** 6,500 times and **(C)** 16,000 times magnification, revealing filamentous strands of approximately 50 nm diameter. **(D)** Cross-sections of three broken fibers.

In Figure 5.8 D, broken cross sections of three fibers were imaged, which revealed that the same filamentous fibrils observed from the side view of the fiber in Figure 5.8 A were found within the fibers as well. From the FESEM images, a proposed hierarchical construct of the fibers is shown in Figure 5.9.

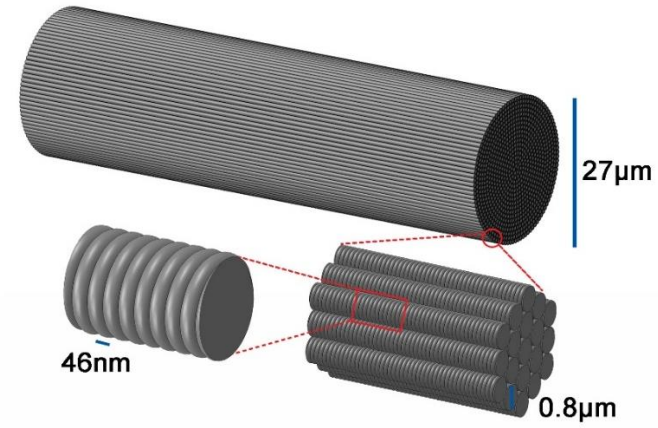

Figure 5.9 Proposed hierarchical structure of self-assembled AA12 peptide fibers. Constructed fiber and its composition of smaller fibrils and filamentous strands with measurements obtained from fiber in Figure 5.8 A to C.

5.3.5 Characterization of fibers

Peptide fibers exhibited birefringent properties as shown in Figure 5.10 A when viewed under polarized light with the optical microscope. The birefringent property is indicative of an anisotropic arrangement of peptides within the fibers, which is in agreement with the aligned fibril packing observed from FESEM imaging (Section 5.3.4). Fibers were then stained with Congo red dye and viewed under polarized light, shown in Figure 5.10 A. The birefringent fibers appeared apple-green at various segments, indicating the presence of amyloid-like structure.

To further characterize the fibers, FTIR spectroscopy measurements were performed on dried fibers to identify the secondary structures present in the fibers, shown in Figure 5.10 B. Distinct amide I, II and III bands were identified from the fiber spectra, and de-convolution of the amide I region was done, with the peak positions obtained from the maxima of the spectra's inverted secondary derivative. Curve-fitting of amide I region gave an estimate of high β-sheet content of 72.9%, 0.6% α-helical and 26.5% random coil secondary structures. With β-sheet content present at high percentages, more than that determined by BeStSel for peptides in solution, it is likely that β-sheet formation could be a mechanism of **AA12** fiber assembly, driven by

the formation of stable intermolecular hydrogen bonds between the Ala-rich sequences under the solvent-altered conditions.

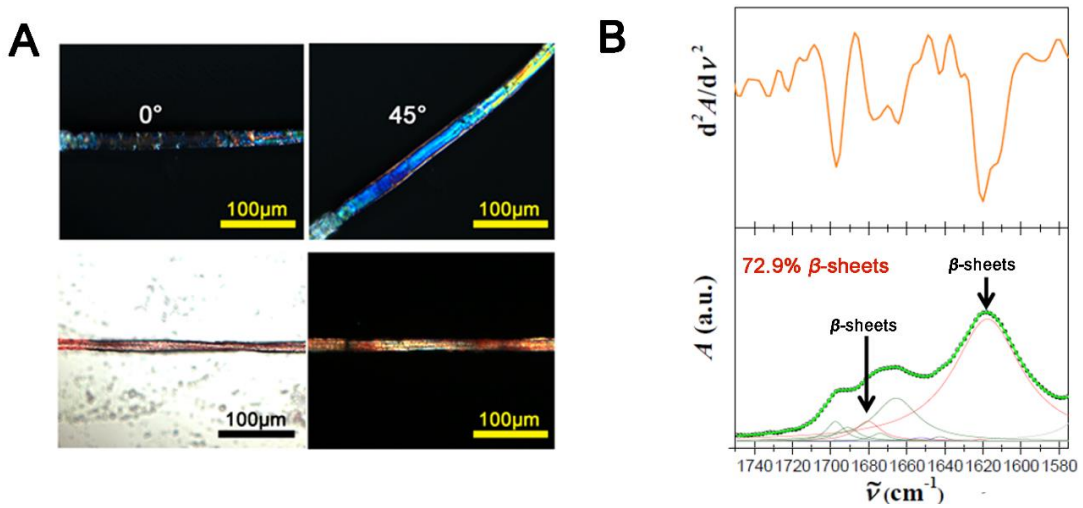

Figure 5.10 Secondary structure characterization of the self-assembled peptide fibers. Optical microscopy images of **(A)** fibers observed under polarized light at 0 ° (top left) and 45 ° (top right) and after Congo red staining under normal light (bottom left) and polarized light microscopy (bottom right). **(B)** De-convoluted FTIR spectra of fibers at the amide I region.

To further explore the properties of **AA12** peptide fibers, chemical, physical and thermal tolerance of the fibers were tested. Fibers resisted to dissolution when exposed to 8M denaturing urea for multiple days. When they were subjected to additional sonication, they resisted dissolution for up to 30 min. To probe the melting temperature and study the thermal degradation of the fibers, a DSC experiment was performed on a bundle of dried fibers. The resulting thermogram is shown in Figure 5.11 A. An endothermic peak was observed at 239.7 °C, with an energy input of 138 J/g for the transition. This phase transition was assigned to a melting event. The thermogram and melting temperature obtained were close to that reported in Latza *et al.*,[9] where a melting temperature of 220 °C was measured for the native SRT complex, which corresponds to the melting and disintegration of the *β*-sheet secondary structures within the native SRT. Therefore 239.7 °C is proposed to be due to *β*-sheets melting in the **AA12** peptide fibers.

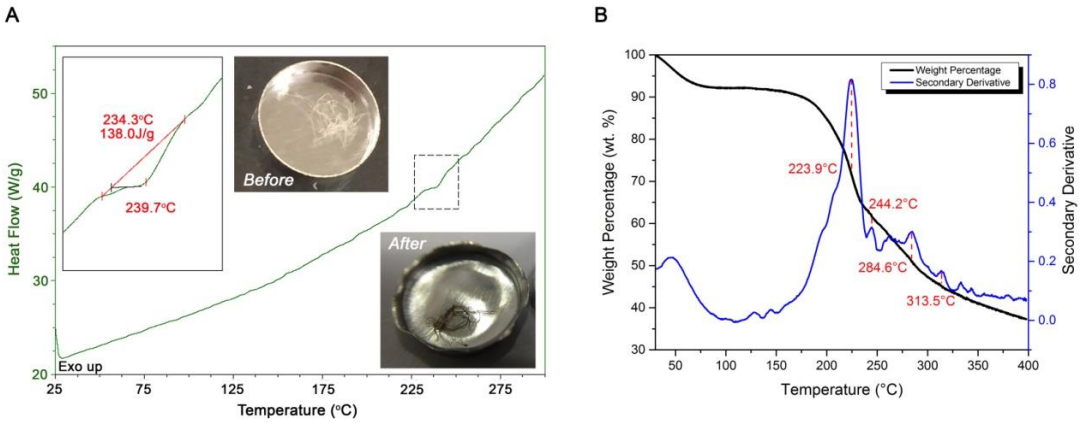

Figure 5.11 DSC and TGA characterizations. (A) DSC thermogram of **AA12** peptide fibers is shown, illustrating an endothermic peak at 239.7 °C (T_m), with onset at 234.3 °C and an energy requirement of 138 J/g. Insets show the zoom-in region of endothermic peak and fibers before and after DSC experiment, in Tzero pans. **(B)** TGA curve of **AA12** peptide powder is shown with the secondary derivative of the curve, highlighting the temperatures of degradation.

TGA experiment was performed on the precursor **AA12** peptide powder (Figure 5.11 B) to investigate the degradation properties of the short peptide. A 8 wt.% decrease in weight was recorded before 100 °C, which was attributed to the loss of water content in the powder. A sharp drop in weight corresponding to a degradation event at 223.9 °C was followed closely by a second degradation event at 244.2 °C. Degradation at 223.9 °C was attributed to the initial decomposition of the peptide, soon after the disintegration of β-sheet secondary structures occurring near 220 °C, as reported by Latza *et al.* for the native SRT complex. Subsequent weight loss was attributed to decomposition events of the amino acids.

The melting temperature of β-sheet secondary structures within the **AA12** peptide fibers obtained from DSC (239.7 °C) was higher than that of native SRT reported by Latza *et al*. and higher than the degradation temperature of the precursor peptide powder as well. This could be explained by the presence of extensive hierarchical structures constructing the fibers that are β-sheet-rich. The structurally mature fibers help to increase the thermal resilience of the structure, hence a higher amount of energy was required to break down the fibers and β-sheet constructs. In

addition, the **AA12** peptide fibers lacks the Gly-rich amorphous sequences, which could also explain their higher melting temperature.

From all the above biophysical characterizations, the fibers formed are highly amyloid-like in behavior and structure. The hierarchy of the fibers' structure extends from the peptide's contour length of *ca*. 45.6 Å (assuming 3.8 Å per residue) to nanofibrils with diameters of *ca*. 46 ± 9 nm. These nanofibrils align in parallel to form fibrils of diameters ca. 0.80 ± 0.14 μm, extending in the direction perpendicular to the nanofibrils. Hundreds of fibrils then bundle together to form fibers with diameters of up to 27 μm and 5 mm long. These fibers have relatively high β-sheet content and are extremely stable against chemical, physical and thermal degradation. To understand the material's properties and their processable range further, structural and mechanical characterization were performed in the following sections.

5.3.6 WAXS

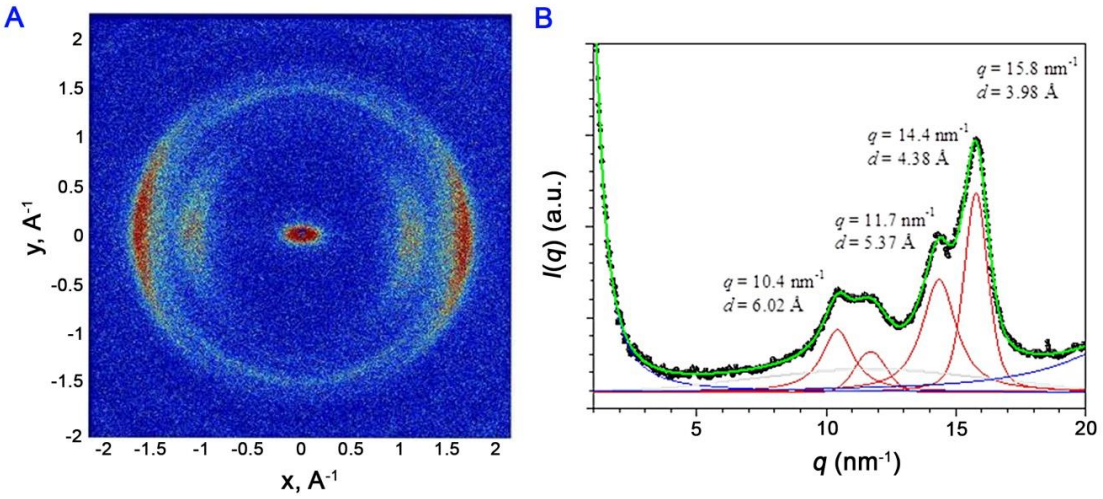

Figure 5.12 WAXS data of AA12 peptide fibers. (A) A representative 2D WAXS pattern and **(B)** the radial azimuthal integration pattern of the intensity as a function of the scattering vector *q*. Fiber axis was oriented vertically.

Molecular scale structural features of the **AA12** peptide fibers were investigated using X-ray scattering. Two-dimensional (2D) scattering pattern of WAXS is displayed in Figure 5.12 A and the radial azimuthal integration pattern of the WAXS pattern is displayed in Figure 5.12 B. The integrated intensity across the

azimuth reveals the presence of 2 main peaks, each with a shoulder peak, and the reflections were measured at q = 10.4, 11.7, 14.4 and 15.8 nm^{-1}, which corresponds to d-spacings of 4.38 Å along the meridian, and to d-spacings of 3.98, 5.37 and 6.02 Å for the equatorial reflections. The meridian peak was attributed to the inter-strand distance between cross-β strands (~ 0.44 nm), while the equatorial peaks were attributed to the inter-sheet distances. The molecular structure is proposed to be made up of a mixture of cross-β and parallel oriented β-sheets,[10] with inter-sheet distances of 0.54 nm and 0.60 nm. These inter-sheet distances do not fall within the classical parallel oriented β-sheets or cross-β dimensions,[11] however they resemble those of more tightly-packed cross-β inter-sheet distances observed from some synthetic polypeptides.[12, 13] Similarly, the inter-strand distance (0.44 nm) was also closer when compared to classical cross-β strand distances.[11] The more compact and tighter packing between the strands and sheets could explain the fiber's higher melting temperature and increased resistance to chemical and physical degradation.

5.3.7 Nanoindentation of self-assembled fibers

The mechanical properties of the **AA12** peptide fibers were characterized by nanoindentation. Fibers were first embed in epoxy resin. After polishing procedures to obtain the surfaces as illustrated in Figure 5.13 A (xx and yy planes), the embedded fibers were imaged via SPM (Figure 5.13 B) prior to indenting with a Berkovich tip. Under hydrated conditions, the modulus obtained in the xx direction was 1.30 ± 0.35 GPa, and in the yy direction 1.40 ± 0.02 GPa. Under dried conditions, the modulus obtained in the xx direction was 7.71 ± 1.23 GPa, and 6.61 ± 0.22 GPa in the yy direction.

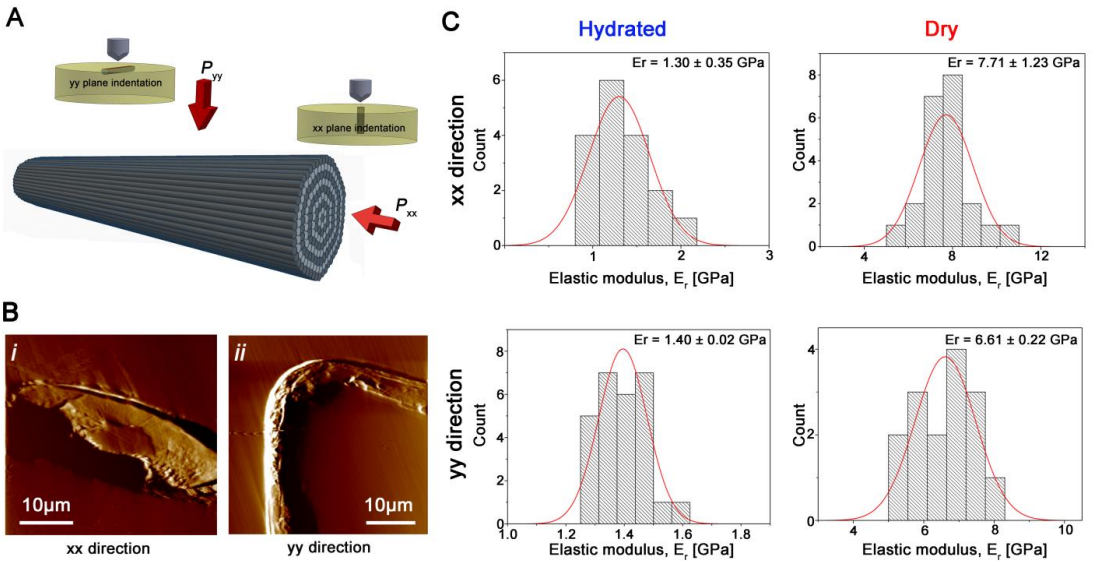

Figure 5.13 Mechanical characterization of peptide fibers via nanoindentation. (A) Schematic illustration of peptide fiber and direction of indentation to probe the mechanical properties from the xx and yy planes. **(B)** SPM images of (i) fiber's cross section (in the xx direction) and (ii) fiber's side section (in the yy direction). **(C)** Indentation results of the fibers in the xx and yy directions under hydrated and dry conditions.

The **AA12** peptide fibers exhibited similar modulus as compared to **A1** peptide fibers (Section 5.3) in both hydrated and dry states. With the addition of His-rich sequence to **A1** peptide, the moduli of the self-assembled fibers were preserved. These **AA12** peptide fibers were also similar in mechanical properties from both planes of indentation, and they exhibited similar robust modulus as the native SRT. Increasing the peptide building blocks' length from 6 to 12 residues and optimizing fiber formation conditions in solution, longer fibers of up to 200 times the length of the **A1** peptide fibers could be achieved (Figure 5.17).

Subsequently, the fibers were observed via FESEM imaging to ensure that the modulus values obtained were indeed from indents performed on the fibers' cross sections (Figure 5.14 B and D). Figure 5.14 shows both the optical microscope images of the xx (Figure 5.14 A) and yy (Figure 5.14 C) planes cross sections of the peptide fibers. Indents could be clearly observed from FESEM images, with two indents on the xx plane cross section indicated with red boxes and enlarged (Figure 5.14 B, right

images). The indents on the yy plane cross section are indicated with red boxes and enlarged in Figure 5.14 D.

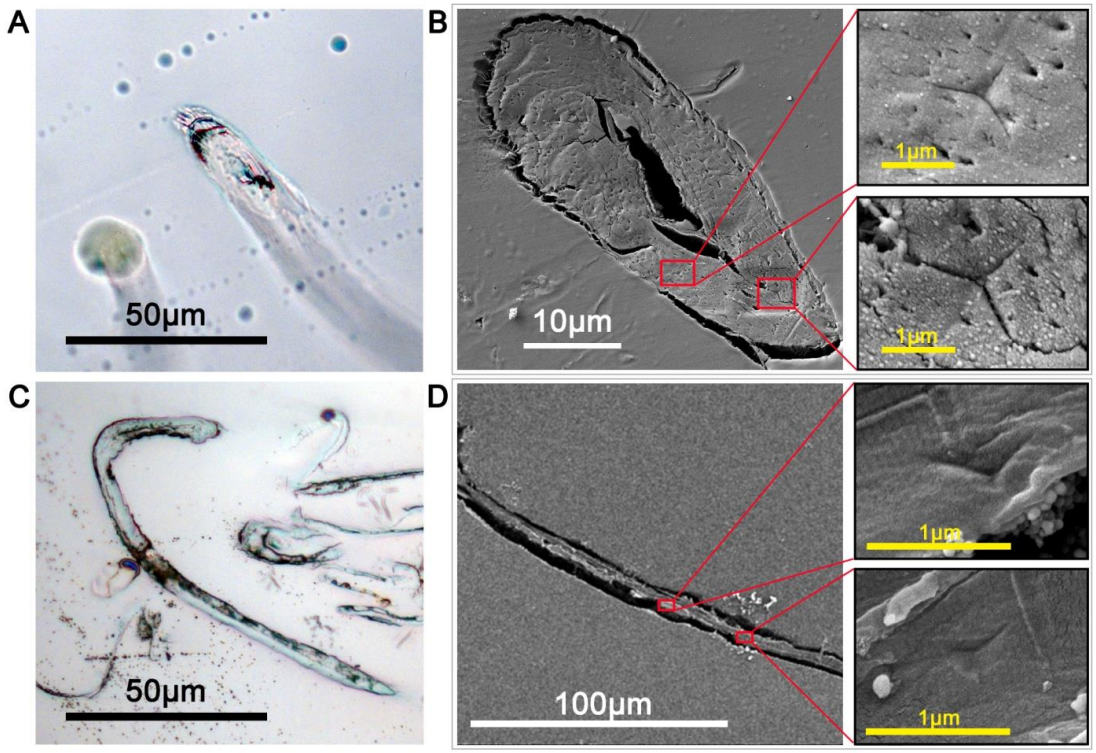

Figure 5.14 Cross-section images of AA12 peptide fibers. Cross-section images of **AA12** fibers from xx direction under **(A)** optical microscope and **(B)** SEM, with berkovich tip indentation imprints enlarged. Cross-section images of **AA12** fibers from yy direction under **(C)** optical microscope and **(D)** SEM, with berkovich tip indentation imprints enlarged.

5.3.8 Proposed structure of self-assembled fibers

MD simulations of peptide **AA12** in solution were performed, with an initial antiparallel fibril arrangement of the peptides, as determined by BeStSel fitting (Section 5.3.2), similar to that done for **A1** peptides in Chapter 4. This arrangement is postulated to be the most plausible arrangement of the peptides, favoring a high amount of stable β-sheets in this orientation. Figure 5.15 A shows a snapshot image during simulation at pH 4 and Figure 5.15 B shows a snapshot image at pH 7, with ribbons representing β-sheet.

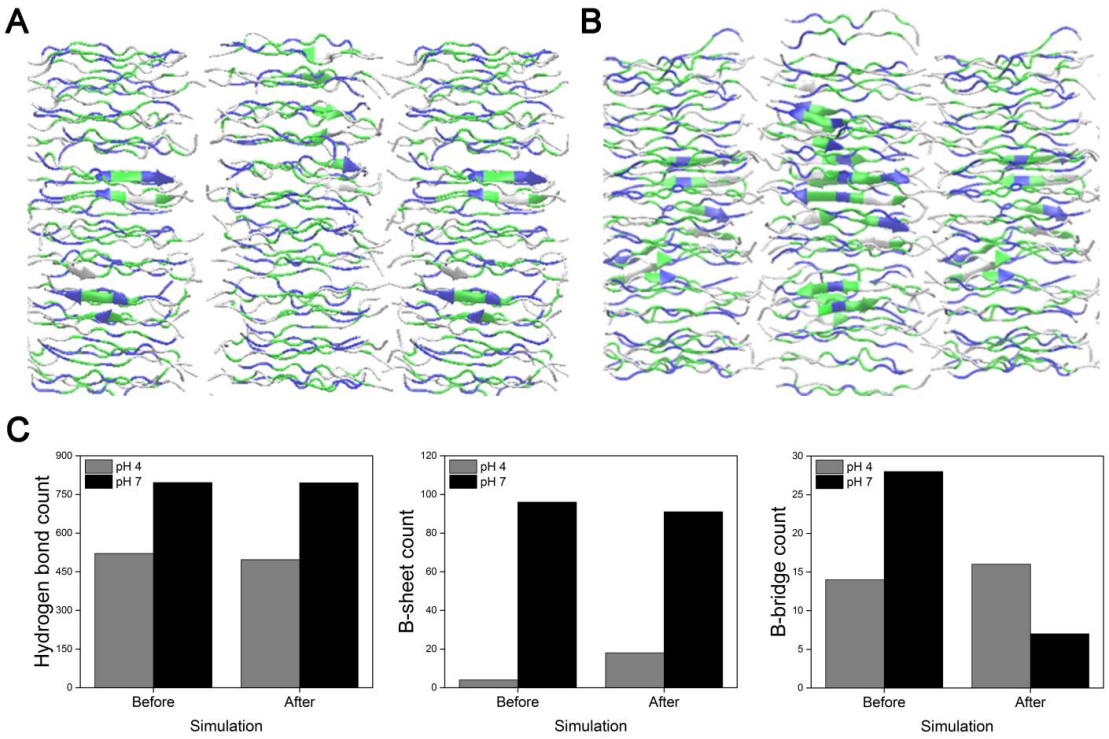

Figure 5.15 ***MD* simulations of peptide AA12.** Snapshots of simulation at **(A)** pH 4 and **(B)** pH 7. **(C)** Summary of simulation results, with hydrogen bond, β-sheet and β-bridge counts recorded before and after simulation.

The results of simulation are summarized in Figure 5.15 C. The total hydrogen bond count of the peptide system at pH 7 was 796 at the start of the simulations and remained relatively unchanged at 795 after simulation. At pH 4 on the other hand, the hydrogen bond count was lower in comparison, with 521 before simulation and 497 after simulation. β-sheet count at pH 4 increased from 4 to 18 after simulation, while β-sheet count at pH 7 was 5 times higher, at 96 before and 91 after simulation. This indicates that the high count of hydrogen bonds recorded at pH 4 did not significantly contribute to the formation of β-sheets, and they could be isolated hydrogen bonds or are involved in hydrogen bonds of non β-sheet secondary structures. β-bridge at pH 4 increased from 14 to 16 counts after simulation, while at pH 7, β-bridge dropped from 28 to 7 counts after simulation.

5.3.9 Discussion

Peptide selection

In the previous Chapter, Ala-rich suckerin peptides were found to spontaneously self-assemble into β-sheet-rich microfibrillar structures that are strongly reminiscent of amyloids, and extensive experimentation and *MD* simulation of these fibers highlighted the high stability of the cross-β structure adopted by Ala-rich modular peptides. With their modular sizes of 6 (**A1** peptide) to 7 (**A2** peptide) residues, they are well within the peptide length of amyloidogenic core sequences, which are usually four to seven amino acids.[14]

Amyloids exhibit a characteristic self-assembly growth model, where an initial lag phase precedes an accelerated growth phase until it reaches saturation (Figure 5.16).[15-19] During the initial lag phase, monomers and oligomers exist together in equilibrium. When oligomers assemble and reach a critical size, they act as seeds for the subsequent propagation of protofibril formation, which then assemble further to form mature amyloid fibrils. Once the seeds are formed, the growth process accelerates until it reaches saturation. Without addition of any precursor material, amyloid growth plateaus at the final saturated stage. With the amyloid-like sequence and behavior that Ala-rich peptides have shown in Chapter 4, it is plausible that these peptides self-assemble into microfibers via a similar growth model of seeding and propagation. They are very likely to constitute the main source of β-sheets in native SRT that contributes to the mechanical robustness of the teeth.[1]

On the other hand, His-rich suckerin peptides were found to be highly soluble under aqueous conditions, and they demonstrated propensity to form β-sheet-rich secondary structures as well, despite their transient states in solution. Considering the self-assembly of suckerin proteins from solution-state into solid-state SRT, assembly of the suckerins would most probably require a high protein concentration and therefore ample protein solubility. Thus, based on previous studies, a conclusion of this Chapter is that the appropriate building block selected from suckerin-19 improves the solubility and drive the self-assembly of longer and larger fibers, while maintaining the mechanical properties of the native SRT. To address the hypothesis and explore the possibly of fabricating suckerin-peptide inspired material, the highly

soluble His-rich peptide sequence was selected and added on to β-sheet seeding **A1** peptide sequence for further studies. This combination was postulated to drive the self-assembly into β-sheet rich fibers, and possess excellent solubility in aqueous conditions.

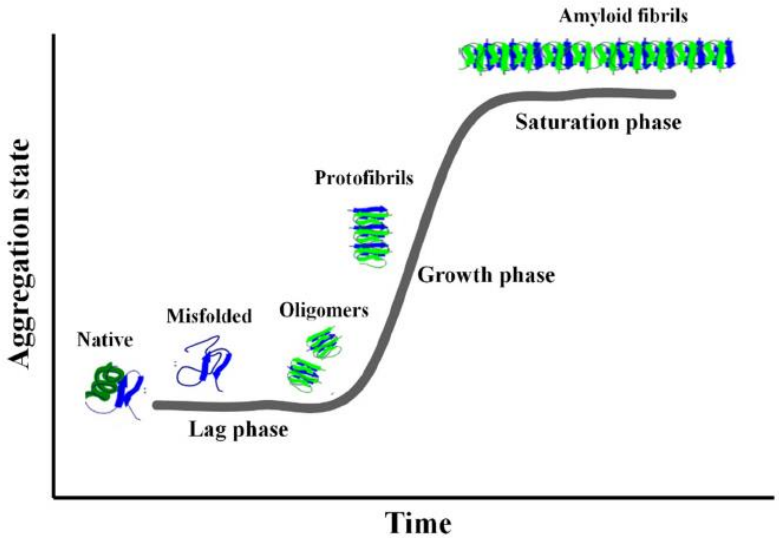

Figure 5.16 Amyloid aggregation phases. Growth of amyloid fibrils classified into three phases, lag phase, growth phase and saturation phase.[15]

*Characterization of **AA12** peptide in fully aqueous condition*

In contrast to DLS measurements of Ala-rich and His-rich peptides in different pH buffered solutions (Chapter 4), peptide **AA12** displayed comparatively no increase in their Z-average size measurements over a 24 hour period under similar conditions (Figure 5.4). Likewise at a concentration of 5 mg/mL, peptide **AA12** was also observed to remain soluble and stable without aggregating in fully aqueous pH buffered solutions of pH 4, 7 and 8.2 over 35 days, whereas peptides **A1** and **A2** formed aggregates during their incubation at pH 4, 7 and 8.6 at a concentration of 2 mg/mL. **AA12** peptide was also highly soluble up to 800 mg/mL in aqueous environments and remained stable in solution, which is a favorable property from a materials processing perspective.

CD spectroscopy showed that there was little to no change in **AA12** peptide spectra at pH 4 and 8.2, while changes in spectral characteristics (maxima and minima) and decrease in intensity were observed at pH 7 after 7 days of incubation (Figure 5.5),

which was similar to the trend observed for Ala-rich and His-rich peptides in Chapter 4. BeStSel predictions (Figure 5.6) identified that **AA12** peptide was mainly composed of β-sheet-rich structures, turns and other structures, whereas helical structures were absent essentially over 35 days. β-sheet structures were found to be fully antiparallel, with mostly relaxed and right-twisted sheets assigned by the de-convolution procedure. The 'others' structures assigned via BeStSel were attributed to PPII secondary structures. In previous studies of the short Ala-rich and His-rich peptides in Chapter 4, PPII was identified to be a highly possible structure adopted by the short peptides, and this transient conformation likely act as a precursor to β-sheets structures. With similar spectra maxima and minima characteristics between the shorter peptides and **AA12** peptides, it is reasonable to postulate that **AA12** peptides adopt PPII structures in solution as well. In summary, addition of His-rich peptides to **A1** peptide sequence improved the solubility while the high propensity for the formation of stable β-sheet and β-turn structures in solution remained unaffected.

MD simulations performed on **AA12** peptides in fully aqueous conditions (Figure 5.15) demonstrated the peptide's capability in forming β-sheet secondary structures that were highly stable at neutral pH when arranged in an antiparallel fibrillar pattern. At pH 4, the β-sheet count was significantly lower although hydrogen bond count remained comparatively high before and after a 200 ns simulation. This could be explained by the protonation of His residues at pH 4, which creates charge-charge repulsion between peptides in solution; thereby causing β-sheet structures to appear transient while a higher count of β-bridges (single hydrogen bond between β-strands) was recorded at pH 4 than at pH 7. *MD* simulations could be performed at increased timescales to observe if the conformations evolve, or if changing simulation force fields could yield different results. In any case, *MD* simulation provided an insightful perspective which support the solution and solid-state characterizations by CD, FTIR, WAXS and Congo red birefringent assay, confirming the high propensity of the **AA12** peptides to form antiparallel β-sheet structures.

*Length-scale comparison between **A1** and **AA12** fibers*

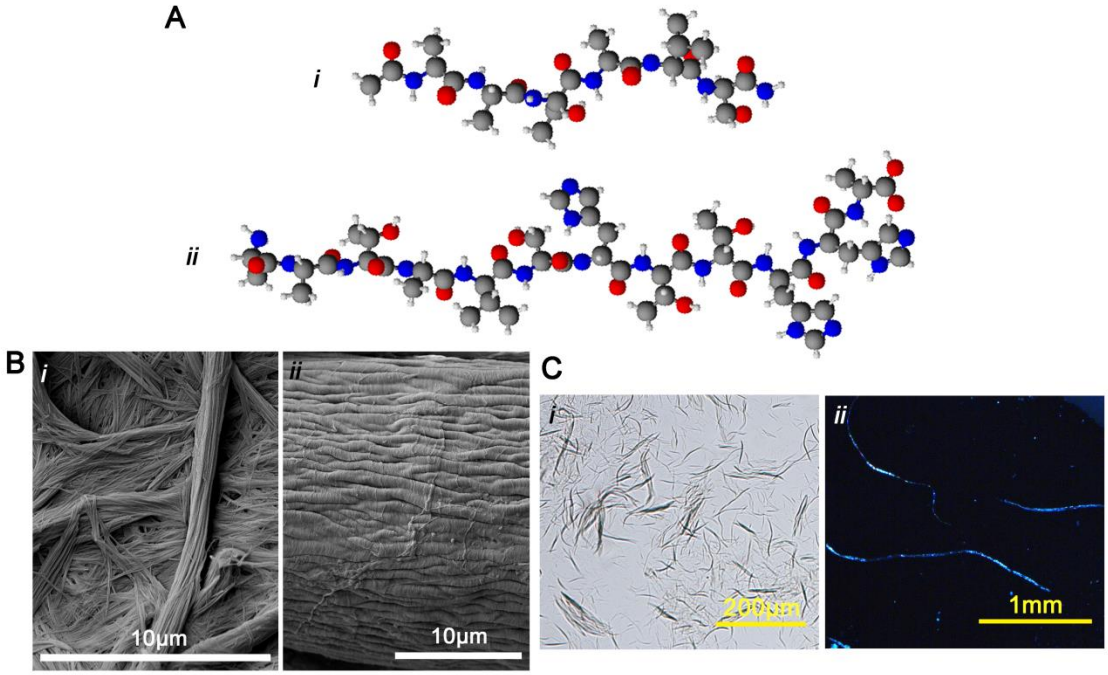

Figure 5.17 Summary of size comparison between A1 and AA12 β-sheet forming SRT peptide. (A) Ball and stick models of peptide (i) **A1** (refer to Chapter 4) and (ii) **AA12**. **(B)** FESEM images of self-assembled (i) **A1** fibers and (ii) side view of **AA12** peptide fiber, which is composed of many smaller fibrils. **(C)** Optical microscope images of (i) **A1** and (ii) **AA12** peptide fibers (viewed under polarized light for clearer illustration).

A summary of the length-scale comparison between solid-state fibers formed by peptide **A1** and **AA12** are shown in Figure 5.17. Ball and stick models of peptide **A1** and **AA12** in Figure 5.17 A illustrate the fundamental molecular structure differences. Assuming each amino acid residue contributes 3.8 Å to the length of the peptide,[20-22] the contour length of peptides **A1** and **AA12** would be 22.8 Å and 45.6 Å respectively. Figure 5.17 B compares the self-assembled fibers imaged by FESEM, showing the length-scale differences between the two, with **A1** peptides forming smaller fiber bundles, while peptide **AA12** formed an advanced hierarchical assembly of fibers, packed tightly together into a single large fiber. Figure 5.17 C compares the optical microscope images of self-assembled fibers. Peptide **A1** fibers are smaller, with lengths at the μm scale, while peptide **AA12** fibers are visible to the naked eye with longer lengths in the cm range. Peptide fibers increased in size with the addition

of His-rich sequence to **A1**, which improved the ease of fiber manipulation and processing.

Characterization of solid-state peptide fibers

Fibers formed by peptide **A1** and **AA12** were mechanically characterized. Microfibers formed by peptide **A1** exhibited modulus values similar to the native SRT (Figure 5.1) in both hydrated and dry states. This indicates that the β-sheet forming sequence indeed contributes to the mechanical property of SRT. Nanoindentation measurements performed on the longer **AA12** peptide fibers yielded similar results (Figure 5.13 C), with their modulus similar to that of the native SRT in both hydrated and dried states. Interestingly, **AA12** peptide fibers exhibit similar mechanical properties when indented from both xx plane and yy planes (Figure 5.13 C). Despite the anisotropy observed at the micro-scale lengths of the hierarchical fiber structures from FESEM (Figure 5.8) and from the fibers' birefringent property (Figure 5.10 A), the mechanical properties exhibited were isotropic. This suggests that load-bearing β-sheets are also orthogonally oriented relative to each other in the fibrils, which is consistent with the X-ray data. The uniformity of the fibers' mechanical properties could be an advantageous property for the fabrication of multi-direction functional materials.

FTIR spectroscopy measurements of the **AA12** peptide fibers revealed that the fibers were composed of high β structure content, with 72.9% β-sheet and 26.5% random coil detected (Figure 5.10 B), with minimal helical structures. From Congo red birefringent staining, various segments of these fibers showed yellow/apple green birefringence under polarized light, indicating the presence of cross-β amyloid structure in the fibers (Figure 5.10 A). The β-structures were identified to be a mix of cross-β and parallel oriented β-sheets from WAXS experiments (Figure 5.12). Similar to microfibers formed by peptide **A1**, **AA12** peptide fibers contained high β-sheet content with birefringent properties, evident that the biophysical properties were preserved even with the addition of His-rich sequence to the short **A1** peptide.

Thermal investigation via DSC (Figure 5.11 A) showed that the **AA12** peptide fibers did not undergo any phase transition between 25 °C to 234 °C, with the β-sheet melting event occurring at 239.7 °C, close to the melting point of β-sheet in the native

SRT (220 °C).[9] **AA12** peptide fibers lack the thermoplastic property of the native SRT material, as the Gly-rich sequences that constitute the amorphous phase for local melting during thermal-processing of the SRT were omitted. Constructed of mainly β-sheets, **AA12** peptide fibers would be stable to high temperatures until the melting temperature of the β-sheets is reached, whereby peptide degradation would follow simultaneously.

A degradation temperature at 223.9 °C (Figure 5.11 B) of the solid-state **AA12** peptide powder was obtained and attributed to the lack of higher-order β-sheet hierarchical structures that were observed for the **AA12** fibers. The solid-state fibers were resistant to harsh physical, chemical and thermal conditions, which allows for a wide range of working conditions for these fibers.

The fiber-forming conditions of **AA12** fiber remains to be optimized. By adjusting the solvent system, **AA12** peptide fibers could be reproducibly assembled from a mild condition of 5% acetonitrile in water, whereas with the increase in acetonitrile concentration, the self-assembly process of the β-sheet seeds could be kinetically controlled to propagate the fiber formation. With the understanding of the fiber's biophysical characteristics, conditions that favor β-sheet formation can be explored, and this would be highly favorable in the amyloid-like peptide fiber assembly.

5.4 Conclusions

Results in this chapter strongly suggest that the self-assembly of suckerin peptides follow an amyloid growth type of process, with a high propensity to form β-sheet seeds in solution, preceding the accelerated assembly into solid-state fibers.

With the addition of His-rich building block to Ala-rich peptide sequence, the resultant peptide of 12 amino acid residues, **AA12**, achieved the assembly of longer and larger fibers in an aprotic-protic solvent combination with mechanical properties that are similar to that of the native SRT. In a fully aqueous environment, **AA12** peptide displayed a high propensity to form stable β-sheet-rich structures observed by CD spectroscopy and was confirmed by *MD* simulation experiments. These β-sheet structures serve as building blocks that subsequently assemble into the solid-state fiber material. These fibers were composed of high β-sheet content, as shown by FTIR spectroscopy, Congo red staining, and WAXS experiments. Fibers assembled form an extensively organized and hierarchical assembly of smaller fibrils, and were resistant to harsh physical, chemical and thermal conditions, with a high β-sheet melting temperature at 239.7 °C.

The results highlight the importance of the amino acid sequence and length, which are crucial to the biophysical and mechanical properties of engineered peptide materials. While optimization of peptide materials from suckerin peptide **AA12** remains to be explored in future work, the solubility of the shorter Ala-rich peptide in aqueous condition was enhanced, and at the same time the solid-state fibers formed achieve biophysical and mechanical properties similar to the native SRT material. With the understanding gained from this chapter and improved processability of the longer peptides, we are a step nearer towards functional SRT peptide-inspired materials.

References

[1] P. A. Guerette, S. Hoon, D. W. Ding, S. Amini, A. Masic, V. Ravi, B. Venkatesh, J. C. Weaver and A. Miserez, *Acs Nano*, **2014**, 8, 7170-7179.

[2] P. A. Guerette, S. Hoon, Y. Seow, M. Raida, A. Masic, F. T. Wong, V. H. Ho, K. W. Kong, M. C. Demirel, A. Pena-Francesch, S. Amini, G. Z. Tay, D. Ding and A. Miserez, *Nat Biotechnol*, **2013**, 31, 908-915.

[3] A. Miserez, J. C. Weaver, P. B. Pedersen, T. Schneeberk, R. T. Hanlon, D. Kisailus and H. Birkedal, *Adv Mater*, **2009**, 21, 401-406.

[4] A. Micsonai, F. Wien, L. Kernya, Y. H. Lee, Y. Goto, M. Refregiers and J. Kardos, *P Natl Acad Sci USA*, **2015**, 112, E3095-E3103.

[5] N. Sreerama and R. W. Woody, *Protein Sci*, **2003**, 12, 384-388.

[6] T. K. K. Mong, A. Z. Niu, H. F. Chow, C. Wu, L. Li and R. Chen, *Chem-Eur J*, **2001**, 7, 686-699.

[7] R. A. Copeland, *Enzymes: A Practical Introduction to Structure, Mechanism, and Data Analysis*, Wiley, **2004**.

[8] M. Vatankhah-Varnoosfaderani, A. GhavamiNejad, S. Hashmi and F. J. Stadler, *Macromol Rapid Comm*, **2015**, 36, 447-452.

[9] V. Latza, P. A. Guerette, D. Ding, S. Amini, A. Kumar, I. Schmidt, S. Keating, N. Oxman, J. C. Weaver, P. Fratzl, A. Miserez and A. Masic, *Nat Commun*, **2015**, 6, 8313.

[10] J. M. Squire, D. A. D. Parry and A. Kajava, *Fibrous Proteins: Amyloids, Prions and Beta Proteins*, Elsevier Science, **2006**.

[11] A. V. Kajava, J. M. Squire and D. A. Parry, *Adv Protein Chem*, **2006**, 73, 1-15.

[12] H. Inouye and D. A. Kirschner, *Adv Protein Chem*, **2006**, 73, 181-215.

[13] L. M. Shinchuk, D. Sharma, S. E. Blondelle, N. Reixach, H. Inouye and D. A. Kirschner, *Proteins-Structure Function and Bioinformatics*, **2005**, 61, 579-589.

[14] J. D. Pham, N. Chim, C. W. Goulding and J. S. Nowick, *J Am Chem Soc*, **2014**, 136, 4446-4446.

[15] C. Iannuzzi, G. Irace and I. Sirangelo, *Molecules*, **2015**, 20, 2510-2528.

[16] S. R. Collins, A. Douglass, R. D. Vale and J. S. Weissman, *Plos Biol*, **2004**, 2, 1582-1590.

[17] B. O'Nuallain, A. D. Williams, P. Westermark and R. Wetzel, *J Biol Chem*, **2004**, 279, 17490-17499.

[18] Q. A. Acton, *Proteins: Advances in Research and Application: **2011** Edition*, ScholarlyEditions, 2012.

[19] P. Arosio, T. P. J. Knowles and S. Linse, *Phys Chem Chem Phys*, **2015**, 17, 7606-7618.

[20] H. P. Erickson, *P Natl Acad Sci USA*, **1994**, 91, 10114-10118.

[21] K. Trombitas, M. Greaser, S. Labeit, J. P. Jin, M. Kellermayer, M. Helmes and H. Granzier, *J Cell Biol*, **1998**, 140, 853-859.

[22] M. Carrion-Vazquez, P. E. Marszalek, A. F. Oberhauser and J. M. Fernandez, *P Natl Acad Sci USA*, **1999**, 96, 11288-11292.

Chapter 6

Discussion and Future Work

Previous chapters investigated the interactions between suckerin peptides and their assembly mechanism, followed by the fabrication and characterization of fiber material formed from these peptides. This chapter briefly summarizes the chronological progress of the findings and work performed in this thesis. In addition, potential prospects of suckerin peptide applications have been highlighted and future research areas have been proposed in this chapter.

6.1 Conclusions

Since initial reports describing the biochemistry and mechanical properties of Humboldt squid SRT,[1] the fundamental understanding of this protein-only extra-cellular tissue has broadened and deeper insights into the structural principles responsible for its intriguing properties from the meso-scale level all the way down to the genetic level have been gained from subsequent studies. This understanding has provided valuable lessons with regard to how Nature employs relatively weak building blocks to construct robust materials using supramolecular and multi-scale assembly design principles.

This thesis has focused on the highly modular nanoscale building blocks of the suckerin-19 protein: first to understand the role of the modular peptides and to investigate the interactions between these highly repeated building blocks. From the first part of the thesis, the modular peptides have been identified as playing specific roles within the protein. They provide load-bearing functions to SRT to withstand shear and compressive forces. Some peptides also appear to increase the solubility of the suckerins in the solution state. Using these insights and taking advantage of the suckerins' modular design, in the second part of the thesis, fibers were successfully fabricated from a selected suckerin peptide sequence, while maintaining the mechanical strength of native SRT. A central feature of both native SRT and the suckerin peptides is the absence of inter-chain covalent crosslinks, which enables the material to be processed under mild conditions, making SRT and suckerin peptides an original renewable and biodegradable natural biopolymer resource.

The studies performed in this thesis have provided detailed biophysical, chemical, structural and mechanical information on the peptide building blocks of SRT. While recombinant suckerins have been engineered into various functional and structural materials, with the information obtained here, the smaller peptide building blocks can be selectively employed to engineer advanced materials with properties that are tailored to the intended application's need. Given the versatility of suckerins and its suckerin peptides, a wide range of further applications may be envisioned in the near future. Ranging from the biomedical field to photonics to additive manufacturing, suckerin peptides may be incorporated into composite materials or nano-scale devices, or engineered into functional or structural materials. With the knowledge gained from

these studies, we have a new molecular bio-toolbox at our disposal to expand the above-mentioned possibilities

6.2 Outlooks and future studies

Recombinant suckerins have so far shown excellent biocompatibility and no cytotoxicity for *in vitro* experiments, and likewise, experiments can be performed on the suckerin peptides to investigate their biocompatibility. The next step would be to expand such studies *in vivo*, with the goal to further explore their applicability in the bioengineering and biotechnology fields. Since the peptides can be synthesized from single amino acid residues with high purity either manually or via automated synthesizers, scale-up of the production from gram scale to kilogram scale may be achieved within a short period of time. This would be an advantage from a production perspective. Potential uses could include tissue engineering scaffolds and drug delivery vehicles, biosensors and molecular switches, printed wearable electronics, multipurpose biomedical devices, or bioelastomer adhesives for wound healing or surgical sutures.

6.2.1 Hetero-peptide interactions

In Chapter 4, a peptide macro-array binding assay was used to study the binary interactions between the modular suckerin peptides. Subsequently, we focused our investigations on the homo-peptide interactions. In future studies, hetero-peptide interactions that exhibit high "hits" can be further investigated for their biophysical and structural properties. CD and FTIR spectroscopy could be used to study the secondary structures formed by these peptides, while DLS could be used to monitor their self-assembly properties. Similar to the experiments in Chapter 4, *MD* simulation of these hetero-peptides could be performed to examine their secondary structure propensities. By studying the interaction properties of the hetero combinations of the building blocks, the combination of functionalities that each peptide sequence inherits could be better understood and utilized for subsequent potential applications.

6.2.2 Affinity and binding strength of peptides

Affinities and binding strengths between suckerin peptides that exhibit strong interactions could be examined to understand their kinetic properties. Using techniques such as Surface Plasmon Resonance (SPR)[2-5] or Quartz Crystal Microbalance (QCM),[5, 6] selected peptides could be immobilized onto a flow cell surface while the complementary peptide could injected to the surface to allow interaction with the immobilized peptides. Association properties between the peptides could be obtained during the injection phase, while dissociation properties could be obtained after the injection stops and natural dissociation of the binding interactions occurs. These association and dissociation phases can be observed on a sensogram (an example of which is shown in Figure 6.1 A).

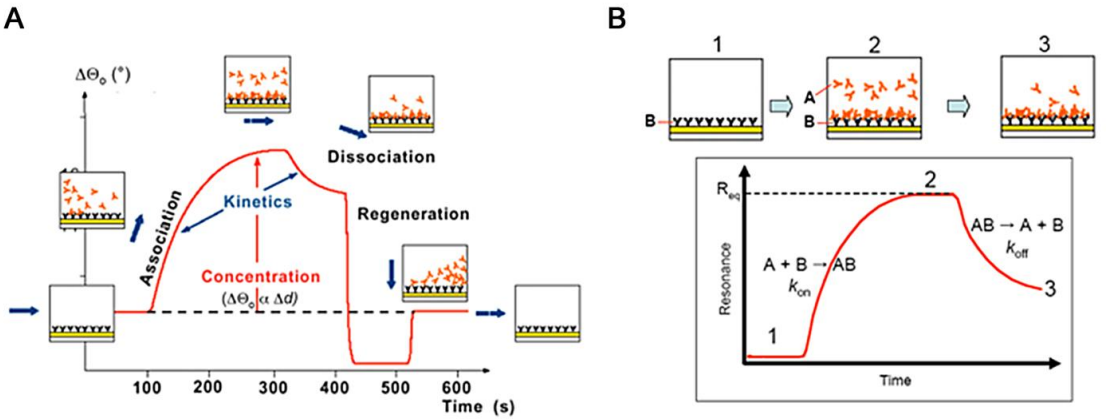

Figure 6.1 Example of sensograms and binding kinetics curves. (A) A sensogram obtained from SPR experiment between examples analyte 'A' and ligand 'B', with association, dissociation and regeneration segments indicated. **(B)** A processed binding kinetics curve obtained from sensogram, where K_{on} (association constant) and K_{off} (dissociation constant) can be derived from the respective curves.

These methods are quantitative, and the association and dissociation constants can be calculated from their respective curves (shown in Figure 6.1 B). The binding strength or binding constant of the peptides can then be calculated with the association and dissociation constant values. Each peptide pair could be quantitatively characterized by their binding strengths, which would be useful parameters for the selection of peptide building blocks to fabricate materials.

6.2.3 Further structural studies

During the H/D exchange NMR studies performed in Chapter 4, an interesting behavior of **A1** peptide was observed at 45 ºC. This behavior was attributed to a plausible phase transition of the peptide around 45 ºC under the given conditions. To further understand the phenomenon, further H/D exchange experiments could be performed at various temperatures around 45 ºC with smaller intervals, such as at 30 ºC, 35 ºC, 40 ºC, 50 ºC, 55 ºC and 60 ºC, to identify the onset and trend of the transition.

Solid state NMR[7-9] could be performed on peptide fibers that are exposed to the range of temperatures mentioned, to obtain 3D arrangements of the peptides within the fibers. These 3D structures would provide insight to the conformation changes observed and explain the transition experienced with the changes in temperature.

Differential Scanning Fluorimetry (DSF) technique[10] could be also used to study the thermal effects on the fibers, including their thermal degradation. This technique has been previously applied to study amyloids and silk proteins,[11] and could provide useful information on the thermal profile of the fibers, which could help explain the phase transition experienced around 45 ºC as well.

6.2.4 Optimize self-assembly of suckerin peptide fibers

In Chapter 5, self-assembly conditions of **AA12** peptide into fibers were explored by using solvent mixtures to promote the formation of fibers from solution. The solvents tested included methanol and acetonitrile in water. While the self-assembly of **AA12** peptide fibers was reproducible in acetonitrile and water mixture, more variations in their concentration composition and other solvent mixtures and conditions could be explored to optimize the solvent-driven self-assembly of these fibers. Polar aprotic solvents of different dielectric constants, such as acetone or Dimethyl Sulfoxide (DMSO), could also be tested to search for a greener or more biocompatible alternative. In addition, with the peptide being highly soluble up to concentrations of 800 mg/mL, an electrospinning technique[12, 13] could also be employed to extrude fiber material from solution.

6.2.5 Biocompatibility and cytotoxicity testing

In order to consider potential biomedical applications, the suckerin peptides should be tested for their biocompatibility and cytotoxicity. Since the recombinant suckerin proteins tested so far have exhibited no cytotoxicity to several cell types,[14] the results are promising for the suckerin peptides. Suckerin peptides could be tested with protocols mentioned in Ding *et al*.[14]

6.2.6 Exploring material types and application possibilities

Ala-rich suckerin peptides spontaneously assemble to form short amyloidogenic fibers as reported in Chapter 4, offering the possibility of developing amyloid-based functional materials and devices that have been described in Chapter 2. Longer Ala- and His-rich suckerin peptide fibers with similar robust mechanical properties as native SRT have also been extruded using mild. These fibers are mechanically tough and may represent promising candidates as load-bearing building blocks for nano-composites.

Certain Gly-rich suckerin peptides have also been tested in preliminary experiments and were shown to be capable of self-assembling into hydrogels (Figure 6.2 A) in aqueous solutions. They form a highly porous structure (Figure 6.2 B), with storage modulus in the kPa range (Figure 6.2 C), whereby their pore sizes and mechanical properties could be tailored by altering the peptides' concentration or by the incorporation of other peptides or polymers.

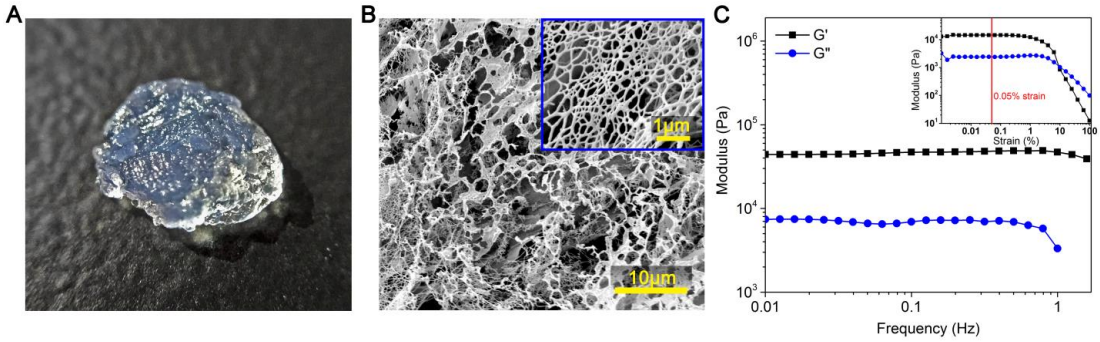

Figure 6.2 Suckerin peptide hydrogel formed by self-assembly in water. (A) Photo of a hydrogel formed by suckerin peptide. **(B)** SEM image of hydrogel's porous network, with inset illustrating the fibrillar structures forming the gel. **(C)** Rheological measurements of peptide hydrogel showing G' and G" at a constant strain of 0.05% over a range of frequency. Inset shows amplitude sweep where linear viscoelastic region was obtained and strain % was selected for frequency sweep.

Incorporation of suckerin short peptides into chitosan hydrogels via crosslinking have also been tested in preliminary studies. With the incorporation of peptides, porosity and moduli of the resultant gels could be tailored. Chitosan-peptide gels with varying pore sizes are presented in Figure 6.3, and these gels have increased moduli values with the addition of the suckerin peptides. The suckerin peptides could be used as additives to increase the moduli[15-17] of soft gels, as well as to adjust the pore sizes to suit to different cell types for 3D cell culture.[18, 19]

Since the length of the peptides is short compared to the suckerin proteins, synthesis and purification processes are simple and high yields can be obtained efficiently, which is favorable for mass scale production. With the easy processing of the peptide into fibers and hydrogels via self-assembly or cross-linking incorporation, the usage of these materials in the biomedical (for instance as 3D cell culture substrates) or cosmetic fields are envisioned.

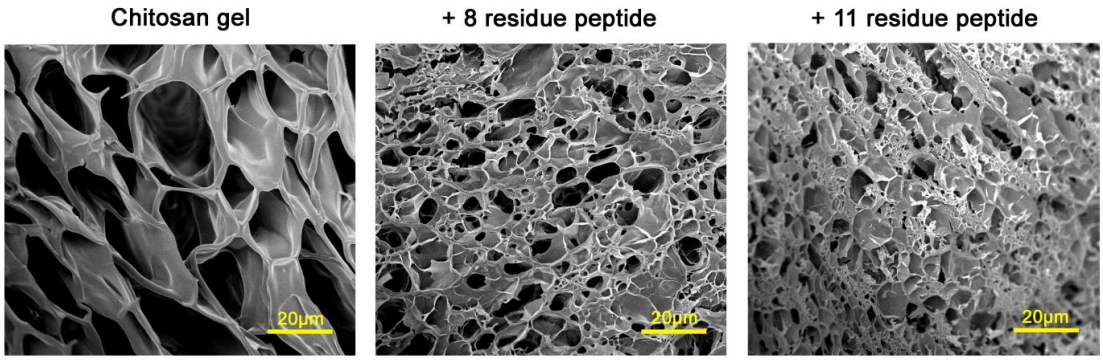

Figure 6.3 FESEM images of porous chitosan hydrogels. Chitosan hydrogels shown with and without addition of suckerin peptides. Pore size of hydrogels decreases with the addition of longer suckerin peptide.

References

[1] A. Miserez, J. C. Weaver, P. B. Pedersen, T. Schneeberk, R. T. Hanlon, D. Kisailus and H. Birkedal, *Adv Mater*, **2009**, 21, 401-406.

[2] B. Liedberg, C. Nylander and I. Lundstrom, *Biosens Bioelectron*, **1995**, 10, R1-R9.

[3] M. I. Aguilar and D. H. Small, *Neurotox Res*, **2005**, 7, 17-27.

[4] M. Piliarik, H. Vaisocherová and J. Homola, in *Biosensors and Biodetection*, eds. A. Rasooly and K. E. Herold, Humana Press, Totowa, NJ, **2009**, pp. 65-88.

[5] D. A. White, A. K. Buell, C. M. Dobson, M. E. Welland and T. P. J. Knowles, *Febs Lett*, **2009**, 583, 2587-2592.

[6] T. P. J. Knowles, W. M. Shu, G. L. Devlin, S. Meehan, S. Auer, C. M. Dobson and M. E. Welland, *P Natl Acad Sci USA*, **2007**, 104, 10016-10021.

[7] R. Tycko, *Annu Rev Phys Chem*, **2011**, 62, 279-299.

[8] M. Tang, G. Comellas and C. M. Rienstra, *Accounts Chem Res*, **2013**, 46, 2080-2088.

[9] S. L. Wang and V. Ladizhansky, *Prog Nucl Mag Res Sp*, **2014**, 82, 1-26.

[10] F. H. Niesen, H. Berglund and M. Vedadi, *Nat Protoc*, **2007**, 2, 2212-2221.

[11] F. Vollrath, N. Hawkins, D. Porter, C. Holland and M. Boulet-Audet, *Sci Rep-Uk*, **2014**, 4.

[12] R. L. Reis, N. M. Neves, J. F. Mano, M. E. Gomes, A. P. Marques and H. S. Azevedo, *Natural-Based Polymers for Biomedical Applications*, Elsevier Science, **2008**.

[13] M. Y. Li, M. J. Mondrinos, M. R. Gandhi, F. K. Ko, A. S. Weiss and P. I. Lelkes, *Biomaterials*, **2005**, 26, 5999-6008.

[14] D. W. Ding, P. A. Guerette, J. Fu, L. H. Zhang, S. A. Irvine and A. Miserez, *Adv Mater*, **2015**, 27, 3953-3961.

[15] K. Saha, A. J. Keung, E. F. Irwin, Y. Li, L. Little, D. V. Schaffer and K. E. Healy, *Biophys J*, **2008**, 95, 4426-4438.

[16] A. Banerjee, M. Arha, S. Choudhary, R. S. Ashton, S. R. Bhatia, D. V. Schaffer and R. S. Kane, *Biomaterials*, **2009**, 30, 4695-4699.

[17] W. S. Kisaalita, *3D Cell-Based Biosensors in Drug Discovery Programs: Microtissue Engineering for High Throughput Screening*, CRC Press, **2010**.

[18] N. Annabi, J. W. Nichol, X. Zhong, C. D. Ji, S. Koshy, A. Khademhosseini and F. Dehghani, *Tissue Eng Part B-Re*, **2010**, 16, 371-383.

[19] C. M. Hwang, S. Sant, M. Masaeli, N. N. Kachouie, B. Zamanian, S. H. Lee and A. Khademhosseini, *Biofabrication*, **2010**, 2, 035003.

List of Publications

Journal Papers

1. **Hiew, S. H.**, *et al.*, Modular peptides of thermoplastic squid sucker ring teeth form amyloid-like cross–β supramolecular networks, **Acta Biomaterialia** 2016, 46,
   41-54.
2. **Hiew, S. H.** and Miserez, A. Squid Sucker Ring Teeth: Multi-Scale Structure-Property Relationships, Sequencing, and Protein Engineering of a Thermoplastic Biopolymer, **ACS Biomaterials Science & Engineering** 2016, DOI: 10.1021/acsbiomaterials.6b00284.
3. **Hiew, S. H.**, *et al.*, Biomimetic peptides form Amyloid-like crystals with Robust Mechanical Properties, ready for submission, 2017.

Oral presentation

A Comprehensive Bottom-up Approach towards Biomimicry: Modular Peptide Interactions of Squid Sucker Ring Teeth Proteins with Silk-Like Sequence.
Euromat 2014, EPFL Lausanne, Switzerland.

Poster presentation

A Comprehensive Bottom-up Approach towards Biomimicry: Modular Peptide Interactions of Squid Sucker Ring Teeth Proteins with Silk-Like Sequence.
7th International Peptide Symposium 2015, Biopolis, Singapore.
Awarded: Best Poster Award